THE APPLICATION OF IN-SITU FOURIER TRANSFORM INFRARED SPECTROSCOPY TO THE ANALYSIS OF FUEL CELL ANODES AND MEMBRANES.

Thesis submitted by:

STEVEN WILLIAM MARK JONES

For the degree of Doctor of Philosophy

Newcastle University

School of Chemical Engineering and Advanced Materials

January 2015

Declaration

I hereby declare that the work embodied in this thesis entitled "The Application of *in-situ* Fourier Transform Infrared Spectroscopy to the Study of Fuel Cell Electrodes and Membranes," is the result of experiments carried out in the School of Chemical Engineering and Advanced Materials at Newcastle University.

Steven Jones,

October 2014,

Newcastle upon Tyne,

United Kingdom.

Acknowledgements

I would first like to thank my supervisor Prof. Paul. A. Christensen for his knowledge, support and friendship in all aspects of my training and development, without which this work would not have been possible.

I would like to thank all of the members of the Christensen Research Group, Abdullah Al-Abduly, Pierrot Attidekou, David Molyneaux, Daniel Lawrence, Panos Moussas, Supandee Manelok, Khalid Zakaria, Douglas Linares-Moya and Nutchapon Chiarasumran for their companionship throughout my studies.

I would also like to thank Neville Dickman for his technical expertise and support during optimization of the spectro-electrochemical cell design.

Finally, I would like to thank the EPSRC for funding this project under the Supergen Hydrogen and Fuel Cells Initiative, and the School of Chemical Engineering and Advanced Materials for providing me with the opportunity and facilities to carry out this research.

Abstract

This work in this thesis reports fundamental studies on fuel cell electrocatalysis and membrane stability, and is primarily of relevance to direct ethanol alkaline fuel cells and proton-exchange membranes based on polybenzimidazole (PBI). During the first part of this project, *in-situ* FTIR spectroscopy was employed to investigate the electrochemical oxidation of ethanol at a polycrystalline Pt electrode in 0.1 M KOH at 25 and 50 ^{o}C. Initially, this part of the project was designed to provide a library of IR spectra of intermediates and products to facilitate the study of the electro-oxidation of small organic molecules at novel, non-noble metal anodes. However, the work on Pt has provided some unexpected insights into this area of electrocatalysis, particularly with respect to the role of intermediates bonded through oxygen rather than carbon, as well as of adsorbed CO. Acetate was the only product observed at lower potentials. Above the transition potential, where at least some of the areas of the thin layer in the spectro-electrochemical cell become acidic, acetaldehyde, acetic acid and a small amount of CO_2 are produced. The temperature dependence of the production of acetaldehyde and acetic acid strongly suggests that the rate determining step is the removal of the first proton from the initially-adsorbed ethoxide species, and it was tentatively suggested that this is also the rds under alkaline conditions.

Ethanol oxidation in alkaline solution at a Pb-modified Pt electrode was also investigated using FTIR. This study provided some very interesting data which support the suggestion that the adsorption mechanism of ethanol is substantially modified in the presence of Pb, with a carbon-bonded intermediate being favoured leading to facile scission of the C-C bond in ethanol. Carbonate formation took place at potentials close to the thermodynamic value and at higher potentials, when Pb was lost to solution, the mechanism of oxidation of ethanol reverts to that found on a normal polycrystalline Pt surface, with the primary product being acetate.

During the second part of this project, undoped, cast films of PBI were investigated as a function of humidity using both H_2O and D_2O, and as a function of temperature up to 100 °C in order to better understand the IR response of this polymer, as well as to provide benchmark data for subsequent studies on acid doped PBI. Marked changes across the mid-IR range were observed during the uptake of water and D_2O.

The use of D_2O proved extremely useful in terms of deconvoluting the complex IR response observed and allowed the IR data to be rationalised in terms of the disruption of the N-H…N inter-chain hydrogen bonded network and changes in the morphology of the polymer.

Table of Contents

List of Figures

List of Tables

List of Publications

1. Christensen, P. A.; Hamnett, A. and **Jones, S. W. M.**, "*In Situ* FTIR Studies of Ethanol Oxidation at Polycrystalline Pt in Alkaline Solution.," *Journal of Physical Chemistry C*, 2012, 116 (46), 24681-24689, DOI: 10.1021/jp308783y

2. Christensen, P. A.; Hamnett, A. and **Jones, S. W. M.**, "An in situ FTIR spectroscopic study of the electrochemical oxidation of ethanol at a Pb-modified polycrystalline Pt electrode immersed in aqueous KOH.," *Physical Chemistry Chemical Physics*, 2013, 15(40), 17268-17276, doi: 10.1039/c3cp53194e.

3. Christensen, P. A. and **Jones, S. W. M.**, "An in situ FTIR study of polybenzimidazole as a function of relative humidity.," *Polymer Degradation and Stability*, 2014, 105, 211-217, DOI: 10.1016/j.polymdegradstab.2014.04.020

4. Christensen, P. A.; Hamnett, A. and **Jones, S. W. M.**, "An In-situ FTIR Study of Ethanol Oxidation at Polycrystalline Platinum in 0.1M KOH at 25 °C and 50 °C.," *Journal of Physical Chemistry C*, 2014, 118(51), 29760-29769, DOI: 10.1021/jp507689d

List of Abbreviations

Nomenclature

B	Beam-splitter (in the Michaelson Interferometer)
C	Concentration /M dm^3
C_1	Direct route for EtOh oxidation via C-C bond retention
C_2	Indirect route for EtOH oxidation via C-C bond cleavage
e^-	Electron
E	Electrode potential /V
E	Oscillating electric vector of an unpolarised IR ray
E_a	Anodic Potential Limit
E_c	Cathodic Potential Limt
E_s	Electric vector of s-polarised light
E_p	Electric vector of p-polarised light
E^o	Standard electrode potential /V
D	Detector of the FTIR spectrometer
d	Distance of the CaF_2 prismatic window from the Pt electrode /m
I	Intensity of transmitted light
I_F	Oxidation peak current during the forward scan of a CV
I_B	Oxidation peak current during the back (reverse) scan of a CV
I_o	Intensity of incident light
l	Optical path length /m
S	IR Source (in the FTIR spectrometer)
S_R	Reference FTIR spectrum
S_s	Sample FTIR spectrum
T	Temperature /^{o}C
x	Retardation of the moving mirror (in the Michaelson Interferometer) from either side of the zero path distance.

Greek Symbols

δ	Asymmetric stretch in organic molecules
λ	Wavelength (light, IR retardation, X-ray etc.)
ε	Extinction Coefficient
θ	Angle of incidence of the IR beam at the Pt electrode
ν_1	Common literature nomenclature for the symmetric stretch of bonds
ν_3	Common literature nomenclature for the asymmetric stretch of bonds

Acronyms

AAEM	Alkali Anion-Exchange Membrane
ADAFC	Alkali Direct Alcohol Fuel Cell
AEM	Anion-Exchange Membrane
ATR	Attenuated Total Reflectance
CE	Counter Electrode
CL	Catalyst Layer
CV	Cyclic Voltammetry/Voltammogram
DAFC	Direct Alcohol Fuel Cell
DEFC	Direct Ethanol Fuel Cell
DEMS	Differential Electrochemical Mass Spectroscopy
DFAFC	Direct Formic Acid Fuel Cell
DMFC	Direct Methanol Fuel Cell
EMIRS	Electrochemically Modulated InfraRed Spectroscopy
EOR	Ethanol Oxidation Reaction
FM	Fixed Mirror (in the Michaelson Interferometer)
FTIR	Fourier Transform InfraRed
GDL	Gas Diffusion Layer
HT-PEMFC	High Temperature Proton-Exchange Membrane Fuel Cell
IEC	Ion-Exchange Chromatography
IEC	Ionic Exchange Capacity
IRE	Internal Reflection Element
LD	Laser Detector (in the FTIR spectrometer)

LSV	Linear Sweep Voltammetry
MCT	Mercury Cadmium Telluride
MEA	Membrane Electrode Assembly
MI	Michaelson Interferometer
MM	Moving Mirror (in the Michaelson Interferometer)
MMO	Mercury/Mercury Oxide (reference electrode)
ORR	Oxygen Reduction Reaction
OTTLE	Optically Transparent Thin-Layer Electrolyte
PAC	Polymer-Acid Complex
PEM	Proton-Exchange Membrane/Polymer Electrolyte Membrane
PEMFC	Proton-Exchange Membrane
PMRS	Polarization Modulation Reflectance Spectroscopy
RDS	Rate-Determining Step
RE	Reference Electrode
RH	Relative Humidity
RHE	Reference Hydrogen Electrode
RL	Reference Laser (in the FTIR spectrometer)
ROMP	Ring Opening Metathesis Polymerisation
RRDE	Rotating Ring Disk Electrode
SCE	Saturated Calomel Electrode
SERS	Surface Enhanced Raman Spectroscopy
SHE	Standard Hydrogen Electrode
S/N	Signal-to-Noise Ratio
SNIFTIRS	Subtractively Normalized Interfacial Fourier Transform Infra-Red Spectroscopy
SXS	Surface X-ray Scattering
UPD	UnderPotential Deposition
WE	Working Electrode

1. Introduction

1.1 Hydrogen Fuel Cells

1.1.1 The Fuel Cell Concept

It is generally accepted that the environmental impact of the use of traditional energy sources such as fossil fuels, coupled with the global rise in energy demand, poses serious challenges in terms of energy sustainability, environmental protection and the search for alternative sources of energy in the future [1]. This has led to significant interest in the concept of a hydrogen-based economy, however it is not yet recognized as a viable alternative worldwide, and considerable advances in the science of sustainable hydrogen production and storage for fuel cell applications are required [1-2].

A fuel cell can be considered as an electrochemical energy converter, in which the chemical energy of a fuel is converted into direct current (DC) electric power in a single step, circumventing the conventional multi-step process of energy conversion associated with fuel combustion [3].

The fundamental concept of the hydrogen fuel cell is very simple, and was first demonstrated by a lawyer and amateur scientist named William Grove in 1839 [4-6]. Figure 1.1(a) shows the experimental procedure employed by Grove, where electrolysis of water into hydrogen and oxygen is achieved via the application of an electric current. Replacing the power supply with an ammeter (see fig. 1.1(b)) allows for reversal of the electrolysis during which a small current flows, due to the recombination of hydrogen and oxygen at the Pt anode and cathode, producing an electrical current [6]. This process can also be considered as the electrochemical combustion of hydrogen [6], producing electrical energy as opposed to the liberation of heat, the overall fuel cell reaction being:

$$2H_2 + O_2 \rightarrow 2H_2O \qquad (1.1)$$

The experiment conducted by Grove provides a reasonable explanation of the fundamental concept of the fuel cell. However, due to the low contact area between the electrolyte, electrode and gas, as well as the large distance between the two electrodes (resulting in high electrolyte resistance), the current generated in this

process was considerably smaller than desired, such that five of Grove's fuel cells were required to electrolyse water into H_2 and O_2 in a single electrolysis cell [6].

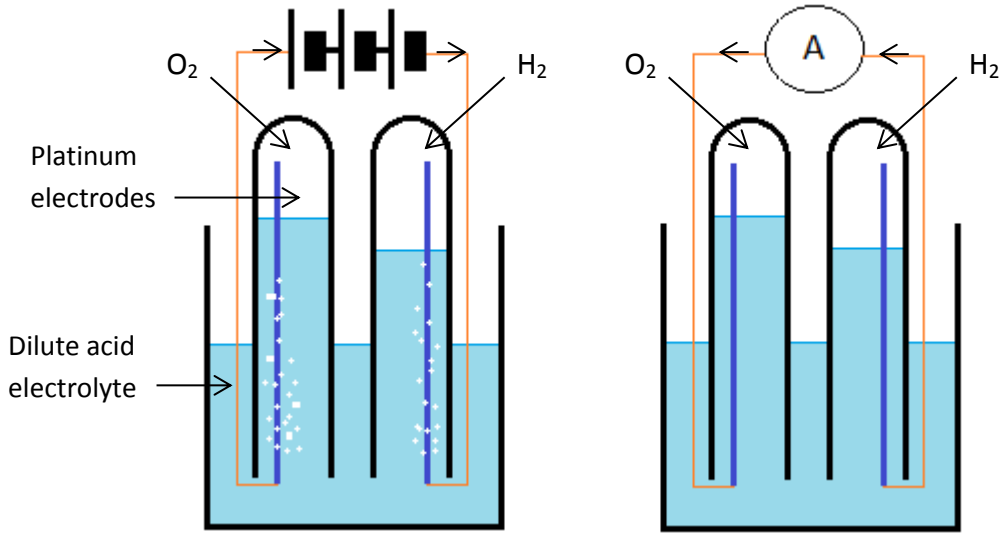

Figure 1.1. (a) The electrolysis of water to H_2 and O_2 via the application of an electric current. (b) The recombination of hydrogen and oxygen to generate a small current. Note: flow of electrons from – to + indicated by arrows.

The reactions which take place at the anode depend on the fuel (the oxidant reduced at the cathode is typically oxygen), whilst the most common electrolyte employed is acidic, as utilised by Grove [6]. Considering the anodic reaction of an aqueous, acid-electrolyte fuel cell, protons are produced via ionization of H_2 gas, which releases electrons as follows [7]:

$$2H_2 \rightarrow 4H^+ + 4e^- \qquad (1.2)$$

At the cathode, oxygen reacts with the electrons and protons produced from the reaction at the anode to form water:

$$O_2 + 4e^- + 4H^+ \rightarrow 2H_2O \qquad (1.3)$$

In order for both of these reactions to occur continuously, a sufficient supply of electrons from the anode must be transferred to the cathode via an external load circuit. Furthermore, the protons must travel through the electrolyte from anode to cathode, hence the use of acidic electrolytes. As well as aqueous acidic electrolytes,

specific polymers can be employed which contain mobile protons, these materials being referred to as proton exchange membranes or polymer electrolyte membranes (PEM's, see section 1.3) [5-7].

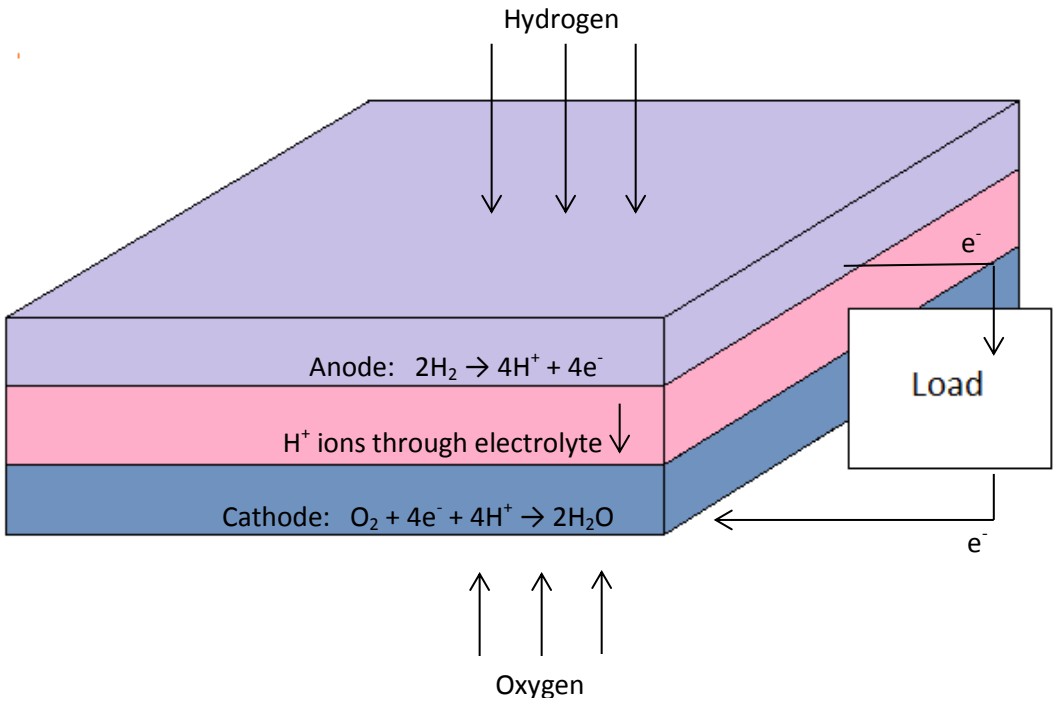

Figure 1.2. Schematic depicting the basic fuel cell construction, showing the half-cell reactions for an acidic electrolyte H_2/O_2 fuel cell. Note: electrons flow from anode to cathode, but conventional current flow is from the cathode to anode [6].

1.1.2. Proton-exchange membrane H_2/O_2 fuel cells

The development of proton-exchange membrane fuel cells (PEM-FCs), also referred to as polymer electrolyte membrane fuel cells, is considered to be one of the most promising routes to sustaining the proposed hydrogen economy [2]. PEM-FCs are based on the highly efficient (ca. 60% [1]) and low polluting conversion of chemical energy from hydrogen, low weight alcohols or formic acid fuel, into electrical energy [1].

PEM-FCs are modular and of simple design, meaning that, in principle, scale-up is easily achieved to sizes suitable for applications such as transport, which currently accounts for approximately 60% of worldwide petroleum consumption [3][8]. In

addition to transport, the application of fuel cells in stationary power generation has the potential to reduce dependency on the electrical grid.

1.1.3. The operation of polymer-electrolyte membrane fuel cells

Central to the design of PEM-FCs is the proton conductive polymer membrane, which acts as the electrolyte, is impermeable to gases and electronically insulating [3]. The electrolyte membrane is sandwiched between the anode and cathode, both of which are porous and electronically conductive. The anode and cathode typically comprise two layers of very high surface area, porous carbon. The layer next to the PEM, the catalyst layer (CL), consists of porous carbon particles coated with particles of the catalyst (eg. Pt) [5][10]. The next layer out, the gas diffusion layer (GDL), is uncoated porous carbon which spreads the H_2 and O_2 gas evenly across the CL [9]. Finally, these layers may be pressed onto a carbon paper or carbon cloth to provide support [6]. Figure 1.3 shows a single H_2/O_2 PEM fuel cell, which yields a working voltage between 0.5 and 0.8 V [5] depending on the load. It should be noted that for practical purposes, individual fuel cells are combined in series to form a stack in order to provide sufficient cell voltage.

A feed of hydrogen is supplied to the anodic side of the membrane electrode assembly (MEA, see section 1.1.4.), where it is oxidised to protons, releasing electrons (1.2). The protons travel through the proton conductive membrane, with the electrons passing from the anode around an external circuit to the cathode. As illustrated by Grove [6], the oxygen fed at the fuel cell cathode reacts with the protons and electrons to produce water (1.2). This water is then transported out of the cell with waste gas.

$$\text{Anode: } H_2 \rightarrow H^+ + e^- \quad E^0 = 0 \text{ V vs. SHE} \tag{1.4}$$

$$\text{Cathode: } ½O_2 + 2H^+ + 2e^- \rightarrow H_2O \quad E^0 = 1.229 \text{ V vs. SHE} \tag{1.5}$$

$$\text{Overall: } H_2 + ½ \rightarrow H_2O \quad E^0 = 1.229 \text{ V vs. SHE} \tag{1.6}$$

The overall redox reaction results in a continuous current of electrons at the external load circuit, thus producing direct electrical current [3].

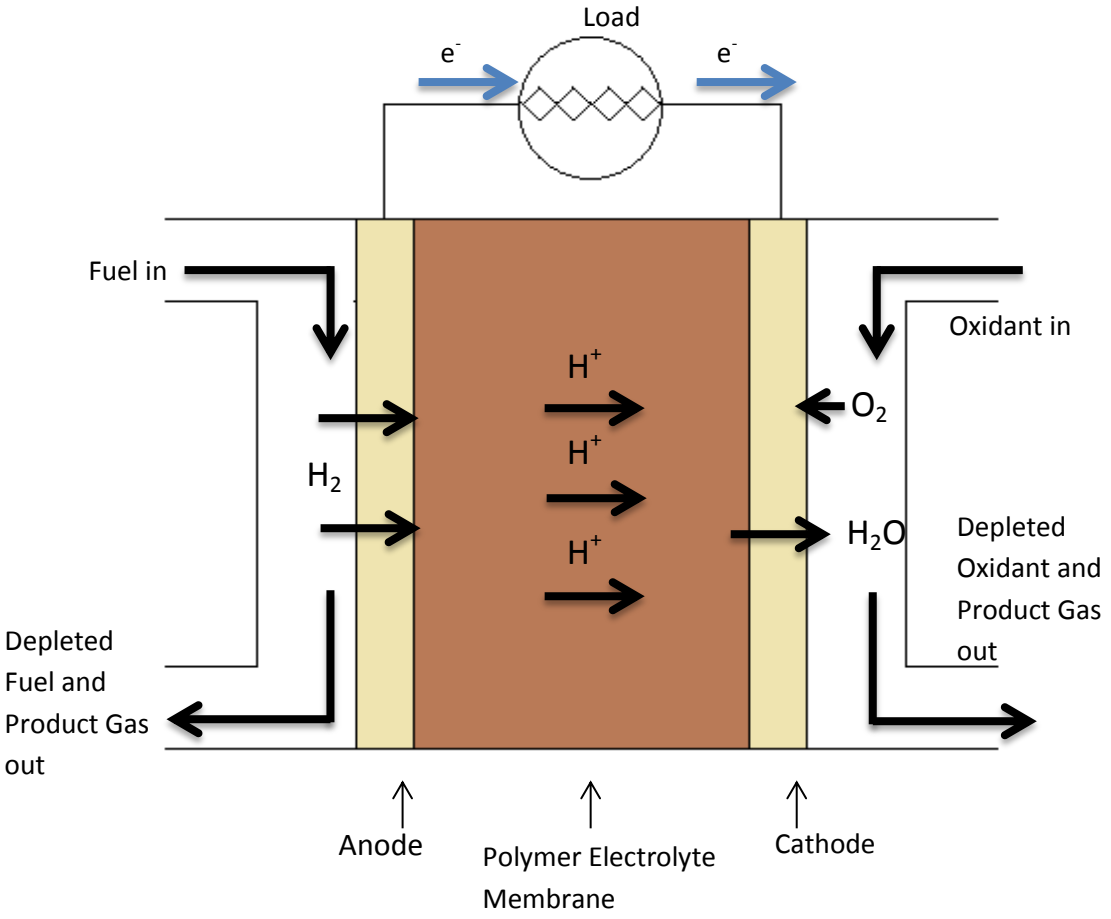

Figure 1.3. Schematic representation of a single PEM-FC, showing the basic operating principles [3].

1.1.4. The membrane electrode assembly

The electrochemical reactions (1.4) and (1.5) take place at the catalyst surface in the CL [4-5]. More specifically, the reaction occurs at an area of the catalyst which is accessible to gas (fuel at the anode and oxygen at the cathode), electrons and protons participating in the reaction (fig. 1.4). The electrons travel through electrically conductive solids (including the catalyst), whereas protons travel through the PEM. In addition, the electrodes must be porous due to the fact that reactant gases travel only through voids, thus allowing gas transport to the reaction sites. Hence, the fuel cell reactions take place at a three-phase boundary, specifically the PEM, solid and void phases [3]. A standard, free standing unit comprised of an anode, polymer-electrolyte membrane and cathode hot-pressed together is called a MEA [11].

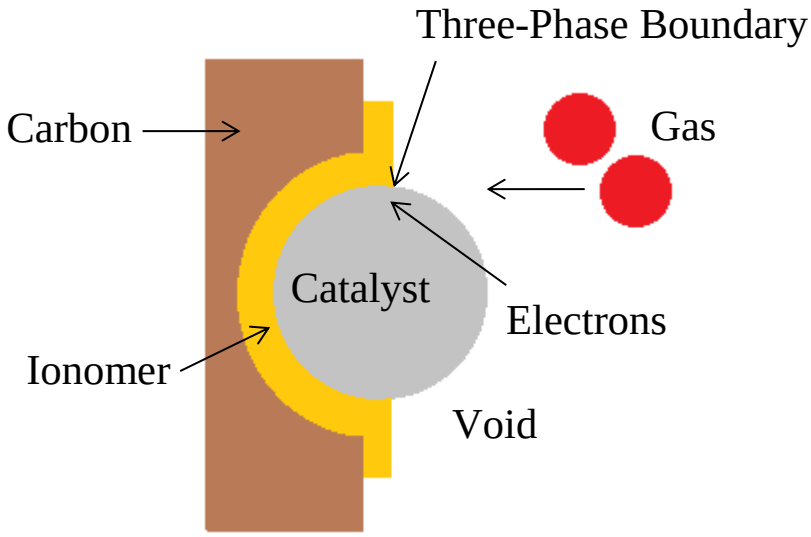

Figure 1.4. Graphical representation of the three-phase boundary at which electrode reactions take place, redrawn from [3].

1.1.5. Hydrogen production for use in fuel cells

One of the greatest challenges to the proposed hydrogen economy comes from the need for an efficient and environmentally friendly method of hydrogen production [12]. The dominant source for production of hydrogen is the steam reforming of hydrocarbon fuels; this is due to the current availability of methanol and propanol, as well as the abundance of natural gas [3][6][13]. Furthermore, steam reforming is the most cost efficient method of hydrogen generation as long as these fuels are cheaply accessible [5][6].

Steam reforming, as the name suggests, is the reaction of hydrocarbons with steam at high temperature (>500 ^{o}C) [3][6][13], in the presence of a metal catalyst, such as nickel, to form carbon monoxide and hydrogen as follows:

$$CH_4 + H_2O \rightarrow CO + 3H_2 \qquad (1.7)$$

Carbon monoxide also reacts with water via the water gas-shift reaction to produce additional hydrogen:

$$CO + H_2O \rightarrow CO_2 + H_2 \qquad (1.8)$$

As shown in (1.8), steam reforming leads to the production of CO_2 which is a disadvantage in terms of PEM-FC operation due to the fact that it dilutes the hydrogen feed to the anode. Another disadvantage associated with steam reforming is the poisoning of Pt-based catalysts at PEM-FC anodes by CO due to its strong adsorption, which leads to the requirement of complex and expensive CO-removal systems [5,13].

Thus, although hydrogen is the most commonly employed fuel in PEM-FCs, production in its pure form is currently expensive, in addition, serious challenges are posed by its handling, transportation and storage [14-16]. As a result, interest has been shown in the use of hydrogen-rich liquid alcohols as fuels for direct alcohol fuel cells (DAFCs) due to their significantly higher energy density, as well as ease of storage, transport and handling [17].

1.2. Direct Ethanol Fuel Cells

1.2.1. Overview

Considerable interest has been shown in the utilisation and development of fuel cells which use alcohols of low molecular weight, such as methanol, ethanol, ethylene glycol and propanol, as opposed to hydrogen [18]. Liquid fuelled PEM-FCs are especially advantageous in electrical vehicle applications [19] due to their low cost and compact nature, with no need for on-board reformers.

Significant attention has recently been focussed on Direct Ethanol Fuel Cells (DEFCs) [20][21], which are based on the electrochemical oxidation of ethanol to produce carbon dioxide, one of the main advantages of which is the high theoretical energy density ($8kWh.kg^{-1}$) [18] of ethanol. This energy arises from the complete oxidation of ethanol, via cleavage of its C-C bond, to CO_2, carbonate or bicarbonate at the fuel cell anode, depending on the pH of the electrolyte used, coupled with O_2 reduction at the cathode [17][20]:

$$C_2H_5OH + 3H_2O \rightarrow 2CO_2 + 12H^+ + 12e^- \quad E^0 = 0.1\ V \tag{2.2}$$

$$C_2H_5OH + 5H_2O \rightarrow 2HCO_3^- + 14H^+ + 12e^- \quad E^0 = 0.18\ V \tag{2.3}$$

$$C_2H_5OH + 5H_2O \rightarrow 2CO_3^{2-} + 16H^+ + 12e^- \quad E^0 = 0.19\ V \tag{2.4}$$

$$O_2 + 4H^+ + 4e^- \rightarrow 2H_2O \qquad E^0 = 1.23\ V \tag{2.5}$$

Ethanol is also considered as a 'green' chemical which can be produced in large quantities as a biofuel via the fermentation of biomass, a process which already exists on the industrial scale [20]. Furthermore, ethanol and CO_2 are considered to be of relatively low toxicity when compared to alternate alcohol fuels such as methanol [22][23]. As a fuel, methanol is the simplest organic alcohol, with faster electrochemical reaction kinetics compared to other alcohols. However, the widespread consumer use of methanol in fuel cells is limited by its toxicity, and ethanol has been recognised as a viable fuel alternative [24].

1.2.2. Ethanol Electrochemical Oxidation Mechanism

Figure 1.5 shows the "dual path" mechanism proposed throughout the literature for the electro-oxidation of ethanol at noble metal catalysts [20][21]: the C_2 or indirect route involves cleavage of the C-C bond in ethanol to produce CO_2 (steps 1 and 2) and is a 12 electron process with a high theoretical energy density. In contrast, the direct oxidation of ethanol does not lead to C-C bond cleavage and results in the production of acetic acid and/or acetaldehyde.

The mechanism of ethanol electro-oxidation at Pt in acid electrolyte depends critically upon whether ethanol is removed from solution following chemisorption; if it is removed, oxidation of the chemisorbed fragments leads only to CO_2 [25-27]. However, in the presence of ethanol, CO_2 is only a minor product (most likely due to the oxidation of initially adsorbed ethanol) with acetaldehyde and acetic acid as the major products (steps 3 and 4 in fig. 1.5), the distribution of the products depending upon ethanol concentration and potential [29-32].

The main reaction pathway for ethanol oxidation in acidic media proceeds with conservation of the C-C bond in ethanol, leading to unwanted, polluting products of acetic acid and/or acetaldehyde, this yielding only 2 and 4 electrons respectively [23][33][34]. Both of these products are stable with respect to further oxidation, which Shao and Adzic [29] suggest is due to the blocking of active sites at the catalyst by adsorbed acetate (CH_3COO^-). In addition, the intermediates in the formation of acetaldehyde and acetic acid remain unclear.

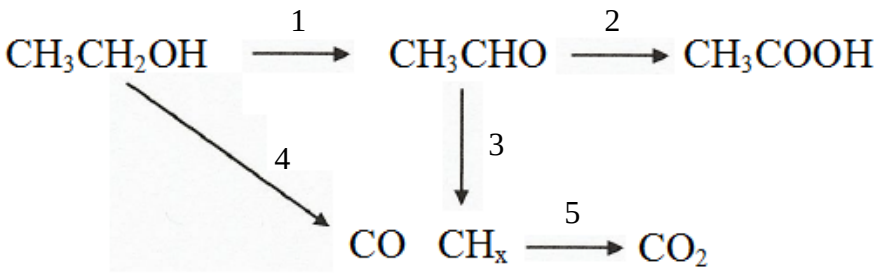

Figure 1.5. Schematic representation of the dual path mechanism proposed for the electrochemical oxidation of ethanol at a noble metal electrodes [20][21].

It is generally accepted that in acid solution, the desired route for ethanol oxidation, which is to produce CO_2, is a complex multi-step process involving adsorption of single carbon fragment intermediates CO_{ads} and $CH_{x,\ ads}$ [20, 35-37]. These fragments require a high overpotential for their oxidation, hence limiting the potential cell voltage as well as the subsequent total efficiency. Furthermore, for practical fuel cell purposes, the reaction rate for the electrochemical oxidation of ethanol at Pt, in acidic media, is too slow [20]. Hence, despite extensive research into catalysts for the ethanol oxidation reaction (EOR) at fuel cell anodes, the conversion to CO_2 and kinetics of this reaction are simply too low when operating in acidic media, thus leading to poor fuel cell performance [17].

1.2.3. Direct ethanol fuel cells in alkali electrolyte

The main advantage of operating fuel cells in an alkali electrolyte is that the kinetics of the oxygen reduction reaction (ORR) at the cathode are significantly increased [17][38], resulting in a higher cell voltage at a given current density when employing a Pt catalyst at both electrodes. In addition, the EOR reaction kinetics are significantly enhanced in DEFCs when an alkali electrolyte is used, thus allowing (in principle) for the use of less expensive, non-precious metal catalysts [17][38][39]. However, there are several key problems which arise from operation in alkaline media, the most serious of which arises from the precipitation of carbonate in the electrolyte when using alcohols (or reformate gas in H_2/air fuel cells, see section 1.1) as a fuel and air as an oxidant [39-41]. Equation (2.6) shows this effect when operating in potassium hydroxide solution:

$$2K^+ + 2OH^- + CO_2 \rightarrow K_2CO_3 + H_2O \qquad (2.6)$$

This reaction leads to dilution of the electrolyte as well as removal of OH^- anions from solution, thus decreasing electrolyte conductivity. This K_2CO_3 precipitate can also block catalyst sites and foul the catalyst surface pores, thus lowering the active surface area and species transport, respectively [17][39-41].

Another problem which can arise when employing liquid alkali electrolytes is leakage at the periphery of the fuel cell, as well as at the pores of the electrodes, the latter referred to as weeping, due to the fact that KOH is a very effective wetting agent [40][41].

In light of the above factors, considerable effort has been invested into the development of Alkali Anion Exchange Membranes (AAEMs) [17][39][42-44]. AAEMs employ a polymeric framework, within which cation head groups (eg. $-NR_3^+$) are immobilised. Furthermore, the membrane is ion-exchanged with OH^- thus providing a mobile network of conducting species. With respect to electrolyte carbonation, the absence of any free metal ions, such as K^+, in the AAEM should prevent the precipitation of any carbonate species. Several studies [45-47] have shown that AAEMs operate successfully in the presence of carbonate species, at both neutral and alkaline pH. For example, Rahim *et al* [46] observed no membrane fouling or loss of electrolyte conductivity when investigating the electrochemical transport of HCO_3^- and CO_2^{3-} through an anion exchange membrane.

The use of AAEMs also eliminates problems arising from the use of a caustic liquid electrolyte. In addition, the generation of OH^- at the cathode, and its subsequent movement to the anode, leads to an electro-osmotic drag [47] across the membrane [48]. This is advantageous in terms of DAFCs as it opposes crossover of methanol from anode to cathode in DMFCs, which has been reported as a major problem in PEMFCs [49].

1.2.4. Typical set-up and operating procedure for an alkali anion-exchange membrane direct ethanol fuel cell

Figure 1.6 illustrates a conventional liquid-feed DEFC based on an anion-exchange membrane (AEM), which consists of a MEA sandwiched between an anode and a bipolar cathode plate. As discussed previously (see section 1.1.3), the MEA is composed of both diffusion and catalyst layers at both the anode and cathode, placed

either side of the AEM. Similar to the function of the proton-exchange membrane in conventional hydrogen PEM-FCs, the AEM acts as a barrier to electrons at the anode and cathode [17]. Furthermore, the membrane facilitates the travel of hydroxyl ions from cathode to anode, and is typically composed of quaternised hydrocarbons [50].

The catalyst layers at both the anode and cathode are generally composed of a catalyst/ionomer mix, thus providing a three-phase boundary for the ORR and Ethanol Oxidation Reactions (EOR). Furthermore, the diffusion layers take similar form to that in PEM-FCs (section 1.1.4) [50].

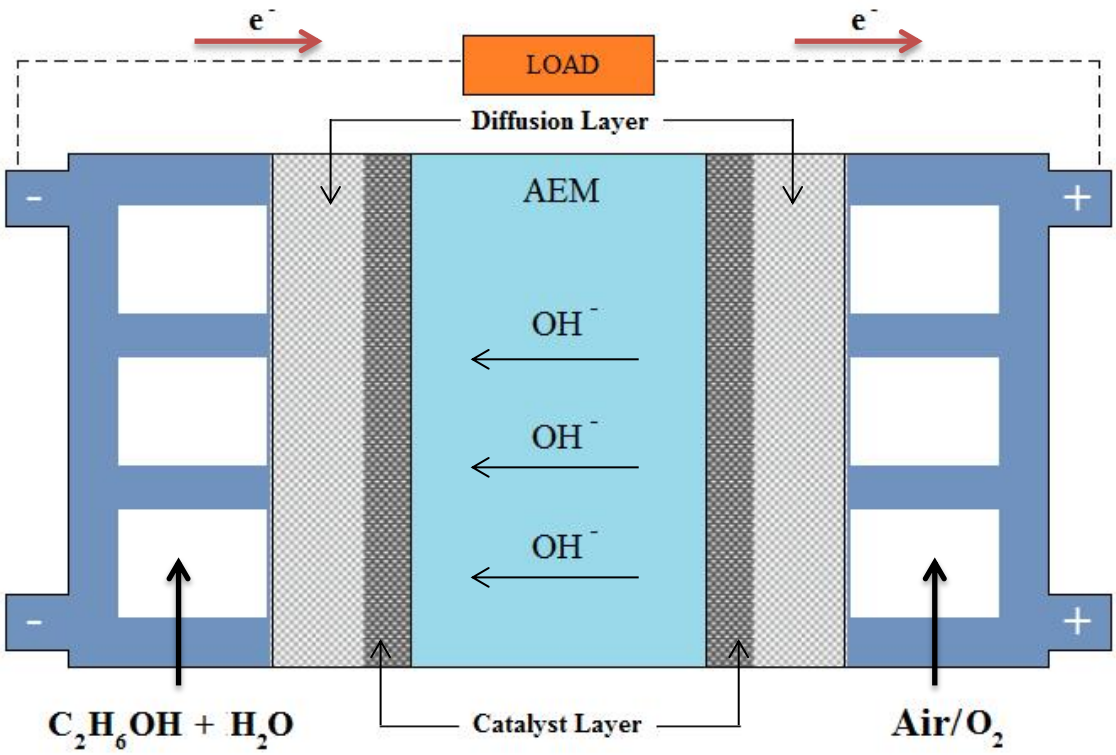

Figure 1.6. Schematic of the conventional setup for a liquid-feed direct ethanol fuel cell, using an alkaline anion exchange membrane (AAEM).

Considering the reaction at the anode, a stream of ethanol is supplied to the flow field where it is directed to the catalyst layer via the anode diffusion layer, before being oxidised to produce CO_2, H_2O and electrons as follows [17]:

$$CH_3CH_2OH + OH^- \rightarrow CO_2 + H_2O + 12e^- \quad (2.7)$$

The water produced from ethanol oxidation is transported through the AEM to the cathode, along with the water in the aqueous ethanol feed, while the electrons are transported to the cathode via an external load circuit. The air/O_2 feed at the cathode diffuses to the catalyst layer, where it subsequently reacts with the water diffusing from the anode, thus yielding hydroxyl ions [17]:

$$3O_2 + 6H_2O + 12e^- \rightarrow 12OH^- \quad (2.8)$$

The hydroxyl ions then diffuse back to the anode where they react as in (2.7), with the overall cell reaction as follows:

$$CH_3CH_2OH + 3O_2 \rightarrow 2CO_2 + 3H_2O \quad (2.9)$$

It is important to note, however, that (2.8) is representative of the complete oxidation of ethanol to CO_2, which to date, has not been observed using the catalysts currently under investigation, and only accounts for a small percentage of the total current produced. Further, it is generally accepted that the main reaction pathway is that which produces acetic acid [20], the direct pathway.

1.2.5. Challenges to the development of alkali anion-exchange membranes

Despite promising reports [51-54], highly conductive and durable AAEM's remain commercially unavailable, largely due to issues surrounding alkaline stability, their durability under hydration and conductivity [41][55]. The main problem with durability is that a higher Ionic Exchange Capacity (IEC) is required for an AAEM than a PEM because the slower diffusion of OH^- relative to protons lowers ionic conductivity, hence requiring higher IEC and increasing water uptake which swells the polymer and leads to loss of mechanical integrity [56]. Thus, the anion exchange membrane must be able to take up sufficient water to form the interconnected domains required for the cathode reaction and the ion flux while retaining its integrity [57]. As yet the US target for AAEM durability of 1-3% loss after 5000 h has not been achieved [58].

In the context of membrane stability, PEMFC electrodes are formulated with a soluble Nafion ionomer, to ensure good ionic contact between membrane and the catalyst particles [41]. An ionomer is the 'conducting glue' that binds the MEA together and plays a major role in building up an effective three-phase boundary that

reduces interfacial resistance and facilitates the transport of ions, and electron transfer, across the catalyst interface [41][59][60]. Ideally, an ionomer should be solution processable, i.e. soluble in water miscible solvents, but should ultimately form a robust solid interface with a hydroxide conductivity that matches that of the membrane. To date, the synthesis of analogous ionomeric solutions for AAEM's has not been achieved [41][59][60] leading to considerable resistive losses in fuel cells based on AAEMs [61]. 'Interfacial solutions' have been tested using KOH and a polymer (eg. polyacrylic acid) [62] or by utilising KOH in the anode stream [63], both methods providing a short term solution, however, in terms of durability, the carbonate problem is still a major issue, hence the term, the ionomer problem. [41].

As a result of the challenges facing the development of AAEM's, until recently, research on alkali direct alcohol fuel cells (ADAFCs) has been a very small fraction of that on the acidic analogues. However, following the work of Varcoe and Stade [42][43] and Thomas *et al* [44], for example, interest has again focussed on ADAFC's. Hence, the next section will aim to provide a brief discussion of the current literature concerning the development of AAEMs.

1.2.6. Recent developments in alkali anion-exchange membranes

Varcoe and Slade [42] developed an AAEM formed by the radiation-grafting of vinylbenzyl Chloride onto poly-(tetrafluoroethylene-co-hexafluoropropylene), FEP, and observed conductivities between 0.010 – 0.035 S cm^{-1} from 20-80 ^{o}C, comparing favourably with Nafion (ca. 0.100 S cm^{-1} over the same temperature range, see section 1.3) [41][64][65]. Unfortunately, the AAEM lacked the physical strength required for fuel cell applications, leading the authors to turn their attention to an AAEM in which the FEP was replaced by poly-(ethylene-co-tetrafluoroethylene), ETFE [66]. Similar to the FEP-based AAEM, there is no β-hydrogen available for Hoffman elimination (see section 1.2.5) in ETFE-based AAEMs [40][41][59]. However, although results were initially promising (Ion-exchange capacity (dry polymer) of 1.42 x 10^{-3} mol(OH) g^{-1} compared to 0.92 x 10^{-3} mol(OH) g^{-1} for Nafion), by the summer of 2006, data on the performance of ETFE-based alkaline fuel cells (H_2/O_2) suggested that improvement beyond a fraction of that achieved with PEM-FCs was not possible [67]. Further, performance data for ETFE-based DMFCs was considerably worse (peak power densities < 10 mW cm^{-2}). The authors

suggested that an insufficient amount of water was reaching the active sites of the cathode catalyst surface as a result of reduced back-transport [67][68]. However, this does not explain the extremely poor performance generally observed in AAEM-based DAFCs [59][69][70]. In a private communication, Dr. Varcoe stated that the inability to develop an ionomer was responsible, and led to the Surrey Group abandoning their research on DAFCs.

More recently, Hibbs *et al* [72] have demonstrated that AAEMs employing a poly(phenylene) backbone, prepared by a Diels-Alder reaction, may achieve ionic conductivities as high as 0.050 S cm^{-1} in liquid water, and are stable under highly basic conditions at elevated temperature (4 M NaOH at 60 ^{o}C). Moreover, several studies [73-77] have shown that polysulfones may undergo successive post-polymerisation modification reactions, leading to highly conductive AAEMs [55]. For example, Xie *et al* [73] investigated the synthesis of a polysulfone AAEM with varied temperature and reaction time, both of which were found to have a significant impact upon membrane conductivity. The AAEMs were synthesized via the addition of a chloromethyl pendant group to polysulfone, followed by reaction with various amines (eg.) to form quaternary pendant groups, which act as the counterion to OH^{-}. The developed AAEMs showed a maximum ionic conductivity of 0.0310 S cm^{-2} at room temperature, which increased to a maximum of 0.0733 S cm^{-2} at 95 ^{o}C. Further, the membranes were stable in concentrated base (up to 8 M KOH) at room temperature; however, the authors did not investigate the stability at higher temperatures.

In the context of AAEM durability and stability, Hickner *et al* [78] reported a highly relevant development that poly(2,6-dimethyl phenylene oxide) containing a quaternised nitrogen-centred side chain with a single C6-alkyl unit had highly conductive ionic domains, exhibited excellent long term stability and retained >90% of its performance after 60 h of fuel cell operation. The performance and stability of this system was attributed to the water uptake behaviour due to an appropriate balance of hydrophobicity and hydrophilicity, arising from the single C6-alkyl chain; polymers with longer alkyl chains exhibited very poor film forming capacity while polymers with multiple alkyl chains had lower hydroxide conductivities. Zhao *et al* [79] attained power densities up to 370 mW cm^{-2} at 50 ºC using pure H_2 and O_2 , and conductivities up to 0.057 S cm^{-1} at 30 ºC. However, no attempt was

made to develop an ionomer, the authors employing a commercial ionomer, and Holdcroft [80] highlights the critical importance of the chemical compatibility between ionomer and membrane. Further, as stated above, it is primarily problems related to the ionomer that have, to date, precluded the use of small organic fuels such as alcohols [J. Varcoe, private communication]. Whilst durabilities of up to 1000 hours in 1 M KOH were also reported by the authors, it is not clear from the paper whether immersion in KOH influences the subsequent measurements of conductivity.

As stated previously (see section 1.2.5), the majority of potential AAEM materials are highly cross-linked polymers and are not amenable to solution processing, thus limiting their use as the ionomer. To this end, a tandem catalytic Ring Opening Metathesis Polymerisation (ROMP)/hydrogenation sequence has recently been used to prepare tetraalkylammonium-functionalised polyethylene with a conductivity of 40 mS cm^{-1} [81][82], which could be used as both an AAEM and as an interfacial ionomer [83], however, the system exhibited poor durability in the fuel cell and for practical applications it will be necessary to improve both stability and conductivity while retaining mechanical integrity [58].

In light of the work discussed above, it is clear that the initial experiments by workers such as Varcoe and Slade [42][43] have inspired several recent developments in the search for AAEMs that are mechanically and chemically robust, display limited swelling and exhibit high ionic conductivity [55][84]. However, despite encouraging data on both stability and conductivity utilising variety of polymer backbones [74-77], the development of AAEM's is still in its infancy compared to PEM technology, and hence new and encouraging materials continue to be reported [41][55]. Moreover, as a result of this recent attention, interest has again focussed on ADAFC's and hence on the study of the mechanisms of the electro-oxidation of alcohols at anode electrocatalysts under alkaline conditions (for a comprehensive review of this literature, see section 3.1). Thus, the primary aim of this project will be to investigate the mechanism of ethanol electro-oxidation in alkaline solution using a combination of *in-situ* FTIR spectroscopy and potentiometric and voltammetry measurements.

In addition to the growing interest in AAEMs and hence ADAFCs, recent developments in PEMs that are both mechanically robust and stable at temperatures above 80 ^{o}C [1] mean that significant attention has turned to the use of High Temperature Polymer-Electrolyte Fuel Cells (HT-PEMFCs) as an alternative to low temperature PEMFCs; and this will be discussed in the following section.

1.3. Polymer-Electrolyte Membranes

1.3.1. Overview

Critical to the design of PEM-FCs is the polymer electrolyte membrane (PEM), which separates the reactant gases and conducts protons (see fig. 1.3) [3]. Thus, PEMs must exhibit low electron conductivity and excellent proton conductivity, minimal water/fuel crossover (especially in DAFCs and Direct Formic Acid Fuel Cells (DFAFCs)), minimal swelling and shrinking, good mechanical strength, prolonged durability (ca. 5000 h for transport aplications [85]) at elevated temperatures and during freeze-thaw cycles [86], low cost and compatibility with electrode materials. However, the PEMs that are currently available do not meet all of these requirements [1].

1.3.2 Nafion in Proton-Exchange Membrane Fuel Cells

Nafion®, which was developed in the late 1960s by DuPont Inc. [87], is the most widely used membrane in low temperature PEM-FCs due to its high proton conductivity (ca. 0.13 S cm^{-1} at 100% relative humidity and 75 ^{o}C [86-89]), moderate swelling in water [90-92], and potential long-term durability (> 60000 h [89]) under fuel cell conditions. Figure 1.7 shows the chemical structure of Nafion, which is based on the co-polymerisation of a hydrophobic perfluorinated polyethylene backbone and a highly hydrophilic sulfonic acid-terminated perfluoro vinyl ether pendant [86][92][93]. Within this structure exists nanoscale domains through which proton transport occurs [87][92]. However, Nafion is only functional in its highly hydrated state and therefore does not perform well at elevated temperature (> 80 ^{o}C) and low relative humidity (< 80%) [94]. Furthermore, in addition to being expensive, DMFCs using Nafion membranes suffer from methanol crossover which poisons the cathode catalyst [95].

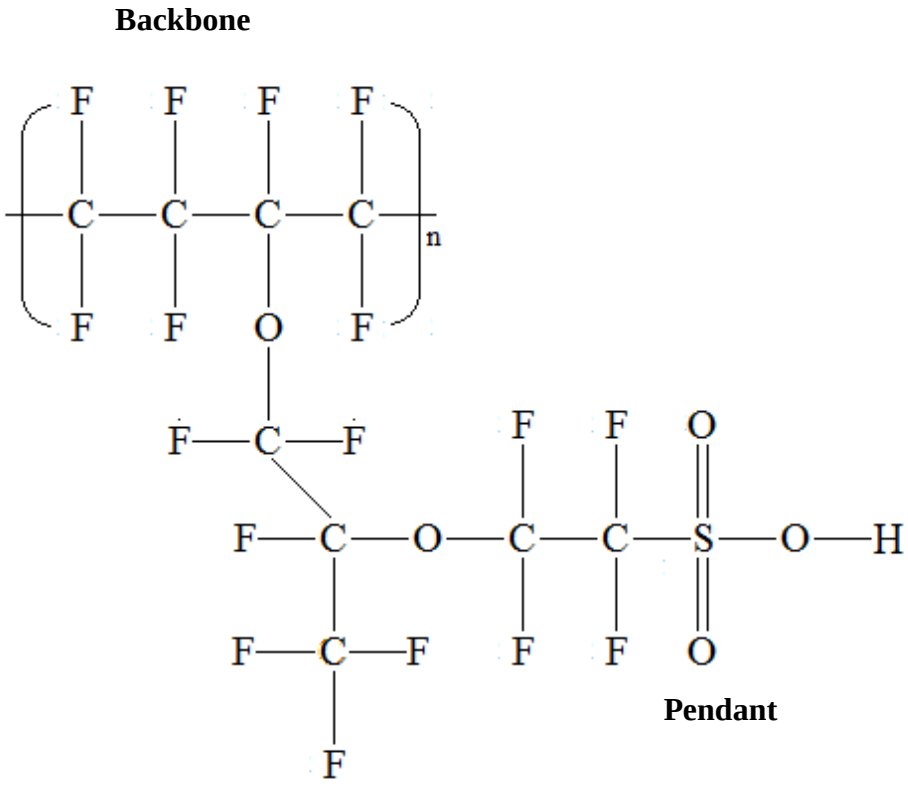

Figure 1.7. Chemical structure of Nafion, redrawn from [85].

1.3.3. Polymer-electrolyte membranes for application at high temperatures and low humidity

HT-PEMFCs have recently been recognised as a possible solution to the technical challenges which fuel cells encounter at low temperature (see section 1.1.4) due to enhanced reaction kinetics, ease of water and heat management and enhanced CO tolerance of the Pt catalyst [96-98]. Thus, the design of stable membranes which retain high proton conductivity and chemical and electrochemical stability under anhydrous conditions (>100 ^{o}C) [99] has been of major interest in recent years [100-107]. Several review papers [1][94][99] have summarized the PEMs currently under investigation for HT-PEMFCs which include: (i) modified perfluorosulfonic acid (PFSA) membranes [1][108-110]; (ii) sulfonated polyaromatic polymers and composite membranes (eg. polyetheretherketone (PEEK) and sulfonated polyetheretherketone (SPEEK)) [1][111-113]; (iii) membranes based polymer-acid complexes (eg. phosphoric acid-doped polybenzimidazole (PBI)) [114-118].

Figure 1.8(a) shows the chemical structure of PBI, which is considered as a promising membrane material for HT-PEMFCs due to its excellent thermal and chemical stability [119-123], mechanical robustness and high tolerance to CO [124]. PBI has a glass transition temperature of 420 °C and is generally believed to be completely amorphous [125].

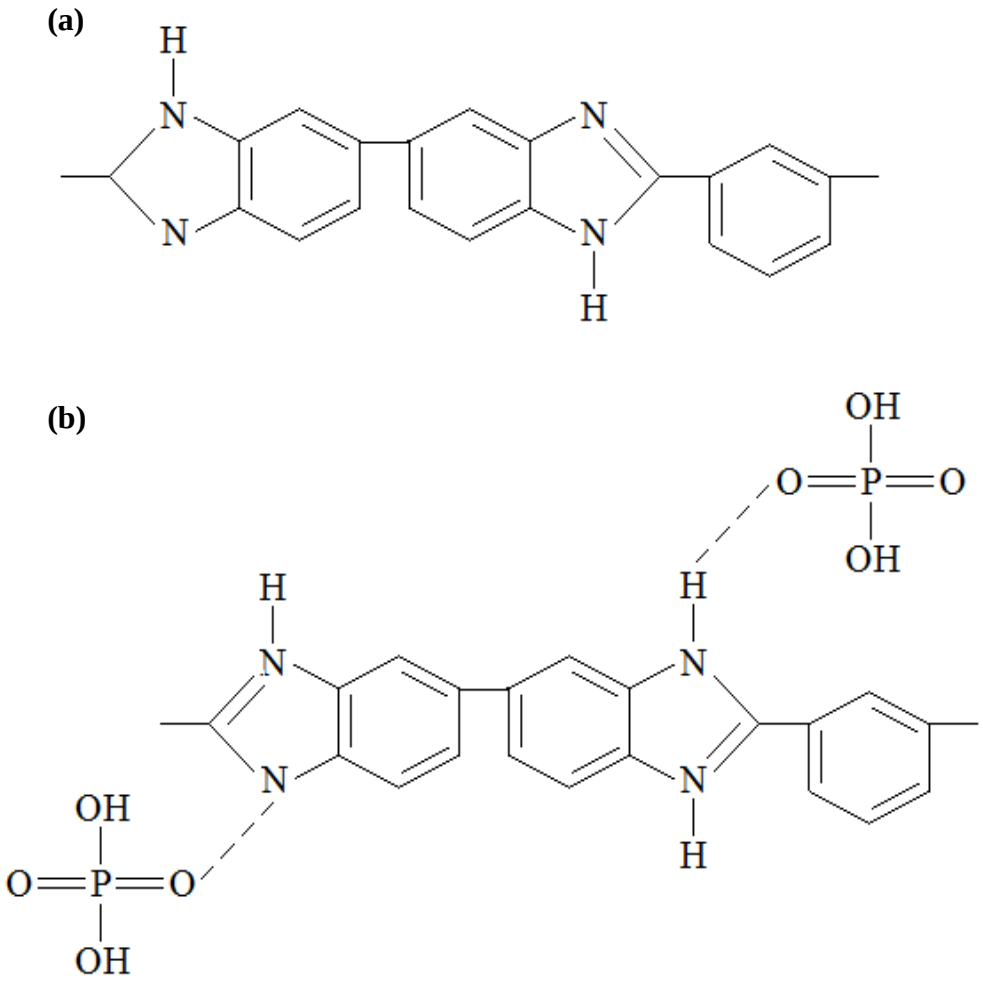

Figure 1.8. Chemical structure of PBI (a) before and (b) after protonation with H_3PO_4, redrawn from [114].

The conductivity of PBI is strongly dependent upon doping with strong acid [123], i.e. polymers bearing basic functional groups such as ether, alcohol, amide, imide or imine groups can act as proton acceptors in the presence of strong acids (see fig. 1.8(b)) [94]. Further, it has been shown [126-127] that high conductivity may only be achieved when doping with amphoteric acids (eg. phosphoric or phosphonic

acid) [94]. An amphoteric species is one that has both proton donor and acceptor sites [128], which, as postulated by Kreuer *et al* [126-127][129], allows them to form dynamic hydrogen bonding networks that facilitate proton transfer via the formation and breaking of hydrogen bonds. In recent years, several studies [114-118] have focussed on improving proton conductivity in PBI-H_3PO_4 polymer acid complexes (PACs) at 120-180 ^oC [1]. For example, Xiao et al [116] demonstrated that the conductivity of PBI-H_3PO_4 PACs synthesised from the sol-gel process (to achieve a high level of acid doping) can reach ca. 0.25 S cm^{-1} at 180 ^oC [116][125]. The authors employed a thick PBI membrane (ca. 250 µm, H_3PO_4 doping level of 32) in a fuel cell at 160 ^oC for 1200 h in the absence of H_2 or O_2 humidification.

Despite a number of molecular studies on both pristine and acid-doped PBI [125][130-136] (see section 6.1 for full discussion), the exact mechanism by which PBI facilitates proton transport remains controversial. Hence, another aim of this project will be to investigate the stability of PBI as a function of relative humidity and temperature using *in-situ* FTIR spectroscopy. I will then attempt to reconcile these data in terms of a mechanism for proton conduction in PBI (see section 6.2).

1.4. In-Situ Infrared Spectro-electrochemistry

1.4.1. Overview

During the past 30 years, *in-situ* IR spectroscopy has become an increasingly utilised and powerful analytical tool in electrochemistry [137], and has developed strongly in terms of both the range of electrochemical systems that may be studied [138-141] and the sensitivity of the technique. As suggested by Christensen [137], this transition may be attributed to the ready availability of research grade, relatively inexpensive FTIR spectrometers. Consequently, the IR detection of organic monolayers is now standard procedure [142-144], and there is a diverse range of applications in fields such as the in-depth study of the double layer [145][146], organometallic electrochemistry [147-149], (photo)-electrocatalysis as a function of temperature [150-152], the semi-conductor interface [153][154] and time resolved studies [137][155][156].

Over the past 50 years, IR spectroscopy has proven to be a highly useful tool in the study of the gas-solid interface [157-159], and has been used to identify reaction

intermediates and products, in addition to the orientation of adsorbed species [160-162]. Consequently, electrochemists were eager to employ the method in conjunction with conventional current/voltage/time techniques, which were incapable of providing such molecular information [137]. Further, in contrast to other *in-situ* spectroscopic techniques (eg. UV-visible spectroscopy), IR spectro-electrochemistry may be conducted at either smooth or rough electrode surfaces, and a wealth of information concerning both the identity and orientation of species at or near the electrode is obtainable [163]. However, in order to collect IR spectra of species in the near-electrode region, two major challenges had to be overcome [137]: (i) common solvents (eg. water) absorb IR light very strongly; (ii) at a time when conventional IR sources were weak, and detectors very noisy [164], sensitivity was a significant problem, as the amount of absorbing species of interest at/near the electrode surface is very small [137]. Hence, this will be discussed in the next section.

1.4.2. The problem of strong solvent absorption in IR spectroelectrochemistry

As discussed at length by Christensen [137], in order to solve the problem of strong solvent absorptions when collecting IR spectra, the path-length that the IR beam travels through the electrolyte must be minimized. Thus, there are three main approaches to minimizing the path-length: transmittance, internal reflectance and, most commonly, the external reflectance approach, which will be employed in this project to investigate both the electrochemical oxidation of ethanol (see Chapters 3-5) and the stability of PBI membranes (see Chapter 6).

1.4.2.1. The transmittance approach

The IR transmittance approach is a method of minimizing the path-length of the spectro-electrochemical cell (see section 2.2 for full details of the spectro-electrochemical cell developed in Newcastle, which was employed for solution-based IR studies during this project) by using an Optically Transparent Thin-Layer Electrolyte (OTTLE) cell. An OTTLE cell employs a “transparent” working electrode (WE), such as a metal minigrid (eg. Au [165]), that is sandwiched between two IR transparent windows. The counter electrode (CE) and reference electrode (RE) are either embedded in a thin section of the cell wall between the two windows, or placed in the cell inlet/outlet tubes. Unfortunately, this approach is insensitive to

changes that occur at, or very close to, the electrode surface [137]. As a result, the IR transmittance approach is generally used for the study of solution species [165][166].

1.4.2.2. The internal reflectance approach

An alternative technique used for minimizing the solution path-length is the Internal Reflectance approach, or Attenuated Total Reflectance (ATR). Figure 1.9 shows a schematic representation of the Kretschmann configuration [137][167][168], commonly used for ATR, which relies upon the total reflection of the IR beam at the internal surface of an IR transparent crystal or internal reflection element (IRE), n_1 in fig. 1.9. IREs that are semiconductors (eg. Si, Ge, ZnSe or GaAs) may be employed as the WE [137][168][169], as was demonstrated first by Mark and Pons [169], who used a Ge IRE to investigate the electro-reduction of 8-quinolinol. However, the IRE is generally coated with a thin metal film (ca. 20 µm [137], n_2 in fig. 1.9) that is in contact with the electrolyte (n_3 in fig. 1.9) [137][167].

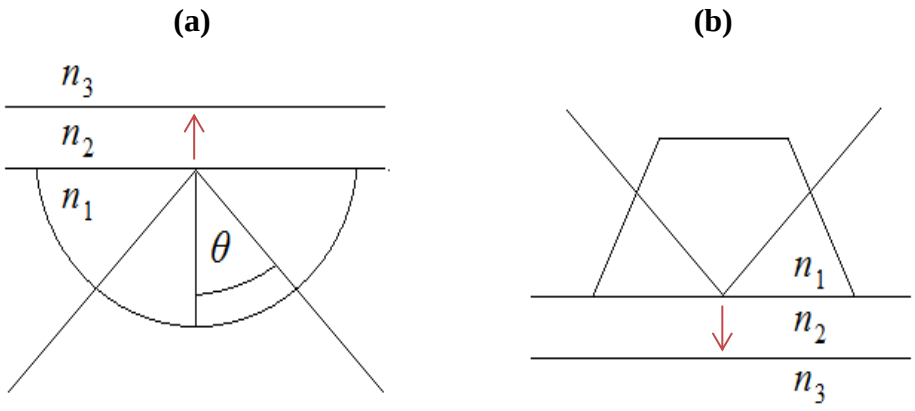

Figure 1.9. Schematic of the Kretschmann configuration for the ATR approach, where: n_1 is the refractive index of the single reflection (a) hemispherical or (b) dove prism, n_2 is the thin metal coating and n_3 is the electrolyte. Redrawn from [137].

At angles of incidence greater than the critical angle, θ_c, total internal reflection occurs on the inner surface of the IRE at the point of incidence [137][167], where the incident and reflected IR rays are then superimposed to form a standing, non-propagating (or evanescent) wave that decays exponentially moving away from the crystal surface, through the metal layer and out into the electrolyte (see [137] or

[167] for full discussion). As a consequence, both the metal layer and the electrolyte will damp the evanescence by absorbing part of its energy. It is therefore crucial that the metal WE layer is sufficiently thick to achieve metallic conduction, but thin enough so that the evanescent wave may sample the electrode-electrolyte interface. Hence, as suggested by Christensen [137], the lack of interest in this method compared to the external reflectance approach (see below) may be attributed to the challenges associated with metal deposition, and with recycling the relatively expensive IREs once the metal coating needs to be replaced.

1.4.2.3. The external reflectance approach

The external reflectance approach is the most commonly exploited *in-situ* IR technique in spectro-electrochemistry [41][137][138][170-173], and was employed for the IR studies carried out in this project. Simply, it involves the trapping a thin layer of electrolyte (ca. 1-25 μm) between a polished, reflective WE and an IR transparent window, such as CaF_2 or ZnSe (see section 2.2) [137][171][172]. Both prismatic and plate windows may be used, however, the former allows for significantly greater signal-to-noise ratios (S/N) [137].

In contrast to ATR, the external reflectance and transmittance approaches are not suitable for the study of fast redox processes as they offer poor RC characteristics [137]. Further, despite the fact that solvent absorptions may be reduced to some extent by employing one of the techniques discussed in section 1.4.2, generally they are still strong and must be annulled in order to observe the weak absorptions of species at or near the electrode surface [137][138][174][175].

1.4.3. Addressing sensitivity problems of in-situ infrared spectroscopy

A "difference" protocol is generally employed to increase sensitivity to the weak absorptions of species at the near-electrode region, and the data manipulation method varies according the type of spectrometer used [137] (see section 2.3.2). The sensitivity problem was historically addressed, particularly in studies focussing on adsorbed species, by utilising the noise and instrumental drift-reducing features of the lock-in detection approach, which has been discussed in detail elsewhere [137][176][177]. Briefly, this approach involves modulating the potential of the WE, typically as a square wave at ca. 10 Hz [176], while the detector of a dispersive IR

spectrometer [177] is "locked-in" to the frequency of this modulation. Consequently, only the signal (and small amounts of noise) modulated at the preset frequency is measured. The wavelength of the light that reaches the detector is then scanned over a predetermined spectral range until the IR spectrum is complete [176][177]. The external reflectance component of this approach is known as Electrochemically Modulated InfraRed Spectroscopy (EMIRS) [137], and produces a signal that is proportional to the difference in the intensity of light reaching the detector between two fixed potentials at each wavelength increment [137][176][177].

The instrumentation required for the EMIRS method is relatively complex compared to modern day Fourrier-Transform InfraRed (FTIR) methods, and the approach is limited to studies on electrochemical systems that are both fast and reversible [137]. Furthermore, the spectra obtained utilising *in-situ* FTIR methods are of a higher quality than those obtained using the lock-in detection approach [178]. Consequently, there has been a significant decrease in the use of the EMIRS method in recent years due to the development of techniques based upon the use of FTIR spectrometers [137][177].

1.4.4. In-situ FTIR spectroscopy

The development of relatively affordable, research grade FTIR spectrometers has led to a significant increase in the volume and diversity of *in-situ* IR studies, which may be attributed to their rapid collection times and inherently high sensitivity [164][179]. In addition to solving the sensitivity problem, FTIR spectrometers allow for simple data collection and manipulation methods, and as a result, have significantly diversified the range of experimental methods to which *in-situ* IR spectroscopy may be applied [137].

The operation of FTIR spectrometers may be described briefly as follows [137][164][179][180]: light covering the whole frequency range (typically 5000-400 cm^{-1}) leaves the source, S, and passes through a Michaelson Interferometer (MI) (see fig. 1.10). In the MI, the light is split into two beams at the beam-splitter, B, transmitting half of the light to a fixed mirror, and half to a moving mirror. Upon reflection, the beams recombine and interfere at the beamsplitter, producing an interference pattern proportional to the sum of interference patterns created by each wavelength in the beam. Systematically changing the difference between the two

path lengths causes the interference patterns to change, producing a detected signal that varies as a function of retardation, x, or distance the moving mirror is away from either side of the zero path difference [164][179][180].

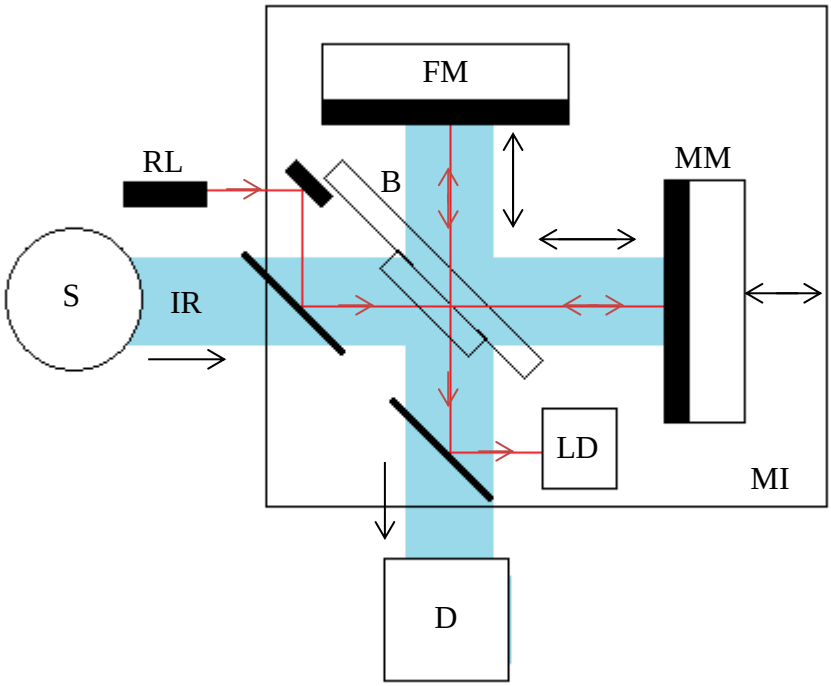

Figure 1.10. Schematic Representation of an FTIR spectrometer: S, IR source; D, Detector; B, Beam-splitter; RL, Reference Laser; LD, Laser Detector; FM, fixed mirror; MM, Moving Mirror; IR, infrared light; MI, Michaelson Interferometer. Redrawn from [137].

A plot of signal intensity vs. retardation collected during smooth movement of the MM is known as an interferogram [137][166][179], and looks nothing like an IR spectrum. However, the spectrometer computer then deconvolutes all of the individual cosine waves that contribute to the interferogram using a mathematical function known as Fourier Transform. This produces a plot of intensity vs. wavelength, or more conventionally wavenumber, which resembles the conventional IR single beam spectrum [137][166]. Following recombination and interference at the beam-splitter, the light reaches the detector, D. The system also employs a

reference laser (RL), which follows the same path through the MI before it is intercepted and directed to the laser detector (LD).

The computational capacity of the FTIR spectrometer and its accurate laser referencing system [137][179] allow for individual scans to rapidly be co-added and averaged, thus producing spectra with improved signal-to-noise ratio (S/N) [179]. In addition, higher energy throughput may be achieved in the interferometer than in dispersive spectrometers, which are restricted by slits, the monochrometer etc. Furthermore, each wavenumber does not need to be scanned successively as the interferometer measures all source wavelengths simultaneously [137][179-181], leading to rapid data collection times (ca. 10 ms). As a result, an entire FTIR spectrum, with sufficient sensitivity to detect species that are adsorbed at the electrode, may be collected in only a few seconds, representing a marked improvement on the collection times required by the EMIRS approach (up to several hours [137]).

1.5. Project aim

The overall aim of the project is two-fold:

1. To investigate the reaction mechanism for the electro-oxidation of ethanol at Pt electrodes in alkaline solution.
2. To investigate the stability of PBI membranes as a function of relative humidity and temperature in order to gain a better understanding mechanism by which it facilitates proton transport.

Preliminary work will focus on the electro-oxidation of ethanol at polycrystalline Pt in 0.1 M KOH at room temperature in order to provide a library of IR spectra of intermediates and products, thus facilitating the studies detailed in (1).

1.6. References

1. Devanathan, R., *Energy and Environmental Science*, 2008, 1, 101-119
2. Crabtree, G.W. and Dresselhaus, M.S., *MRS Bulletin*., 2008, 33(4), 421-428
3. Barbir, F., *PEM fuel cells: theory and practice*, Academic Press Inc., pp33-34, 2005.

4. Rayment, C. and Shermant, S., *Introduction to Fuel Cell Technology*, Notre Dame, pp12-1 3, 2003.
5. Cook, B., *An Introduction to Fuel Cell Technology*, Vancouver: Heliocentris, pp205-207, 2001.
6. Larminie, J.; Dicks, Andrew., *Fuel cell systems explained*, England: Wiley and Sons Ltd., 2003.
7. Vielstich, W.; Lamm, A.; Gasteiger, H.A., *Handbook of Fuel Cells*, Chichester: John Wiley and Sons Ltd., 2003
8. Carpenter Jr, J.A.; Gibbs, J.; Pesaran, A. A.; Marlino, L. D; Kelly, K., *MRS Bulletin*, 2008, 33(4), 439-444
9. Ge, J.; Higier, A.; Liu, H.; *Journal of Power Sources*, 2006, 149(2), 922-927
10. Song, D.; Wang, Q.; Liu, Z.; Navessin, T.; Eikerling, M.; Holdcroft, S., *Journal of Power Sources*, 2004, 126(2), 104-111
11. Ramasamey, R.P., *Proton exchange membrane fuel cells – membrane electrode assemblies*, Encyclopaedia of Electrochemical Power Sources, Elsevier UK, 787-805, 2009.
12. Liu, S.; Zhang, K.; Fang, L.; Li, Y., *Energy Fuels*, 2008, 22(2), 1365-1370
13. Clarke, S.H.; Dicks, A.L.; Pointon, K.; Smith, T.A.; Swann, A., *Catalysis Today*, 1997, 38(4), 411-423
14. Chalk, S.G.; Miller, J.F., *Journal of Power Sources*, 2006, 159(1), 73-80.
15. Balat, M., *International Journal of Hydrogen Energy*, 2008, 33(15), 4013-4029
16. Jones, R.H.; Thomas, G., *Journal of Minerals, Metals and Materials*, 2007, 59, 50-55.
17. Zhao, T.S.; Li, Y.S.; Shen, S.Y., *Frontiers of Energy & Power Engineering*, 2010, 4(4), 443-458
18. Zhou, W.; Zhou, Z.; Song, S.; Li, W.; Sun, G.; Tsiakaris, P.; Xin Q., *Applied Catalysis B: Environmental*, 2003, 46, 273–285
19. Nacef, M.; Affoune, A. M., International Journal of Hydrogen Energy, 2011, 36, 4208-4219.
20. Lai, S.C.S.; Kleijn, S.E.F.; Ozturk, F.T.Z.; van Rees Vellinga, C.T.; Koning, J.; Rodriguez, P.; Koper, M.T.M., *Catalysis Today*, 2010, 154, 92-104.
21. López-Atalaya, M.; Morallón, E.; Cases, F.; Vázquez, J. L.; Pérez, J. M., 1994, *Journal of Power Sources*, *52*, 109

22. Lai, S.C.S.; Koper, M.T.M., *Physical Chemistry Chemical Physics*, 2009, 11, 10446–10456.
23. Quian, Q.Y.; Yang, C.; Zhou, Y.; Yang, S., *Journal of Electroanalytical Chemistry*, 2011, 660, 57-63.
24. Shen, S.Y.; Zhao, T.S.; Xu, J.B.; Li, Y.S., *Journal of Power Sources*, 195, 2010, 1001–1006.
25. Iwasita, T.; Dalbeck, R.; Pastor, E.; Xia, X., *Electrochimica Acta*, 1994, 39, 1817-1823
26. Iwasita, T.; Pastor, E. *Electrochimica Acta*, 1994, 39, 531
27. Ianniello, R.; Schmidt, V. M.; RodrIguez, J. L.; Pastor, E. *Journal of Electroanalytical Chemistry*, 1999, 471, 167-179
28. Wang, Q.; Sun, G. Q.; Jiang, L. H.; Xin, Q.; Sun, S. G.; Jiang, Y. X.; Chen, S. P.; Jusys, Z.; Behm, R. J. *Physical Chemistry Chemical Physics*, 2007, 9, 2686-2696.
29. Shao, M. H.; Adzic, R. R. *Electrochimica Acta*, 2005, *50*, 2415-2422.
30. Camara, G. A.; Iwasita, T., *Journal of Electroanalytical Chemistry*, 2005, 578, 315-321.
31. Camara, G. A.; de Lima, R. B.; Iwasita, T., *Journal of Electroanalytical Chemistry*, 2005, 585, 128-131.
32. Colmati, F.; Tremiliosi-Filho, G.; Gonzalez, E. R.; Berna, A.; Herrero, E.; Feliu, J. M., *Faraday Discussions.*, 2009, 140, 379-307.
33. Camara, G.A; Iwasita, T., *Journal of Electroanalytical Chemistry*, 2005, *578*, 315-321.
34. Lai, S.C.S; Koper, M.T.M., *Faraday Discussions*, 2008, 140, 399-416.
35. Xia, X. H.; Liess, H. D.; Iwasita, T., *Journal of Electroanalytical Chemistry*, 1997, 437, 233-240.
36. Wang, Q.; Sun, G.Q.; Jiang, L.H.; Xin, Q.; Sun, S.G.; Jiang, Y.X.; Chen, S.P.; Jusys, Z; Behm, R.J., *Physical Chemistry Chemical Physics*, 2007, 9, 2686-2696.
37. Lai, S.C.S.; Kleyn, S.E.F.; Rosca, V.; Koper, M.T.M., *Journal of Physical Chemistry C*, 2008, 112, 19080-19087.
38. An, L.; Zhao, T.S., *International Journal of Hydrogen Energy*, 2011, 36, 9994-9999

39. Hongying, H.; Wang, S.; Jin, W.; Jiang, Q.; Sun, L.; Jiang, L.; Sun, G., *International Journal of Hydrogen Energy*, 2011, 36(8), 5104-5109
40. McLean, G.F.; Niet, T.; prince-Richard, S.; Djilali, N., *International Journal of Hydrogen Energy*., 2002, 27, 507.
41. Moya, D.L., 2012, *Fundamental and Applied studies on the development of an alkaline anion exchange membrane-based direct alcohol fuel cell*, Ph.D. thesis, Newcastle University.
42. Varcoe, J.R.; Slade, C.T., *Fuel Cells*, 2005, 5(2), 1615-6846
43. Xiaocheng, L.; Wu, L.; Liu, Y.; Ong, A.L.; Poynton, S.D.; Varcoe, J.R.; Xu, T., Journal of Power Sources, 2012, *in press.*
44. Thomas, O.D.; Soo, K.J.W.Y.; Peckham, T.J.; Kulkarni, M.P.; Holdcroft, S.; *Journal of the American Chemical Society*, 2012, DOI: 10.1021/ja303067t
45. Simpson, A. E. and Buckley, C. A., 1st Symp. *Adv. Rev. Osmosis and Ultrafiltr*., Toronto, 1988, 335.
46. Lounis, A.; Gavach, C., *Journal of Membrane Science*, 1990, 54, 63-74.
47. Kim, J. W.; Park, S. M., *Journal of the Electrochemical Society*, 2003, 150, 560-566.
48. Larmanie, J.; Dicks, A., 2004, *Fuel Cell Systems Explained*. 2nd edn. Chichester, UK: Wiley and Sons Ltd.
49. Chao, X.; Amir, F.; Li, X.; Ward, T., *International Journal of Hydrogen Energy*, 2010, 35(4), 1769-1777.
50. Yanagi, H; Fukuta, K., *ECS Trans*, 2008, 16(2), 257–262
51. Varcoe, J. R.; Slade, R. C. T.; Yee, E. L. H.; Poynton, S. D.; Driscoll, D. J.; Apperely, D. C. *Chemistry of Materials*, 2007, 19, 2686–2693.
52.. Tanaka, M.; Fukasawa, K.; Nishino, E.; Yamaguchi, S.; Yamada, K.; Tanaka, H.; Bae, B.; Miyatake, K.; Watanabe, M. *Journal of the American Chemical Society*, 2011, 133, 10646–10654.
53. Zha, Y. Disabb-Miller, M. L.; Johnson, Z. D.; Hickner, M. A.; Tew, G. N. *Journal of the American Chemical Society*, 2012, 134, 4493–4496.
54. Thomas, O. D.; Soo, K. J. W. Y.; Peckham, T. J.; Kulkarni, M. P.; Holdcroft, S. *Journal of the American Chemical Society*, 2012, 134, 10753–10756.
55. Kostalik IV, H. A.; Clark, T. J.; Robertson, N. J.; Mutolo, P. F.; Longo, J. M.; Abruna, H. D.; Coates, G. W., *Macromolecules*, 2010, 43, 7147–7150 7147

56. Switzer, E. E.; Olsen, T. S.; Datye, A. K.; Atanassov, P.; Hibbs, M. R.; Fujimoto, C.; Cornelius, C. J., *Electrochim. Acta*, 2010, *55*, 3404–3408.
57. Kostalik, H.; Clark, T. J.; Robertson, N. J.; Mutolo, P. F.; Longo, J. M.; Abruna, H. D.; Coates, G. W., *Macromolecules* 2010, 43, 7147–7150.
58. Hickner, M. A.; Herring, A. M.; Coughlin, E. B. *Journal of Polymer Science B.*, 2013, *51*, 1727–1735.
59. Varcoe, J.R.; Slade R. C. T., *Fuel Cells*, 5, 2005, 187-200
60. McLean G.F.; Niet T.; Richard S.; Djilali N., *International Journal of Hydrogen Energy*, 27, 2002, 507-526.
61. Matsuoka K.; Iriyama, Y.; Abe, T.; Matsouka, M.; Ogumi, Z.; *Journal of Power Sources*, 2005, 150, 27-31.
62. E. Agel, J. Bouet and J. F. Fauvarque, *Journal of Power Sources*, 2001, 101, 267-274.
63. Yu E.H. and Scott K., *Electrochemistry Communications*, 2004, 6, 361-365.
64. Slade, R. C. T.; Varcoe, J. R., *Solid State ionics*, 2005, 176(5-6), 585-597
65. Silva, R. F.; De Francesco, M.; Pozia, A., *Journal of Power Sources*, 2004, 134(1), 18-26
66. Varcoe, J. R.; Slade, R. C. T., *Electrochemistry Communications*, 2006, 8(5), 839-843
67. Varcoe, J. R.; Slade, R. C. T., *Journal of Physical Chemistry B.*, 2006, 110(42), 21041-21049
68. Varcoe, J. R.; Slade, R. C. T.; Lam How Yee, E.; Poynton, S. D.; Driscoll, D. J.; Apperly, D. C., *Chemistry of Materials*, 2007, 19(10), 2686-2693
69. Antolini, E.; Gonzalez, E. R.; *Journal of Power Sources*, 2010, 195(11), 3432-3450
70. Yu, E. H.; Krewer, U.; Scott, K., *Energies*, 2010, 3(8), 1499-1528
71. Varcoe, J. R., Private Communication.
72. Hibbs, M. R.; Fujimoto, C. H.; Cornelius, C. J. *Macromolecules*, 2009, 42, 8316–8321.
73. Wang, G.; Wenig, Y.; Chu, D.; Chen, R.; Xie, D. J., *Journal of Membrane Science*, 2009, 332, 63–68.
74. Hibbs, M. R.; Hickner, M. A.; Alam, T. M.; McIntyre, S. K.; Fujimoto, C. H.; Cornelius, C. J., *Chemistry of Materials*, 2008, 20, 2566–2573

75. Wang, J.; Zhao, Z.; Gong, F.; Li, S.; Zhang, S. *Macromolecules*, 2009, 42, 8711–8717.
76. Yan, J.; Hickner, M. A. *Macromolecules* 2010, 43, 2349–2356
77. Zhou, J.; Unlu, M.; Vega, J. A.; Kohl, P. A., *Journal of Power Sources*, 2009, 190, 285–292.
78. Li, N.; Leng, Y.; Hickner, M. A.; Wang, C.-Y. *Journal of the American Chemical Society*, 2013, *135*, 10124–10133
79. Zhao, Y.; Hongmei, Y.; Fen, X.; Yanxi, L.; Zhigang, S.; Boalian, Y., *Journal of Power Sources*, 2014, 269, 1-6.
80. Holdcroft, S., *Chemistry of Materials*, 2014, 26(1), 381–393
81. (a) Clark, T. J.; Robertson, N.J.; Kostalik, H. A.; Lobkovsky, E. B.; Mutolo, P. F. Abruna, H. D. Coates, G. W. *Journal of the American Chemical Society*, 2009, *131*, 12888–12889.
82. Robertson, N.J.; Kostalik, H.A.; Clark, T. J.; Mutolo, P. F. Abruna, H. D. Coates, G. W. *Journal of the American Chemical Society*, 2010, *132*, 3400–3404.
83. Kostalik, H. A.; Clark, T. J.; Robertson, N.J.; Mutolo, P. F. Longo, J. M.; Abruna, H. D. Coates, G. W. *Macromolecules*, 2011, *43*, 7147–7150.
84. Noonan, K. J. T.; Hugar, K. M.; Kostalik IV, H. A.; Lobkovsky, E. M.; Abruna, H. D.; Coates, G. W., *Journal of the American Chemical Society*, 2012, 134, 18161−18164.
85. J. Marcinkoski, J. P. Kopasz and T. G. Benjamin, *International Journal of Hydrogen Energy*, 2008, DOI: 10.1016/j.ijhydene.2007.12.068, in press.
86. Devanthan, R., *Energy and Environmental Science*, 2008, 1, 101-119.
87. Resnick, P. R.; Grot, W. G., *of E. I. du Pont de Nemours and Company, Wilmington, DE*, Sept 12, 1978; U.S. Patent 4, 113, 585.
88. Bauer, F.; Denneler, S.; Willert-Porrada, M., *Journal of Polymer Science, Part B: Polymer Physics*, 2005, 43(7), 786-795
89. Rozie`re, J.; Jones, D. J., *Annual Review of Materials Research*, 2003, 33, 505–555.
90. Hickner, M. A.; Ghassemi, H.; Kim, Y. S.; Einsla, B. R.; McGrath J. E., *Chemical Reviews*, 2004, 104, 4587–4612.

91. Sahu, A. K.; Pitchumani, S.; Sridhar, P.; Shukla, A. K., *Nafion and modified-Nafion membranes for polymer electrolyte fuel cells: An overview, Bull. Materials Science*, 32 (2009) 1-10.
92. Mauritz, K.A.; Moore, R.B., *Chemical Reviews*, 2004, 104, 4535−4585.
93. Szajdzinska-Pietek, E.; Wolszczak, M.; Plonka, A.; Schlick. S., *Macromolecules*, 1999, 32, 7454-7460
94. Qingfeng, Li; Jensen, J.O.; Savinell, R.F.; Bjerrum, N., *Progress in Polymer Science*, 34, 2009, 449–477
95. Ramya, K.; Dhathathreyan, K.S., *Journal of Membrane Science*, 311, 2008, 121–127.
96. Li, M. Q.; Shao, Z. G.; Scott, J., *Journal of Power Sources*, 2008, 183, 69
97. Li, Q.; He, R.; Jensen, J. O.; Bjerrum, N. J.; *Chemistry of Materials*, 2003, 15, 4896
98. Mader, J.; Xiao, L.; Schmidt, T. J.; Benicewicz, B. C., *Advances in Polymer Science*, Vol. 216, Ed. G. E. Scherer, 2008, pp63
99. Zhang, J., Journal of Power Sources, 160, 2006, 872-891
100. Hogarth, M., in: G. Hoogers (Ed.), *Fuel Cell Technology Handbook*, CRC Press, New York, 2003, pp. 7–10.
101. Tricoli, V., *Journal of the Electrochemical Society*, 145, 1998, 3798–3801.
102 Ren, X.; Springer, T. E.; Zawodzinski, T. A.; Gottesfeld, S., *Journal of the Electrochemical Society*, 147, 2000, 466–474.
103. Ling, J.; Savadago, O., *Journal of the Electrochemcal Society*, 151, 2004 A1604–A1610.
104. Bauer, B.; Jones, D. J.; Roziere, J.; Tchicaya, L.; Alberti, G.; Casciola, M.; Massinelli, L.; Peraio, A.; Besse, S.; Ramunni, E., *Journal of New Materials for Electrochemical Systems*, 3, 2000, 87–92.
105. Alberti, G.; Casciola, M.; Palombari, R., *Journal of Membrane Science*, 2000, 172, 233–239
106. M. Doyle, S.K. Choi, G. Proulx, *Journal of the Electrochemical Society*, 2000, 147, 34–37.
107. R.W. Kopirzke, C.A. Linkous, G.L. Nelson, *Polymer Degradation and Stability*, 2000, 67, 335–344.
108. A. S. Arico`, V. Baglio, A. D. Blasi, V. Antonucci, L. Cirillo, A. Ghielmi and V. Arcella, *Desalination*, 2006, 199, 271–273.

109. X. Du, J. Yu, B. Yi, M. Han and K. Bi, *Physical Chemistry Chemical Physics*, 2001, 3, 3175–3179.

110. K. D. Kreuer, M. Schuster, B. Obliers, O. Diat, U. Traub, A. Fuchs, U. Klock, S. J. Paddison and J. Maier, *Journal of Power Sources*, 2008, 178, 499–509.

111. Kreuer, K. D., *Journal of Membrane Science*, 2001, 185, 29–39

112. B. Yang and A. Manthiram, *Journal of Power Sources*, 2006, 153, 29–35.

113. G. Ye, N. Janzen and G. R. Goward, *Macromolecules*, 2006, 39, 3283–3290.

114. Scott K.; Wu, X., *Fuel Cells*, 12, 2012, 583-588.

115. Q. Li, R. He, J. O. Jensen and N. J. Bjerrum, *Fuel Cells*, 2004, 4, 147–159.

116. Xiao, L.; Zhang, H.; Scanlon, E.; Ramanathan, L. S.; Choe, E. W.; Rogers, D.; Apple, T.; Benicewicz, B. C., *Chemistry of Materials*, 2005, 17, 5328–5333.

117. Zhai, Y.; Zhang, H.; Zhang, Y.; Xing, D., *Journal of Power Sources*, 2007, 169, 259–264.

118. Perry, K. A.; More, K. L.; Payzant, E. A.; Meisner, R. A.; Sumpter, B. G.; Benicewicz, B. C., *Journal of Polymer Sci., Part B: Polymer Physics*, 2013, 52(1), 26-35.

119. Samms, S. R.; Wasmus, S.; Savinell, R. F., 1996, *Journal of the Electrochemical Society*, 143, 1225-1232.

120. Kerres, J.; Ullrich, A.; Meier, F.; Haring, T., 1999, *Solid State Ionics*, 125, 243-249.

121. Cassidy, P. E., 1980, *Polybenzimidazoles. In: Thermally stable polymers: synthesis and properties*, Marcel Dekker, Inc., New York, Sect. 6.10, 6.18-2

122. Hogarth, W. H. J.; Diniz da Costa, J. C.; Lu, G. Q., 2005, Journal of Power Sources, 142, 223-237.

123. Aili, D.; Cleemann, L. N.; Li, Q.; Christensen, E.; Bjerrum, N. J., 2012. *Journal of Materials Chemistry*, 22, 5444-5453.

124. Li, Q.; He, R.; Gao, J.; Jensen, J. O.; Bjerrum, N. J., 2003, Journal of the Electrochemical Society, 150, A1599-A1605.

125. Bouchet, R.; Siebert, E., 1999, Solid State Ionics, 118, 287-299.

126. Schuster, M.; Rager, T.; Noda, A.; Kreuer, K. D.; Maier, J., *Fuel Cells*, 2005, 5, 355-365

127. Paddinson, S. J.; Kreuer, K. D.; Maier, J.; *Physical Chemistry Chemical Physics*, 2006, 8, 4530-4543

128. IPAC, *Compendium of Chemical Terminology*, (Ed. 2), The Gold Book, Amphoteric, (Accessed from: http://goldbook.iupac.org/A00306.html) on 20th August 2014

129. Steininger, H.; Schuster, M.; Kreuer, K. D.; Kaltbeitzel, A.; Bingol, B.; Meyer, W. H.; et al., *Physical Chemistry Chemical Physics*, 2007, 9, 1763-1773

130. Musto, P.; Karasz, F. E.; MacKnight, W. J., 1989, *Polymer*, 30, 1012-1021.

131. Musto, P.; Wu, L.; Karasz, F. E.; MacKnight, W. J., 1991, *Macromol* 24, 4762-4769.

132. Brooks, N. W.; Duckett, R. A.; Rose, J.; Ward, I. M.; Clements, J., 1993, *Polymer*, 34, 4038-4042.

133. Glipa, X.; Bonnet, B.; Mula, B.; Jones, D. J.; Rozière, 1999, *Journal of Materials Chemistry*, 9, 3045-3049.

134. Li Q, He R, Berg RW, Hjuler HA, Bjerrum NJ, 2004, *Solid State Ionics*, 168:177

135. Musto, P.; Wu, L.; Karasz, F. E.; MacKnight, W. J., 1991, *Polymer*, 32:3

136. Musto, P; Karasz. F. E.; MacKnight, W. J., 1993, *Polymer*, 34, 2934-2945.

137. Christensen, P. A., *Encyclopedia of electrochemistry, Vol. 3: instrumentation and electroanalytical Cheimistry*, Wiley, Germany, 536-538, 2003.

138. Beden, B.; Lamy, C.; Infrared reflectance spectroscopy in *Spectroelectrochemistry: Theory and Practice* (Ed.: R. J. Gale), Plenium Press, New York, 1988, p189

139. Foley, J. K.; Korzeniewski, C.; Daschbach, J. J.; in: Electroanalytical Chemistry, A Series of Advances (Ed.: A. J. Bard), Mercel Dekker, New York, pp. 309-440, 1986, Vol. 14.

140. Bewick, A.; Pons, B. S. in: *Advances in Infrared and Raman spectroscopy* (Eds.: R. J. H. Clark, R. E. Hester), Wiley-Heyden, London, 1985, Vol. 2

141. Christensen, P. A.; Hamnett, A.; *Comprehensive Chemical Kinetics*, 1989, 29, 1-6.

142. Christensen, P. A.; Hamnett, A.; Higgins, S. J., *Analyst*, 1994, 119, 735

143. Climent, V.; Rodes, A.; Ortis, J. M.; et al, *Journal of Electroanalytical Chemistry*, 1999, 467, 20.

144. Hoon-Kholsa, M.; Fawcett, W. R.; Goddard, J. D.; et al, *Langmuir*, 2000, 16, 2356-2362.
145. Marinkovic, N. S.; Calvente, J. J.; Kloss, A., *Journal of Electroanalytical Chemistry*, 1999, 467, 325-334.
146. Shingaya, Y.; Ito, N., *Surface Science*, 1997, 386, 34-47.
147. Atwood, C. G.; Greiger, W. E.; *Journal of the American Chemical Society*, 2000, 122, 5477-5485.
148. Ito, T.; Hamaguchi, T.; Nagino, H.; Yamaguchi, T.; Washington, J.; Kubiak, C. P., *Science*, 1997, 277, 660-663.
149. Yamaguchi, T.; Imai, N.; Ito, T.; et al., *Bulletin of the Chemical Society of Japan*, 2000, 73, 1205-1212.
150. Hori, Y.; Koga, O.; Wanabe, Y.; et al., Electrochimica Acta, 1998, 33, 1389-1394.
151. Christensen, P. A.; Eameaim, J.; Hamnett, A., Physical Chemistry Chemical Physics, 1999, 1, 5315-5321.
152. Kardash, D.; Huang, J. M.; Korzeniewski, C.; Langmuir, 2000, 16, 2019
153. Ekstrom, G. N.; Mcquillan, A. J.; Journal of Physical Chemistry B., 1999, 103, 10, 562-571.
154. Li, J. J.; Wang, R. Q.; Liu, Z. F.; Cai, S. M.; Xiao, X. Y.; Sun, S. G., *Molecular Crystals and Liquid Crystals*, 1999, 337, 525.
155. Osawa, M.; Katsumasa, Y.; Ataka, K.; et al., *Langmuir*, 1994, 10(3), 640-642.
156. Ataka, K.; Nishima, G.; Cai, W. B.; et al., *Electrochemical Communications*, 2000, 2, 417-421.
157. Kataoka, S., *Journal of Photochemistry and Photobiology A: Chemistry*, 2004, 163, 323–329.
158. Sun, R. D.; Nakajima, A.; Fujishima A.; Watanabe, T.; Hashimoto, K., Journal of Physical Chemistry B, 2001, 105, 1984-1990.
159. Henderson, M. A., *Surface Science*, 2002, 46, 5
160. Bradshaw, A. M.; Hoffmann, F. M., *Surface Science*, 1978, 72, 513-535.
161. Smith, G. W.; Carter, E. A., *Journal of Physical Chemistry*, 1991, 95, 2327-2339
162. Steininger, H.; Lehwald, S.; Ibach, H., *Surface Science*, 1982, 123, 264.
163. Ashley, K., *Talanta*, 1991, 38(11), 1209-1218.

164. Williams, D. H.; Fleming, I., *Spectroscopic Methods in Organic Chemistry*, (5th Ed.), Mc-Graw-Hill, UK, 1995, pp28-30

165. Atwood, C. G.; Geiger, W. E.; Bitterwolf, T. E., *Journal of Electroanalytical Chemistry*, 1995, 395, 279-285

166. Klerk-Engels, B.; Hartl, F.; Vrieze, K., *Inorganica Chimica Acta*., 254, 1997, 239-250

167. Seshadri, S. R., *Journal of Applied Physics*, Vol. 70, No. 7, 1991.

168. Tolstoy, V. P.; Chernyshova, I.; Skryshevsky, V. A., in: *Handbook of Infrared Spectroscopy of Ultrathin Films*, p112, 168

169. Mark, H. B.; Pons, B. S.; *Analytical Chemistry*, 1966, 38, 119

170. Christensen, P. A.; Linares-Moya, D. *Journal of Physical Chemistry C*. 2009, *114* (2), 1094-1101.

171. Christensen, P. A.; Hamnett, A.; Linares-Moya, D. *Physical Chemistry Chemical Physics* 2011, *13* (24), 11739-11747

172. Christensen, P. A.; Jones, S. W. M. and Hamnett, A., *Journal of Physical Chemistry C*., 2012, 116, 24681−24689.

173. Lai, S. C. S. and Koper, M. T. M., *Physical Chemistry Chemical Physics*, 2009, 11, 10446-10456.

174. Beden, B.; Lamy, C.; Bewick, A.; et al., *Journal of Electroanalytical Chemistry*, 1981, 121, 343

175. Murray, R. W.; Heineman W. R.; O'Dom G. W., *Analytical Chemistry*, 1967, 39, 1666.

176. Bewick, A.; Kunimatsu, K.; Pons, B. S.; Russel, J. W., *Journal of Electroanalytical Chemistry*, 160, 1984, 47-61

177. Clark, R. J. H.; Hester, R. E.; *Spectroscopy for Surface Science*, Wiley, 1998, York, Vol. 26, pp219-221

178. Proenca, L.; Lopes, M. I. S.; Fonseca, I.; et al., Electrochimica Acta., 1998, 44, 1423.

179. Perkins, W. D., Journal of Chemical Education, 1987 (Ed.; F. A. Settle Jr.), 64(11), A269-A271

180. Stuart, B., Infrared Spectroscopy: Fundamentals and Applications, Wiley, 2004, pp18-25.

181. Griffiths, P. R.; De Haseth, J., *Fourier Transform Infrared Spectroscopy*, John Wiley and Sons inc., Canada, pp47-49, 2007.

2. Experimental

2.1. Reagents

Reagent	Analysis	Supplier
Acetic Acid CH_3COOH	≥ 99.9%	Sigma-Aldrich Cat No. A6283
Ethanol absolute C_2H_5OH	> 99.5% ACS	Sigma-Aldrich Cat No. 459844
Ethylene Glycol $HOCH_2CH_2OH$	> 99+%	Sigma-Aldrich Cat No. 10,246-6
Potassium Hydroxide KOH	> 85%	Sigma-Aldrich Cat No. P1767
Millipore Water H_2O	18.2 MΩ.cm	Millipore
Polybenzimidazole (PBI)	>99%	Between Lizenz GmbH, Germany
Lead (IV) Acetate $Pb(CH_3COO)_4$	Reagent Grade, 95%	Sigma-Aldrich Cat No. 185191
Bismuth (III) Acetate $Bi(CH_3COO)_3$	≥99.99% Trace Metal Basis	Sigma-Aldrich Cat No. 401587
Platinum (polycrystalline) Pt	99.99%	Metals Crystals and Oxides

Sulfuric Acid H_2SO_4	95.0 – 98.0 %	Sigma-Aldrich Cat No. 258105
Carbon Monoxide CO (g)	Research Grade 100%	BOC
Hydrochloric Acid HCl	Research Grade 37%	Sigma-Aldrich Cat No. 43,316-0
Nitric Acid HNO_3	69%	Riedel de Haen Cat No. 30702

Table 2.1. List of reagents employed in the work presented in this thesis.

2.2. The electrochemical cell

The glass cell employed in the cyclic voltammetry CV experiments (see section 2.5) was designed and constructed in-house, and comprised two halves (see figs. 2.1(a) and 2.1(b)). The bottom half of the cell was a 50 cm^3 receptacle fitted with a heating/cooling jacket for temperature control (see section 2.3.1), and two SQ13 screw-threaded joints through which the counter electrode, CE (Pt/Ti Mesh, see fig. 2.2), and the luggin capillary of the reference electrode were directed. The top half of the cell was fitted with a B14 socket to house the N_2 sparging inlet, which was retracted during measurements to maintain a N_2 blanket over the electrolyte (see section 2.5) [1]. In addition, the top half of the cell was fitted with two SQ13 Screw-threaded inlets. One of the inlets housed the N_2 bubbler, which prevents oxygen entry and maintains a positive N_2 pressure within the cell [1]. The second inlet was used for admitting the working electrode, WE (Pt foil, see fig. 2.2). The CV experiments were carried out at 0, 25 and 50 ^oC and, in addition to the Pt WE and Pt/Ti CE, a mercury/mercury oxide (MMO) reference electrode was employed (E^o = +0.850 V vs. SHE) [2].

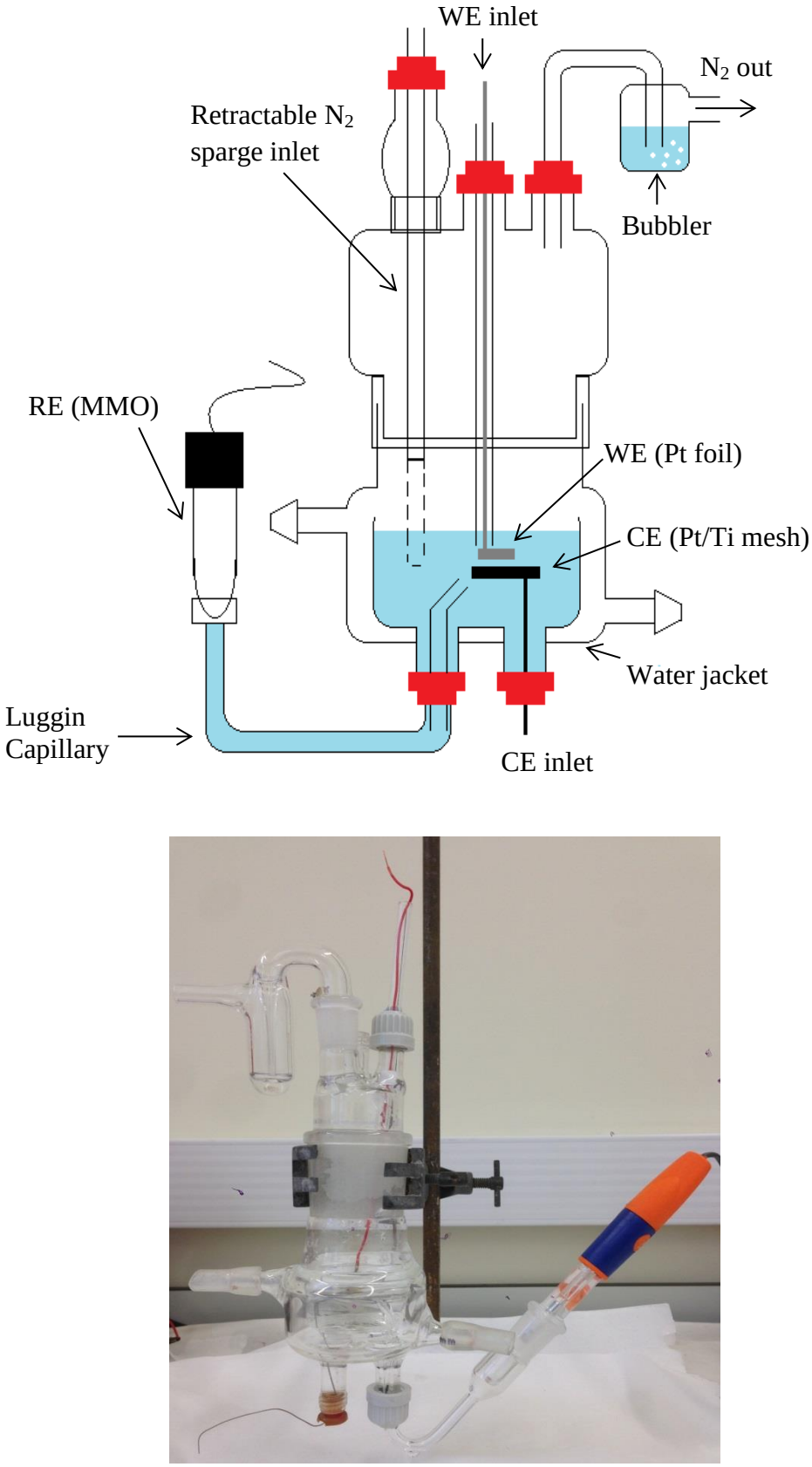

Figure 2.1. (a) Schematic and (b) photograph of the two-piece electrochemical cell employed during the CV experiments in this study.

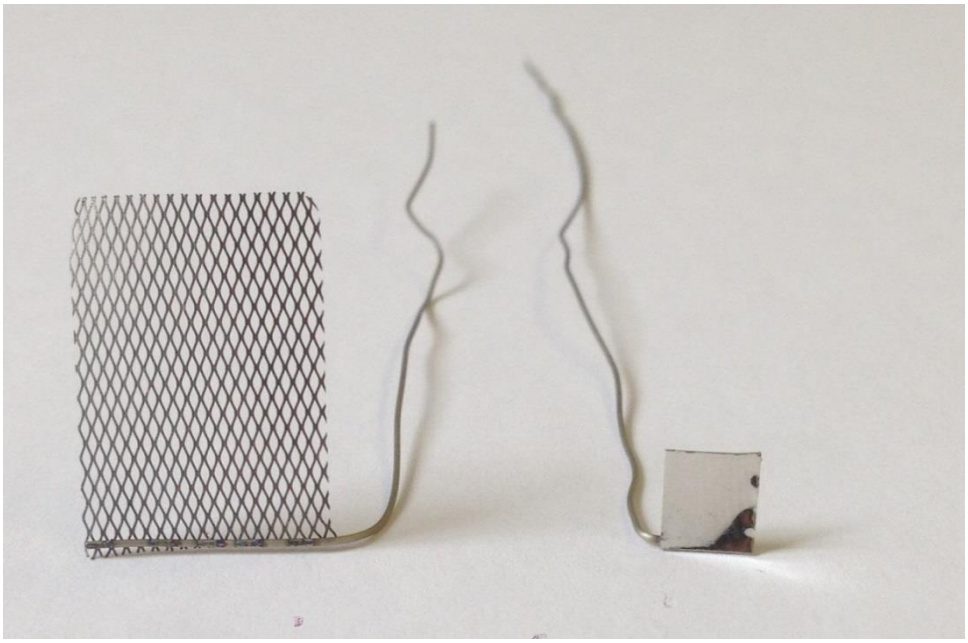

Figure 2.2. Photograph of the Pt foil working electrode and Pt/Ti counter electrode employed during the CV experiments on ethanol oxidation in 0.1 and 0.25 M KOH, at 0, 25 and 50 ^{o}C.

2.3. The spectro-electrochemical cell

2.3.1. Basic Design

In-situ FTIR experiments in aqueous solution were carried out in a spectro-electrochemical cell (see fig. 2.3) which was designed and constructed in-house. The glass cell was mounted on the lid of the sample compartment of the FTIR spectrometer via a specially designed base-plate, and a hemispherical calcium fluoride (CaF_2, Medway Optics) prism was employed as the cell window. The cell contained the reflective polycrystalline Pt working electrode, a 3 cm^2 Pt mesh counter electrode and a mercury/mercury oxide (MMO) reference electrode, RE, and was designed to allow electrolyte exchange under potential control. In order to minimise the electrolyte thickness between the working electrode and the CaF_2 window, the electrode was pushed against the window via a screw and pushed-rod arrangement (see fig. 2.5) [1], trapping an electrolyte layer ca. 1-3 μm thick.

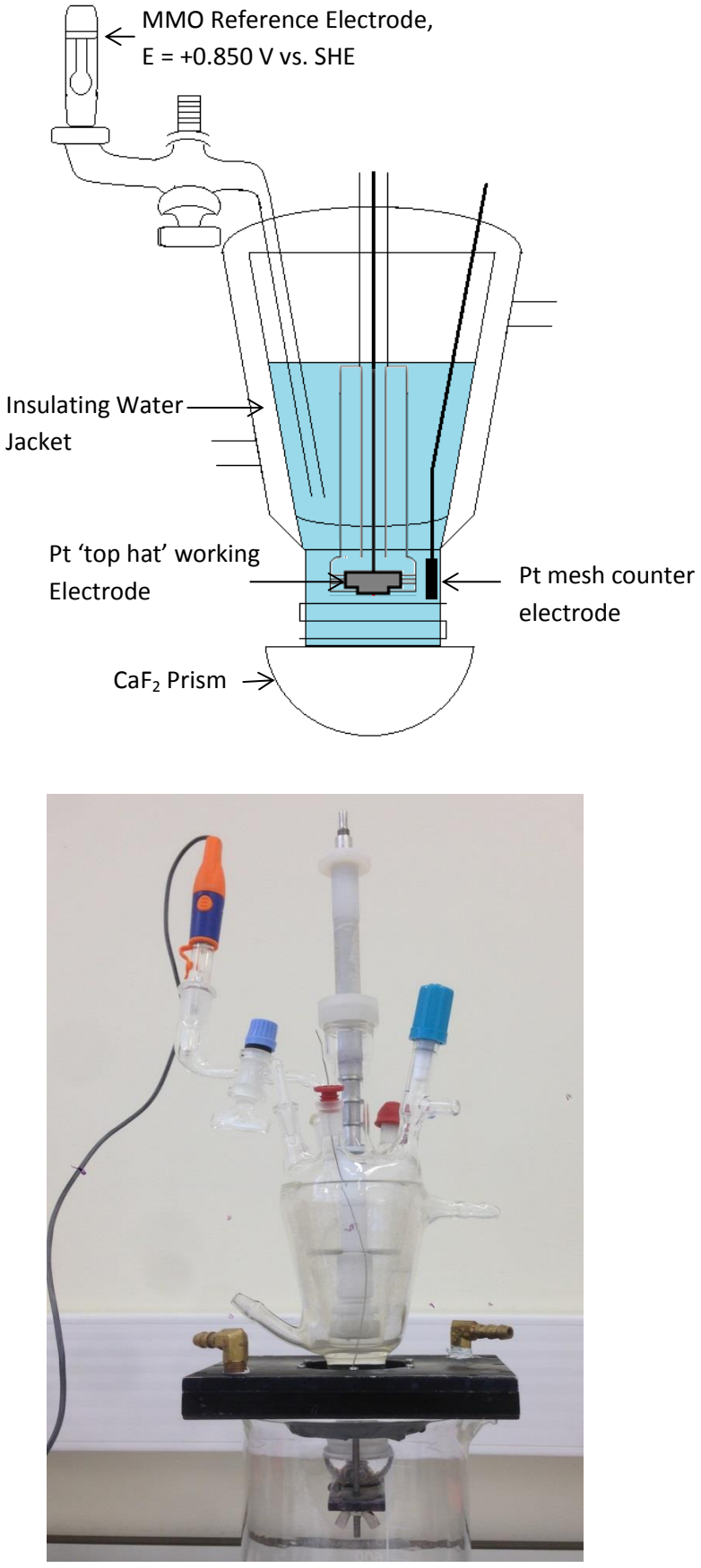

Figure 2.3. (a) Photo and (b) schematic of the spectro-electrochemical FTIR cell

The spectro-electrochemical cell was fitted with a heating/cooling jacket, thus allowing for control of the electrolyte temperature within the cell, using a Grant GD120 R1 water bath. Insulated pipes running from the water bath were passed through the cell jacket and hollow cell base, allowing water to flow and maintain the required electrolyte temperature in the bulk of the cell and thin layer.

2.3.2. Working Electrode

A reflective 'top hat' constructed from polycrystalline Pt (see fig. 2.4) was employed as the WE in the *in-situ* FTIR tests, with a polished area of ca. 0.64 cm^2 exposed to solution in the cell.

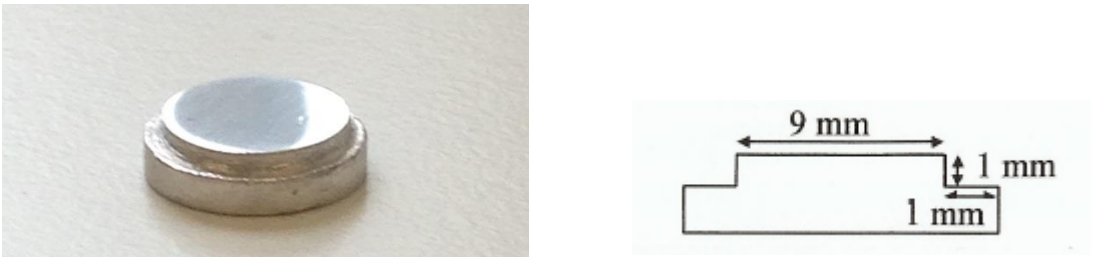

Figure 2.4. (a) Photo and (b) schematic of the reflective Pt top hat disc used as a working electrode for catalysis of the Ethanol electro-oxidation reaction.

Electrical contact to the potentiostat (Autolab PGSTAT12) was achieved via the use of a steel push-rod and screw which were connected to the top hat disc via a nylon screw-head and a PTFE body, as shown in figs. 2.3(a) and (b).

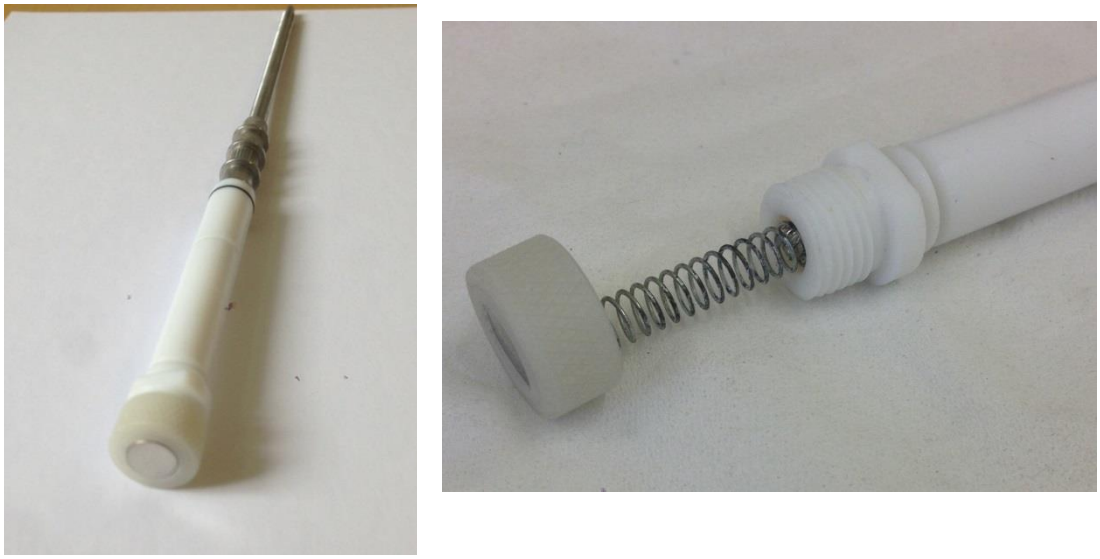

Figure 2.5. Photograph of (a) the electrode and steel push-rod in the PTFE body arrangement and (b) the spring connection from the Pt top hat to the steel rod body.

2.4. In-situ FTIR spectroscopy

The FTIR spectrometer was a Varian FTS-7000 model employing a liquid nitrogen cooled, mercury cadmium telluride (MCT) detector.

2.4.1. FTIR sample compartment mirror setup

Figures 2.6(a) and (b) shows the configuration of the optical bench employed for solution phase FTIR experiments during this project. The bench was designed by other workers in Newcastle [3] to fit to the bottom of the sample compartment of the FTIR spectrometer. Further, the mirrors were attached to the base plate and positioned to direct the IR beam towards the CaF_2 prismatic window (E in fig 2.6(a)) via mirrors A and B, before subsequently being reflected towards mirrors C and D by the Pt working electrode, thus directing it to the MCT detector of the FTIR spectrometer.

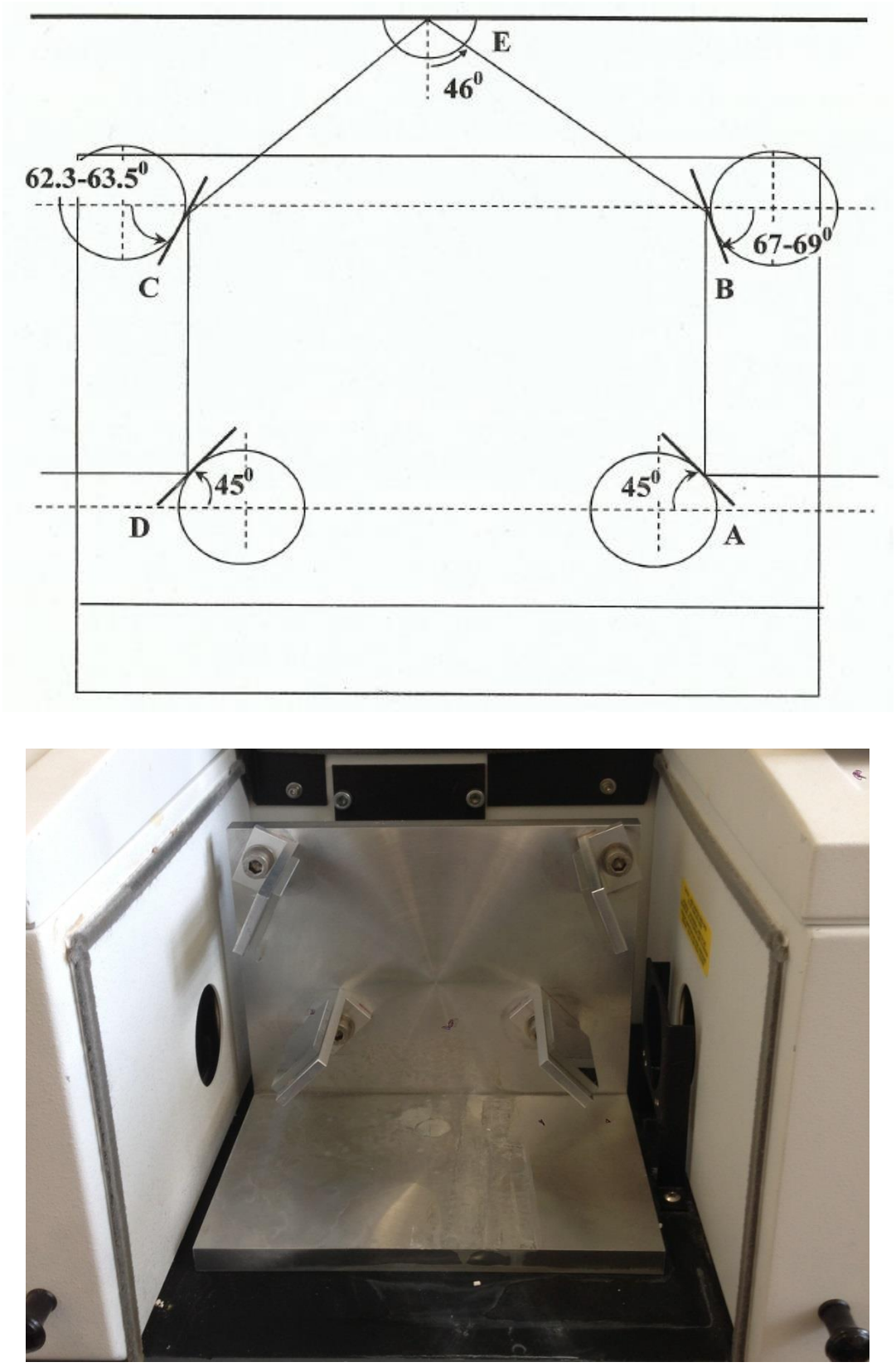

Figure 2.6. (a) Schematic and (b) photograph of the mirror configuration within the FTIR sample compartment, thus allowing for reflectance of the IR beam at the Pt working electrode.

Figure 2.7(a) shows a schematic representation of arrangement of the mirrors and spectro-electrochemical cell with the WE pushed against the CaF_2 window. As may be seen from the figure, the angle of incidence of the IR beam at the CaF_2/electrolyte interface was 46^o, (assuming 0 beam divergence, n = 1.41, k = 0^{25} [1][4]), giving an angle of incidence at the Pt electrode of 50^o [1][4]. Furthermore, for a beam divergence of ± 6^o, the incidence on the inner side of the CaF_2/electrolyte interface is well below the critical angle and thus precludes any enhancement due to total internal reflectance [1][4].

2.4.2. Typical Spectro-electrochemical analysis procedure

Prior to the addition of ethanol, a cyclic voltammogram was recorded with the cell containing only 0.1M KOH, after which the potential was then set to a reference potential of either -0.75 V or -0.85 V vs. MMO before addition of absolute ethanol to a concentration of 1 M. The solution was then mixed thoroughly and then left for ten minutes, thus allowing sufficient diffusion of ethanol throughout the KOH electrolyte, with the Pt electrode continuously under potential control.

Following the addition of ethanol, the working electrode was carefully pushed against the CaF_2 prism, before purging of FTIR sample compartment of water vapour and CO_2 for approximately 70 minutes. With the potential held at the reference value, a reference spectrum, S_R, was recorded (100 co-added and averaged scans, $8cm^{-1}$ resolution, 47s per scan set), before the potential was then increased from -0.75 to 0.4V vs. MMO in 0.1V steps, holding the cell at each potential for 2 minutes.

The spectra recorded at each potential during the potential sweep are presented in this report as:

$$\text{Absorbance} = -\log_{10}(S_S/S_R) \qquad (2.10)$$

the difference spectra resulting from this data manipulation show peaks pointing upwards which are representative of a gain in absorbing species at S_S with respect to the reference spectrum at S_R, and vice versa. Following the potential sweep, cyclic voltammograms were again recorded.

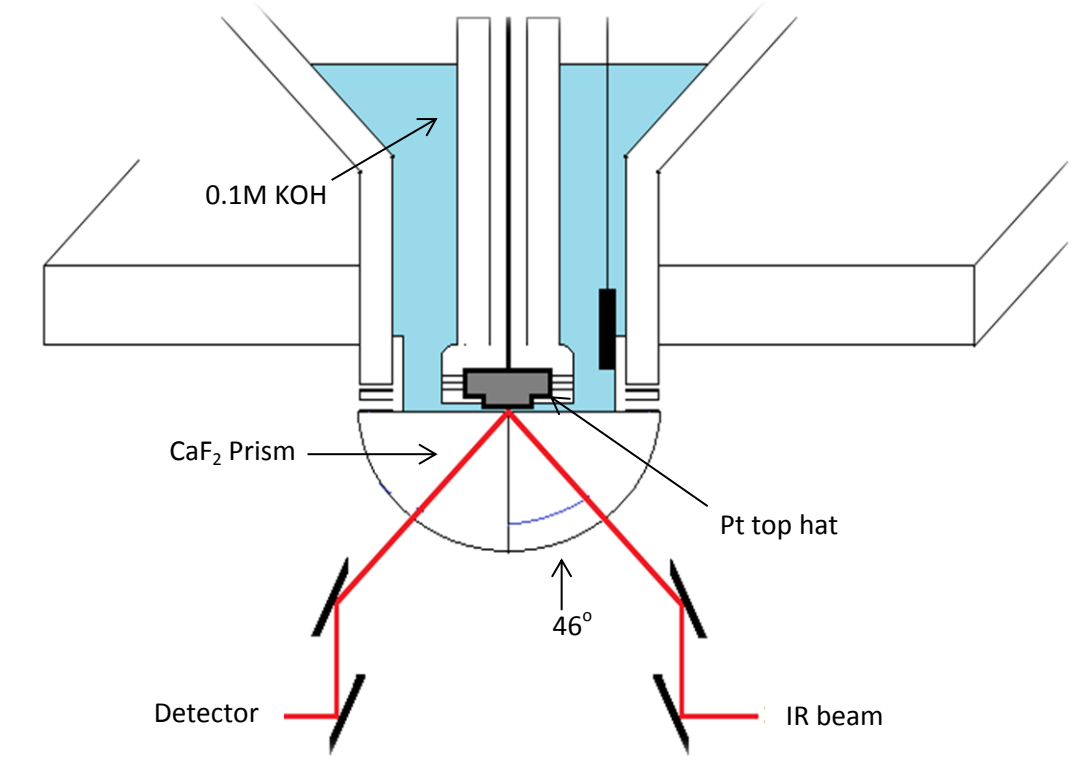

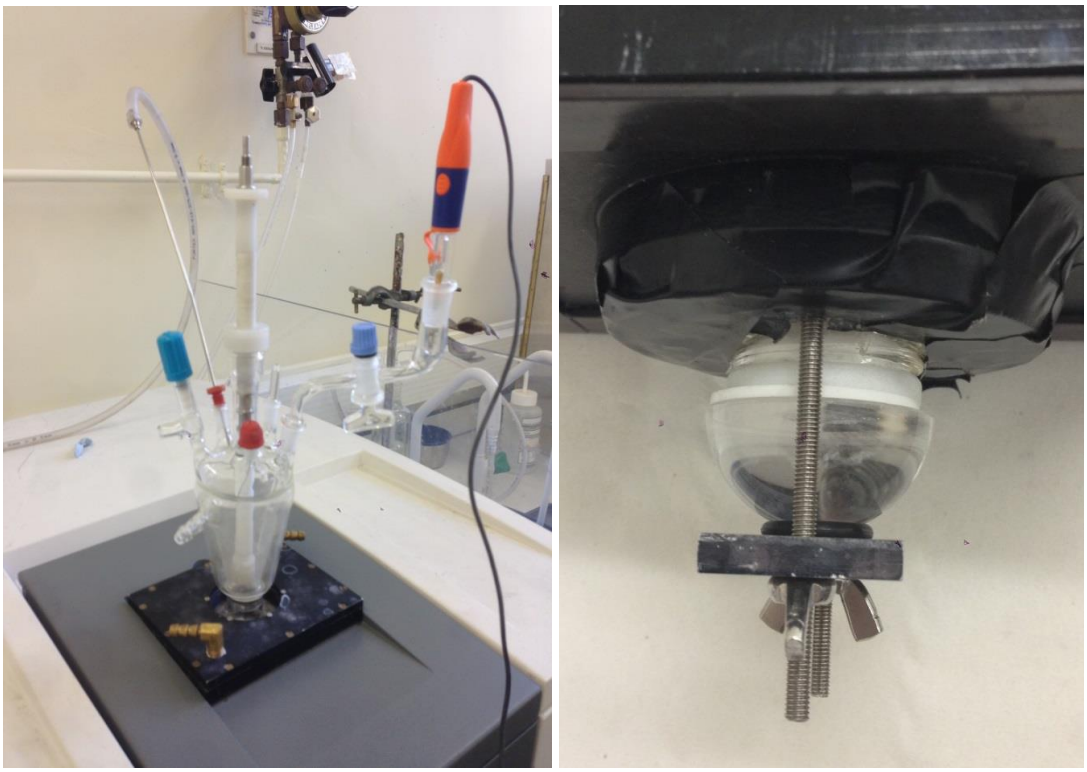

Figure 2.7. (a) Schematic representation and (b) photograph of the spectro-electrochemical cell mounted to the sample compartment of the FTIR spectrometer, and the mirror configuration utilised within the sample compartment.(c) Photograph of the CaF_2 prismatic window fixed to the bottom of the cell and base plate.

For the ethanol oxidation experiments in the presence of a Pb co-catalyst (see Chapter 4), Pb was deposited on the pc-Pt electrode, following the work of He *et al* [5], as follows: 1 mM Pb(IV) acetate (Aldrich, 95%) + 0.25 M KOH was admitted into the IR cell and the potential held at -0.85 V vs MMO for 15 minutes, after which half the electrolyte was replaced by 0.25 M KOH (still under potential control) eight times, reducing the Pb(IV) acetate concentration in solution to $< 10^{-6}$ M. Ethanol was then added to the electrolyte, via a pipette, to a final concentration of 1 M, and the solution agitated thoroughly to ensure effective mixing. Based on the seminal papers by Clavilier et al [6] and Feliu and co-workers [7] on Pb deposition on well-defined Pt surfaces in acid and alkaline solution, the electrochemical response of the Pb shows that the metal is irreversibly adsorbed on the Pt, rather than having undergone underpotential deposition (upd). The Pb was removed from the Pt electrode by immersing the latter in aqua regia and washing with Millipore water, these repeated several times.

2.4.3. The single beam reference spectrum

Figure 2.8 shows a typical single beam reference spectrum recorded at a potential of -0.85 V vs. MMO, from which an approximation of the optical path length, and hence the thickness of the thin layer, may be calculated. As discussed previously, 0.1 M KOH was employed as an electrolyte for ethanol electro-oxidation experiments. Consequently, absorptions for liquid water were to be expected in the FTIR spectra, and it is generally accepted that water is highly hydrogen bonded and exhibits three principle absorptions in the mid-IR range [8-11]: $1640cm^{-1}$ due to H-O-H deformation, $3450cm^{-1}$ due to the O-H asymmetric stretch and at $3615cm^{-1}$ due to the O-H symmetric stretch. Considering the absorption band at ca. $1640cm^{-1}$ in the single beam reference spectra (see fig 2.8), an approximation for the optical path length can be made using the Beer-Lambert law:

$$\mathrm{Log}_{10}(I_0/I) = \varepsilon\, c\, l \qquad (1.2)$$

Where: ε = extinction coefficient for water ($M^{-1}cm^{-1}$), c = concentration of water (M), l = optical path length (cm), I and I_o are the intensities of the transmitted and incident light respectively.

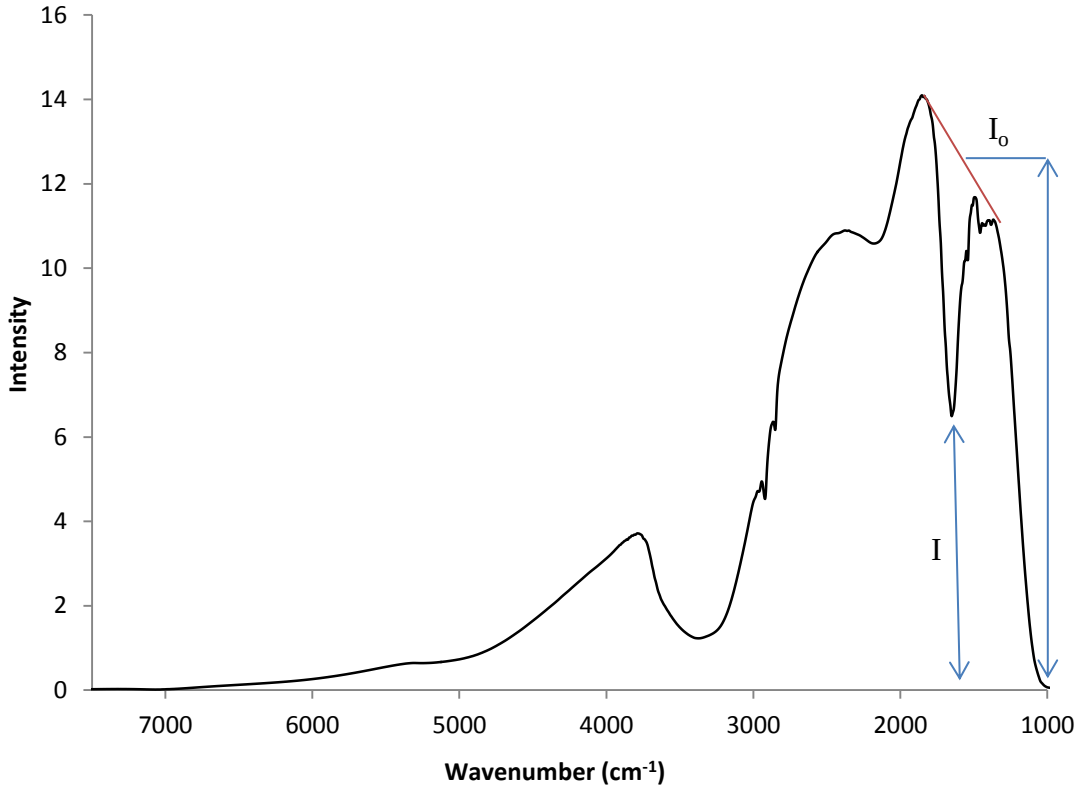

Figure 2.8. Single beam reference spectrum recorded at -0.85V vs. MMO at 25°C, in N_2 saturated 0.1M KOH + 1M EtOH (8cm^{-1} resolution, 100 scans, 47 seconds per scan set).

Taking an approximation for 'I_o' of 12.4 and 'I' of 6.7 from fig. 2.6, and using the extinction coefficient of 21.8 $M^{-1}cm^{-1}$ [12] and liquid water concentration of 55.56 $molL^{-1}$, an approximate optical path length of 2.2μm can be calculated.

Figure 2.9 shows a schematic representation of the approximate relationship between the distance (d) of the prismatic window from the Pt electrode, and the optical path length. From the figure, it may be seen that:

$$\text{Cos } \theta = d/(l/2) \qquad (2.11)$$

And hence:

$$d = (l/2) \text{ Cos } \theta \qquad (2.12)$$

As discussed previously (see section 2.3), the angle of incidence of the IR beam was 46°, giving an angle of incidence at the Pt electrode of 50° [1][4]. Hence, taking θ as 50 and l as 2.2 μm (fig. 2.8), an approximate value for the thin layer thickness of 1.8 μm may be calculated using equation 2.12.

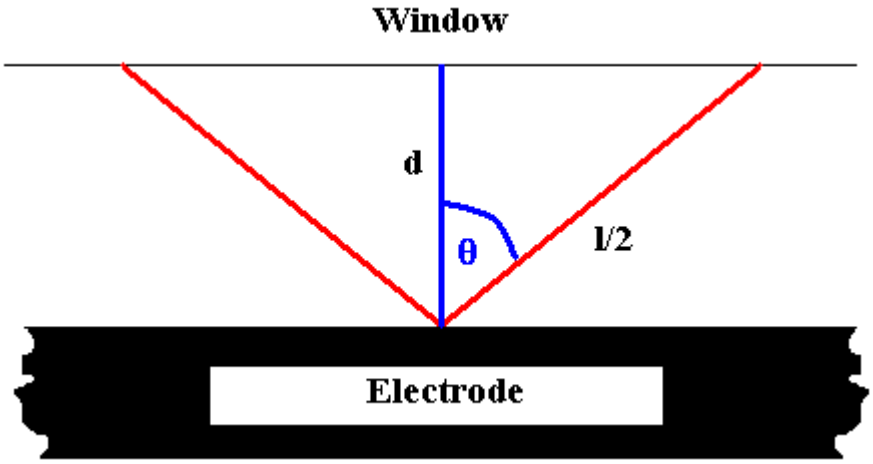

Figure 2.9. Schematic showing the optical path length, l, and thin layer thickness, d.

2.4.4. Alignment using the single beam reference spectrum

Table 2.2 shows a summary of the preliminary *in-situ* FTIR experiments carried out to investigate the ethanol oxidation reaction at 25 °C. The large number of experiments allowed for the optimization of the spectro-electrochemical procedure, paying attention both to the presence and absence of specific IR features, as well as the effect imposed by the size of the optical path length and hence approximate thin layer thickness. Furthermore, by optimizing the position of the electrochemical cell when mounted to the FTIR sample compartment, and hence the alignment of the Pt top hat with respect to the IR beam, the signal observed in the FTIR single beam spectra were enhanced considerably. Griffiths & de Haseth [13] state that poor mirror alignment dramatically reduces the wavenumber at which the greatest intensity in the spectrum may be observed, i.e. spectral information at high wavenumbers may be lost. As may be seen from table 2.2, the maximum intensity of the major band at 1900 cm^{-1} in the single beam reference spectrum (see fig. 2.8) was significantly greater when using the alignment in runs 7 and 8 than in runs 1-6. Thus, despite the fact that I/I_0 was greater in runs 3-6, the configuration of cell and mirrors

employed in run 8 was selected for the experiments discussed in this thesis due the greater amount of source energy and sufficiently low optical path length (< 3 μm).

T /^{o}C	Run	Date	I_{1900} /V	I/I_0	L /μm
25	1	27/01/12	3.56	0.67	3.0
25	2	03/02/12	2.84	0.70	3.0
25	3	16/04/12	8.49	0.81	2.7
25	4	17/04/12	6.14	0.85	4.2
25	5	20/04/12	5.48	0.83	2.4
25	6	20/04/12	5.26	0.87	2.4
25	7	23/05/12	12.0	0.71	3.0
25	8	31/05/12	14.2	0.72	2.6

Table 2.2. Summary of the preliminary in-situ FTIR experiments carried out at 25 ^{o}C, where T = temperature (^{o}C), L = optical path length (μm), I_{1900} = the maximum intensity of the major band at 1900 in the single beam reference spectrum (V).

2.5. Cyclic Voltammetry

Cyclic voltammetry (CV) is a technique employed by electrochemists to monitor the response in an electrochemical system when applying a large periodic potential change [14]. The conventional electrochemical cell used to carry out CV is sealed to prevent entry of air, and the electrolyte is usually purged with an inert gas (eg. N_2). This is necessary so as to remove O_2 from the system under study, reduction of which would interfere with the CV response.

The conventional cell configuration is comprised of three electrodes (WE, CE and RE) immersed in an electrolyte [14]. As discussed previously, a Pt foil WE and Pt/Ti Mesh CE (see fig. 2.2), and a MMO RE were employed in the CV experiments carried out during this project. During a CV experiment, the potential of the WE with respect to the RE is cycled repeatedly between an anodic and cathode limit (see fig.

2.10) at a fixed scan rate while the current is monitored as a function of WE potential [14-16].

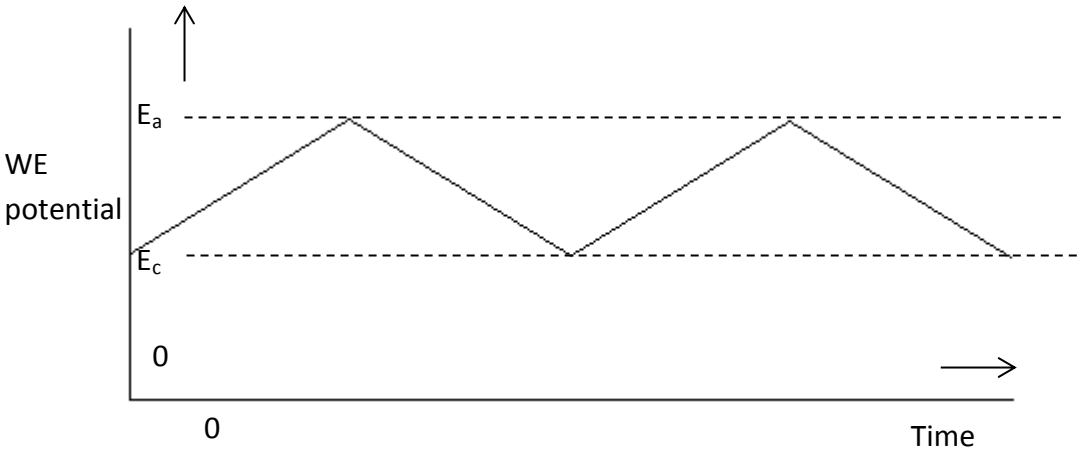

Figure 2.10. Potential with respect to time during a CV experiment, where E_a and E_c are the respective anodic and cathodic potential limits.

Ideally, the WE and CE are co-facially aligned at as small a distance as possible, without being in contact, to optimize electron transfer and hence minimize resistance between the two electrodes. However, the thin layer configuration employed during the FTIR experiments in this study does not allow for such positioning, leading to restricted diffusion and hence uncompensated resistance [15-17]. This can lead to a voltage drop between the reflective WE and RE [14].

2.6. Gas-Phase In-Situ FTIR Experiments

2.6.1. FTIR spectrometer

Gas-phase *in-situ* FTIR experiments were carried out using a Varian 670-IR spectrometer equipped with a ceramic, air-cooled infrared source and a cooled DLaTGS detector. A Specac reflectance accessory with an environmental chamber (see fig. 2.11) allowed IR spectra to be collected from the sample under a controlled atmosphere from room temperature to 800 ^{o}C and pressures from vacuum to 34 atm. Further, N_2 gas was admitted into the environmental chamber via a pipe network (see figs. 2.12(a) and (b)), allowing for control of both flow rate and relative humidity.

2.6.2. Relative Humidity

Figure 2.12 shows a schematic of the apparatus used for the control of relative humidity during *in-situ* FTIR experiments. From the figure, it may be seen that N_2 was passed through a jacketed Dreschel bottle containing saturated aqueous NaCl (200 cm^3). The temperature of the Dreschel bottle was maintained constant between 4-40 ^oC using a Grant LTC1 Water Recycler. The relative humidity of the N_2 exiting the Dreschel bottle was monitored using a Testo 605-H1 humidity meter, and fig. 2.13 shows the relative humidity of the N_2 gas entering the environmental sample chamber as the temperature of the saturated NaCl (aq) was increased.

2.6.3. Preparation of the PBI samples

Ti discs of 0.95 cm^2 were coated in PBI, by casting from dimethylacetamide (DMAc), and allowed to dry at room temperature for ca. 24h. The PBI was dissolved in the DMAc in a PTFE digestion vessel using microwave heating to a concentration typically of 5-10 wt%. Thus, ca. 0.1 cm^3 PBI/DMAc was placed on the Ti disc using a pipette and allowed to dry. The mass of PBI was then calculated from the mass of the disc and disc+dry film. The density of the dry PBI was taken as 1.3 g cm^{-3} [18] and the loading of dry film calculated accordingly.

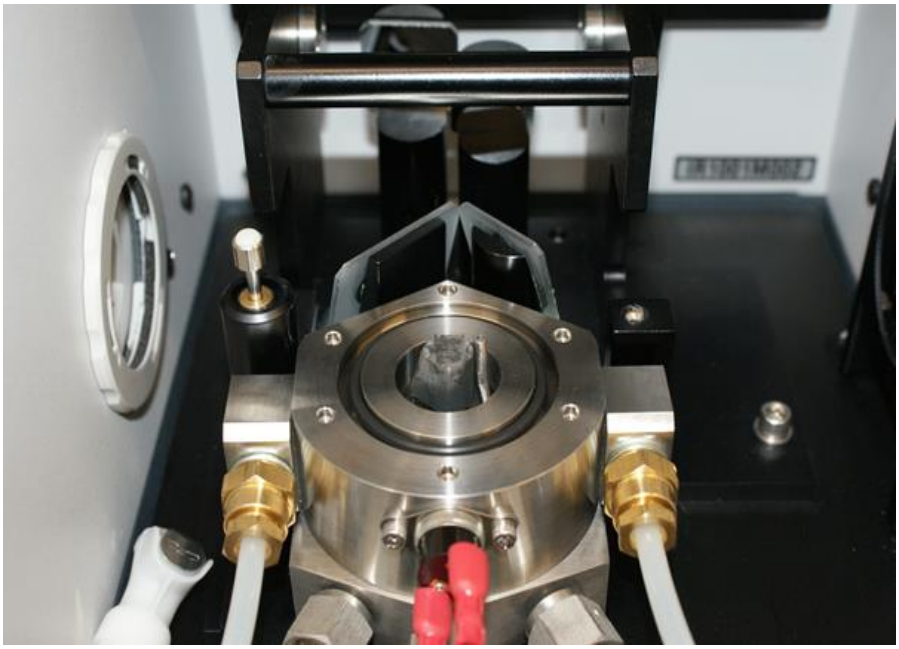

Figure 2.11. The environmental chamber employed for the gas phase in-situ FTIR experiments at both varied temperature and relative humidity.

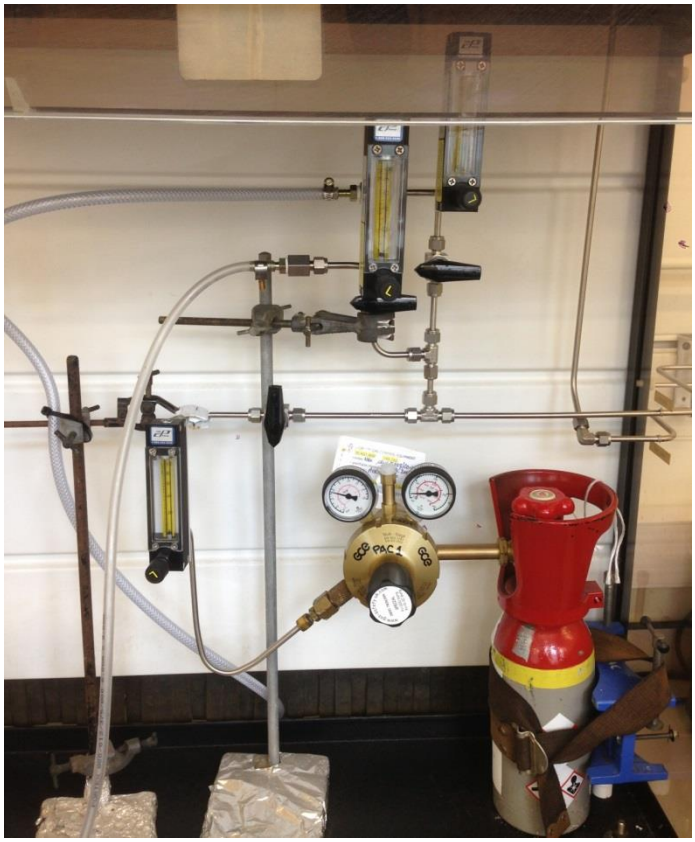

Figure 2.12. (a) Photograph of the FTIR spectrometer and pipelines used to control the flow rate and relative humidity of N_2 entering the environmental chamber. (b) Enlarged photograph of the gas pipelines.

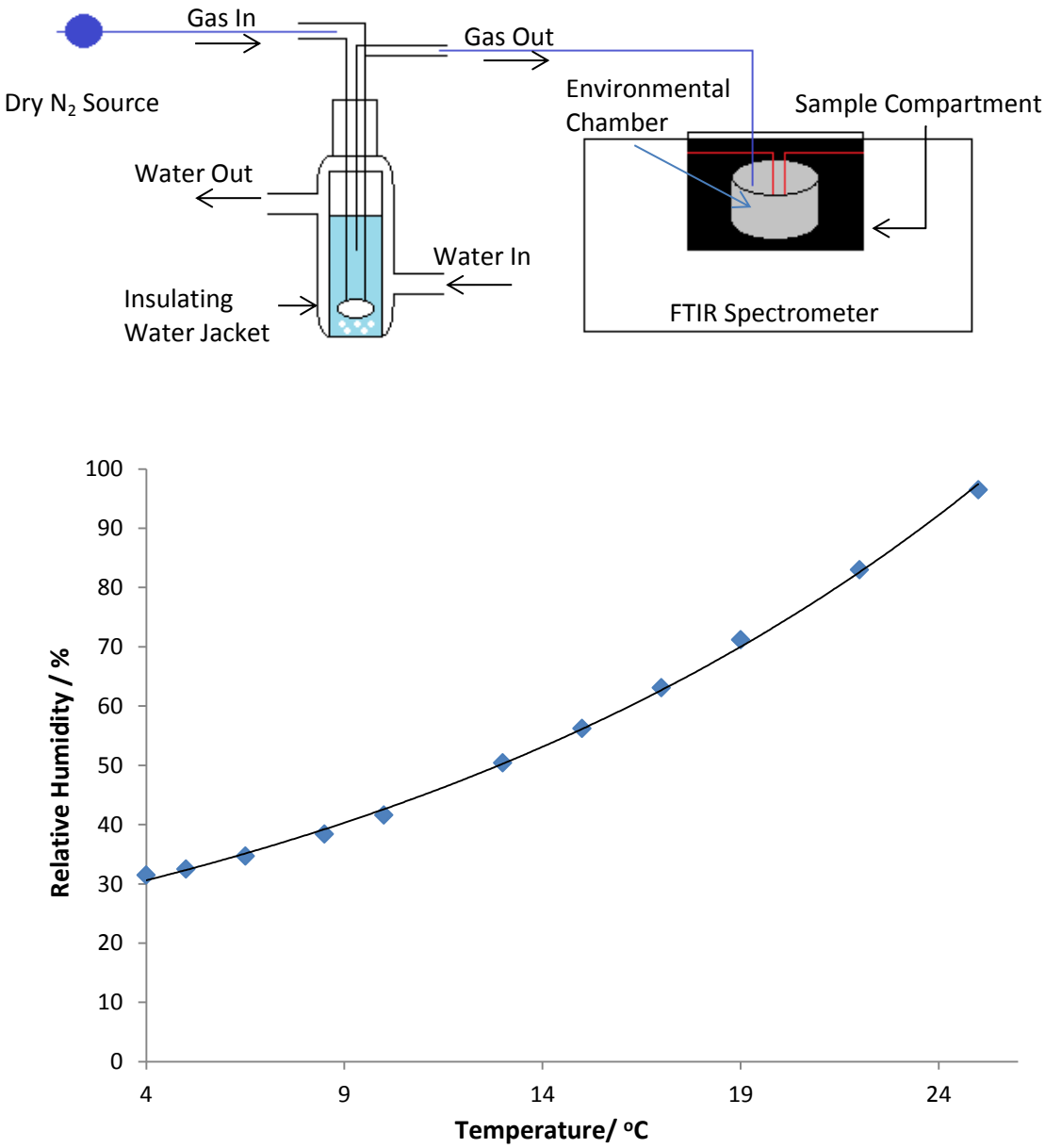

Fig. 2.13. (a) Schematic representation of the apparatus used to control the relative humidity in the environmental chamber during the in-situ FTIR experiments on PBI. (b) The relative humidity of the N_2 gas entering the FTIR environmental chamber after passing through the jacketed Dreschel Bottle as a function of temperature.

2.6.4. Typical In-Situ FTIR Analysis Procedure - Polybenzimidazole

For absolute spectra, the PBI-coated Ti disc was placed in the sample attachment and mounted on the central, heated pillar of the chamber, which was then purged with N_2

for approximately 50 minutes. A spectrum (S_S, 250 co-added scans and averaged scans at 4 cm^{-1} resolution, ca. 5 minutes per scanset) was collected and normalised to a reference spectrum (S_R) collected from the uncoated Ti disc under the same conditions.

For transmission spectra, a PBI-coated CaF_2 disc was placed in a press-lock holder attachment in the sample compartment, which was then purged and a spectrum collected which was normalised to the uncoated CaF_2 disc.

During the experiments conducted as a function of temperature and humidity, the reference spectrum (S_R, 250 co-added scans and averaged scans at 4 cm^{-1} resolution, ca. 5 minutes per scanset) was collected and a second spectrum taken at the reference point (dry N_2, 25 °C), after which spectra (S_S) were collected with increasing relative humidity or temperature. The difference spectra were presented as in the solution-phase experiments (see eqn. 2.10).

2.7. References

1. Moya D.L., 2012, *Fundamental and Applied studies on the development of an alkaline anion exchange membrane-based direct alcohol fuel cell*, Ph.D. thesis, Newcastle University, 2012.
2. Ives, D. J. G.; Janz, G. J. eds, *Reference Electrodes Theory and Practice*, New York, Academic Press, 1961.
3. Christensen, P. A.; Hamnett, A.; Linares-Moya, D. *Physical Chemistry Chemical Physics*, 2011, *13* (24), 11739-11747.
4. Faguy, P. W.; Fawcett, W. R., *Applied Spectroscopy*, 1990, 44, 8, 1309-1316.
5. He, Q.; Shyam, B.; Macounova, K.; Krtil, P.; Ramaker, D. and Mukerjee, S., *Journal of the American Chemical Society*, 2012, 134, 8655 – 8661.
6. Clavilier, J.; Orts, J. M.; Feliu, J. M. and Aldaz, A., *Journal of Electroanalytical Chemistry*, 1993, 293, 197-208.
7. Feliu, J. M.; Fernandex-Vega, A.; Orts, J. M. and Aldaz, A., *J. Chim Phys.*, 1991, 88, 1493-1518.

8. Lutz, H., *Bonding and Structure in Water Molecules in Solid Hydrates: Correlation of Spectroscopic and Structural data, in: Solid Materials, Springer*, 1988, Berlin, 97-125.

9. Iwasita, T.; Xia, X.; Journal of Electroanalytical Chemistry, 1996, 411, 1-2, 95-102.

10. Du, Q.; Freysze, E.; Shen, Y. R., Physical Review Letters, 1994, 72, 2, 238-241.

11. Verma, D.; Katti, K.; Katti, D., *Spectrochimica Acta, Part A: Molecular and Biomolecular Spectroscopy*, 2007, 67, 3-4, 784-788.

12. Venyaminov, S. Y.; Prendergast, F. G., *Analytical Biochemistry*, 2007, 248, 234–245.

13. Griffiths, P. R.; De Haseth, J., *Fourier Transform Infrared Spectroscopy*, John Wiley and Sons inc., Canada, 47-49, 2007.

14. Christensen, P. A.; Hamnett, A. *Techniques and Mechanisms in Electrochemistry*, 1 ed.; Blackie Academic & Professional, an imprint of Chapman & Hall: Oxford, 1994.

15. Faguy, P.W.; Fawcett, W., Applied Spectroscopy, 1990, 44(8), 1309-1316.

16. Lin, W.F.; Christensen, P.A.; Hamnett, A.; Zei, M.S.; Ertl, G., *Journal of Physical Chemistry B,* 2000, 104, 28, 6642-6652.

17. Lin, W.F.; Christensen, P.A.; Jin, J.M.; Hamnett, A., 2007. *In-situ spectroscopic studies of adsorption at the electrode and electrocatalysis*, Elsevier, 99-138.

18. Berke, A.; Dvořák, V.; Němec, I. and Zýka, J., *Journal of Electroanalytical Chemistry*, 1962, 4, 150 – 155.

3. In-Situ FTIR studies on the oxidation of ethanol at polycrystalline Pt in aqueous 0.1M KOH at 25 ^{o}C

3.1. Introduction

3.1.1. Overview

This chapter presents in-situ FTIR studies on the electrochemical oxidation of ethanol at polycrystalline Pt in 0.1M KOH; the data obtained with C_2H_5OH are compared to results obtained using C_2D_5OD under the same conditions. The work continues earlier studies in Newcastle by other workers on methanol and formate oxidation [1][2], and supports the model formulated on the basis of these papers that, in contrast to acidic solution, under alkaline conditions intermediates are formed bonded through O rather than C, and that a number of mechanistic pathways are available differing very little in terms of activation energy.

Initially, this project was designed to provide a library of IR spectra of intermediates and products to facilitate the study of the electro-oxidation of small organic molecules at novel, non-noble metal anodes by *in-situ* Fourier Transform InfraRed (FTIR) spectroscopy. However, the work on Pt has provided some unexpected insights into this area of electrocatalysis, particularly with respect to the role of intermediates bonded through oxygen rather than carbon, as well as of adsorbed CO. The study of ethanol oxidation at Pt is timely given the current interest in ethanol as a sustainable fuel and since, in contrast to the *in-situ* FTIR literature on the electro-oxidation of ethanol in acid solutions, studies in alkaline solution are far less frequent; in fact, only a few examples of ethanol oxidation at Pt electrodes in alkaline solution could be found, including FTIR the studies by López-Atalaya and co-workers [3] (see fig. 3.1), Lai *et al*. [4] (see fig. 3.2) and Feliu *et al* [5] (see fig. 3.4).

3.1.2. FTIR studies on ethanol oxidation in alkaline solution

López-Atalaya and co-workers [3] employed the Subtractively Normalized Interfacial Fourier Transform Infra-Red Spectroscopy (SNIFTIRS) [6] approach to study ethanol electro-oxidation at Pt(110) and Pt(100) electrodes in aqueous NaOH and Na_2CO_3.

In the study by López-Atalaya, the potential was stepped back and forth in a square wave between 0.05V and 0.35V vs RHE, and the co-added and averaged scans collected at 0.35V normalized to those taken at 0.05V. The authors observed linearly bonded CO at Pt(110) and multibonded CO at Pt(100), and claimed to have also detected linearly adsorbed CO at both Pt (111) and Pt(100), but these bands were very weak.

The SNIFTIRS approach is a method of increasing signal-to-noise, but is only suitable for absorptions that: (i) shift in frequency with potential and (ii) do so in a completely reversible manner as the potential is switched repeatedly. Any absorptions arising from species produced in an irreversible manner will be averaged out. In addition, there is some concern that such potential modulation can influence the surface chemistry taking place [6][7].

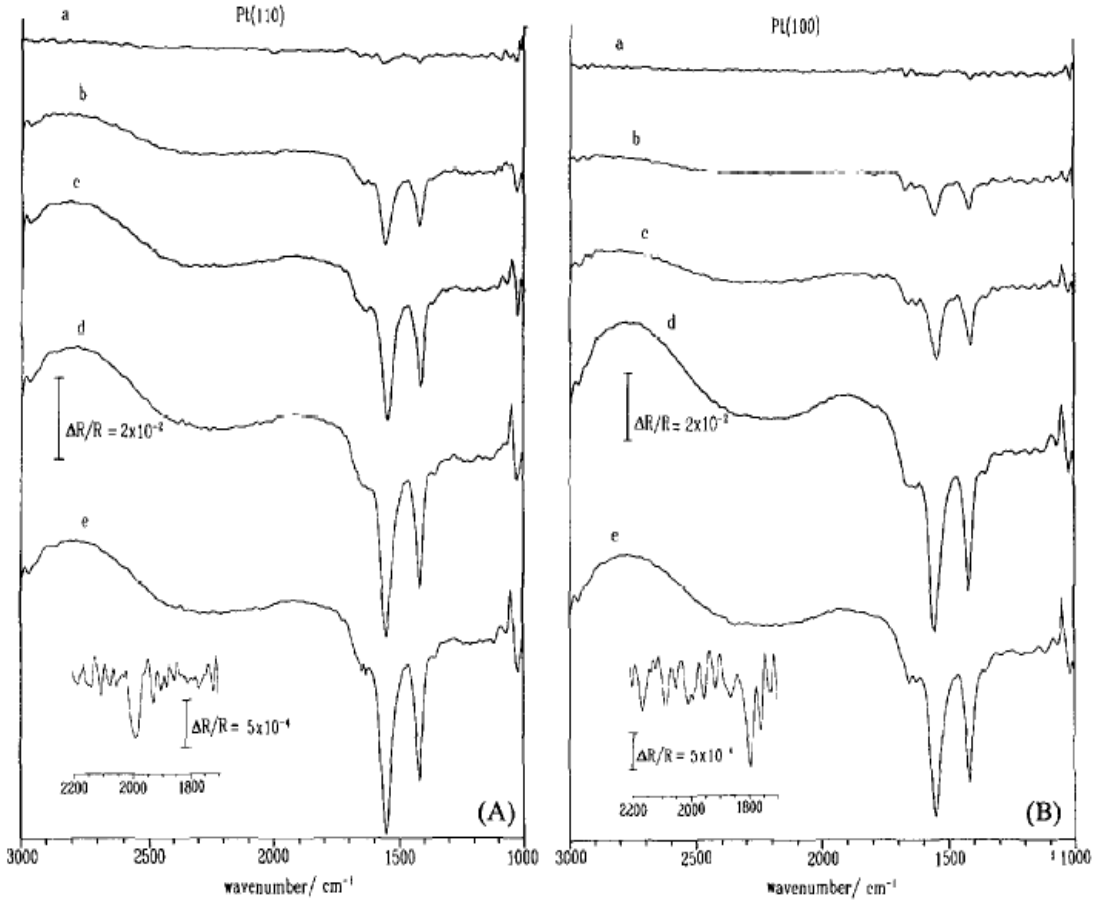

Figure 3.1. In-situ FTIR spectra of Pt(110) and Pt(100) in 0.1M NaOH + 0.1M EtOH collected by Lopez-Atalaya and co-workers during a slow potential scan from 0.05V to 1.00V vs. RHE at 1mVs^{-1} [3].

López-Atalaya *et al* also collected *in-situ* FTIR spectra during a slow potential scan from 0.05 V vs. RHE to 1.00V at $1mVs^{-1}$ (see fig. 3.1). The spectra were collected over small potential ranges, and were identified with the midpoint potential of the range, normalized to the reference spectrum collected at 0.05 V.

Whilst the authors observed (very weak) bands due to linear CO_{ads} at Pt(110) and multiply bonded CO at Pt(100), the spectra were dominated by features due to the loss of OH^- (which were not assigned by the authors) and to the gain of acetate ions in solution at 1550 cm^{-1} and 1415 cm^{-1}, attributed to the symmetric and asymmetric stretches of COO^- (ν_s and ν_{as} respectively). The authors did not attempt to place their data in the context of a model for ethanol oxidation at Pt.

The more recent paper by Lai and co-workers [4] presents a comprehensive study of ethanol electro-oxidation at polycrystalline gold and platinum electrodes as a function of pH using cyclic voltammetry, in-situ external reflectance FTIR spectroscopy and SERS (see fig. 3.2).

In 0.1 M NaOH, Lai et al. observe CO_2 formation at 0.36V (a remarkably low onset potential), suggesting that the pH is dropping below the $pK_{a,1}$ of H_2CO_3 (6.37) at least in some regions across the Pt surface [2]. In addition, the authors observe the oxidation of adsorbed CO at a similarly low potential and close to that observed in acidic solution. Furthermore, the only band attributed to a solution species other than CO_2 was a weak feature at 1381 cm^{-1}, assigned by the authors to the CH_3 bend of solution acetate based on a paper by Colmati and co-workers [8]. However, if the latter feature was apparent, then the far more intense absorptions due to the asymmetric and symmetric stretches of solution acetate ions [3] should also be present. Apart from the above, the authors observed bands due only to adsorbed species: CO, acetate and bicarbonate, all of which is very singular. The inappropriate assignment by the authors of a band at 1585 cm^{-1} to the asymmetric stretch of adsorbed acetate was made on the basis of IR studies on aqueous solutions of alkaline earth and copper acetates [9]; further, on the basis of the surface selection rule [10] (and references therein), the asymmetric stretch of bidentate acetate would not be observed.

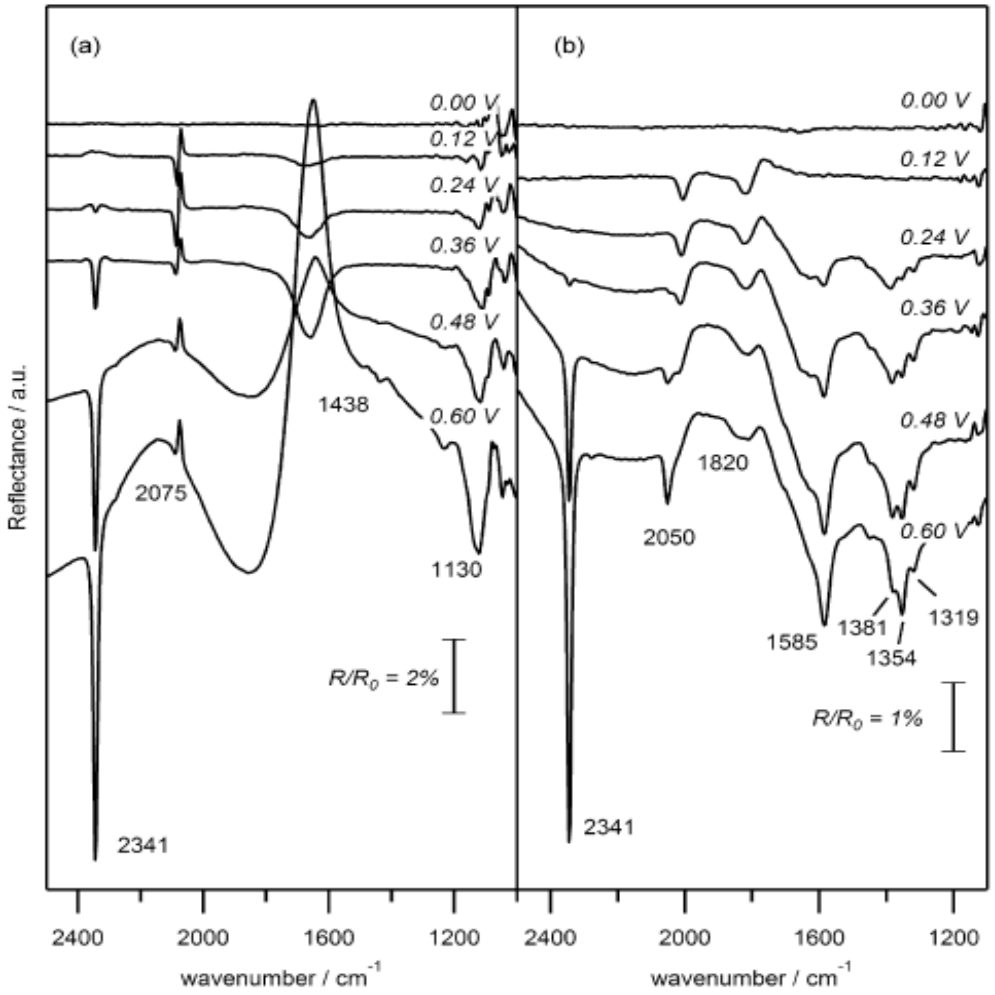

Figure 3.2. In-situ FTIR spectra collected by Lai et al during a potential sweep at 10 mVs^{-1} from 0 to 0.60V using 0.5M ethanol in (a) 0.1M $HClO_4$ and (b) 0.1M NaOH [4].

To understand why the asymmetric stretch of bidentate acetate is not observed it is necessary to consider the Greenler effect, a critical aspect of *in-situ* FTIR spectroscopy [11]. Thus, when an unpolarized IR ray having an oscillating electric vector E (see fig. 3.3) is incident on an electrode surface, it may be assessed in terms of two limiting polarizations: s-polarized light which has the electric vector E_s oscillating perpendicular to the plane of reflection, and p-polarized with an electric vector E_p oscillating parallel to the plane, the plane defined as containing both the incident and reflected rays. Furthermore, the p-polarized electric vector may be resolved into the E_{px} and E_{pz} components which oscillate parallel and perpendicular, respectively, to the electrode surface. The incident and reflect rays interfere to

produce a standing wave at the point of incidence at surface, proportional to E_i^2, where E_i is the electric vector of relevant polarization [11-12]. At all angles of incidence (θ in fig. 3.3), the standing wave intensities from s and p_x polarized light are zero, and very small over a distance commensurate with the wavelength of the incident IR ray, depending upon solvent absorptions and surface reflectivity [11-12].

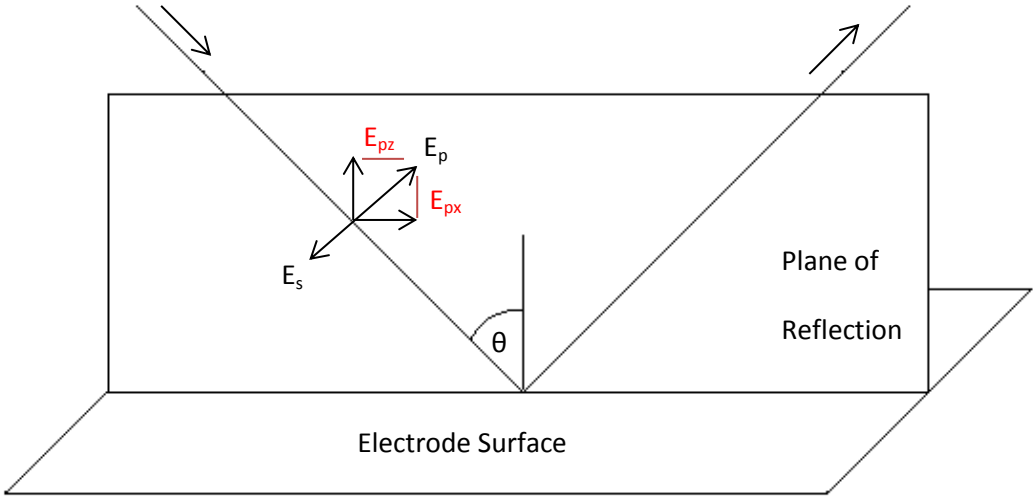

Figure 3.3. Schematic representation of s- and p- polarized light incident at a reflective electrode surface (eg. Pt). θ is the angle of incidence. Redrawn from [11].

In contrast, the intensity of p_z depends upon the angle of incidence and rises to a maximum of 3-4 times that of the incident intensity at high angles of incidence [11]. Hence, the p_z component of a p-polarized IR ray is sensitive to both solution and adsorbed species, providing the latter exhibits a significant dipole change during vibrations perpendicular to the surface [13-15]. However, the p_x and p_y components are "blind" to species near to, or adsorbed at the electrode surface. Thus, any vibrations having dipole changes that are parallel to the surface, such as that during the asymmetric stretch of bidentate acetate, will be invisible to both p and s-polarized light [11].

Returning to the work by Lai *et al* [4], in contrast to the IR data obtained in pH 12 0.1 M NaOH, in pH 12 phosphate buffer, the authors observed no CO_2 or adsorbed species. Instead, only solution acetate was seen (strong bands due to the

asymmetric stretch at 1550 cm^{-1} and symmetric stretch at 1415 cm^{-1}, but no band was observed at 1385 cm^{-1} due to the CH_3 bend). The absence of adsorbed species was attributed by the authors to the strong inhibition of active sites by adsorbed phosphate.

Solution acetate was observed at polycrystalline Pt in KOH during this project (see section 3.2.2.), similar to López-Atalaya and co-workers and, on the basis of straightforward electrochemical considerations, the complete lack of solution acetate ions observed by Lai et al [4] in the experiments in pH 12 NaOH is highly unlikely. In addition, there is no indication in their paper of the thin layer thickness in the various FTIR experiments. Although the authors do not present the range above 2400 cm^{-1} in their spectra, there is clear water movement in the pH 1 spectra and in the spectra in pH 12 phosphate buffer, as may be judged from H-O-H deformation band near 1640 cm^{-1}; however there is no such evidence for water movement in the pH 12 NaOH spectra. These observations coupled with the very low onset potential for the oxidation of adsorbed CO (and the fact this is close to that observed in acid solution), and the formation of CO_2 suggest that the thin layer in the experiment in NaOH was abnormally thin, such that the pH in the layer became acidic almost as soon as charge passed, and only adsorbed species were observed.

Two papers have been published recently concerning *in-situ* FTIR studies of ethanol oxidation in alkaline solution at polycrystalline Pd electrodes [16][17] and hence are useful in providing band assignments for intermediates and products of ethanol oxidation. In particular, Zhou et al obtained their assignments for acetate by comparison with the transmission spectrum of $NaOOCH_3$. They also provide assignments for C_2H_5OH bands. Their assignments are presented in table 3.1.

Most recently, Feliu and co-workers [5] investigated the EtOH oxidation reaction in alkaline electrolyte at Pt (100), Pt (110) and Pt(111) single crystal electrodes via cyclic voltammetry, chrono-amperometry and *in-situ* FTIR spectroscopy. Figure 3.4 shows the FTIR spectra collected by the authors at Pt(100) during the oxidation of 0.2 M EtOH + 0.1 M NaOH over the potential range from 0.2-0.95 V vs. RHE. As may be seen from the figure, the spectra are dominated by gain features at ca. 1550 and 1415 cm^{-1} (similar to the spectra collected at Pt(110) and Pt(111)), attributed by

the authors to the symmetric and asymmetric stretching vibrations of solution COO^-. Further, in contrast to the work by Lopez-Atalaya and co-workers [3] and Lai *et al* [4], the authors did not observe CO_{ads} at low potentials (i.e. before the drop in thin-layer pH due to the depletion of solution OH^-). Feliu et al [5] suggested that acetate, and possibly acetaldehyde, were the main oxidation products at all three electrode morphologies, and postulated that acetaldehyde was not detected in the FTIR spectra (see fig 3.4) due to its polymerization via aldol condensation in alkaline medium.

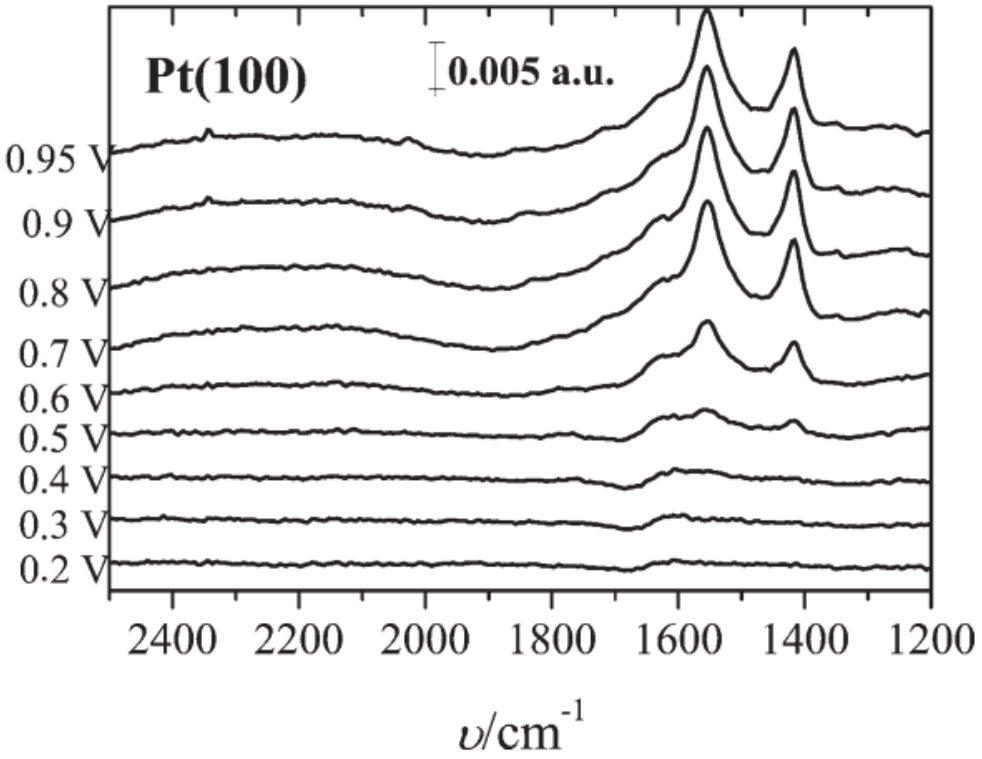

Figure 3.4. In-situ FTIR spectra collected by Feliu et al [5] during oxidation of 0.2 M EtOH + 0.1 M NaOH at Pt(100) over the potential range from 0.2-0.95 V vs. RHE.

In an earlier study, Feliu and co-workers [18] studied the ethanol oxidation mechanism at Au (110), Au (210) and polycrystalline Au electrodes in alkaline media. From their *in-situ* FTIR data collected in 0.1 M EtOH + 0.1 M NaOH (see fig. 3.5 for the spectra collected at polycrystalline Au), and similar to the work discussed above, the authors attributed bands at ca. 1415 and 1548 cm^{-1}

to the symmetric and asymmetric stretching vibrations of COO^- in solution, which they observed using all three electrode morphologies.

Band / cm^{-1}	Assignment
1551	ν_s CH_3COO^-
1415	ν_{as} CH_3COO^-
1348	CH_3COO^-
1018	CH_3COO^-
1390	CO_3^{2-}
1085	C-O stretch C_2H_5OH

Table 3.1. The assignments of the spectral features observed by Zhou et al [16].

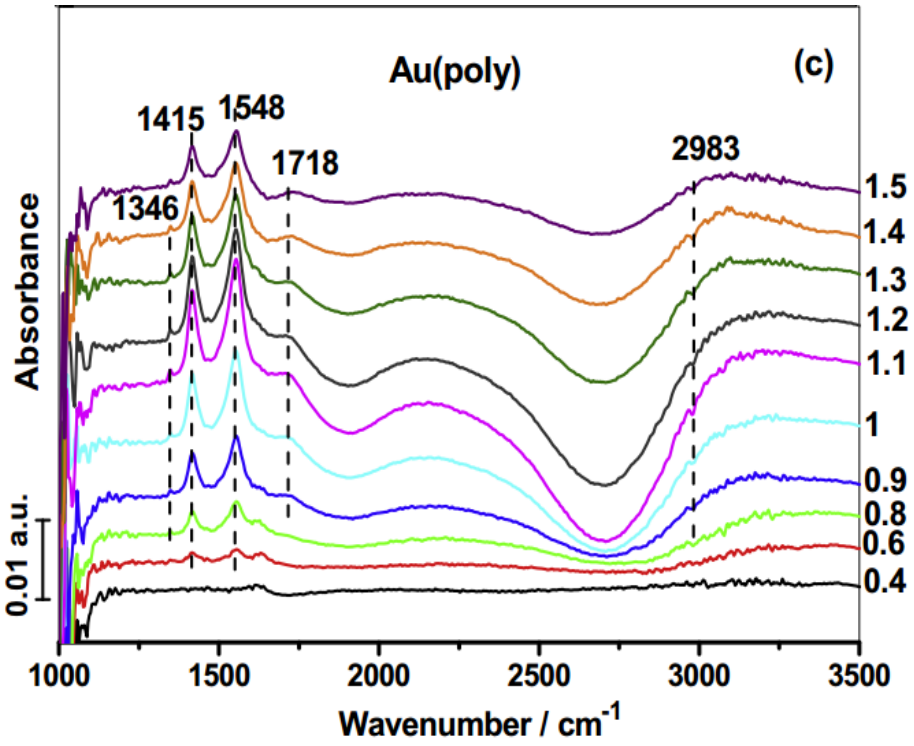

Figure 3.5. In-situ FTIR spectra collected by Feliu et al [18] at polycrystalline Au in 0.1 M NaOH + 0.1 M EtOH, normalized to a reference spectrum collected at 0 V vs. RHE.

Returning to fig. 3.5, the authors assigned a band at ca. 1346 cm^{-1} to the symmetric C-H bend of the methyl group in acetate, and a loss feature at ca. 2383 cm^{-1} was attributed to the C-H stretch of the methyl group in ethanol.

Feliu *et al* postulated that at low potentials, OH_{ads} facilitates the removal of the hydroxyl hydrogen from ethanol, thus promoting its dissociative adsorption at the electrode surface:

$$CH_3CH_2OH + Au(OH)_{ads} \rightarrow CH_3CH_2O^* + Au + H_2O \qquad (3.1)$$

The authors state that the ethoxy species is an unstable radical ($CH_3CH_2O^*$) which will rapidly react with solution OH^- (eq. 3.2) or OH_{ads} (eq. 3.3) depending on the electrode potential, explaining why no ethoxy species were detected during their FTIR measurements.

$$CH_3CH_2O^* + OH^-_{sol} \rightarrow CH_3CHO + 2H_2O + e^- \qquad (3.2)$$

$$CH_3CH_2O^* + Au(OH)_{ads} \rightarrow CH_3CHO + H_2O \qquad (3.3)$$

As may be seen from fig. 3.5, a broad loss feature was observed near 2700 cm^{-1} which was attributed by the authors to the loss of solution OH^- in the thin layer due its reaction with adsorbed ethoxy. The peak at 2700 cm^{-1} was tracked by a loss feature at ca. 1870 cm^{-1}, which may also be attributed to solution OH^-, however, this was not assigned by Feliu *et al*. The authors concluded that, in alkaline media, acetate is the only product of ethanol oxidation at Au regardless of electrode morphology. Furthermore, they stated that in addition to facilitating the removal of the hydroxyl hydrogen from ethanol at low potentials, OH_{ads} most likely stabilizes the resulting adsorbed ethoxy species by controlling the surface charge density. At higher potentials the authors postulate that solution OH^- promotes the further oxidation of ethoxy and that acetaldehyde is a key intermediate that reacts with solution OH to form acetate. Hence, a weak band near ca. 1718 cm^{-1}, only observed at polycrystalline Au, was attributed to the C=O vibration of acetaldehyde or acetic acid and grew in intensity with increasing potential. However, the latter is unlikely when considering that no features were observed near 1280 cm^{-1} [19][20] and 1390 cm^{-1} [16][21], which are characteristic of the O-H deformation and C-O stretching, respectively, in the COOH group of acetic acid. Furthermore, there is no band at ca. 2340 cm^{-1} due to CO_2 and hence no evidence

for a drop in the pH of the thin layer, or at least in some regions across the electrode surface [2] (a pH of ≤ 4.75 (the pK_a of acetic acid [22]) would be required to facilitate the formation of acetic acid).

3.1.3. The ethanol oxidation reaction mechanism in alkaline solution

In terms of a model for ethanol oxidation at Pt in alkaline solution, the most often quoted is the Dual Path mechanism for ethanol oxidation in acid solution (see scheme 3.1 and section 1.1.1 for full discussion), which is generally taken as representative of the alkaline case as well [3-4]. The presence of CO_{ads} is taken as evidence for the "indirect path" (steps 1, 3, 5 and/or 1, 4, 5) resulting in bond cleavage and CO_2 formation. As discussed in section 1.1.1, the "direct path" (steps 1 and 2) produces acetic acid and acetaldehyde, both of which are stable with respect to further oxidation due, it is generally believed, to the blocking of the Pt surface by some of the chemisorbed fragments [9][23]; Shao and Adzic [9] suggest that the blocking of active sites is due to adsorbed acetate. In addition, the intermediates in the formation of acetaldehyde and acetic acid remain unclear [19][24-25]. Hence, whilst there is general agreement around the broad principles encapusulated in scheme 3.1, the exact details of the mechanism whereby solution ethanol is oxidised to acetic acid, acetaldehyde and small amounts of CO_2 remains controversial [4][20].

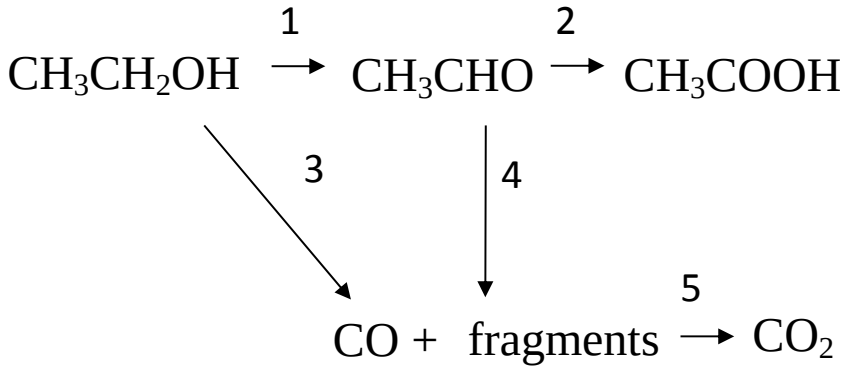

Scheme 3.1. The dual path mechanism.

Given the dearth of experimental data available for EtOH oxidation in alkaline solution, it does not seem unreasonable to turn to the wealth of data available in acid solution for support. Thus, Iwasita and co-workers [26][27] postulated that the chemisorption of ethanol at Pt results in CO_{ads}, Pt-OCH_2CH_3 (adsorbed ethoxy), Pt_2COHCH_3 and $PtCOCH_3$, all of which are oxidised only to CO_2. This work was supported by Ianniello [28] who studied the chemisorption of ethanol at porous Pt electrodes. Iwasita postulated that, apart from CO_{ads}, > 60% of the chemisorbed fragments were due to C_2 species, and hence that C-C bond cleavage occurs predominantly only at higher potentials (ie. 0.7V vs RHE), and thus after chemisorption. In contrast, other workers [29-31] postulate that chemisorption is primarily dissociative, resulting in CO_{ads} and other C_1 fragments, and Lai et al [4] suggest that $C_2H_5O^-$ is the reactive form of ethanol in alkaline solution (pH > 11) and that this is adsorbed to form ethoxy on the Pt surface (see scheme 3.2 for Lai *et al's* proposed mechanism). The adsorbed ethoxy then is oxidised to acetaldehyde: this can either react with adsorbed OH in a Langmuir-Hinshelwood [1-4] mechanism to form acetate, or undergo Aldol condensation [5][32] which deactivates it to further reaction.

3.1.4. The role of adsorbed CO during oxidation of ethanol at platinum in alkaline solution

Similar to the work by Iwasita and co-workers [26][27] and Ianniello [28] in acid solution, most studies on ethanol oxidation in alkaline electrolyte infer the existence of some form of adsorbed CO (CO_{ads}) [33]. However, this is generally without any direct, molecular evidence for its formation. For example, Jiang et al [34] observe two peaks in the forward sweep of cyclic voltammograms of carbon-supported Pt particles in aqueous NaOH/ethanol. By comparison to the case in acid solution [35] the peak to lower potential was assigned primarily to the complete oxidation of ethanol, and the second to its partial oxidation to acetate ions. As carbonate was a product, then it followed that CO_{ads} was the intermediate. Similarly, López-Atalaya et al [3] attribute stripping peaks in the voltammogram of ethanol chemisorbed on single-crystal Pt surfaces to the oxidation of CO_{ads} as the peaks were the same as observed when CO gas was adsorbed onto the electrodes (see section 3.1.2).

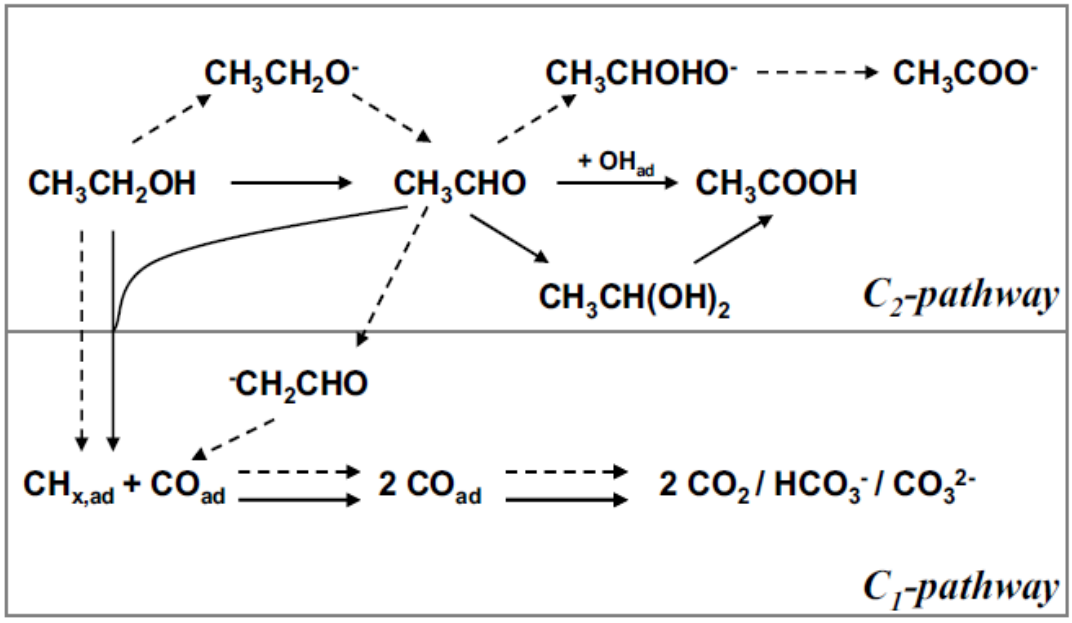

Scheme 3.2. The reaction mechanism for the ethanol oxidation reaction proposed by Lai et al [4]. Solid arrows denote the reaction mechanism at low electrolyte pH, while dashed arrows denote the mechanism at high pH.

Overall, under alkaline conditions, there is a heavy reliance on voltammetry to provide evidence for the dual path mechanism, despite the inability of the technique to provide molecular information. Further, there is some confusion with respect to the interpretation of the hysteresis generally observed in cyclic voltammogramms of Pt in ethanolic hydroxide solutions between the forward and reverse sweeps. Thus, Dutta and Datta [33] employ the ratio of the ethanol oxidation peak currents in the forward and back (reverse) sweeps, I_F/I_B, as a measure of the efficacy of the stripping of the Pt oxide at removing adsorbed, carbonaceous fragments. The higher this ratio, the more effective the oxidation of adsorbed species. In an earlier paper [36], they postulated that the formation of surface oxides activated the Pt surface to the oxidation of adsorbed species. However, in general, it is accepted that oxidation of adsorbed ethanol takes place via reversibly-adsorbed OH_a, and the oxidation of the Pt to Pt-OH or Pt-O inhibits ethanol oxidation at higher potentials [34][37]. The higher I_F/I_B, the more effective OH_{ads} is at oxidising adsorbed species. The extent of the hysteresis between the forward and reverse scans in a cyclic voltammogram at potentials ≤ that of the anodic peak in the reverse scan is also taken as an indication

of the coverage by strongly adsorbed species [4][5][24][37]; the greater the hysteresis, the greater the influence of adsorbed species (such as CO_{ads}). For example, Lai *et al* [38] observed very little hysteresis between the forward and reverse scans at potentials below the anodic peak in the reverse scan (ca. 0.6 V vs. RHE) in the CV's of polycrystalline Pt in 0.1 M NaOH+0.5 M ethanol at room temperature (see fig. 3.6). The authors suggested that this may indicate that the oxidation of adsorbed species does not play a major role; and that surface species are formed but are stable up to 0.65 V vs. RHE. However, the authors also postulated that the oxidation of surface species may occur, but very slowly compared to the timescale of the CV experiment depicted in fig. 3.6. Similar behavior was observed by Dimos and Blanchard [39] in their CVs of planar Pt in 1 M EtOH+1 M KOH.

A further example of the pitfalls of relying upon techniques incapable of providing molecular information to provide analytical data is provided by the work of Caram and Guitiérrez [40]. The authors employed polarization modulation reflectance spectroscopy (PMRS) to study methanol and ethanol chemisorption in acid and alkaline electrolyte at a polycrystalline Pt electrode. A peak at 270 nm was observed for methanol and ethanol in 0.5M $HClO_4$, and attributed to linearly-adsorbed C≡O (CO_L). The same feature was observed for methanol chemisorption in 1M NaOH, but not observed in the PMRS spectrum of ethanol in 1M NaOH, despite the amount of adsorbed CO, as estimated from cyclic voltammetry via oxidative stripping, being the same as observed with methanol under the same conditions. The authors could not explain the absence of the CO_L peak. It does not seem unreasonable to suppose that the stripping peak from ethanol chemisorption in NaOH was (primarily) due to adsorbed species other than CO_L.

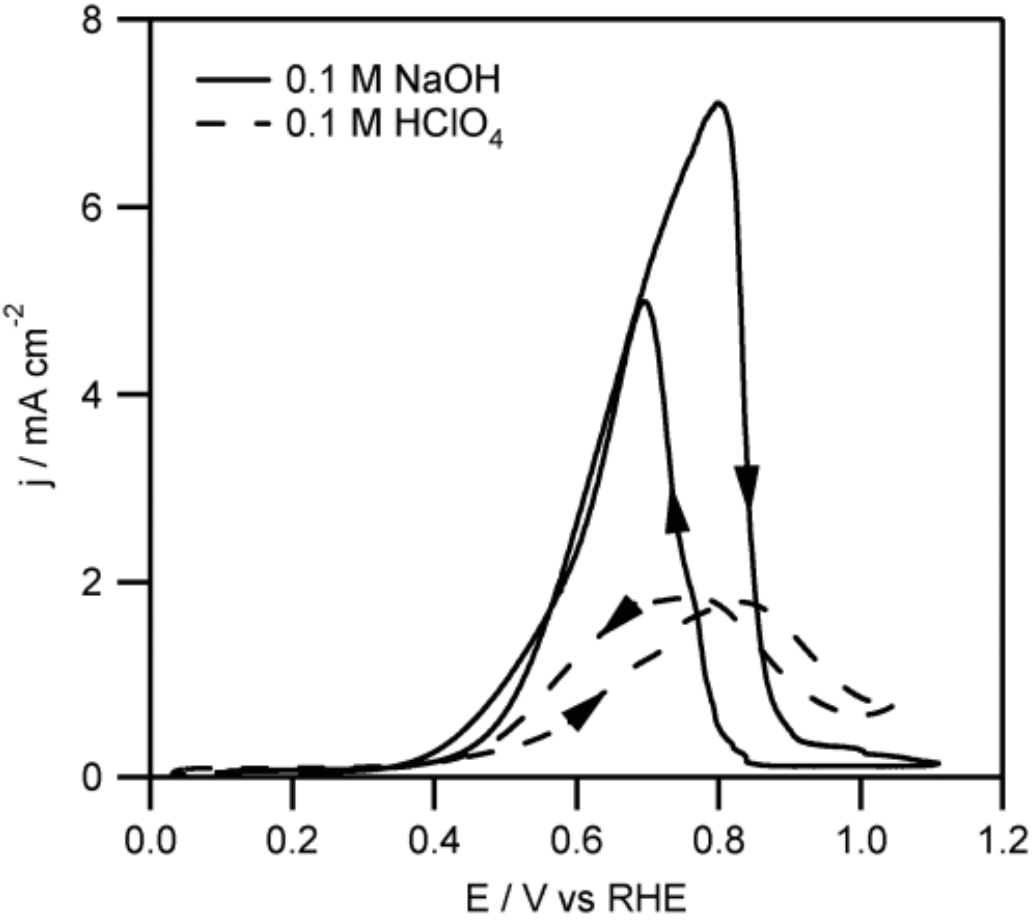

Figure 3.6. CV's of polycrystalline Pt in 0.5 M EtOH + 0.1 M NaOH (solid line) and 0.1 M $HClO_4$ (dashed line) collected by Lai et al [38], scan rate 10 mV s^{-1}, arrows indicated scan direction.

There are papers reporting molecular data to support the indirect path. Thus, Dutta and Datta [33] analysed the products from 1M ethanol oxidation in 0.5M NaOH at carbon-supported Pt particles using ion exchange chromatography (IEC). The authors' IEC data appeared to show carbonate production favoured over acetate at all the temperatures studied, 20 – 80 ºC, and increasing with increasing temperature. However, the ordinate axes on the relevant plots were unlabeled in terms of units, and no attempt appeared to have been made to render the IEC data quantitative. In the study which was discussed in section 3.1.2, Lai et al [4] also presented Surface Enhanced Raman (SER) spectra collected from a Pt electrode covered with chemisorbed ethanol in the absence of ethanol in solution. Bands were

observed at 440 and 515 cm^{-1}, attributed to two different forms of linearly adsorbed CO, and at 1960 and 2035 cm^{-1} attributed to bridge-bonded and linearly adsorbed CO, respectively. These were taken as evidence for the presence of adsorbed CO in the voltammetric experiments using single crystal Pt electrodes. However, it is not clear that the SERS electrode, consisting of electrochemically roughened gold on which Pt was electrodeposited a few monolayers thick, is representative of bulk Pt. The authors maintained that the thickness of the platinum layer was high enough to mask the electrochemical properties of the gold layer beneath. In contrast, in previous studies of metallic multilayer nanostructured catalysts by other workers in Newcastle, it has been found that overlying layers even hundreds of monolayers thick are unable to mask the influence of the underlying layers [41][42]. Further, a correlation between the SERS band intensities and, for example, the observed Faradaic current, was not attempted.

As discussed earlier (see section 3.1.2), Lopéz-Atalaya et al [3] observed weak features due to linearly adsorbed and multiply-bonded CO_{ads}, but the only product observed using all three electrodes was acetate. They concluded that adsorbed CO was responsible for poisoning the Pt(111) electrode (the other electrodes deactivated primarily due to structural modifications). The conclusions of Lopéz-Atalaya and co-workers [3] are in direct contrast to the theory of Lai and Koper [38] based on the latter's studies of ethanol oxidation at single crystal Pt electrodes in 0.1 M NaOH. Lai and Koper postulate that adsorbed CO is the only strongly adsorbed intermediate at co-ordinately unsaturated surfaces such as Pt(110), whilst CH_x is responsible for poisoning surfaces with long terraces, such as Pt(111).

Overall, the evidence in favour of adsorbed CO as a key intermediate in the oxidation of ethanol in aqueous alkaline electrolyte, and the postulate that chemisorption of ethanol at Pt under such conditions takes places via cleavage of C-H bonds, are not convincing.

3.1.5. Summary

Based on the previous work in Newcastle on methanol oxidation [1][2] and on the considerations above, it is likely that the oxidation of ethanol in alkaline solution proceeds through initial adsorption of ethanol itself through oxygen and not through C_1. It is postulated that this adsorption is extensive, even at quite low potentials, and the initial process is:

$$EtOH + OH^- + Pt(s) \rightarrow Pt_s\text{-}O\text{-}CH_2CH_3 \ (I) \qquad (3.4)$$

Subsequent oxidation gives rise to removal of successively one and then two hydrogens attached to C_1 yielding:

$$Pt_s\text{-}O\text{-}CH_2CH_3 \ (I) \rightarrow Pt_s\text{-}O\text{-}CH(OH)CH_3 \ (II) \rightarrow Pt_s\text{-}O\text{-}C(=O)CH_3 \ (III) \qquad (3.5)$$

and acetaldehyde can be desorbed from the surface after the first two-electron oxidation and acetate after the second, both desorptions being driven by the excess ethanol in solution which adsorbs and replaces the oxidised intermediates.

Further, it may be postulated that once acetate has formed, if it is not desorbed then provided the entire surface is not covered with strongly adsorbed ethanol it may form a bidentate adsorbate. In principle there are two possible forms of ligation: the first is to coordinate through the carbonyl oxygen to give $Pt_s\text{-}O\text{-}C(CH_3)\text{-}O\text{-}Pt_s$ (IV) and the second is for proton abstraction to occur from the CH_3 moiety followed by ligation through the carbon as $Pt_s\text{-}O\text{-}C(=O)\text{-}CH_2\text{-}Pt_s$ (V); as will be seen below, there is some IR evidence for the second of these species (V), but the first (IV) presents problems for the *in situ* IR technique since the main carbonyl type absorptions will not be seen owing to the surface selection rule. The fate of these two adsorbates will be different: the first (IV) will prove difficult to oxidise further; proton abstraction might lead, in the case of substantial coverage, to polymer formation, but no evidence for this was observed. However the second bidentate intermediate (V) can be further oxidised by C-C scission, which is known to be a minority process on Pt under ordinary operating conditions [43], but which leads to the formation of both carbonate and Pt-C≡O, both of which have been observed by previous workers in Newcastle and others. Hence, C-C bond scission most probably involves the presence of this

second intermediate (V), and IR has been used to try to establish a signature band for it.

3.2. Results

3.2.1. Cyclic voltammetry of ethanol at polycrystalline Pt in 0.1 M KOH

Figure 3.7 shows the cyclic voltammogram of the Pt (foil, 1 cm x 1 cm) electrode recorded in 0.1M KOH in the absence of ethanol at 25 ^{o}C. As there are no redox-active couples present in solution, the current-potential behavior observed in fig. 3.7 corresponds to the formation and removal of chemisorbed hydride and oxide layers at the Pt surface [44]. Thus, the hydrogen underpotential deposition/stripping (H_{upd}) region below ca. -0.45V vs. MMO may be seen [44-47], this due to the formation and stripping of reversibly adsorbed H at the Pt electrode.

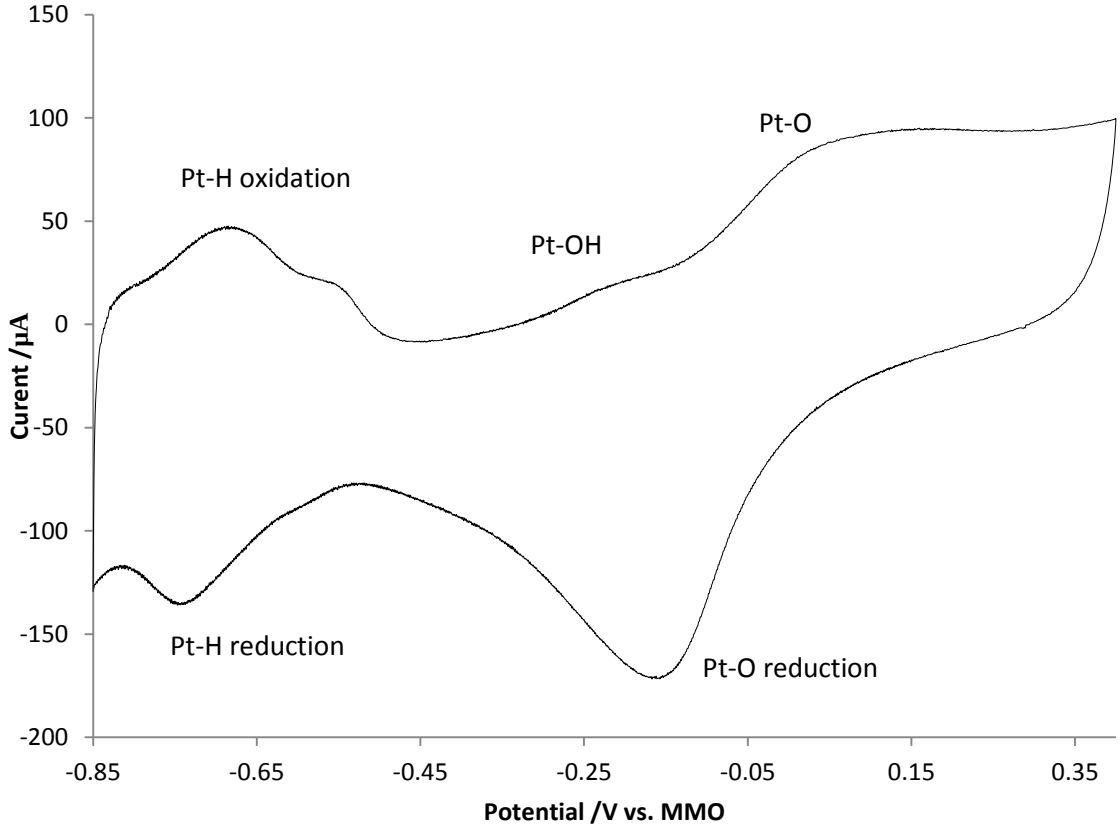

Figure 3.7. CV of the polycrystalline Pt (foil, 1 cm^2) working electrode recorded in 0.1M KOH, in the absence of ethanol, at 22^{o}C (-0.85 to 0.4V; scan rate of 100mVs^{-1}).

Furthermore, compared to Pt in acidic electrolyte, there is an additional wave which immediately follows hydrogen desorption in the anodic scan at -0.5V vs. MMO, with maximum at ca. -0.20V; this may be assigned to the reversible chemisorption of OH at Pt via the hydroxide discharge process [1][44][46]:

$$Pt + OH^- \rightarrow Pt\text{-}OH + e^- \quad (3.6)$$

The wave with an onset under the OH_{ads} peak and a peak near 0.1 V can be assigned to the irreversible formation of an oxide layer (Pt-O) during the anodic scan [1][44]:

$$Pt\text{-}OH + OH^- \rightarrow Pt\text{-}O + H_2O + e^- \quad (3.7)$$

Above 0.4 V, oxygen evolution takes place, and at even higher potentials, a phase oxide of thickness significantly larger than a monolayer may form at the Pt surface [44]. As the potential sweep is reversed in direction, the chemisorbed oxide layer at the electrode surface is reduced/stripped, as shown by the wave near -0.1 V, together with any oxygen gas in proximity to the electrode. [4][44][48]. At ca. -0.5 V during the cathodic scan, there is a small double layer region followed by the deposition of hydride [44] as:

$$Pt + H_2O + e^- \rightarrow P\text{-}H + OH^- \quad (3.8)$$

At potentials below -0.85 (i.e. close to the thermodynamic potential for the H_2/H_2O couple), hydrogen evolution occurs and can be re-oxidised as the potential direction is again reversed [44].

Figure 3.8 shows cyclic voltammograms of the Pt electrode collected in 0.1 M KOH in the presence of 1M ethanol, demonstrating the typical behavior for oxidation of small organic molecules at a Pt electrode [49]. As can be seen from the figure, the hydrogen adsorption region is blocked by chemisorbed fragments of ethanol [34][37][38]. The onset of ethanol oxidation was observed at ca. -0.60 V and commences with OH_{ads} formation [37]. This oxidation ceases once appreciable coverage of the Pt by oxide has taken place [35][38].

On the cathodic scan, oxidation of ethanol only commences once the oxide starts to strip from the surface. Due to phase oxide formation on the anodic scan [45], stripping the oxide leaves a highly active surface hence the large anodic

currents [45][48][50]. In contrast to the CV's reported by Lai *et al* [38] (see section 3.1.3) and Dimos and Blanchard [39], there is considrable hysteresis between the forward and reverse scans at potentials below the anodic peak in the reverse scan, ie. -0.13 V vs MMO, suggesting coverage by strongly adsorbed species [4][24][37]. As discussed earlier (see section 3.1.3), the greater the hysteresis, the greater the influence of adsorbed species (such as CO_{ads}). The CVs collected by both Lai *et al* and Dimos and Blanchard were carried out at 10 mV s^{-1} scan rate. However, Chen and Schell [51] collected their CV's at 100 mV s^{-1} (as in this study) and observed similar hysteresis to that shown in fig 3.8.

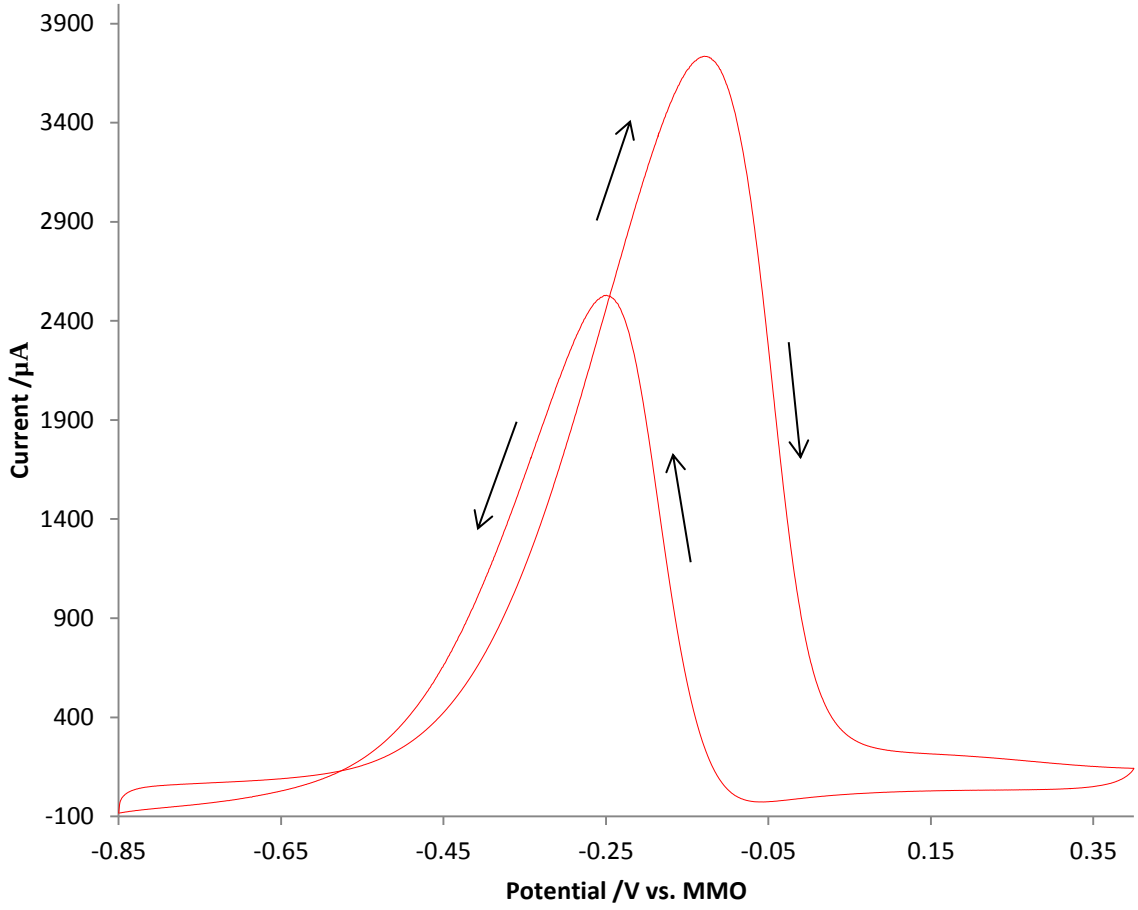

Figure 3.8. (a) CVs of the Pt (foil)working electrode recorded in 0.1M KOH, in the presence of 1 M ethanol at 25 ^{o}C (-0.85 to 0.4V; scan rate of 100mVs^{-1}). Scan direction indicated by arrows.

3.2.2. In-situ FTIR studies at 25 °C up to -0.1V

Figure 3.9 shows the current/time profile observed during the in-situ FTIR experiment depicted in figs. 3.10(a) and (b). The current transients observed declined sharply at potentials where appreciable coverage by platinum oxide occurs, i.e. at potentials greater than -0.1V. Features due to the oxidation of ethanol were only observed at potentials > -0.7V vs MMO, i.e. from the onset of the formation of adsorbed OH, in agreement with the cyclic voltammetry data on polycrystalline Pt in aqueous base, see [1][2] and references therein (and fig. 3.8). However, as may be seen from fig. 3.9, anodic current flows at -0.8V and -0.7V, as well as at higher potentials.

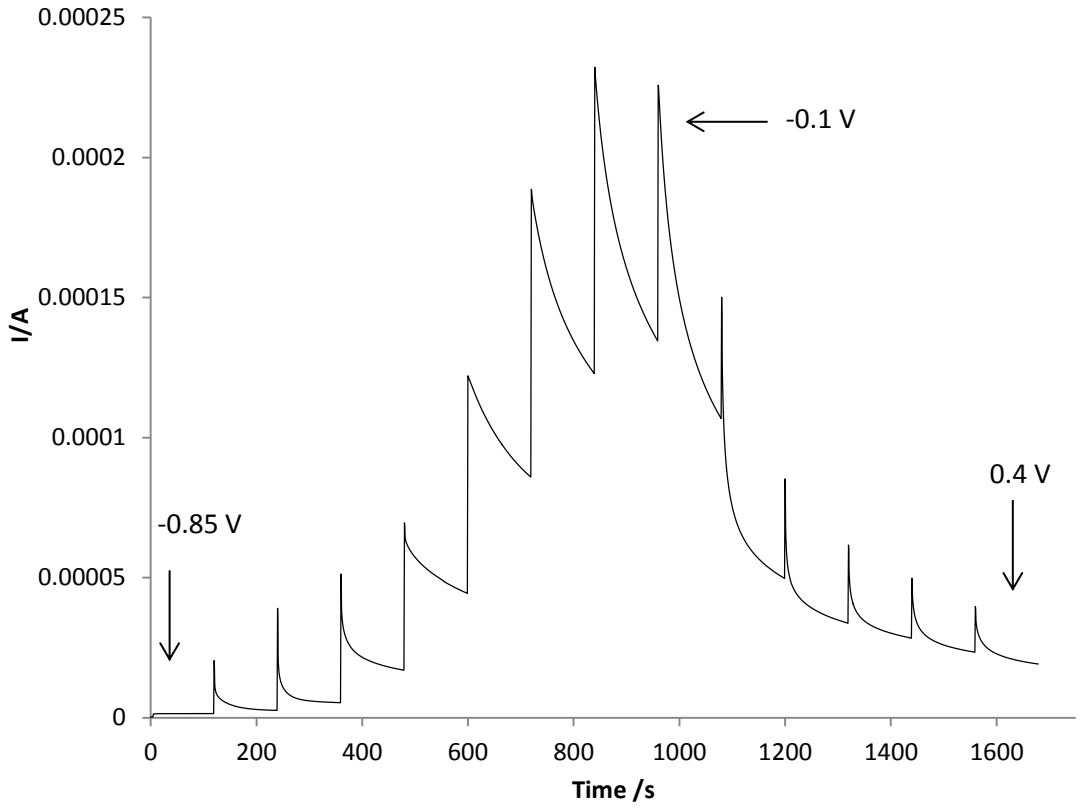

Figure 3.9. The current observed during the FTIR experiment in N_2 saturated 0.1 M KOH + 1.0 M EtOH. The potential was stepped from -0.85V to +0.4V vs MMO.

Figure 3.10(a) shows spectra collected at 25 °C from -0.6V to -0.1V vs MMO normalised to the spectrum collected at -0.85V, and fig. 3.10(b) spectra collected at -0.7V to -0.5V in the same experiment.

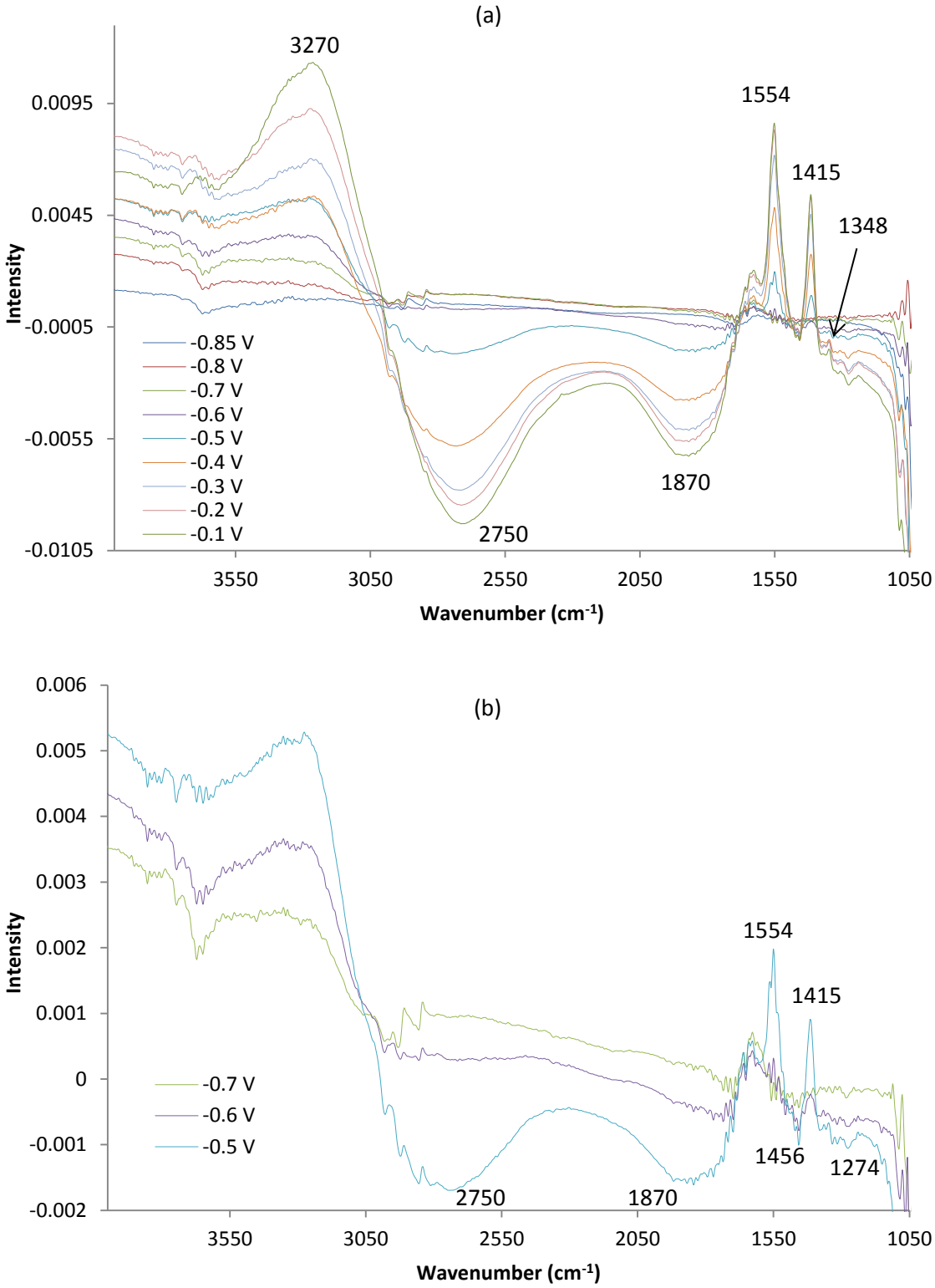

Figure 3.10. Spectra (8 cm^{-1} resolution, 100 scans, 47 s per scan set) collected from (a) -0.85 to -0.1 V and (b) -0.7 to -0.5 V vs. MMO as the potential of the polycrystalline Pt electrode was stepped up from -0.85V vs MMO in N_2 saturated 0.1M KOH + 1M EtOH.

As may be seen from fig. 3.10(a), the spectra are dominated by the solution OH^- loss feature [1][2][51] with peaks near 2750 cm^{-1} and 1870 cm^{-1}, and gain features due to water (O-H stretch 3270 cm^{-1} and HOH deformation near 1635 cm^{-1}). The assignment of the solution OH^- features was confirmed by performing a separate experiment in which 0.1 M KOH was diffused into the thin later containing deionized water only, over a period of 10 minutes, the spectra from which are presented in fig. 3.11. As may be seen from the figure, two broad gain features near 2700 and 1890 cm^{-1} were observed and increased as a function of time as KOH entered the thin layer.

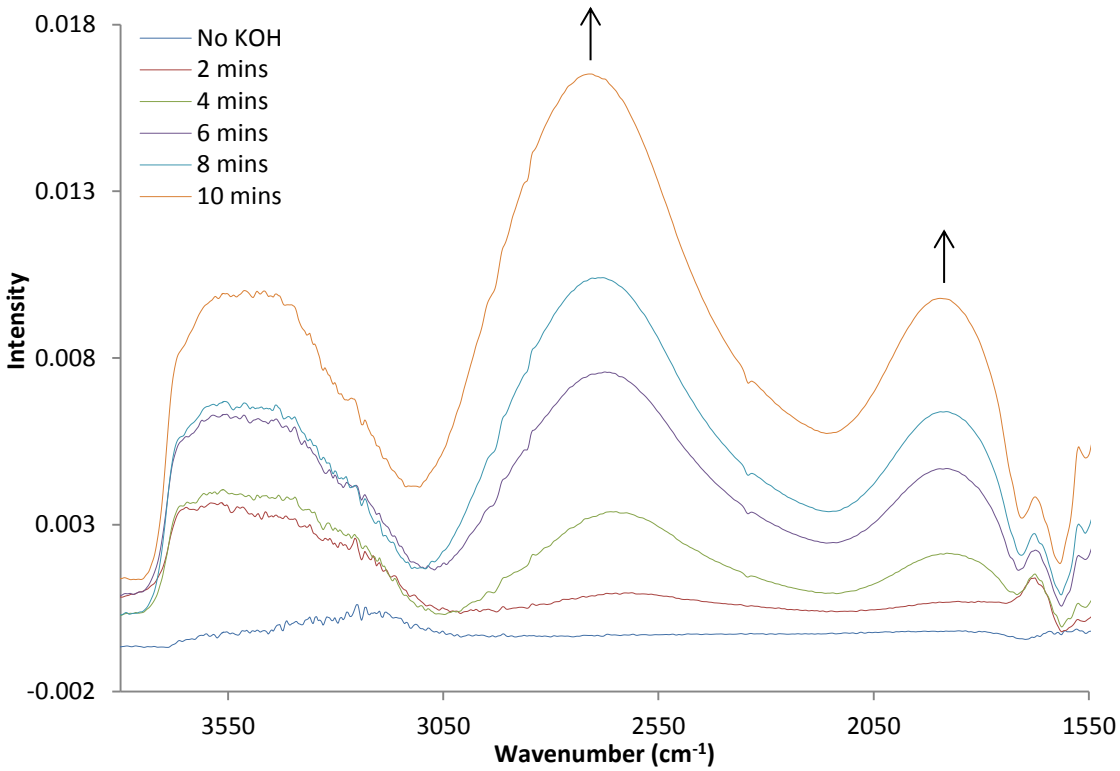

Figure 3.11. Spectra (8 cm^{-1} resolution, 100 scans, 47 s per scan set) collected during a separate experiment in which 0.1 M KOH was diffused into the thin layer containing deionized water only.

Figure 3.12 shows the IR spectra of (a) aqueous NaOH and (b) bulk water collected by Stangret and Smeichowski [53] during their study of the hydration of hydroxide anions in aqueous solution by FTIR ATR spectroscopy.

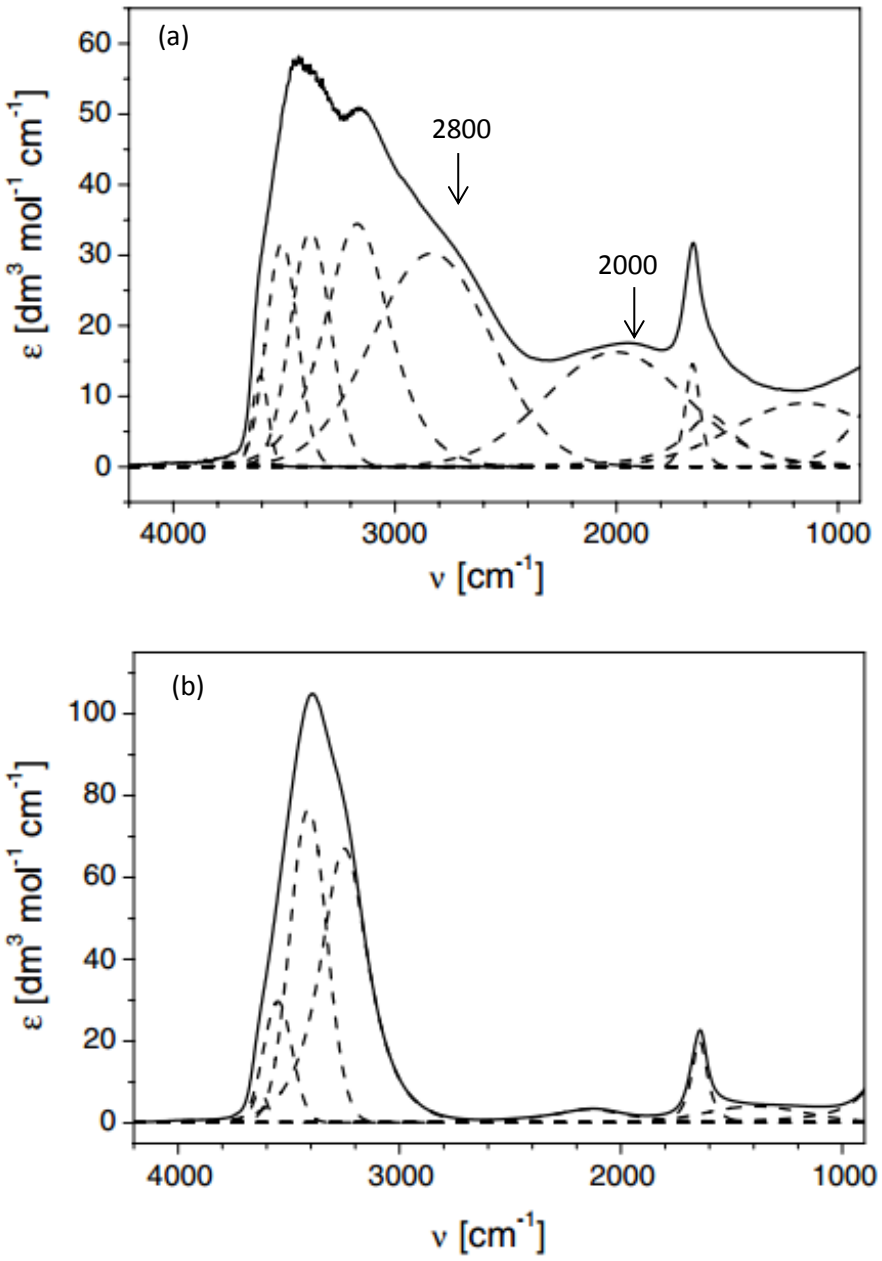

Figure 3.12. Deconvoluted affected H_2O spectrum presented by Stangret and Smeichowski [56] for (a) NaOH and (b) bulk H_2O.

As may be seen from fig. 3.12, the deconvoluted, "affected H_2O" spectrum for NaOH clearly shows a significant contribution from two broad features near 2800 and 2000 cm^{-1}, similar to those observed in fig. 3.11 at ca. 2700 and 1890 cm^{-1}. Thus, the loss features at ca. 2750 cm^{-1} and 1870 cm^{-1} in

fig. 3.10(a) were unambiguously attributed to the loss of solution OH^- from the thin layer.

Returning to fig. 3.10, there is also the gain of features at -0.6V near 1554 cm^{-1}, 1415 cm^{-1} and 1348 cm^{-1} (weak) which may be attributed unambiguously to acetate ions in solution (see for example [3][16][17][21][54]). The weak 1274 cm^{-1} loss feature which may be seen in figs. 3.10(a) and (b) growing in at potentials > -0.6V to -0.1V was observed in all the experiments at 25 ºC in this potential region.

The intensities of the 3270 cm^{-1} (O-H stretch of water), 1870 cm^{-1} (solution OH^-), 1554 & 1415 cm^{-1} (solution acetate) and 1274 cm^{-1} bands, normalised to their maximum values, are plotted as a function of potential in fig. 3.13.

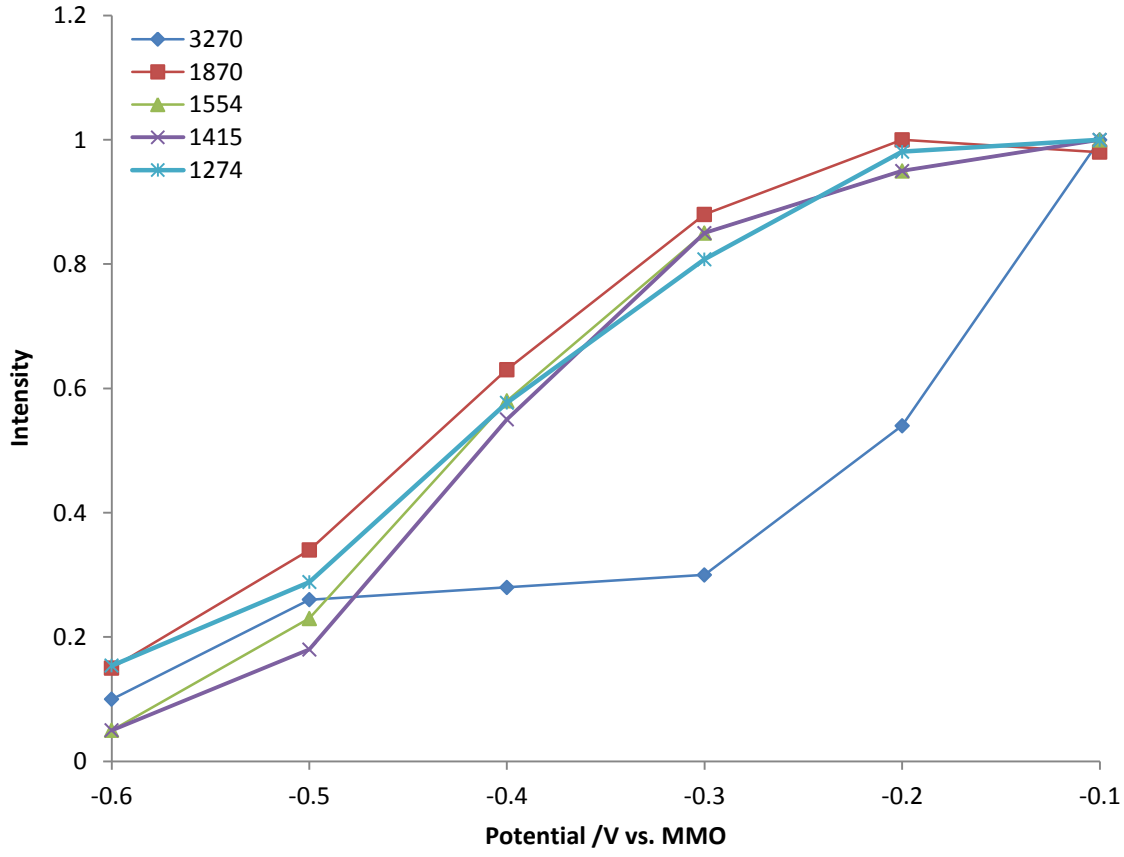

Figure 3.13. Plots of the band intensities of the features in fig. 3.10(a) normalised to their maximum values (at -0.1V): (i) 3270, (ii) 1870, (iii) 1554, (iv) 1415 cm^{-1} and (v) 1274 cm^{-1}.

From figs. 3.10(a) and (b) it can be seen that the 1554, 1415 & 1348 cm^{-1} and 1274 cm^{-1} bands increase steadily in intensity up to -0.1V; from fig. 3.13 it is clear that the ν_{as} (1554 cm^{-1}) and ν_s (1415 cm^{-1}) bands of the AcO^- track each other, as expected, and also track the 1870 cm^{-1} & 1274 cm^{-1} features, suggesting that the loss of solution OH^- may reflect the formation of adsorbed OH followed by the latter's subsequent reaction with adsorbed ethanol fragments to give the acetate product. The 3270 cm^{-1} band shows a markedly different potential dependence. The possible species responsible for the 1274 cm^{-1} absorption are limited, by the chemical simplicity of the system, to C, H and O –containing fragments of ethanol. It does appear that the species is an intermediate in the formation of acetate. Figures 3.14(a) & (b) show an analogous experiment to that depicted in figs. 3.10(a) & (b) using 1.0 M C_2D_5OD.

As may be seen from the figure, whilst the bands due to solution acetate are observed, at 1539 cm^{-1} and 1409 cm^{-1} (shifted to lower frequencies by the deuteration [55]), the 1274 cm^{-1} feature is absent, suggesting the presence of C-D bonds, and hence its absorption has shifted below the cut-off of the CaF_2 window.

Figure 3.15 compares the transmittance spectra of pure C_2D_5OD and C_2H_5OH, from which it may be seen that the 2238, 2104, 1175, 1112 and 1064 cm^{-1} bands are due to the loss of solution C_2D_5OD. Bands between 1220 cm^{-1} and 1257 cm^{-1} observed during studies on the oxidation of methanol and ethanol in acidic solution have been attributed [26][56] to species of the form $M_xCH_{3-x}OH$ (M = Ir or Pt, x = 1 or 2). On the basis of the postulated mechanism in equations (1) to (10), the 1274 cm^{-1} band may be tentatively assigned to $CH_3(OH)CHOPt$ (II) as a key intermediate in the direct path to acetate.

Interestingly, the amount of solution acetate present at -0.2V was 17% higher using C_2D_5OD than C_2H_5OH, suggesting the kinetic isotope effect, and supporting the postulate raised in previous studies in Newcastle [1][2] that a number of mechanistic pathways are available during the electro-oxidation of small organic molecules under alkaline conditions at polycrystalline Pt which differ very little in activation energy.

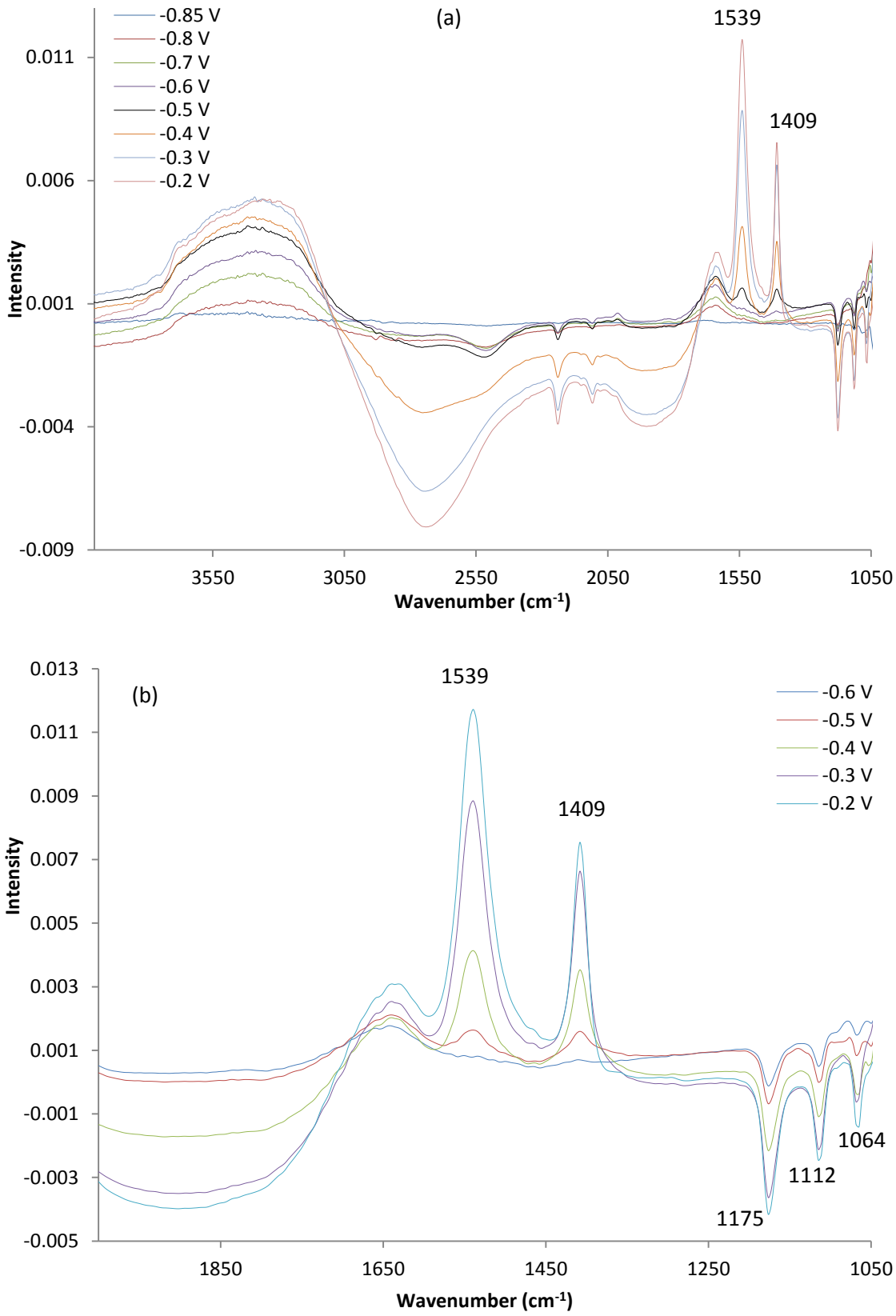

Figure 3.14. Repeat of the experiment depicted in fig. 3.10(a) using 1M C_2D_5OD from -0.85 to -0.2 over the spectral range from (a) 4000-1050 cm^{-1} and (b) 2000-1050 cm^{-1}.

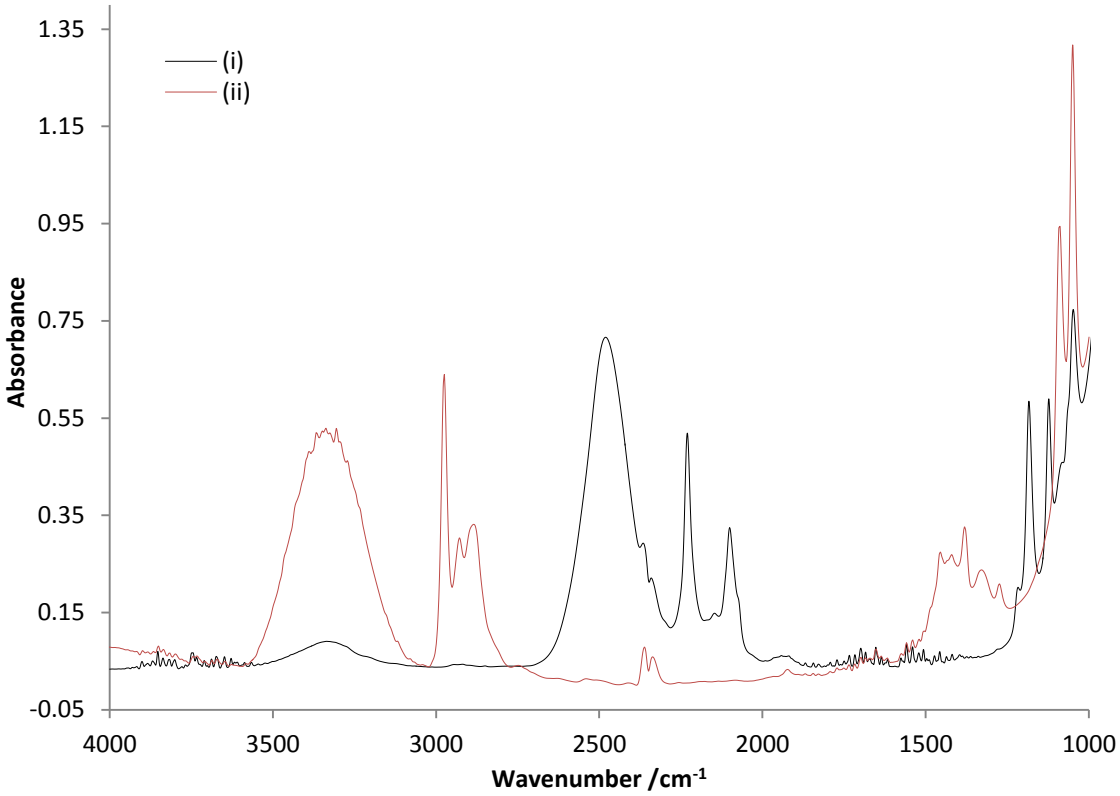

Figure 3.15. Transmission spectra of pure (i) C_2D_5OD and (ii) C_2H_5OH. The alcohols were pressed between two 25 mm diameter CaF_2 plates held in a Specac Presslok holder (see section. 2.5.1).

The water band near 3270 cm^{-1} in fig. 3.10(a) dominates the spectra and hence warrants some explanation. Firstly, it is important to try and assess whether this is an artifact as it appears in the region between 2750 cm^{-1} and 3750 cm^{-1}; i.e. the spectral range in which the ν_1 and ν_3 O-H (symmetric and asymmetric respectively) stretches absorb strongly [57]. However, from fig. 3.16 it is clear that there is significant source energy in the O-H stretching region. Bertie and Whalley [58] attribute a strong absorption near 3200 cm^{-1} to "ice like" water; i.e. water tetrahedrally co-ordinated by hydrogen bonds [59][60]. In the paper by Bertie and Whalley, the H-O-H deformation (δ) band is very broad and weak, and barely discernible in the spectrum. The 3270 cm^{-1} band in fig. 3.10(a) is accompanied by a weak δ H-O-H absorption near 1635 cm^{-1}, much weaker than that of bulk water (see fig. 3.12). Hence, it appears that highly hydrogen-bonded, ice-like water is being

gained as the oxidation of ethanol to acetate proceeds, or perhaps as $CH_3CH(OH)OPt$ (II) is being removed from the surface.

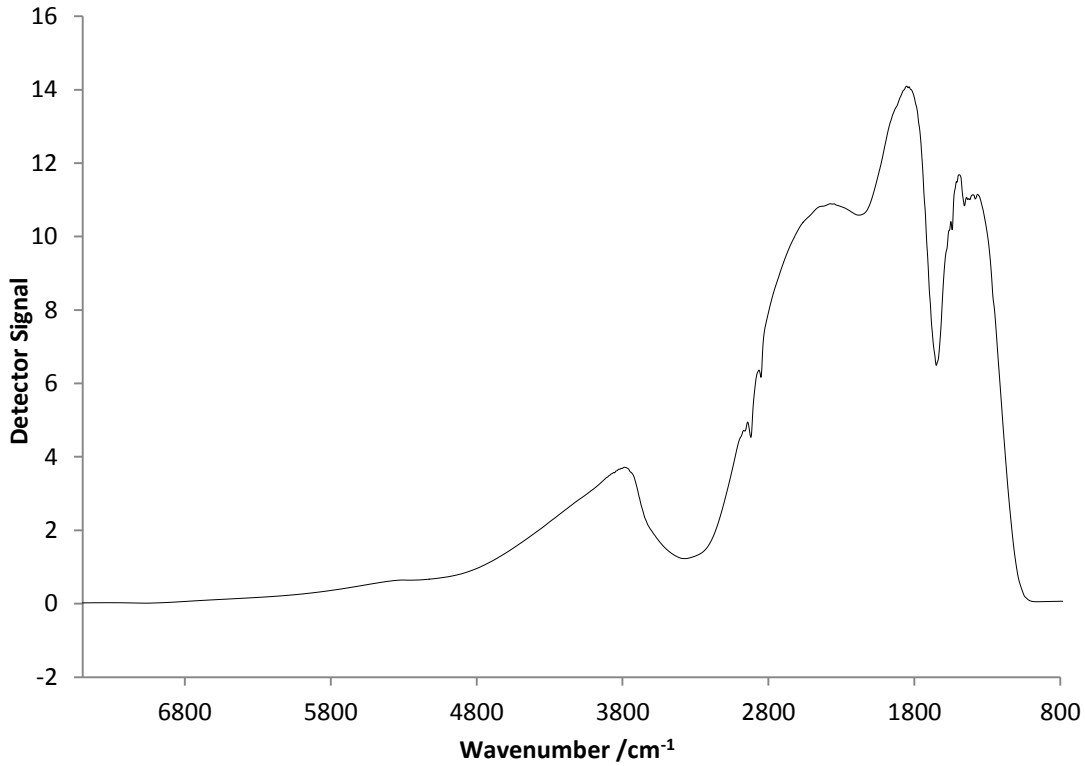

Figure 3.16. The single beam (reference) spectrum (8 cm^{-1} resolution, 100 co-added and averaged scans) taken at -0.85V during the experiment conducted at 25 °C.

There are no other gain features apparent in figs. 3.10(a) and (b), suggesting that the Pt electrode is selective for AcO^- production from ethanol. Apart from very weak absorptions due to multiply-bonded, adsorbed CO, López-Atalaya et al [3] also observed only solution acetate in the FTIR spectra obtained during the electro-oxidation of ethanol at Pt(100), Pt(111), and Pt(110) in 0.1 M NaOH; they claim also to observe a feature near 1350 cm^{-1} they 'tentatively attributed' to HCO_3^-, but this was not evident in the spectra presented in the paper, and the potential at which the species is observed was not specified.

Fang et al [17] and Zhou and co-workers [16] infer the production of HCO_3^- and CO_3^{2-}, respectively, from the asymmetry of the 1415 cm^{-1} acetate band, Fang refers to this band being present in the spectra in figs. 2(e) and (f) in the paper; unfortunately, these figures are omitted from the paper. Zhou *et al* postulate that

CO_3^{2-} is produced at higher potentials, i.e. ≥ +0.2 V vs SCE (approximately +0.14 V vs MMO).

In order to determine whether carbonate and/or bicarbonate was formed during the experiment depicted in figs. 3.10(a) and (b), fig. 3.17 compares the spectrum obtained at -0.1 V in fig. 3.10(a) to the spectrum obtained by diffusing 0.1 M KOH+0.1 M sodium acetate into the spectro-electrochemical cell containing 0.1 M KOH [1][2]. As may be seen from the figure, the frequencies of the various AcO^- bands are the same as are the full widths at half peak height (ca. 32 cm^{-1}) suggesting that very little, if any, carbonate is produced in this potential region, and there is no evidence for CO_L.

From fig. 3.17 it may be seen that the 'valley' between the ν_{as} and ν_s acetate bands is deeper and structured in fig. 3.10(a) compared to the spectrum of the solution acetate, suggesting the presence of loss features in the former. In addition, there appears to be shoulders on the low frequency side of the 1554 cm^{-1} band in fig. 3.10(a) and features in the C-H stretching region. Close inspection of fig. 3.10(b), showing the spectra at low potentials, suggests that the distortion of the acetate gain features is due to loss features that appear at potentials as low as -0.7V, and these are accompanied by loss features in the C-H stretching region. This is explored further in section 3.2.3.

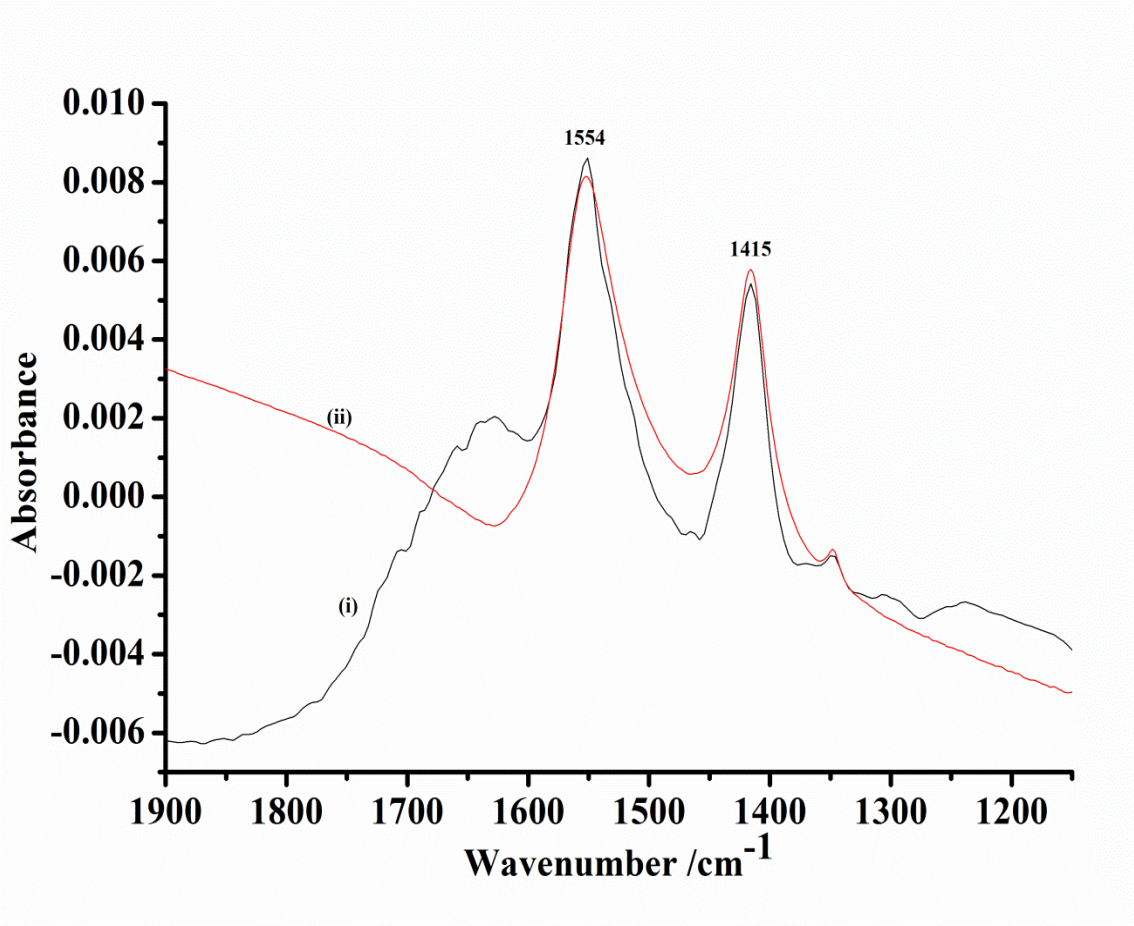

Figure 3.17. (i) The spectrum collected at -0.1V in fig. 3.10(a), compared to (ii) a spectrum of 0.1M sodium acetate in 0.1M KOH, see text for details. The acetate spectrum has been reduced and offset to facilitate comparison, and has had its baseline adjusted to match that of (i).

In order to investigate the effect of ethanol in solution, an experiment was carried out in which 1M ethanol+0.1M KOH was admitted into the IR cell containing 0.1M KOH at -0.65V vs MMO and the potential held for 30 minutes, after which the electrolyte was replaced by 0.1M KOH (still holding the potential at -0.65V), reducing the ethanol concentration in solution to $< 10^{-7}$ M. The electrode was then pushed against the prismatic cell window and the FTIR instrument flushed with nitrogen for 60 minutes; a reference spectrum was collected after which the potential of the Pt electrode was stepped up, further spectra taken and normalised to the reference spectrum according to the manipulation in equation (2.11).

Figure 3.18 shows the IVt data observed during the FTIR data collection; there appears to be two distinct regions of behaviour: ≤ -0.1V and > -0.1V vs MMO. From the IR spectra collected up to -0.1V, apart from the gain of ice-like water and the loss of solution OH^-, the only clear absorption was due to the gain of solution carbonate at 1395 cm^{-1} [1]; the intensity of this feature as a function of potential is shown in fig. 3.19(a).

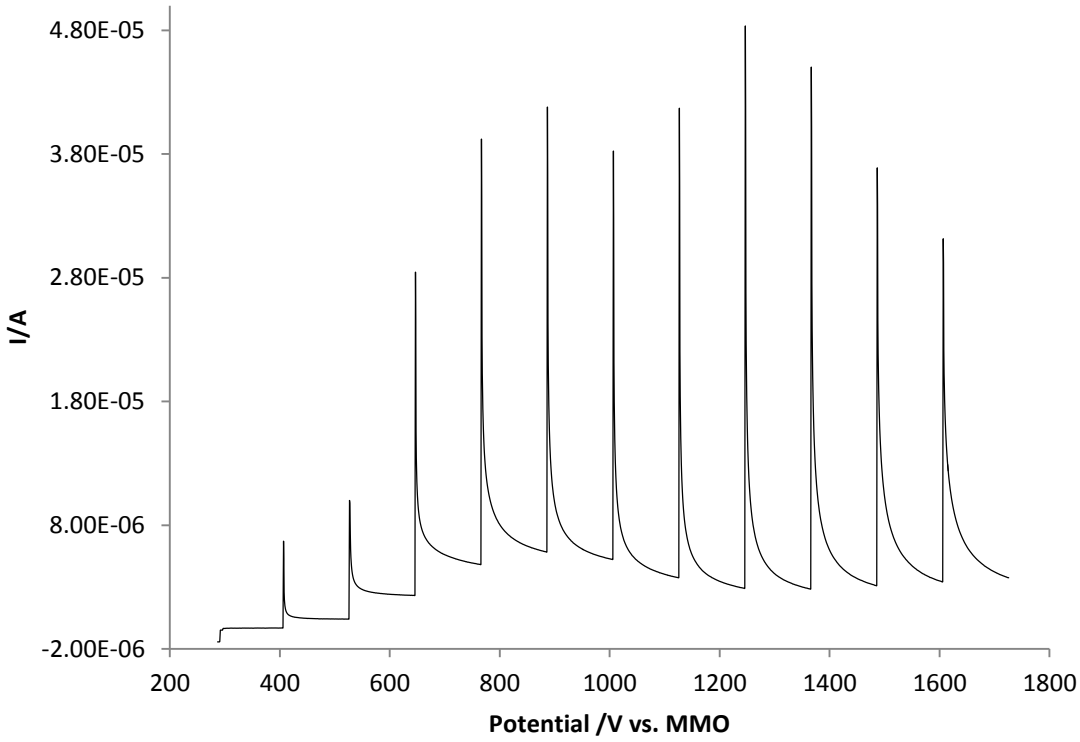

Figure 3.18. Current/time response during an experiment in which ethanol (1M ethanol in 0.1M KOH) was chemisorbed at -0.65V vs MMO and the solution replaced with 0.1M KOH, after which the potential was stepped up to +0.4V and spectra (8 cm^{-1} resolution, 100 scans, 47 s per scan set) collected at each step.

On the basis of fig. 3.19 it was decided to normalise the spectra collected at potentials > -0.1V to that taken at -0.1V and the result is shown in fig. 3.19(b). Apart from the H-O-H deformation of ice-like water (accompanied by the O-H stretch, not shown) and the CO_3^{2-} gain feature, loss features near 2985, 2913 and 2846 cm^{-1} may be observed. From fig. 3.19(b), the loss features near 2985, 2913 and

2846 cm^{-1} in fig. 3.19(b) do not appear to be due to solution ethanol. Iwasita and Pastor [26][27] attributed bands at 2960 cm^{-1}, 2920 cm^{-1} and 2850 cm^{-1} to the C-H absorptions of adsorbed ethoxy following ethanol chemisorption at Pt in aqueous $HClO_4$ & H_2SO_4, and we also attribute the bands in fig. 3.19(b) to adsorbed ethoxy.

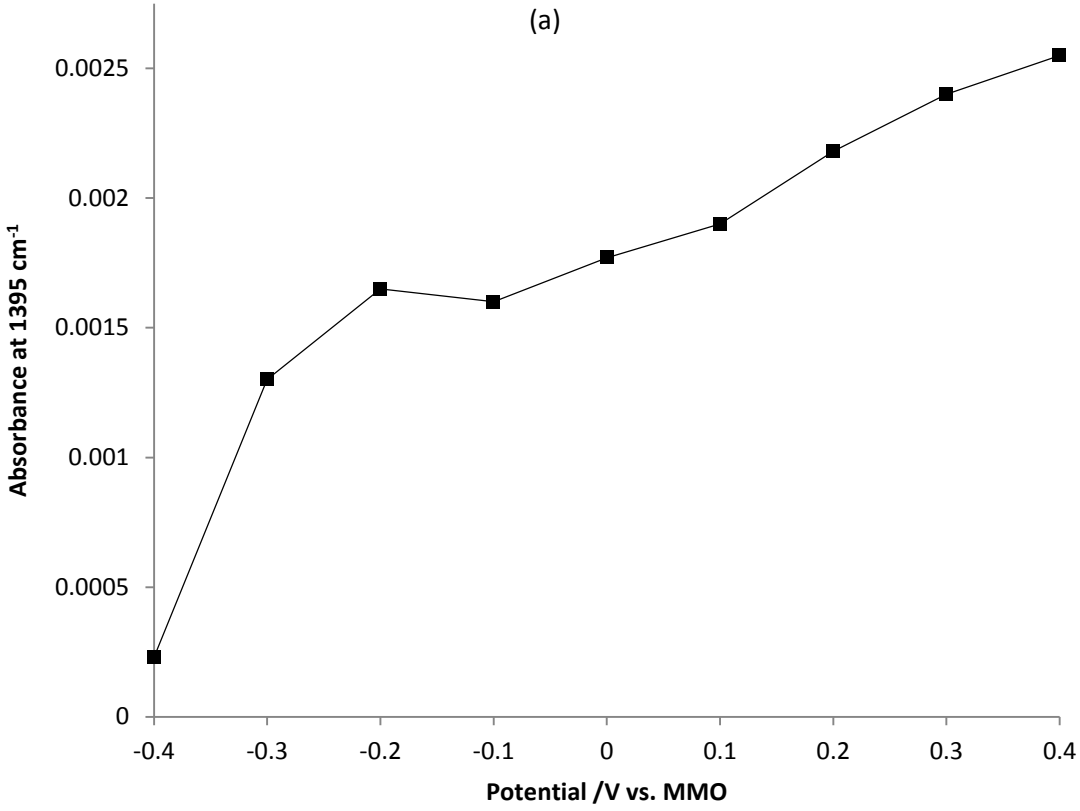

Figure 3.19. (a) Plot of the absorbance of the CO_3^{2-} band at 1395 cm^{-1} vs potential from the experiment in fig. 3.18.

The data in figs. 3.18, 3.19(a) and 3.19(b) is a most interesting result. From these data, it appears that ethanol (probably as ethoxy) strongly adsorbs on Pt; it is evident that in the absence of competing solution ethanol, the initial oxidation product(s) does/do not desorb to give solution acetate, but remains on the surface and is/are subject to further oxidation. It is also evident that the reason this does not happen under normal circumstances is that ethanol adsorbs more strongly than acetate and this is displaced from the surface more rapidly than it can be further oxidized; this postulate is supported by the work of Morin and co-workers [49] in their study of

ethanol oxidation at Pt single crystal electrodes as a function of pH. It is not, therefore, the case that the Pt surface is inactive for the complete oxidation of ethanol, but rather that the partial oxidation product is lost before complete oxidation can take place. The peak at 2168 cm^{-1} is, as yet, unassigned and is under further investigation.

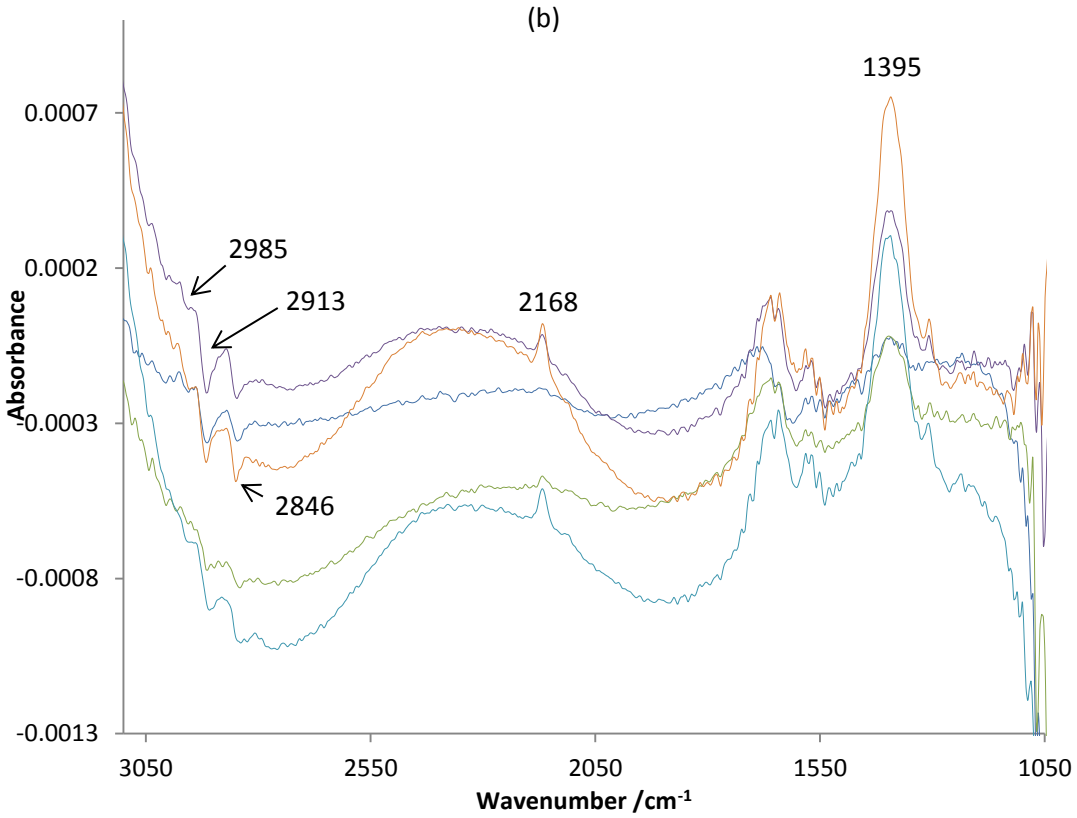

Figure 3.19.(b) The spectra collected at potentials > -0.1V normalised to that taken at -0.1V in the experiment depicted in fig. 3.18.

3.2.3. In-situ FTIR studies at 25 °C up to 0.4V

As shown in fig. 3.20, the loss of absorbing species postulated in the preceding section was confirmed by normalising the spectra collected at higher potentials to that taken at 0V.

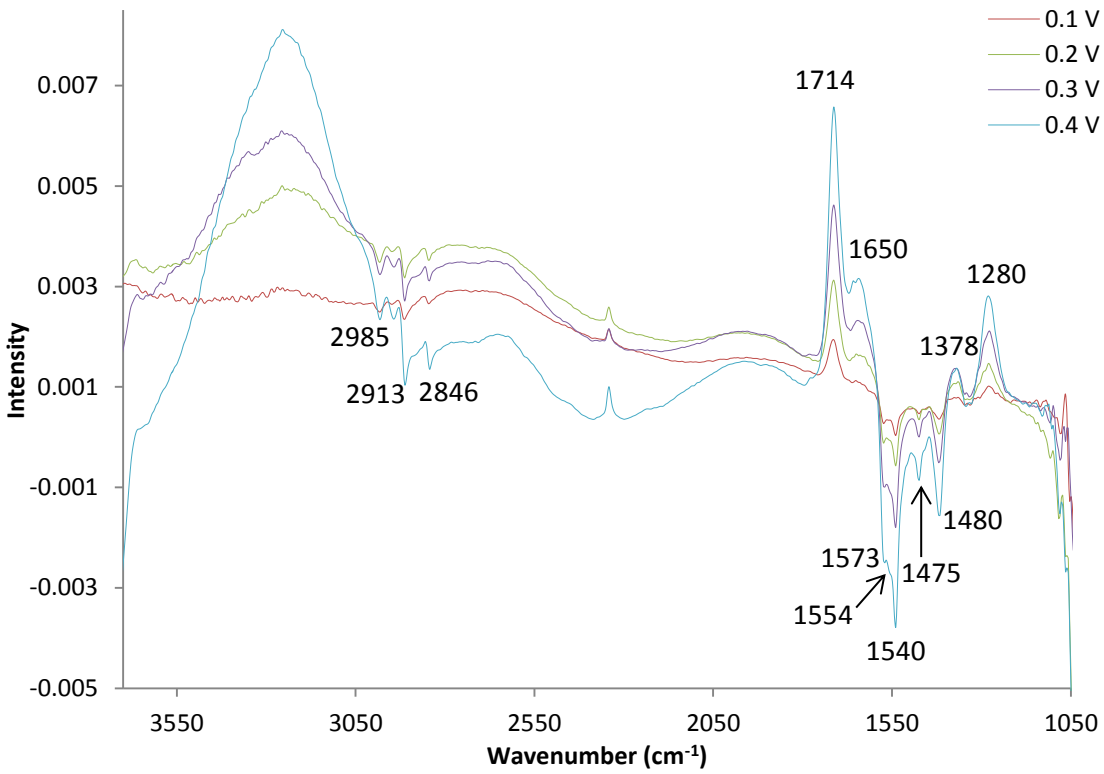

Figure 3.20. The spectra collected at 0.1V to 0.4V in the experiment depicted in fig. 3.10(a) normalised to that taken at 0V.

Figure 3.21 shows the spectra collected in fig. 3.20 enlarged over the spectral range from (a) 4000 – 2050 cm^{-1} and (b) 2050 – 1000 cm^{-1}. As may be seen from the figures, the water bands near 3310 cm^{-1} and 1635 cm^{-1} shift to ca. 3250 and 1650 cm^{-1}, respectively, and continue to increase; there are no gain features due to AcO^-, but a new band grows in at 2340 cm^{-1} due to CO_2 suggesting that the pH in the thin layer is $\leq$ 6.37 [1][2][61]. There is also the gain of a broad structure between 3000 and 1750 cm^{-1} which tracks new bands at 1715, 1378 and 1280 cm^{-1} suggesting these features are all due to a single species. Under acidic conditions, it would be expected that the oxidation of ethanol at Pt-based electrocatalyst would result in a mixture of acetaldehyde, acetic acid and CO_2 [16][39][51]. At this point, it is useful to refer back to the work presented by Feliu and co-workers [18] (see section 3.1.2), who attributed a band at ca. 1715 cm^{-1} to the presence of either acetaldehyde or acetic acid. As discussed earlier, the authors did not observe any features at ca. 1738 or 1280 cm^{-1}.

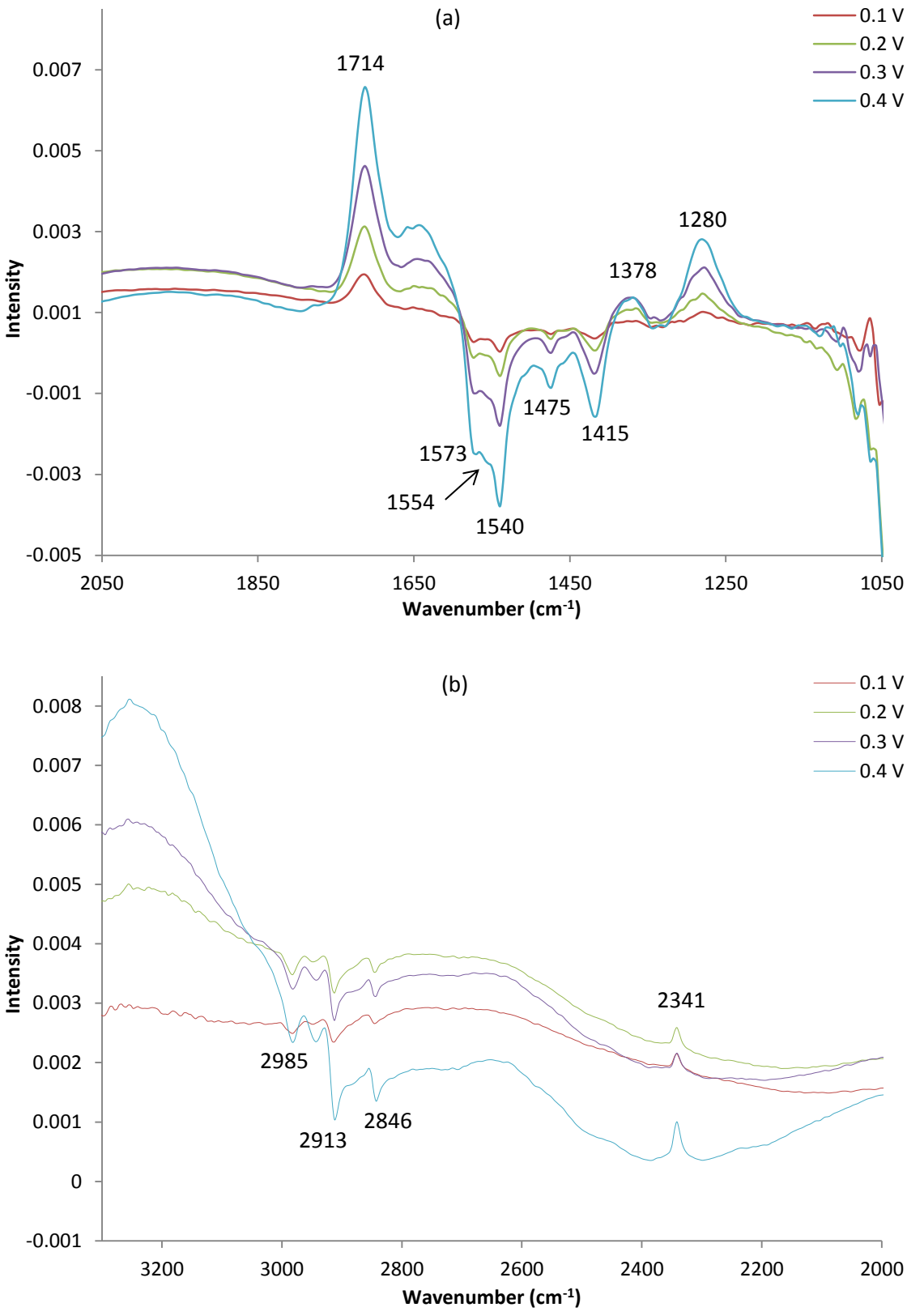

Figure 3.21. The spectra depicted in fig. 3.20 over the spectral range from (a) 2050 – 1050 cm^{-1} and (b) 3300 – 2000 cm^{-1}.

To obtain an in-situ FTIR spectrum of acetic acid, a diffusion experiment was carried out in which 0.1M acetic acid in water was diffused into the spectroelectrochemical cell containing water, and the entry of the acid into the thin layer monitored, and a typical spectrum so obtained is shown in fig. 3.22 and the principal features listed in table 3.2, along with their assignments. It is clear that the principal gain features in fig. 3.20 are due to acetic acid, and hence the pH in the thin layer is ≤ 4.75 (the pK_a of acetic acid[22]).

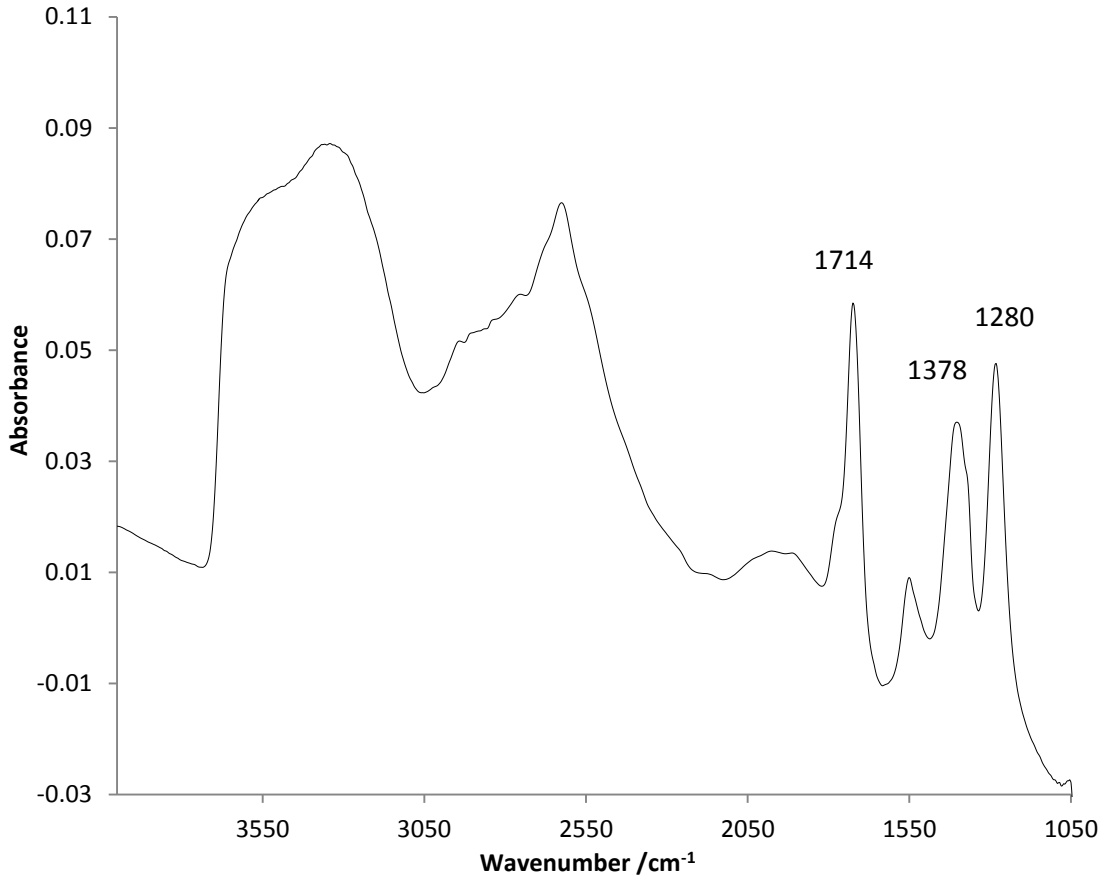

Figure 3.22. Spectrum (8 cm^{-1} resolution, 100 co-added and averaged scans) collected 10 minutes after diffusing an aqueous solution of 0.1 M CH_3COOH into the spectro-electrochemical cell initially containing water.

In addition to the gain features discussed above, a number of loss features are present in fig. 3.20 that increase in intensity as the potential is increased, and these are listed in table 3.3. In order to assign the various loss features in fig. 3.20, it proved helpful to assess spectra from across all the preliminary experiments carried

out during the optimization the system. Thus, fig. 3.23(a) shows the spectra collected at 0.1V and 0.4V in fig. 3.20 with the former enhanced and offset to allow direct comparison.

Band /cm^{-1}	**Assignment**	**Reference**
1283	O-H deformation in COOH group.	[19][20][21][62][63]
1369 - 1375	Acetaldehyde, possible contribution of formate or CO_3^{2-} in alkaline solution.	[17][20][64][65]
1390 - 1392	C-O stretching in COOH group.	[16][21]
1715	Acetic acid	[19][20][21][62][63][64]
2616 - 2625	O-H stretch broad band	[20][62][63]

Table 3.2. The assignment of the bands attributable to CH_3COOH in figs. 3.20 and 3.21.

Figures 3.23(b) and 3.24 show spectra taken at room temperature, the same potentials and normalised in the same manner as those in fig. 3.23(a) during preliminary experiments under varied thin layer thickness. Figure 3.25 shows spectra obtained at 0.1 to 0.4V during the experiment depicted in fig. 3.20 normalised to the spectrum collected at 0 V, at 50 ºC. Figure 3.25 clearly shows that the C-H stretches, 1573 and 1475 cm^{-1} bands are not due to the same species as responsible for the 1554, 1540 and 1415 cm^{-1} features as the

former absorptions are all absent (the effect of temperature will be detailed in chapter 5).

Band /cm^{-1}	**Assignment**
2985, 2913, 2846	C-H stretches of adsorbed ethoxy
1573	ν_s adsorbed unidentate acetate, Pt_s-O-C(=O)CH_3
1475	C-H deformation of adsorbed unidentate acetate, Pt_s-O-C(=O)CH_3
1554	ν_{as} solution acetate
1415/1418	ν_s solution acetate
1540	Uncoordinated C=O stretch of bidentate adsorbed carbonate or C=O stretch of $PtCH_2COOPt$

Table 3.3. The assignment of the loss features observed at higher potentials. See text for details.

Curvature of the baseline in the region of the C-H stretches gives the impression of bipolar bands, see fig. 3.24, but where pronounced curvature is absent, see fig. 3.23, there is no evidence of bipolarity. Figure 3.25 clearly shows that the 1554 cm^{-1} and 1418 cm^{-1} are due to the same species, actually solution acetate with the latter band distorted by underlying absorption(s). Figure 3.25 also suggests that the 1540 cm^{-1} band does not have any attendant features, at least at frequencies down to 1150 cm^{-1}.

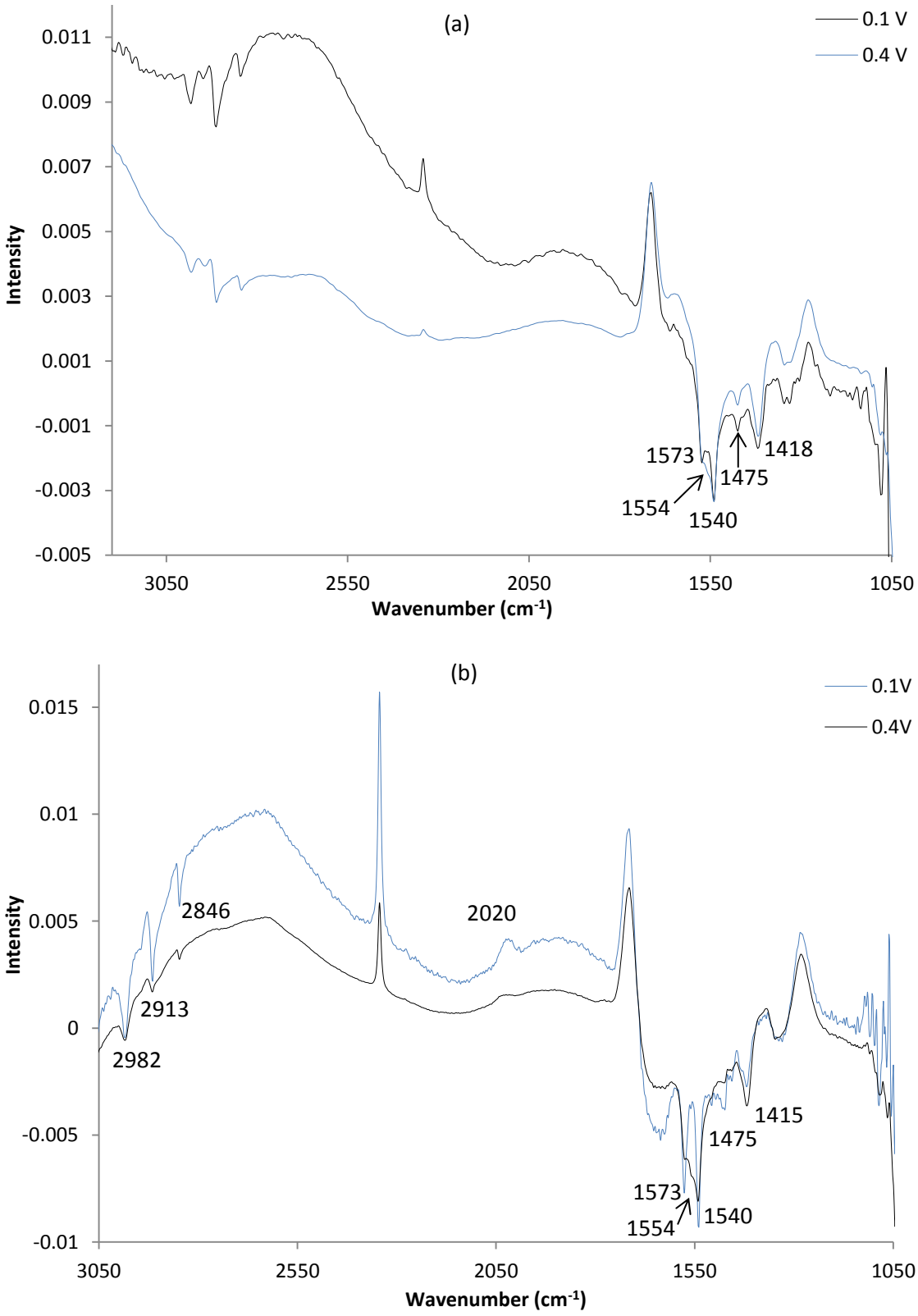

Figure 3.23. The spectra collected at 0.4V and 0.1V in (a) fig. 3.20 and (b) a repeat of the experiment in fig. 3.20. The spectrum at 0.1 V has been enhanced by a factor of 5 and 6, respectively, and offset for clarity.

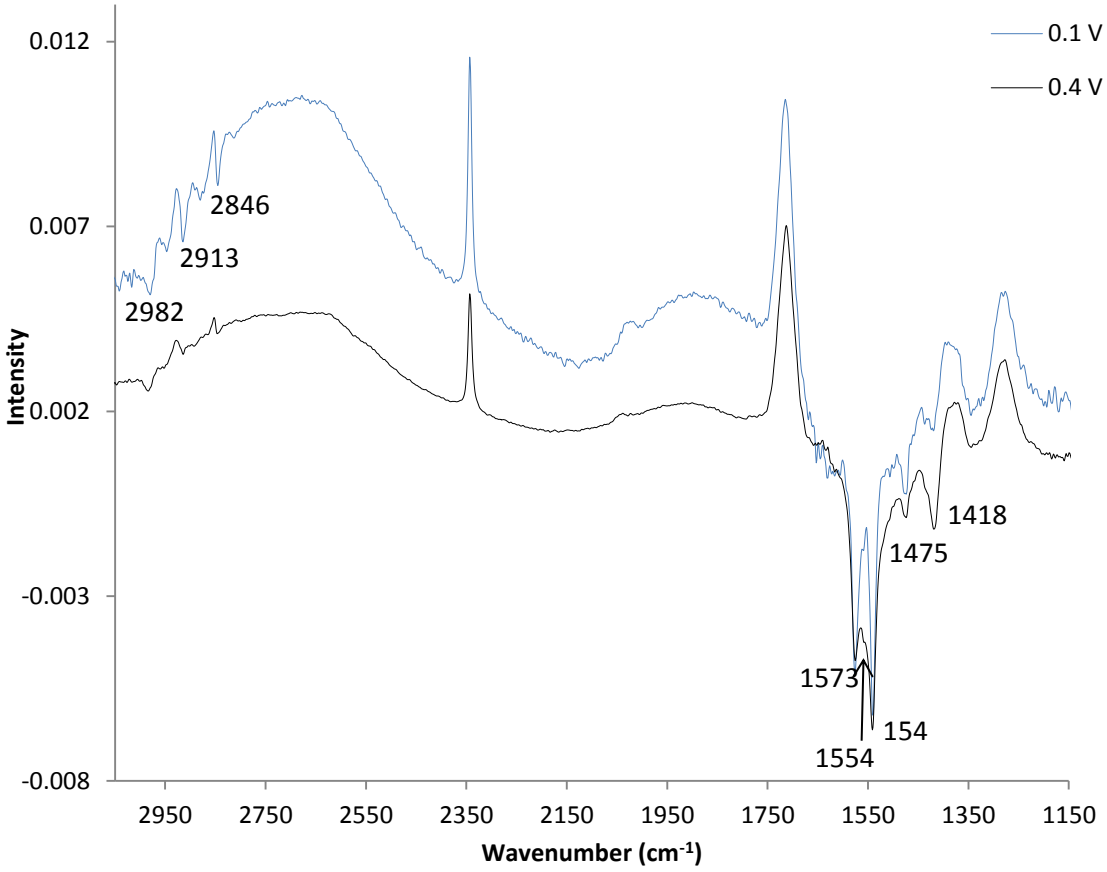

Figure 3.24. Spectra collected at 0.4V and 0.1V in a second repeat of the experiment in fig. 3.20, normalized to 0 V. The spectrum at 0.1 V has been enhanced by a factor of 3.3 and offset.

Taking the 1540 cm^{-1} band first, Iwasita and co-workers [66-68] observed a feature at 1530 – 1540 cm^{-1} during studies on the electrochemical reduction of CO_2 at Pt(111) in perchloric acid which they attributed to the uncoordinated C=O stretch of bidentate carbonate (ie adsorbed through both O atoms), and this does not seem unreasonable; however, an alternative, possible assignment is that it is due to the C=O stretch of Pt_s-O-C(=O)-CH_2-Pt_s (V).

The most likely explanation for the 1573 cm^{-1} feature is the asymmetric stretch of bidentate acetate [69][70]; but, as Shao and Adzic [9] state, such a vibration should not be IR active according to the Surface Selection Rule [71], in contrast to the assignment of Lai et al [4]. Thus, the 1573 cm^{-1} band is tentatively assigned to acetate adsorbed through one O atom (Pt_s-O-C(=O)CH_3) (V), and the 1475 cm^{-1} feature to the C-H deformation of the same species[69][70].

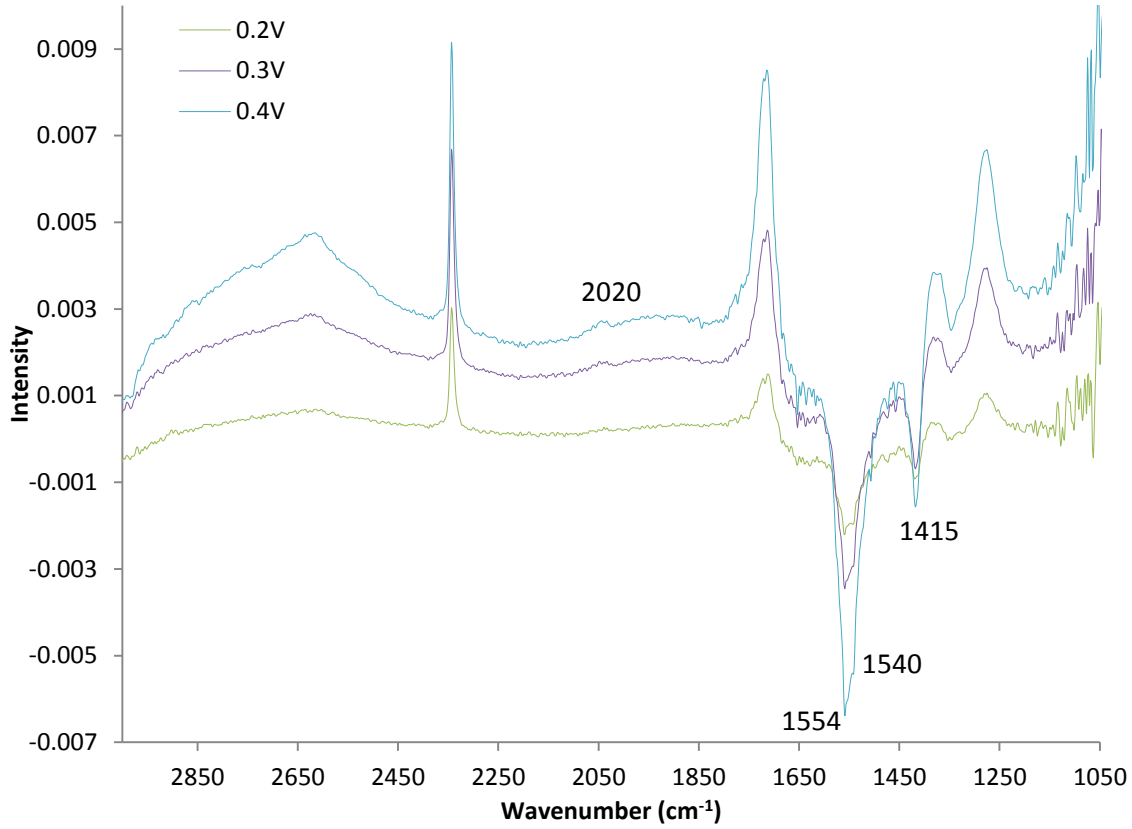

Figure 3.25. Spectra collected during a repeat of the experiment in fig. 3.20 except at 50 °C at 0.2V, 0.3V and 0.4V, normalised to the spectrum taken at 0.1V.

Linearly adsorbed CO (CO_L) was often observed at higher potentials in repeats of the experiment in figs. 3.10 & 3.17, see figs. 3.23(b), 3.24 and 3.25, but only in conjunction with the loss of the adsorbed C-O species and gain of CO_2. This supports the mechanism postulated in the introduction, and suggests that CO_L is only observed when the pH in the thin layer has become neutral or acidic. In a previous paper by Christensen *et al* [2], significant variations in pH across the electrode surface in in-situ FTIR cells was predicted and confirmed experimentally.

3.3. Conclusions

The arguments leading to Tables 3.2 and 3.3 are critical to the identification of a plausible mechanism and these arguments are summarised below. Before going into

detail, however, we would want to emphasise that at higher potentials, with the passage of considerable charge, there is a substantial change in pH in the electrolyte immediately above the electrode and trapped in the thin layer. Other workers in Newcastle have already signaled this in earlier work [2] and have shown that this swing in pH arises from the relatively slow diffusion of OH^- ions across the electrode surface. The timescale for this diffusion is tens of minutes for an electrode of the radius that we use. A second effect is the exhaustion of reactant in the thin electrolyte layer, which leads to further changes in the ambient conditions at the electrode surface; the impact of this second effect is the greater the thinner the electrolyte, since exhaustion proceeds more rapidly. As we have already seen above, this is also a serious problem since under normal circumstances ethanol preferentially drives the desorption of acetate, whereas under ethanol starvation conditions, further ligation of acetate occurs with C-C bond scission taking place.

Turning to the data presented in this study, it is clear that the IR spectra strongly support the acetaldehyde-acetate route, and also support the idea that even at -0.85V the surface is substantially covered with adsorbed ethanol, since we only see this as a loss feature at higher potentials (where ethanol starvation and inhibition of ethanol adsorption by Pt-OH species both operate). With regard to acetaldehyde and acetate, Table 3.2 shows that there is IR evidence for both, and there are loss features in Table 3.3 that can plausibly be assigned to absorbed ethoxy formed at low potentials. We are confident, therefore, that the initial low-potential chemistry involves primarily adsorption through O and successive two-electron oxidations to CH_3CHO and CH_3COO^-. An interesting observation is the possible presence of formate; assuming this arises from C-C bond scission of the Pt_s-CH_2-C(=O)-O-Pt_s intermediate, then this suggests that the bond scission may be initiated by OH^- attack on the $–CH_2$- group leading to C-adsorbed methanol and adsorbed formate, the latter of which will desorb in the presence of ethanol rather than undergo further oxidation to carbonate.

A critical experiment, described above, was the oxidation of adsorbed ethanol species in the absence of solution ethanol. This clearly leads to carbonate, and there is no evidence for adsorbed CO; the obvious conclusion being that under ethanol starvation conditions, acetate is *not* desorbed but forms some intermediate that undergoes C-C bond scission.

At higher potentials, the pH decreases very markedly and the spectra show strong loss features as carbonate is replaced by CO_2 and acetate by acetic acid. However, there is also a band at 1573 cm^{-1}; there is no obvious solution species to account to this band, and we now believe that it arises from a carbonyl species adsorbed on the surface. It is important to re-emphasise that this cannot be the symmetric bidentate O,O bonded acetate species, since the carbonyl absorptions here would be parallel to the surface and therefore not visible in the IR. We believe that this is the Pt_s-CH_2-C(=O)-O-Pt_s species; the assignment is a plausible one, and would certainly fit the other suggestions above. What is more difficult to determine is whether the formation of this species does occur only at lower pH values. However, this does not appear to be the case: formation of carbonate takes place from species derived from the partial oxidation of adsorbed ethoxy even at higher pH values.

Finally, the results in this chapter may be summarized as follows: there is good evidence that the Pt surface is extensively covered with adsorbed ethoxy even at low potentials, since only loss features and no gain features were seen. There is good evidence also that oxidation of this adsorbed species gives rise to solution acetate species which is the predominant product under conditions of ethanol excess in solution. It has been established that under conditions of ethanol starvation, the adsorbed acetate species can form a further intermediate that we have tentatively identified at Pt_s-CH_2-C(=O)-O-Pt_s on the basis of IR and chemical likelihood, and this is the dominant route under ethanol starvation conditions. This analysis demonstrates that Pt is intrinsically capable of fully oxidising ethanol to carbonate in alkaline solution but that under normal fuel-cell operating conditions this is unlikely to be the dominant route, a fact that has serious implications for the operation of ethanol-based fuel cells.

3.4. References

1. Christensen, P. A.; Linares-Moya, D. *Journal of Physical Chemistry C*. 2009, 114 (2), 1094-1101.
2. Christensen, P. A.; Hamnett, A.; Linares-Moya, D. *Physical Chemistry Chemical Physics,* 2011, 13 (24), 11739-11747.

3. López-Atalaya, M.; Morallón, E.; Cases, F.; Vázquez, J. L.; Pérez, J. M. *Journal of Power Sources*, 1994, 52 (1), 109-117.
4. Lai, S. C. S.; Kleijn, S. E. F.; Fatma T.Z. Öztürk, F. T. Z.; van Rees Vellinga, V. C.; Koning, J.; Rodriguez, P. and Koper, M. T. M. *Catalysis Today*., 2010, *154* (1-2), 92-104.
5. Buso-Rogero, C.; Herrero, E.; Feliu, J. M., *ChemPhysChem*, 2014, 15, 2019-2028
6. Russell, A. E.; Blackwood, D.; Anderson, M. R.; Pons, S., *Journal of Electroanalytical Chemistry,* 1991, 304 (1-2), 219-231.
7. Christensen, P. A.; Hamnett, A. In *Comprehensive Chemical Kinetics. New Techniques for the Study of Electrodes and their Reactions*. Vol. 29, 1st ed.; Compton, R. G., Hamnett, A., Eds.; Elsevier: Amsterdam, 1989, p. 1.
8. Colmatti, F.; Tremiliosi-Filho, G.; Gonzalez, E. R.; Berná, A.; Herrero E. and Feliu, J. M. *Faraday Discussions,* 2008, 140, 379-397.
9. Quile's, F. and Burneau, A. *Vibrational Spectroscopy,* 1998, 16 (2), 105-117.
10. Shao, M. H. and Adzic, R. R. *Electrochimica Acta.* 2005, 50 (12), 2415-2422.
11. Christensen, P. A., *Encyclopedia of electrochemistry, Vol. 3: instrumentation and Electroanalytical Cheimistry*, Wiley, Germany, 536-538, 2003.
12. Christensen, P. A.; Hamnett, A., *Techniques and Mechanisms in Electrochemistry, Chapman and Hall, Glasgow*, 1994.
13. Greenler, R. G., *Journal of Chemical Physics*, 1966, 44, 310.
14. Greenler, R. G., *Journal of Chemical Physics*, 1968, 50, 1963.
15. Greenler, R. G., Snider, D. R., Witt, D.; Sorbello, R. S., *Surface Science,* 1982, 118, 415-428
16. Zhou, Z. Y.; Wang, Q.; Lin, J. L.; Tian, N.; Sun, S.G., *Electrochimica Acta*, 2010, 55 (27), 7995-7999.
17. Fang, X.; Wang, L.; Shen, P. K.; Cui, G.; Bianchini, C. *J. Power Sources*, 2010, 195 (5), 1375-1378.
18. Beyhan, S.; Uosaki, K.; Feliu, J. M.; Herrero, E., *Journal of Electroanalytical Chemistry*, 2013, 707, 89-94.
19. Camara, G. A.; Iwasita, T. *Journal of Electroanalytical Chemistry*, 2005, *578* (2), 315-321.

20. Xia, X. H.; Liess, H. D.; Iwasita, T. *Journal of Electroanalytical Chemistry,* 1997, *437* (1-2), 233-240.
21. Wang, Q.; Sun, G. Q.; Jiang, L. H.; Xin, Q.; Sun, S. G.; Jiang, Y. X.; Chen, S. P.; Jusys, Z.; Behm, R. J. *Physical Chemistry Chemical Physics,* 2007, *9* (21), 2686-2696.
22. Lide; David, R., *CRC Handbook of Chemistry and Physics*. 74th ed.; CRC Press: Boca Raton, 1994, pp 8-45.
23. Leung, L. W. H.; Chang, S.-C.; Weaver, M. J. *Journal of Electroanalytical Chemistry & Interfacial Electrochemistry*, 1989, *266* (2), 317-366.
24. Colmati, F.; Tremiliosi-Filho, G.; Gonzalez, E. R.; Berna, A.; Herrero, E.; Feliu, J. M. *Faraday Discussions,* 2009, *140*, 379-397.
25. Heinen, M.; Jusys, Z.; Behm, R. J. *Journal of Physical Chemistry C*., 2010, *114* (21), 9850-9864.
26. Iwasita, T. and Pastor, E., *Electrochimica Acta*,1994, *39* (4), 531-537.
27. Iwasita, T.; Dalbeck, R.; Pastor, E.; Xia, X. *Electrochimica Acta*, 1994, *39* (11-12), 1817-1823.
28. Ianniello, R.; Schmidt, V. M.; RodrIguez, J. L.; Pastor, E. *Journal of Electroanalytical Chemistry*, 1999, *471* (2), 167-169.
29. Gootzen, J. F. E.; Visscher, W.; van Veen, J. A. R. *Langmuir*. 1996, 12, 5076.
30. Beden, B.; Morin, M. C.; Hahn, F.; Lamy, C. *J. Electroanalytical Chemistry & Interfacial Electrochemistry,* 1987, p. 229,353.
31. Schmiemann, U.; Müller, U.; Baltruschat, H. *Electrochimica Acta*. 1995, *40* (1), 99-107.
32. Wurtz, C. A. *Bulletin de la Société Chimique de France*. 1872, *17*, p. 436
33. Dutta, A. and Datta, J., *International Journal of Hydrogen Energy,* 2013, 38, 7789-7800.
34. Jiang, L.; Hsu, A.; Chu, D.; Chen, R., *International Journal of Hydrogen Energy*, 2010, 35, 365-372.
35. Schmidt, T. J.; Ross, P. N.; Markovic, N. M., *Journal of Physical Chemistry B*, 2001, 105, 12082-12086.
36. Mahapatra, S. S.; Dutta, A. and Datta, J., *Electrochimica Acta*, 2010, 55, 9097-9104.

37. Ma, L.; Chu, D. and Chen, R., *International Journal of Hydrogen Energy,* 2012, 37, 11185-11194.
38. Lai, S. C. S. and Koper, M. T. M., *Physical Chemistry Chemical Physics*, 2009, 11, 10446-10456.
39. Dimos, M. M.; Blanchard, G. J. *Journal of Physical Chemistry C.* 2010, *114*, 6019-6026.
40. Caram, J. A. and Gutiérrez, C., *Journal of Electroanalytical Chemistry*, 1992, 323, 213-230.
41. Freitas, R. G.; Pereira E. C.; Christensen, P. A., *Electrochemical Communications*, 2011, 13, 1147-1150.
42. Freitas, R. G.; Antunes, E. P.; Christensen, P. A.; Pereira, E. C., *Journal of Power Sources*, 2012, 214, 351-357.
43. Gomes, J. F., *Journal of Catalysis*, 2013, 302, 67-82.
44. Hamann C.H., Hamnett A., Wielstich W., *Electrochemistry*, Wiley VHC, 2nd Ed., 2007, Weinheim, New York.
45. Sheng, W.; Gasteiger, H. A.; Shao-Horn, Y.; *Journal of the Electrochemical Society*, 2010, 157(11), B1529-B1536
46. F. C. Nart and W. Vielstich, in: *Handbook of Fuel Cells: Fundamentals, Technology and Applications*, Vol. 2, W. Vielstich, A. Lamm, and H. A. Gasteiger, Editors, p. 302, John Wiley & Sons, New York (2003).
47. He, C.; Song, S.; Liu, J.; Maragou, V.; Tsiakaras, P., *Journal of Power Sources,* 2010, 195, 7409–7414
48. He, Q.; Shyam, B.; Macounova, K.; Krtil, P.; Ramaker, D. and Mukerjee, S., *Journal of the American Chemical Society,* 2012, 134, 8655 – 8661.
49. Morin, M. C.; Lamy, C.; Leger J.-M.; Vasquez, J.-L. Aldaz, A. *Journal of Electroanalytical Chemistry,* 1990, *283*(1-2), 287 – 302.
50. Camara, G. A.; de Lima, R. B.; Iwasita, T. *Journal of Electroanalytical Chemistry*, 2005, *585* (1), 128-131.
51. Chen, S.; Schell, M., Journal of Electroanalytical Chemistry, 1999, 478, 1-2, 108-117.
52. Christensen, P. A.; Hamnett, A., *Journal of Electroanalytical Chemistry & Interfacial Electrochemistry,* 1989, *260* (2), 347-359.
53. Stangret M., Smeichowski J., *Journal of Molecular Science*, 2007, 834, 239-248.

54. DeLima, R. B.; Varela, H. *Gold Bulletin*. 2008, *41* (1), 15-22.
55. Greenler, R. G. *Journal of Chemical Physics,* 1962, *37* (9), 2094-3000
56. Nichols, R. J. and Bewick, A. *Electrochimica. Acta*, 1988, *33*, 1691-1694
57. Lutz, H. In *Solid Materials*. Vol. 69. Springer: Berlin / Heidelberg, 1988: pp 97-125.
58. Bertie, J. E.; Whalley, E. *Journal of Chemical Physics,* 1964, *40* (6), 1637-1645.
59. Ataka, K.; Yotsuyanagi, T.; Osawa, M. *Journal of Physical Chemistry,* 1996, *100*, 10664-10672.
60. Gragson, D. E.; McCarty, B. M.; Richmond, G. L. *Journal of the American Chemical Society,* 1997, *119* (26).
61. Christensen, P. A.; Hamnett, A.; Linares-Moya, D.; *Physical Chemistry Chemical Physics,* 2011, *13* (12), 5206-5214.
62. Iwasita, T.; Rasch, B.; Cattaneo, E.; Vielstich, W. *Electrochimica Acta.* 1989, *34* (8), 1073-1079.
63. Socrates, G. *Infrared Characteristic Group Frequencies*, 1st ed.; Wiley Interscience: Bath, 1980.
64. Yu, Z.; Chuang, S. S. C., *Journal of Catalysis,* 2007, *246* (1), 118-126.
65. Vigier, F.; Coutanceau, C.; Hahn, F.; Belgsir, E. M.; Lamy, C. *Journal of Electroanalytical Chemistry,* 2004, 563 (1), 81-89.
66. Rodes, A.; Pastor, E.; Iwasita, T., *Journal of Electroanalytical Chemistry,* 1994, *373* (1-2), 167-175.
67. Iwasita, T.; Nart, F. C.; Rodes, A.; Pastor, E; Weber, M., *Electrochimica Acta.,* 1995, *40* (1), 53-59.
68. Iwasita, T.; Rodes, A; Pastor, E., *Journal of Electroanalytical Chemistry,* 1995, *383* (1-2), 181-189.
69. Yee, A.; Morrison, S. J.; Idriss, H. *Journal of Catalysis,* 1999, *186* (2), 279-295.
70. Yee, A.; Morrison, S. J; Idriss, H. *Journal of Catalysis*, 2000, *191* (1), 30-45.
71. Greenler, R. G.; Snider, D. R.; Witt, D. *Surface Science*, 1982, *118* (3), 415-428.
72. Lin, W. F.; Christensen, P. A.; Hamnett, A.; Zei, M. S.; Ertl, G. *Journal of Physical Chemistry B*, 2000, *104*, 6642-6652

73. Lin, W. F.; Christensen, P. A.; Hamnett, A. *Journal of Physical Chemistry B*, 2000, 104, 12002-12011.
74. Lin, W.-F.; Christensen, P. A.; Jin, J. M.; Hamnett, A. In *In-situ Spectroscopic Studies of Adsorption at the Electrode and Electrocatalysis*; 1st ed.; Sun, S.-G., 2007.
75. Christensen, P. A.; Wieckowski, A., Eds.; *Elsevier Science,* B.V.: Amsterdam, 2007, 99-138.
76. Griffiths, P. R.; de Haseth J. A. *Fourier Transform Infrared Spectrometry.* Wiley-Interscience: New York, 1986, 39-41.

4. An in-situ FTIR spectroscopic study of the electrochemical oxidation of ethanol at a Pb-modified polycrystalline Pt electrode immersed in aqueous KOH.

4.1. Introduction

4.1.1. Overview

This chapter details the study of the mechanism of ethanol oxidation in alkaline solution at a platinum electrode modified with an irreversibly-deposited layer of lead using *in situ* FTIR spectroscopy. This study provides support for the suggestion that the adsorption mechanism of ethanol is substantially modified in the presence of Pb, with a carbon-bonded intermediate being favoured leading to facile scission of the ethanol C-C bond. Furthermore, the formation of carbonate takes place at potentials close to the thermodynamic value. At higher potentials, where Pb has desorbed, the mechanism of oxidation of ethanol reverts to that found at a normal polycrystalline Pt surface, with the primary product being acetate.

As discussed in section 1.7, there has been a resurrection of interest in recent years in the use of alkaline fuel cells [1-4], because both alcohol oxidation and oxygen reduction are more facile under alkaline conditions than acid [5]. It has been suggested that the enhanced kinetics in alkaline solution may arise from the readier availability of 'active oxygen' in the form of reversibly adsorbed OH [6], and it is certainly true that there is a wider range of moderately active catalysts available: eg. Pd is inactive towards ethanol oxidation under acid conditions, but is more active than Pt in alkali [7]. However, whilst the selective oxidation of ethanol to CO_3^{2-} at Pt in alkaline media has been reported at high overpotentials (see [8] and references therein), the problem of incomplete oxidation at the lower, commercially significant, potentials still remains. The work on ethanol oxidation presented in Chapter 3 supports this postulate in terms of oxidation in alkaline media, with clear evidence of ethanol adsorption at Pt through O rather than through C, and with evidence that it is adsorption through the latter of which is necessary for C-C cleavage.

4.1.2. Significantly enhanced C-C bond cleavage in ethanol using a Pb co-catalyst

Recently, He and co-workers [8] reported a marked enhancement in the cleavage of the C-C bond of ethanol at Pt nanocrystals supported on carbon in 0.25 M KOH in

the presence of $Pb(OAc)_4$ as co-catalyst. The extent of this enhancement appears to depend critically on the conditions of the experiment, possibly owing to the hydrolysis of the lead tetra-acetate itself to PbO_3^{2-} in alkaline solution; but all experiments show an enhancement. Figure 4.1(a) shows the cyclic voltammograms collected by He *et al* [8] at Pt/C in 0.25 M KOH + 1 M EtOH in the absence and presence (1 and 3 mM) of Pb(IV) acetate in solution. From the figure, it may be seen that there are two distinct peaks near 0.7 and 0.9 V during the forward-going scan of the CV in the absence of Pb(IV). This is in contrast to the CVs at Pt in 0.1 M KOH + 1 M EtOH presented in this thesis (see fig. 3.7), and the typical behaviour for oxidation of ethanol at Pt at 25 ^{o}C in alkaline solution demonstrated across the literature [9]. However, this was not acknowledged by the authors.

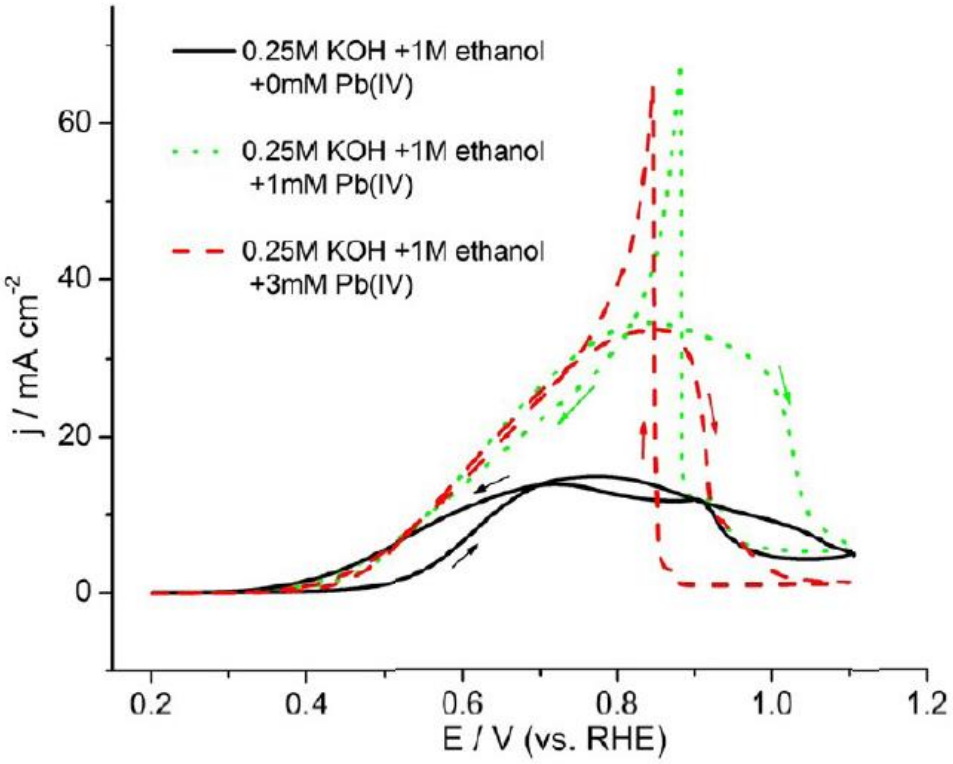

Figure 4.1. (a) Cyclic Voltammograms collected by He et al [8] at Pt/C (E-TEK, 30%) in 0.25 M KOH + 1 M EtOH with 0, 1 and 3 mM Pb(IV) acetate in solution.

As may be seen from figure 4.1(a), the authors observed a 3-fold increase in current density upon addition of Pb(IV). Furthermore, although no significant difference in the ethanol oxidation rate was observed between the CVs collected in the presence of

1 mM and 3 mM Pb(IV), the potential window available for ethanol oxidation was increased from ca. 0.55-0.9 V to 0.45-0.9 V, which He *et al* attributed to a change in surface chemistry.

The authors postulated the mechanism shown in scheme 4.1; in this, the presence of upd Pb on the Pt surface and Pb(IV) in solution could facilitate the formation of a C-C bonded intermediate that could, in turn, be oxidised completely to carbonate (C_1 and $C_{2\prod}$ pathways in scheme 4.1). Complete oxidation of ethanol was postulated over the potential range which the upd Pb (deposited at potentials below 0.4V vs RHE) was oxidised to adsorbed $HPbO_2^-$ at ca. 0.46V to 0.77V vs RHE, the latter providing the necessary 'active oxygen' (see scheme 4.2 and discussion below).

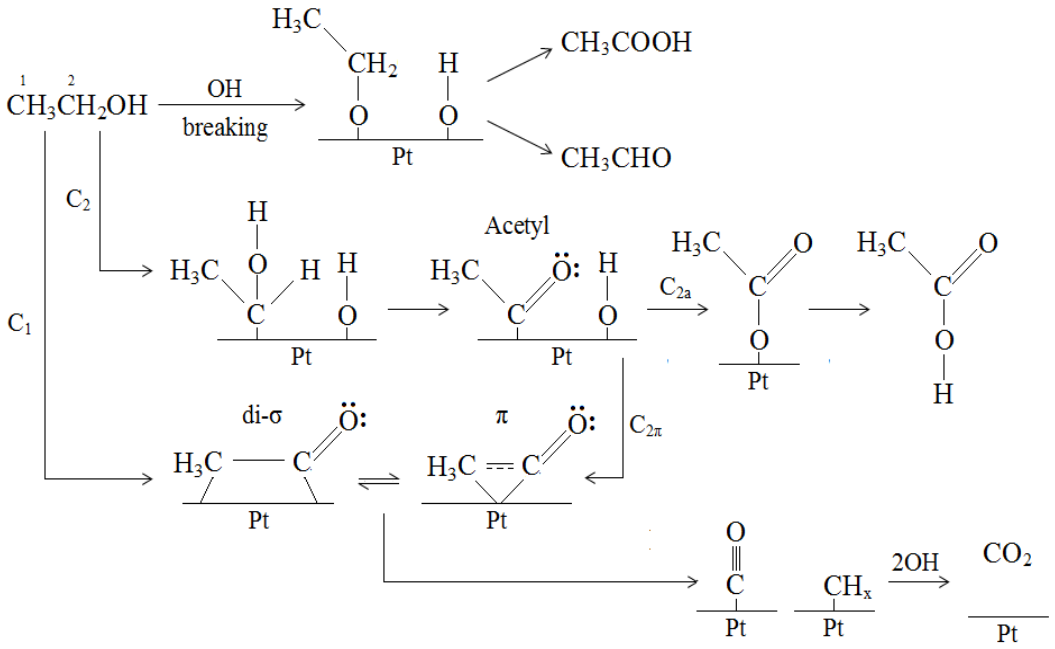

Scheme 4.1. The mechanism proposed by He et al. for the oxidation of ethanol at Pt. Redrawn from [8].

Figure 4.1(b) shows the chronoamperometry data collected from Pt/C in 0.25 M KOH in the presence of 1 mM Pb(IV) acetate and pre-deposited Pb. As may be seen from the figure, without the solution Pb(IV), the activity was observed to decline and the authors postulated that this was due to poisoning by adsorbed CO or other intermediates from the chemisorption of ethanol, and that the Pb(IV) solution species

plays a major role in activating the C-C bond in conjunction with the Pb on the surface. An alternative possible explanation is that adsorbed CO displaces the Pb as was observed in acidic solution for Pb adlayers on Pt(100) and Pt(111) [10][11]. For example, Lucas *et al* [10] investigated the structural effects of CO adsorption at Pt-bimetallic surfaces (Pt(100)) by a combination of voltammetry and *in-situ* surface X-ray scattering (SXS) using a rotating ring disk electrode (RRDE). The authors monitored the flux of Pb^{2+} to and from the RRDE during the electro-oxidation of CO at $PtPb_{upd}$ and $PtCu_{upd}$ and demonstrated that as the potential was stepped positively from the point of upd (0.22 V and 0.2 V vs. SCE for Pb and Cu respectively), the onset for CO oxidation was identical the that obtained at normal Pt, indicating that Pb and Cu adatoms can be displaced by CO_{ads}. Hence, returning to the study by He *et al* [8], it does not seem unreasonable to suggest that, if CO is an intermediate in the oxidation of EtOH at PtPb in the absence of solution Pb(IV) acetate, it displaces upd Pb, thus causing the decline in activity depicted in fig. 4.1(b).

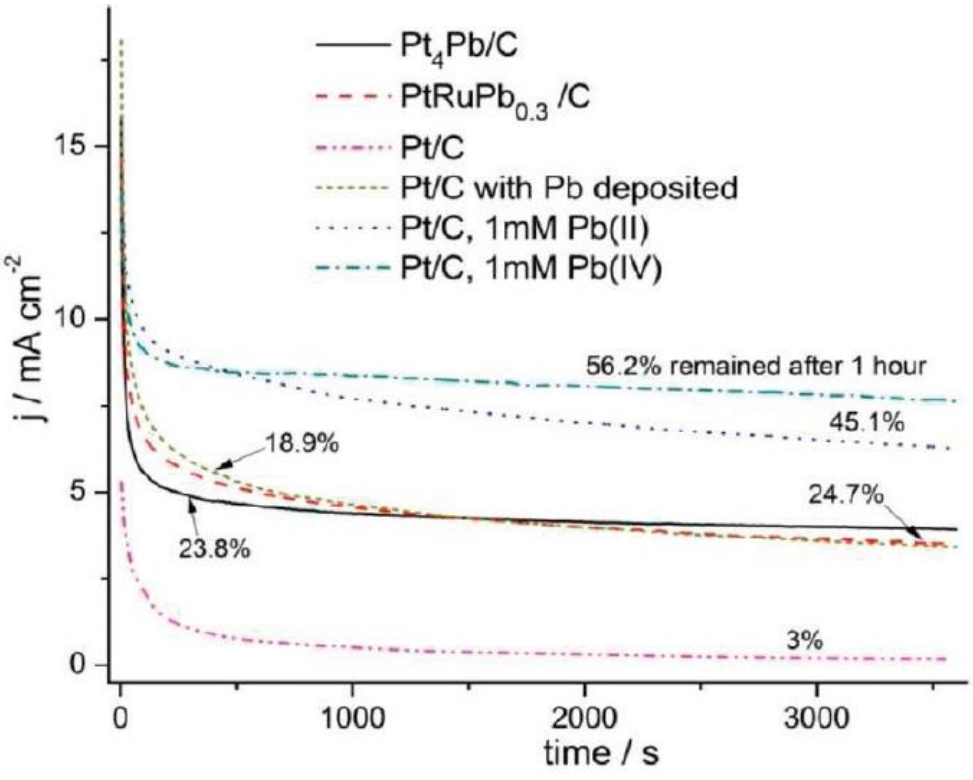

Figure 4.1(b) Chronoamperometry data collected by He et al Pt/C in 0.25 M KOH in the absence and presence of 1 mM Pb(IV) acetate and upd Pb.

Figure 4.1(b) also shows the chronoamperometry data collected at Pt_4Pb/C and $PtRuPb_{0.3}/C$, however, no attempt was made by the authors to compare these data to that collected at Pt/C in the presence of solution Pb(IV) acetate and upd Pb.

As stated previously, it was suggested by the authors that the presence of solution Pb(IV) acetate plays a major role in the catalytic enhancement observed in figs. 4.1(a) and 4.1(b). Thus, scheme 4.2 shows the reaction mechanism presented by He *et al* for enhanced C-C bond breaking in the presence of Pb(IV) both at the Pt surface and in solution.

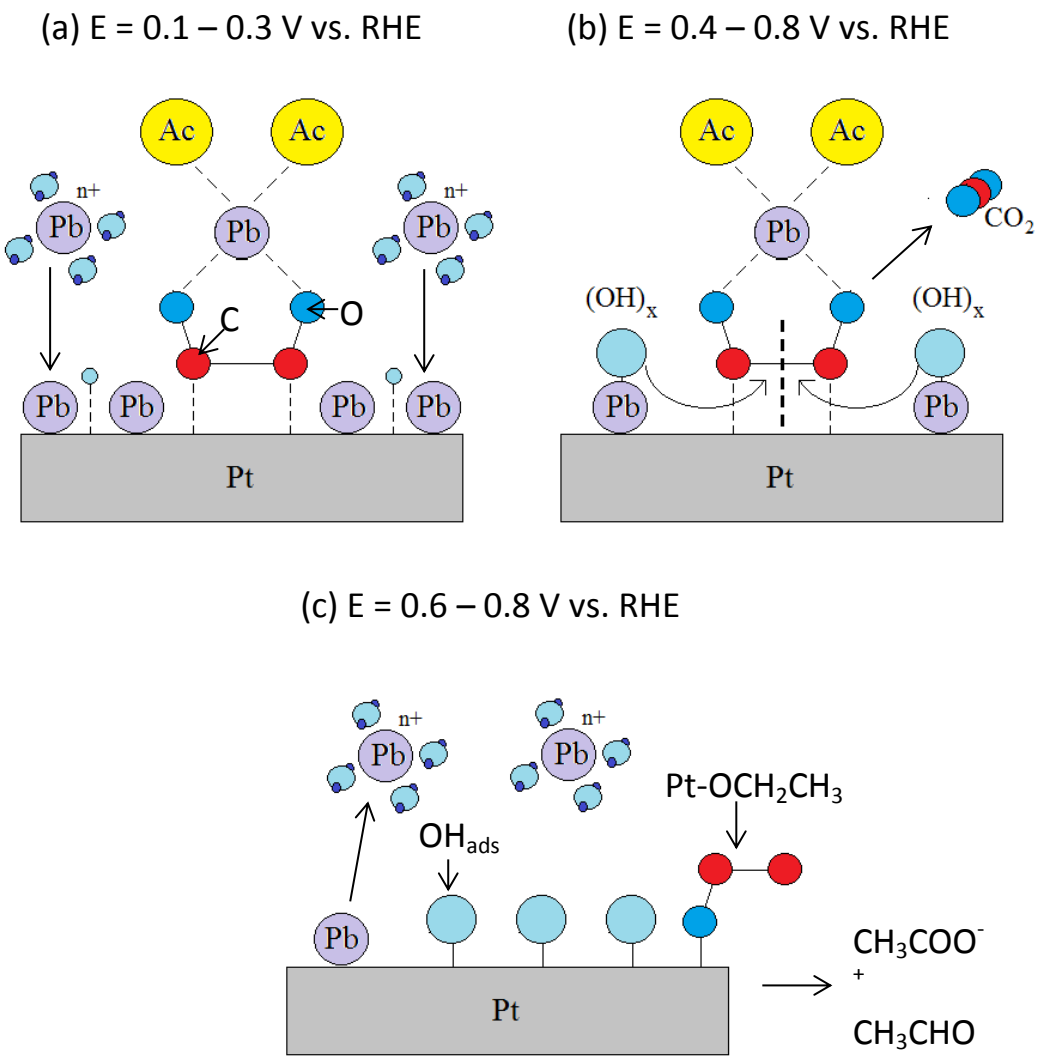

Scheme 4.2 The mechanism for the enhancement C-C bond cleavage in ethanol at Pt in the presence of both solution Pb(IV) acetate and upd Pb. Redrawn from [8].

As may be seen from scheme 4.2(a), it was postulated by the authors that both a Pb-acetate-chelate complex and Pb adatoms (at Pt) are formed simultaneously at potentials < 0.3 V, thus isolating ethanol from Pt whilst modifying the Pt surface (a process not realised in the presence of upd Pb only). As shown by scheme 4.2(b), He *et al* suggest that ethanol then bonds to the Pt surface through carbon, as opposed to oxygen (OH pathway in scheme 4.1), where it then reacts with OH adsorbed on Pb adatoms, leading to C-C bond breaking and hence CO_2 production. As may be seen from scheme 4.2(c), the authors propose that at higher potentials (ca. 0.6-0.8 V), as the Pb adatoms leave the Pt surface, the mechanism returns to that which is expected at normal Pt (C_2 pathway in scheme 4.1), thus yielding C_2 oxidation products.

The postulated mechanism for enhancement of C-C bond breaking at Pt in the presence of Pb by He *et al* was supported only by the Differential Electrochemical Mass Spectrometry (DEMS) data at 0.67 V and 0.77 V, and the actual potential range over which this occurs was not verified by experiment and no other molecular, analytical data were presented. In addition, the authors stated that the DEMS experiments were problematic, with no multi-electron products (eg. acetate) detected below 700 mV. Thus, the mechanism presented in scheme 4.2 should be treated with caution, as significantly more molecular analysis on this complex system is required.

In order to provide molecular information as a function of potential, this chapter presents an initial, in-situ FTIR spectroscopic study of the effect of the presence of Pb on the oxidation of ethanol at polycrystalline Pt in 0.25M KOH. For this study, a polycrystalline Pt electrode was employed with Pb pre-deposited, to avoid optical problems due to deposition taking place during spectral data collection. No lead solution species were thus present at the commencement of the FTIR experiments discussed below.

4.2. Results and Discussion

4.2.1. Voltammetry

Figure 4.1(a) shows cyclic voltammograms of a Pt mesh electrode with and without the Pb layer in 0.25M KOH.

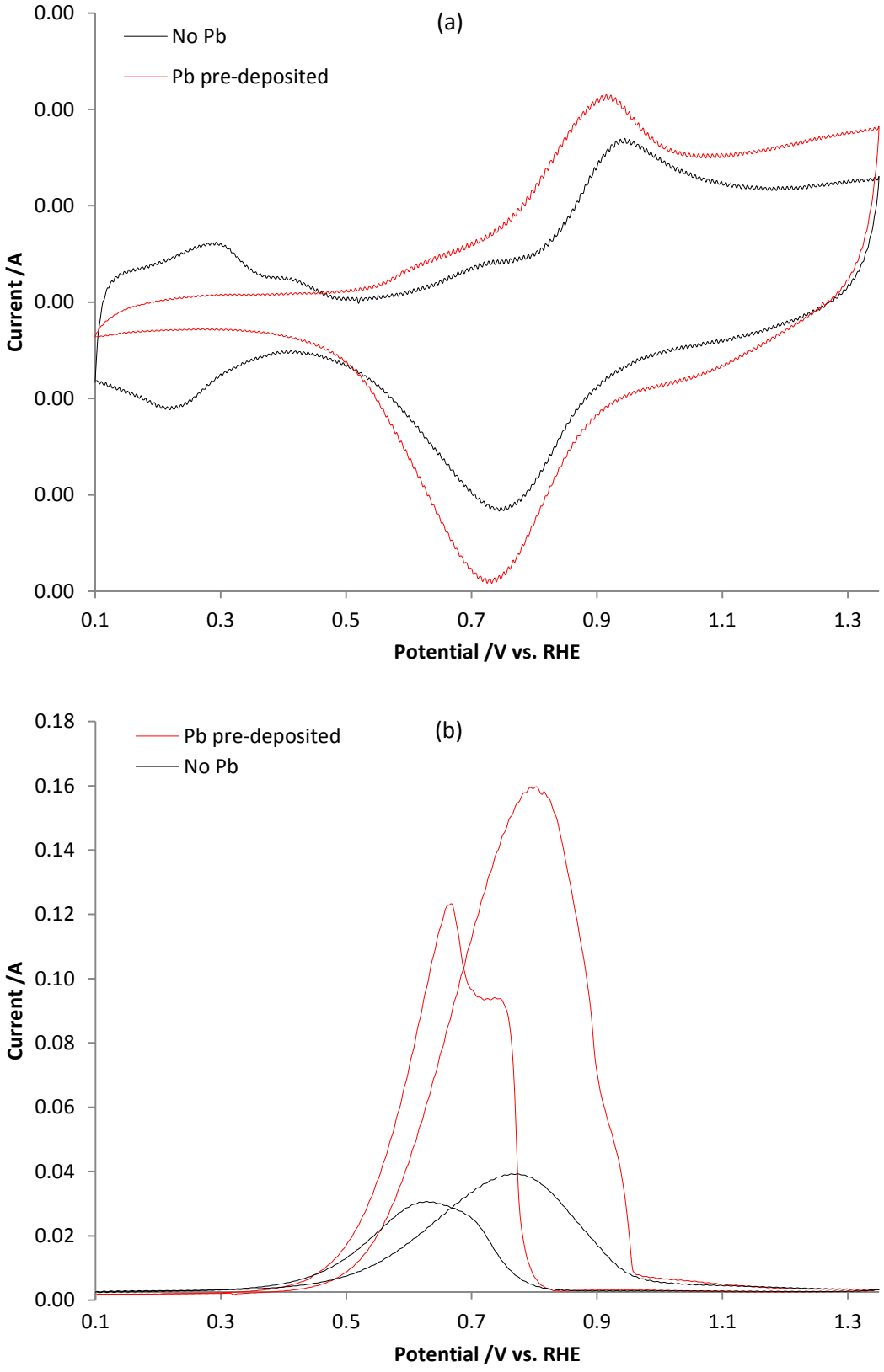

Figure 4.1. Cyclic voltammograms of the Pt mesh electrode in (a) 0.25M KOH and (b) 0.25M KOH + 1M EtOH, in the absence and presence of an irreversibly-adsorbed Pb layer, scan rate 100 mV s^{-1}.

The CV in the presence of the Pb is very similar to that presented by He et al [8], allowing for the different morphologies of the Pt electrodes, and the peak potentials of the oxide stripping features (and the hydride features in the absence of Pb) were employed to confirm the conversion between the MMO reference electrode employed and the RHE scale. Hence, all potentials in this chapter will be quoted vs. RHE, thus simplifying the discussion of the data presented in this chapter when comparing it to the work presented by He *et al*.

As may be seen from fig. 4.1(a), the deposition of Pb suppresses the adsorption of hydrogen completely (on the timescale of the experiment), and the anodic region of the voltammogram is enhanced due to the oxidation of Pb initially to adsorbed oxo-hydroxide species of lead [12] and to $HPbO_2^-$ in solution, a process that commences at about 0.46V [13], but which is very irreversible [12][14]:

$$Pb + 2OH^- \rightarrow [Pb(OH)_2]_{ads} + 2e^- \quad (1)$$

Further oxidation continues both of the lead layer and the underlying Pt in the region 0.70 - 1.20V vs. RHE, and certainly at the higher potentials in this range, oxidation of the lead to Pb(IV) is possible.

The thermodynamic potential for oxidation of $HPbO_2^-$ to PbO_3^{2-} at pH 13.3 is given by Carr and Hampson [13] as E^0 (NHE) = 1.40 - 0.0886pH; converting this to RHE gives 1.00V, and this would therefore account for the obvious rise in current at the most positive potentials (≥ ca. 1.00 V) in fig. 4.1(a) compared to Pt itself. Thus, it is postulated that at potentials above 1.00 V, Pb(II) is oxidised to Pb(IV) as follows:

$$[Pb(OH)_2]_{ads} + 2OH^- \rightarrow PbO_2 + 2e^- \quad (2)$$

He *et al* [8] suggest that the current above 0.80 V (ie. below the thermodynamic potential for oxidation of $HPbO_2^-$ to PbO_3^{2-}) could be due to this oxidation process, however, this seems improbable on the basis of Carr and Hampson's article. Furthermore, oxidation of Pb(II) to $Pb(OAc)_4$ is known to occur at about 1.40 V vs. RHE in dilute acetic acid [15], and in alkaline solution, the E^0 value vs. RHE will be given approximately as $2.20 - 0.0886pH \approx 1.00V$, which does account for the increasing current beyond 1.00 V in fig. 4.1(a), as compared to Pt.

The considerable irreversibility in the anodic current associated with the oxidation of the lead layer is interesting: lead adsorbed on single-crystal Pt surfaces is known to attain essentially complete coverage on all low index faces [12][16], a result entirely consistent with the disappearance of the hydride structure. However, polycrystalline and nanocrystalline Pt will have micro-regions of well-defined surface structure interspersed with less regular arrangements of Pt atoms at the interfaces between these regions: the lead will probably adsorb to lower coverage in these interfacial areas of the surface, leading to a surface structure at low potentials consisting of well-defined lead islands and gaps between these islands where there is a lower lead coverage. Oxidation of such a structure will then begin at the edges of the island superstructures, presumably initially by formation of adsorbed Pb-OH, and will progress at different rates on different Pt surface structures, accounting for the obvious broadness of the oxidation process. In addition, the oxidation may well proceed in two stages on each surface region, the first oxidation creating a still adsorbed oxo-hydroxide Pb surface and the second step being further oxidation and removal of this as $HPbO_2^-$. Further oxidation of this as a solution species to $Pb(OAc)_4$ and PbO_3^{2-} in solution then taking place at more positive potentials.

Figure 4.1(b) shows the voltammograms in the presence of 1 M ethanol. In agreement with the work of He and co-workers, there is a significant enhancement in the currents of both the peak in the anodic sweep and the anodic (auto-oxidation) peak on the return (cathodic) sweep due to oxidation of the ethanol at the freshly-exposed Pt following oxide stripping. The former is enhanced by a factor of > 4 in the presence of Pb (compared to the threefold enhancement observed by He et al). However, there are also some differences: thus, He et al observe a marked shift in onset potential of 150 mV to more negative potentials, such a shift is not evident in fig. 4.1(b) (but is in the IR data, see below). Furthermore, He and co-workers observed that the auto-oxidation peak observed as the Pt oxide starts to strip in the cathodic sweep was very sharp and twice that of the anodic peak current; in contrast, as can be seen in fig. 4.1(b), both features are broad, the auto-oxidation feature is lower than the anodic peak and clearly comprises two distinct processes, at 0.74V and 0.66V. It is likely that these differences probably reflect the difference in morphology between the polycrystalline Pt electrode employed in this work and the nanoparticulate Pt employed by He et al.

4.2.2. Infrared data

Figure 4.2 shows the current/potential response observed during FTIR experiments with (i) and without (ii) Pb in which the potential of the reflective Pt working electrode was stepped up from 0.10 V, spectra collected at each step and normalised to the reference taken at 0.10 V.

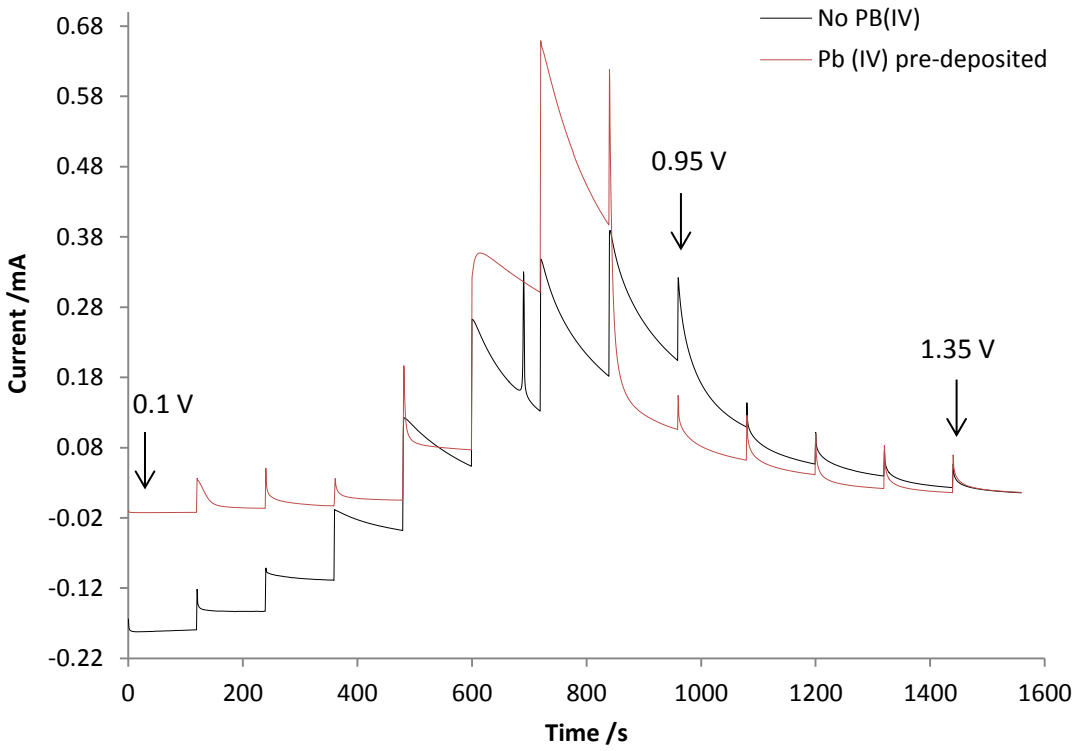

Figure 4.2. The current/time profile observed during the FTIR experiment in figure 4.3, compared to that observed without Pb.

The spectra collected from the Pb-modified electrode are shown in in figs. 4.3(a)-(c). The spectra in fig. 4.3(a) show: the growth of water gain features near 3335 cm^{-1} and 1647 cm^{-1}, the loss of OH^- (broad bands near 2700 and 1875 cm^{-1} [17-19]), the gain of a band due to bridge-bonded CO (CO_B) at 1862 cm^{-1} [20][21], the gain of a band near 1395 cm^{-1} with a small gain feature at ca. 1300 cm^{-1}. The CO_B and 1300 cm^{-1} features may be seen more clearly in fig. 4.3(b) which shows only the spectrum collected at 0.25 V.

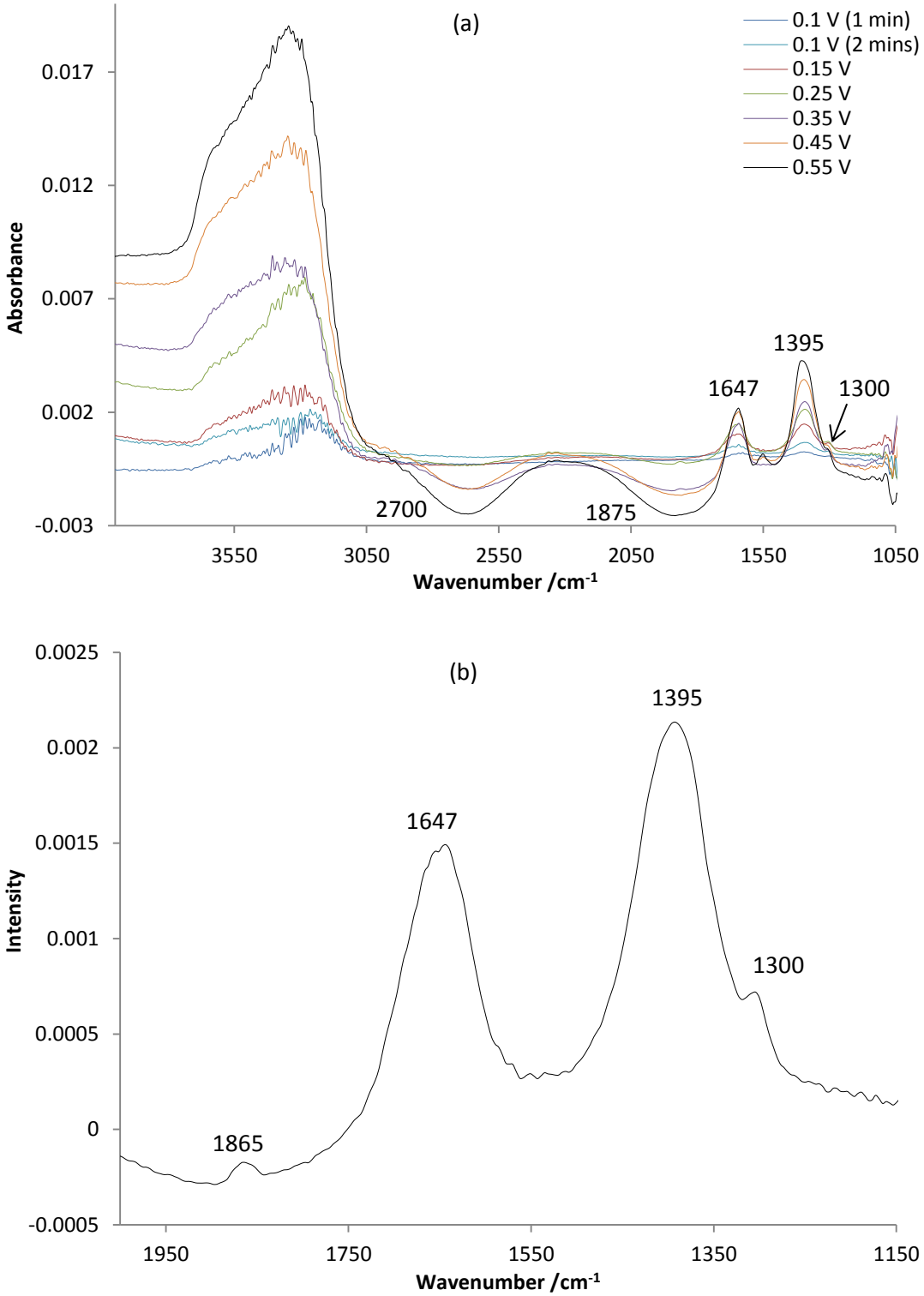

Figure 4.3. (a) Spectra (8 cm^{-1} resolution, 100 scans, 47 s per scan set) collected from 0.1 to 0.55 V vs. RHE at Pb-modified Pt (see section 2.3) in N_2-saturated 0.25 M KOH + 1 M EtOH (b) Spectrum collected at 0.25V in fig. 4.3(a) from 2000-1150 cm^{-1}.

The 1395 cm^{-1} band was unequivocally assigned to solution carbonate by adding Na_2CO_3 dissolved in 0.1M KOH into the FTIR cell containing 0.1M KOH and following the diffusion of the CO_3^{2-} ions into the thin layer with time. The spectrum of CO_3^{2-} so obtained is shown in fig. 4.4; also shown is the spectrum collected at 0.45V in fig. 4.3(a) for comparison.

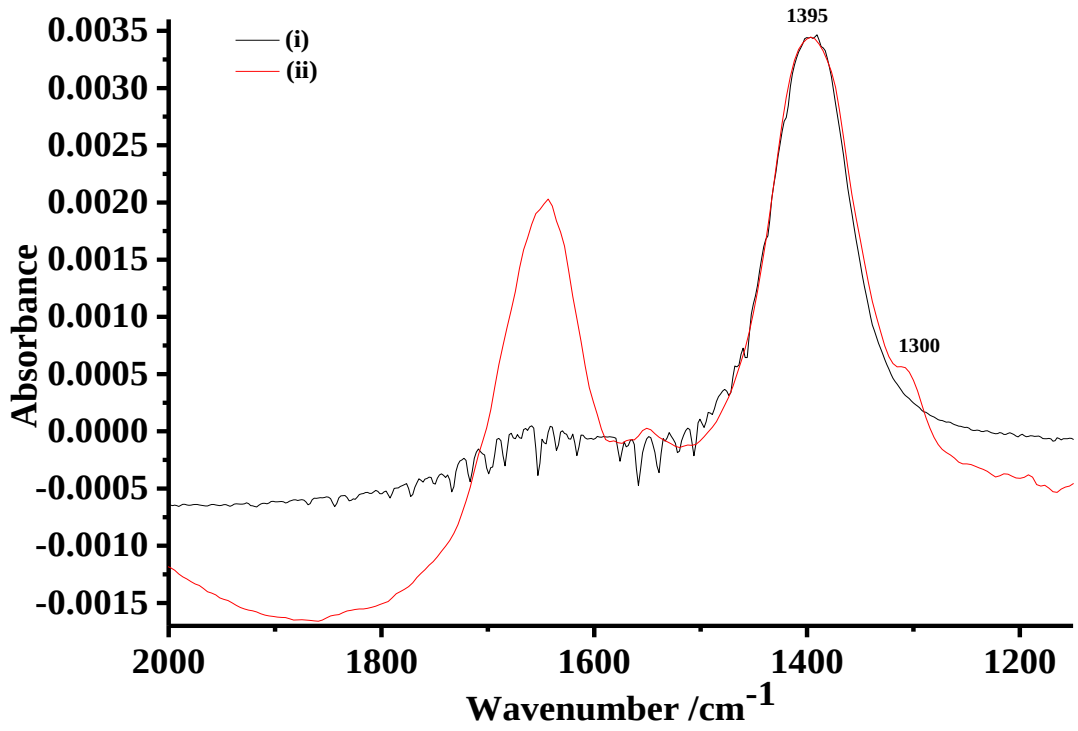

Figure 4.4. The spectrum of (i) aqueous carbonate compared to (ii) that collected at 0.45V in fig. 4.3(a). See text for details.

The CO_B feature appears at 0.10V, increases in intensity to 0.35V after which it decreases and is absent at 0.45V, see fig. 4.5 which shows plots of the intensities of the various features observed in fig. 4.3(a) as a function of potential. The 1300 cm^{-1} feature appears at the same potential, its intensity increases to a maximum at 0.25V before decreasing. On the basis of the potential dependence of the intensities of the latter feature and the carbonate band, it is clear that the two features are associated with different processes; the 1300 cm^{-1} feature may tentatively be attributed to HCO_3^- associated with water molecules in the Inner Helmholtz Plane [22-24]. The frequency of this feature is postulated as being strongly dependent upon the

electrolyte [23] and has been observed at 1319 cm^{-1} in alkaline electrolyte [24]. The presence of CO_B (as opposed to linearly-adsorbed C≡O) is noteworthy as CO in bridging and threefold sites on Pt is generally believed to be a poison, blocking the active sites and reducing catalytic activity [25]. The 1862 cm^{-1} band is only present at low potentials and its potential dependence does not appear to suggest it is intermediate in the formation of CO_3^{2-}. Hence, CO_B may only be a product from the initial chemisorptions of ethanol, blocking the surface until a sufficiently high potential is attained for it to be oxidised.

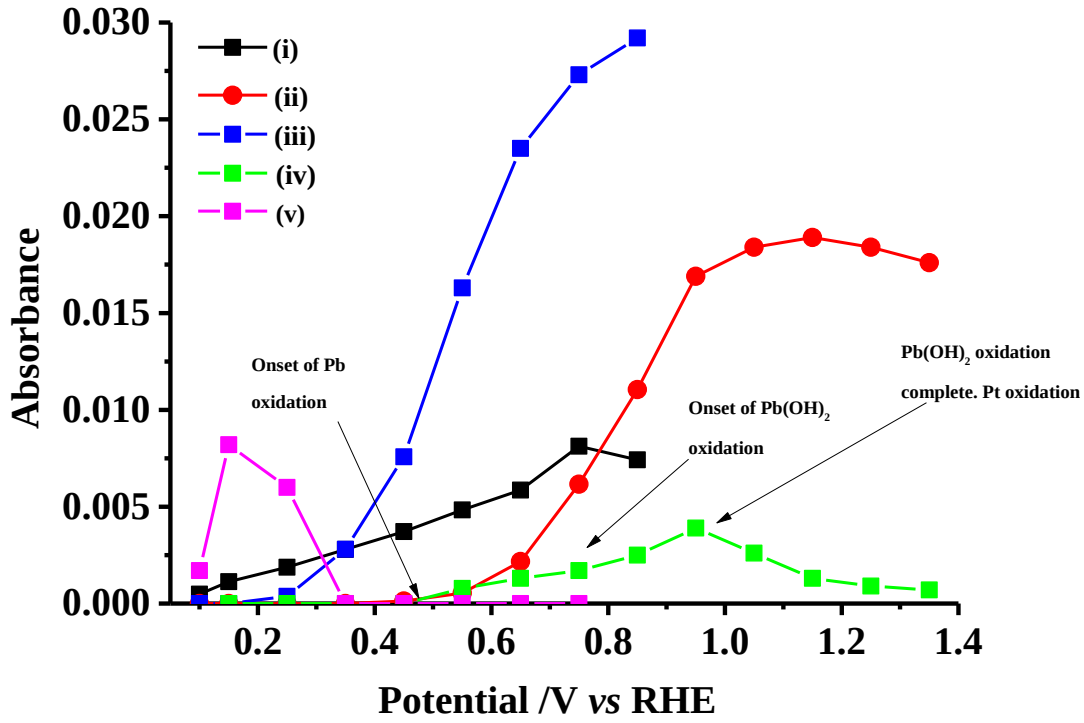

Figure 4.5. Plots of the band intensities of the features in fig. 4.3 and in an analogous experiment in the absence of Pb (see figs. 4.7 and 4.8): (i) CO_3^{2-} Pb/Pt, (ii) 1554 cm^{-1} Pb/Pt, (iii) 1554 cm^{-1} Pt, (iv) 3680 Pt-OH and (v) CO_B x 1000.

Figure 4.3(c) shows the spectra collected from -0.4 to -0.1 V vs. MMO during the experiment depicted in figs. 4.3(a) and (b). As may be seen from the figure, the spectra are dominated by features due to solution acetate (1554 and 1415 cm^{-1}[3]), with an inflexion (arrowed) to the low wavenumber side of the latter feature. This, and the fact that the 1554 cm^{-1} band appears *less* intense than the feature at

1415 cm^{-1} [19], suggest the continuing growth of the carbonate band. The variation in intensity of the carbonate feature between 0.65V and 0.85V was estimated by increasing the intensity of the 1395 cm^{-1}carbonate band in the spectrum taken at 0.45V by factors sufficient to annul its contribution following subtraction from the spectra taken at these potentials. Thus, it was found that increasing the absorbance of the 1395 cm^{-1} band taken at 0.45V by factors of 1.58, 2.18 and 2 and subtracting the resultant spectra from those collected at 0.65V, 0.75V and 0.85V, respectively, resulted in spectra showing no carbonate features and the 1554 & 1415 cm^{-1} bands of acetate in the correct intensity ratios, see fig. 4.6. Plots of the 1554 cm^{-1} acetate and 1395 cm^{-1} carbonate bands are plotted as a function of potential in fig. 4.5, which also shows the corresponding plot of the 1554 cm^{-1} band in the absence of Pb. No carbonate was observed in the latter experiment (nor in the work in 0.1 M KOH [19]).

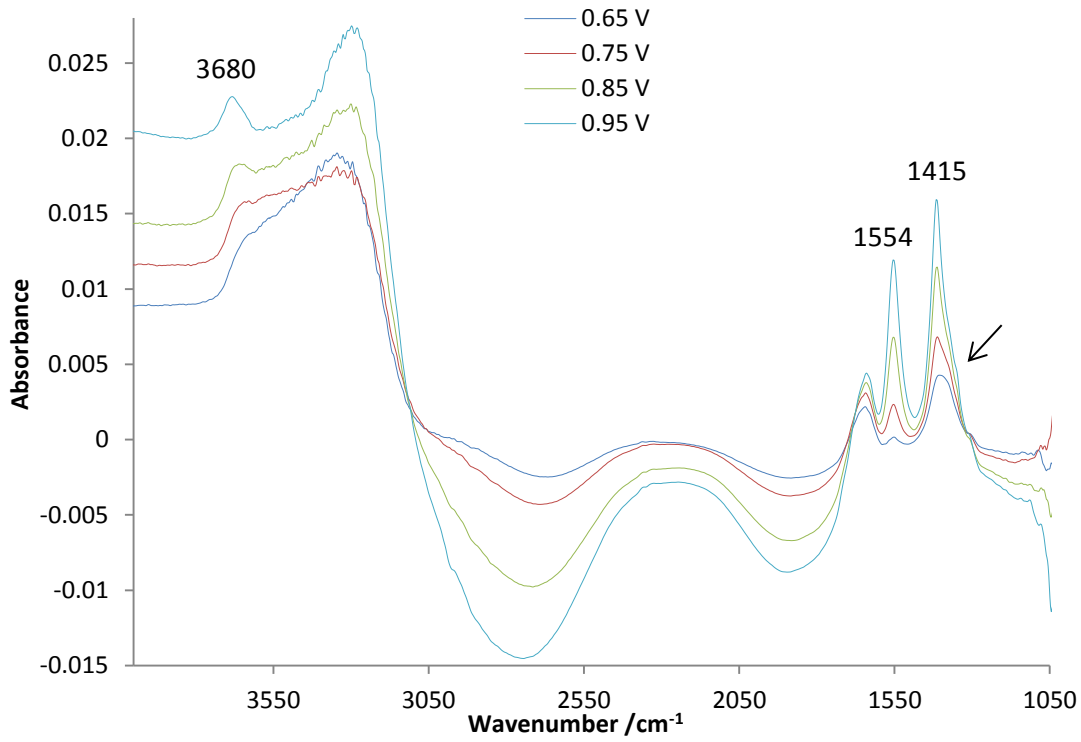

Figure 4.3(c) Spectra collected at (i) 0.55, (ii) 0.65, (iii) 0.75 and (iv) 0.85V during the experiment depicted in (a).

Returning to fig. 4.3(c), it can be seen that, at potentials > 0.45V, ie around the onset of oxidation of the lead layer and the production of acetate (see fig. 4.5), a relatively

sharp peak appears at ca. 3680 cm^{-1} and grows in intensity up to 0.95V, after which it decreases, see figs. 4.5 and 4.7(a) and (b). Intriguingly, if the IR response of acetate oxidation on Pt alone with no lead is studied, then a similar peak is seen at 3680 cm^{-1} but referenced to the spectrum at -0.85 V, this peak is now a *loss* feature (see fig. 4.8), and a similar loss feature is observed for the oxidation of ethanol on Pt without Pb present (see figs. 4.9 and 4.10; fig. 4.9 is taken from the earlier work in 0.1 M KOH [19] and fig. 4.10 shows a repeat of the experiment in fig. 4.9 except using 0.25 M KOH). The presence of this sharp band at such a high frequency was ascribed in Chapter 3 to the presence of 'isolated' Pt-OH species, isolated in the sense that they are not part of any extended H-bonded structure. This is well established as an idea in the literature: in the limit, as hydrogen bonding is reduced, one would expect a narrow high-frequency band to reflect an O-H stretch free from hydrogen-bonding [26], and this concept has found application in the study of the IR absorptions of the water of hydration and O-H stretches in ionic crystals [27]. Certain ionic crystals have OH^- ions essentially free from hydrogen bonding, and frequencies as high as 3700 cm^{-1} have been observed, e.g. $Mg(OH)_2$ [28].

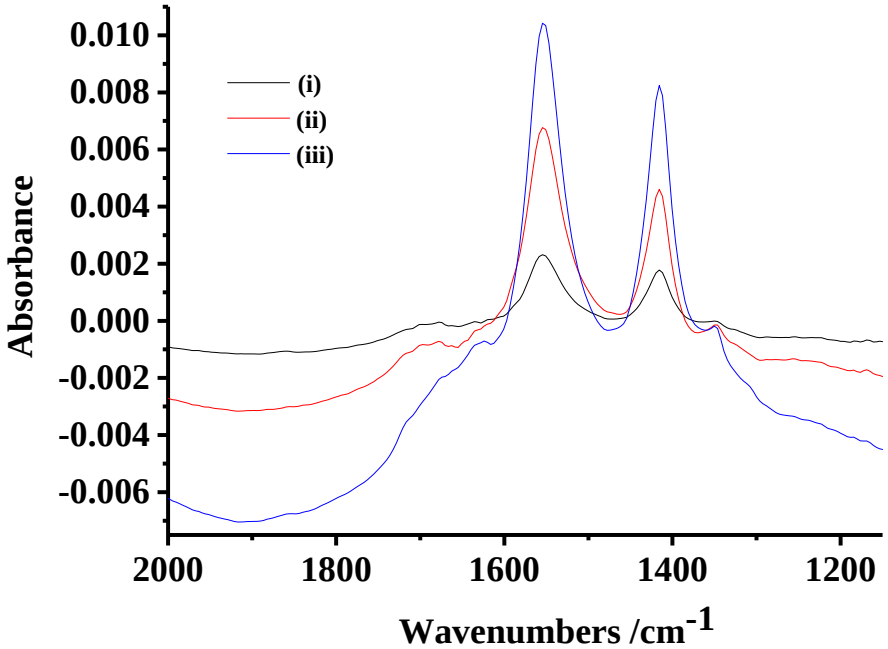

Figure 4.6. The spectra collected at 0.55V to 0.85V in fig. 4.3 after subtracting the underlying carbonate absorption at 1395 cm^{-1}. The spectrum collected at 0.45V was multiplied by 1.58, 2.18 and 2 and the resulting spectra subtracted from those collected at (i) 0.65V, (ii) 0.75V and (iii) 0.85V, respectively.

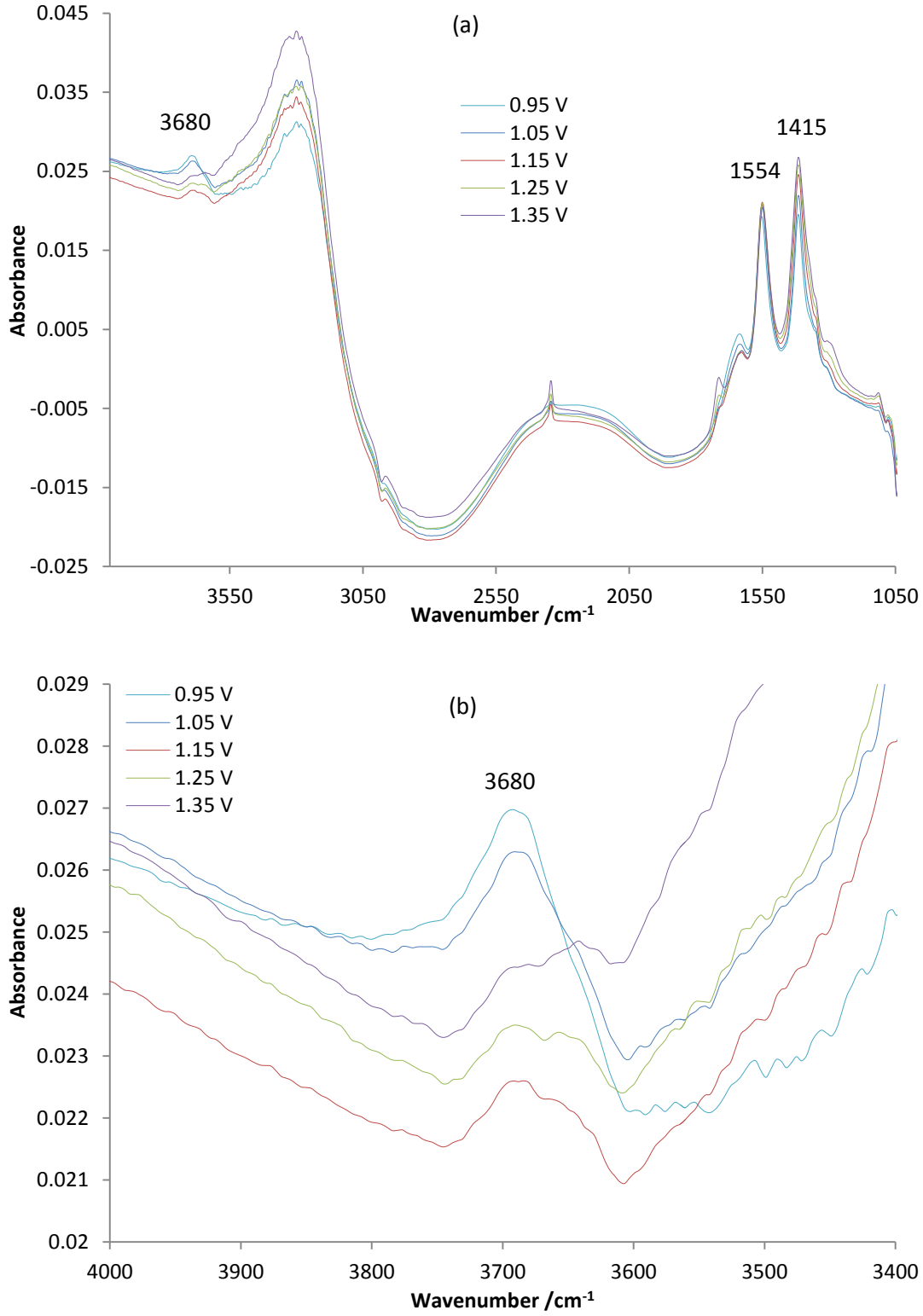

Figure 4.7. The spectra collected from 0 to 0.4 V in the experiment depicted in fig. 4.2 over (a) the full spectral range and (b) showing the Pt-OH spectral region.

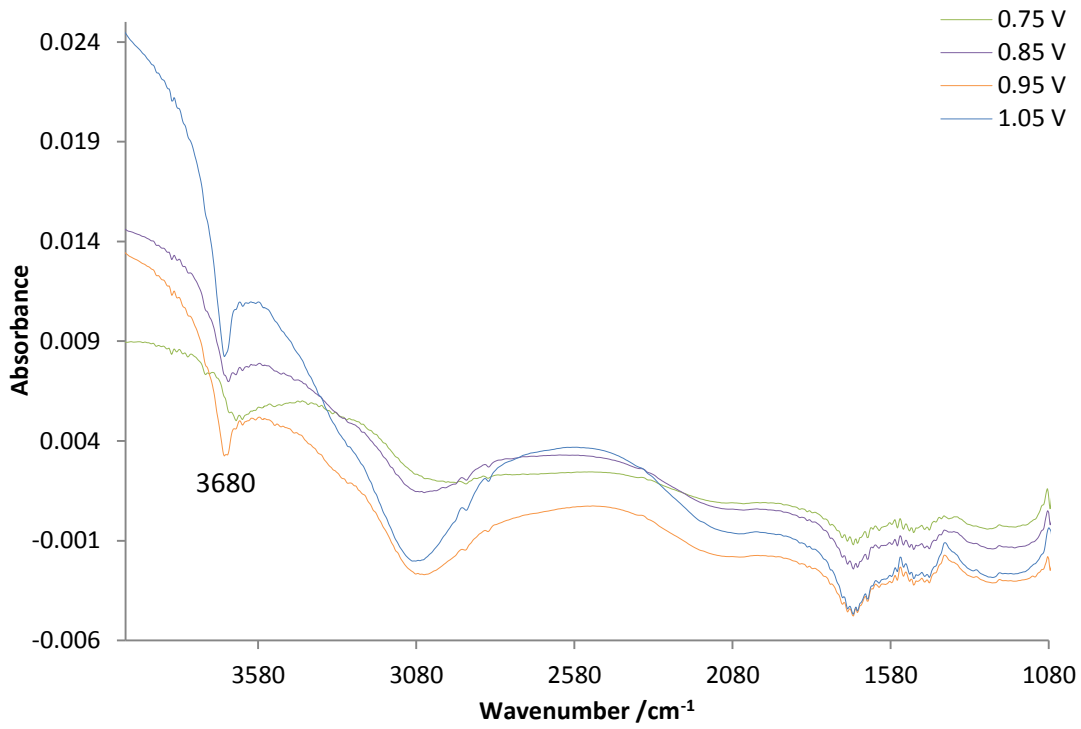

Figure 4.8. Spectra (100 co-added and averaged scans at 8 cm^{-1} resolution, ca. 35 s per scanset) collected at (i) 0.75V, (ii) 0.85V, (iii) 0.95V and (iv) 1.05V from a polycrystalline Pt electrode immersed in 0.25M KOH and 0.5M sodium acetate during an experiment in which the potential was held at 0.1V, the reference spectrum collected, a second spectrum taken at the same potential, and then the potential stepped to 0.15V, and increased in 100 mV increments, with further spectra collected at each step.

Physically, 'isolated' O-H, ie adsorbed OH species without extensive hydrogen bonding to water molecules, could arise if, for example, they formed in small islands or domains, or were in some other way 'protected' from H-bonding. Given that acetate adsorbs extensively at lower potentials on Pt in the presence of both ethanol and acetate ions in solution, and that O-O adsorbed acetate will present a relatively hydrophobic outer Helmholtz layer, this high frequency OH stretch may be tentatively ascribed to adsorbed OH occupying single sites in regions where otherwise the dominant adsorbate is acetate itself. Some further support for this comes from the fact that the higher the concentration of KOH used as the supporting electrolyte, the larger this loss feature in the spectra derived from the Pt surfaces

without Pb present for both acetate and ethanol oxidation (compare figs. 4.9 and 4.10).

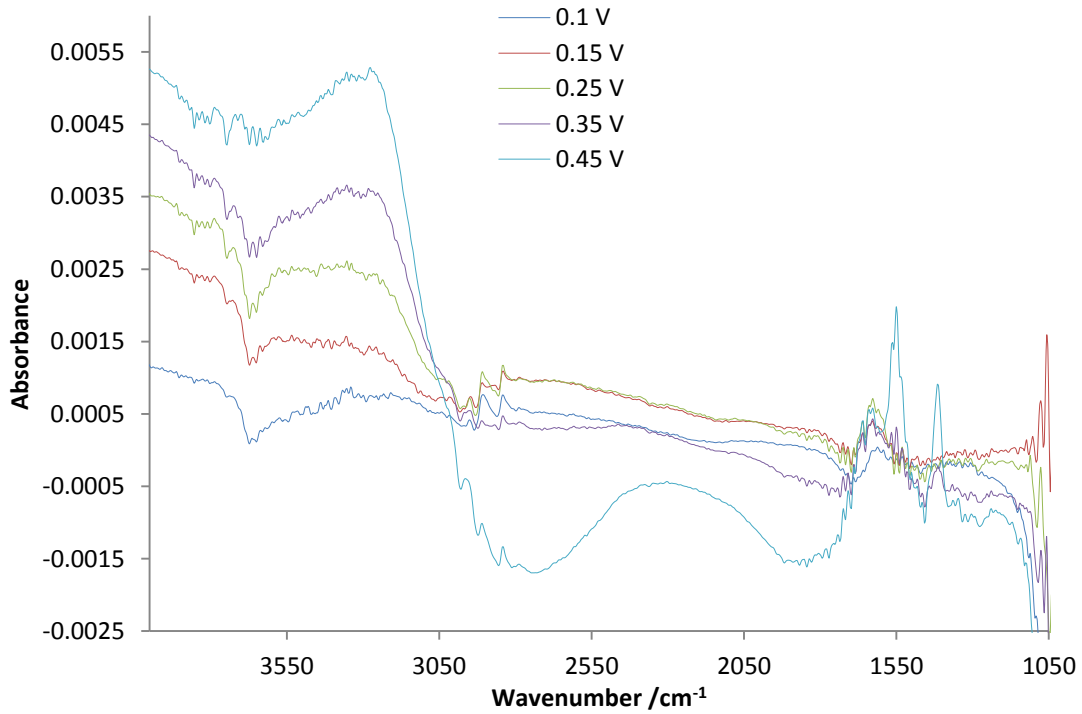

Figure 4.9. Spectra (100 co-added and averaged scans at 8 cm^{-1} resolution, ca. 35 s per scanset) collected at (i) 0.10V, (ii) 0.15V, (iii) 0.25V, (iv) 0.35V and (v) 0.45V from a polycrystalline Pt electrode immersed in 0.10M KOH and 1.0M ethanol during an experiment in which the potential was held at 0.1V, the reference spectrum collected, a second spectrum taken at the same potential, and then the potential stepped to 0.15V, and increased in 100 mV increments, with further spectra collected at each step.

However, the 3680 cm^{-1} feature is present as a *gain* when lead is present on the surface. Furthermore, this gain feature grows steadily with potential above the point at which the surface begins to lose Pb. If this band is due to OH associated with adsorbed acetate, then its behaviour is understandable: there is evidently very little adsorbed acetate on the Pb-covered surface, and only once the Pb starts to be removed does sufficient co-adsorption of acetate and OH take place.

This then raises a further point: if there is no adsorbed acetate, then conversion of ethanol to acetate at the surface is not taking place at lower potentials. Indeed, it is

evident that at low potentials the route taken by the ethanol during oxidation must be quite different from that observed on pure Pt surfaces. Support for this comes not only from the clear evidence for the formation of carbonate at astonishingly low potentials, but also the appearance of a bridged CO species, which was not seen on normal Pt. This bridged CO species vanishes at potentials lower than those associated with the oxidation of the adsorbed Pb, and there is no obvious correlation with the formation of carbonate.

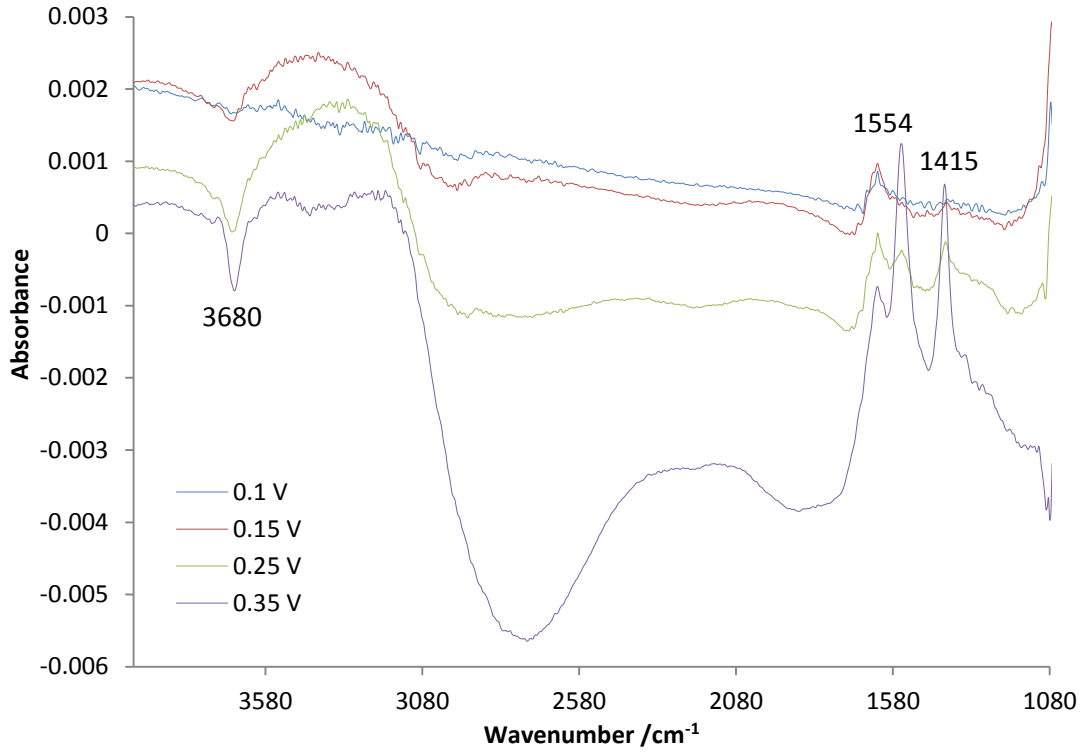

Figure 4.10. Repeat of the experiment in fig. 4.9, except the electrolyte was 0.25M KOH. (i) 0.10V, (ii) 0.15V, (iii) 0.25V and (iv) 0.35V. Current/time profile shown in fig. 2(ii).

We therefore have the following observations: (i) there is little adsorbed acetate on the Pt-Pb surface; (ii) the Pt-Pb surface has a high coverage of Pb at low potentials; (iii) the coverage of Pb on Pt begins to decrease above about 0.45 V; (iv) bridge-bonded CO forms at low potentials on Pt-Pb but disappears above 0.40 V; (v) carbonate is observed, even at the reference potential (0.1 V), as a product of the oxidation of ethanol on Pt.

To reconcile these observations, the Pt-Pb can be pictured with the structure discussed above: much of the surface is formed from well-ordered microcrystalline low-index surfaces (A), but with regions between them where the coverage of the lead is lower (B). Ethanol does not adsorb on lead itself, so oxidation of ethanol must take place by adsorption on those areas of the surface not covered with Pb. Adsorption must take place either through the O or C_1 atoms of the ethanol; the former would be the normal route on Pt in KOH, and it has been postulated (see [19] and section 3.3) that in the absence of solution ethanol, the adsorbed ethoxide can bond through the C_2 carbon giving rise to a cyclic intermediate for which C-C bond cleavage is reasonably facile. However, it is also possible that the small areas of exposed Pt between the Pb islands are appreciably more hydrophobic, and actually favour adsorption through C_1; cyclisation as postulated by He et al. could then take place as shown in scheme 4.1.

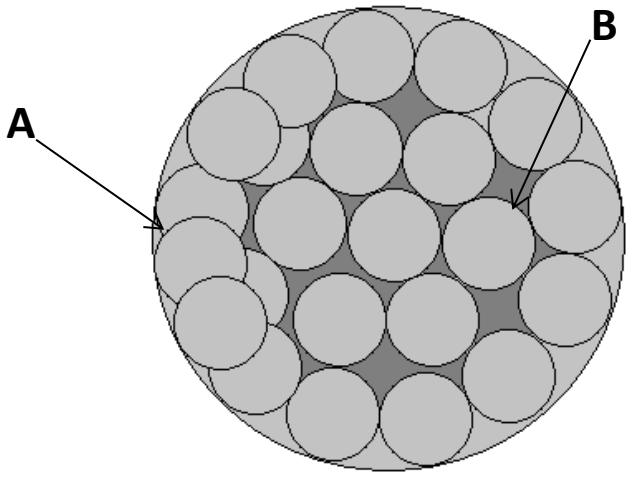

Scheme 4.3. Schematic representation of the proposed structure for the Pb-modified polycrystalline Pt electrode ((A) shows the well-ordered microcrystalline low-index surfaces and (b) the regions of lower Pb Coverage).

It is clear that ethanol is oxidised to carbonate even at 0.10V at the Pb-modified electrode; in fact, two spectra were recorded at 0.10V, one 2 minutes after the first, which clearly showed oxidation taking place even at this low potential, see fig. 4.11. This is a remarkable result, as the standard potential is close to 0 V. Interestingly, Lai and Koper [29] observed adsorbed CO at a Pt/roughened gold anode from

ethanol chemisorptions in alkaline solution at ca. 1960 cm^{-1} using SERS at potentials as low as 0.10V vs RHE; thus it appears that the surface of Pt can be engineered either physically (as Lai and Koper did) or chemically (as in this study) to allow the generation of adsorbed ethanol fragments at very low potentials. Whatever the details of the intermediate adsorbate, it is clear that the actual oxidation process is extremely facile once the ethanol is adsorbed, and this suggests the existence of some form of adsorbed OH at very low potentials. This is not an impossibility: Schmidt and co-workers [30] have reported that OH adsorption takes place in the H_{upd} region at Pt in alkaline solution, such that the coverage of these species cannot be determined by simple coulometry. In addition, this OH must be adsorbed on Pt and not on Pb; there is no evidence for the latter at these very low potentials. One possibility is that the OH is actually adsorbed on the Pt adjacent to adsorbed Pb sites, and the picture becomes one of Pb islands on the surface surrounded by OH_{ads} species (see scheme 4.4). Adsorbed ethanol forming next to such a site would be oxidised easily, and the site could continually recharge, permitting a catalytic cycle to develop.

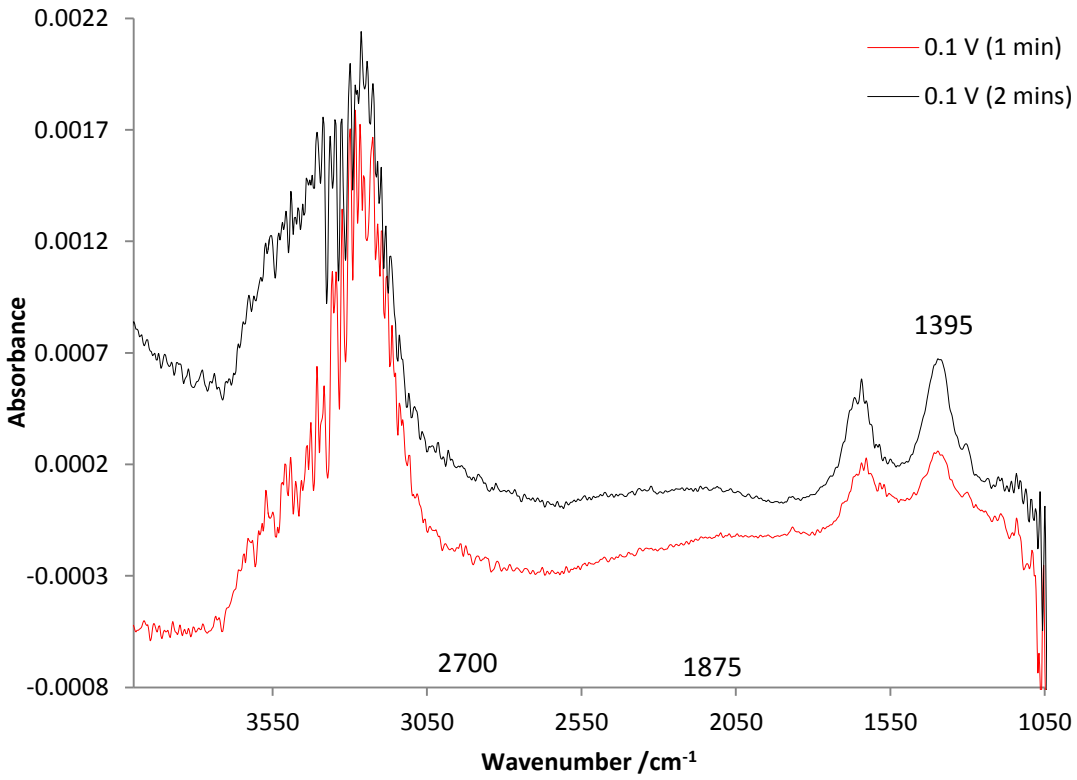

Figure 4.11. Spectra collected at 0.10 V vs. RHE after (i) 1 and (ii) 2 minutes during the experiment depicted in fig. 4.3.

At higher potentials, the Pb islands start to become oxidised, and also shrink as the Pb is lost to solution as $HPbO_2^-$. As the islands shrink, the Pt surface exposed becomes more and more similar to normal Pt, giving rise to a transition from carbonate to acetate formation. It would appear that only at the lowest potentials, with rather small regions of exposed Pt between Pb islands, is the behaviour such that carbonate is the main product.

Despite the fact that the current passed during the FTIR experiment using the Pb-modified electrode is higher (see figs. 4.1 & 4.3), significantly more acetate is produced using the unmodified electrode, (see figs. 4.5 and 4.12), supporting the observation of appreciable carbonate as an additional product in the former experiment. It can be seen from fig. 4.5 that the intensity of the 1554 cm^{-1} acetate band in the absence of Pb is ca. 2.5x that in its presence, in approximate agreement with the threefold increase in charge required to produce carbonate over acetate.

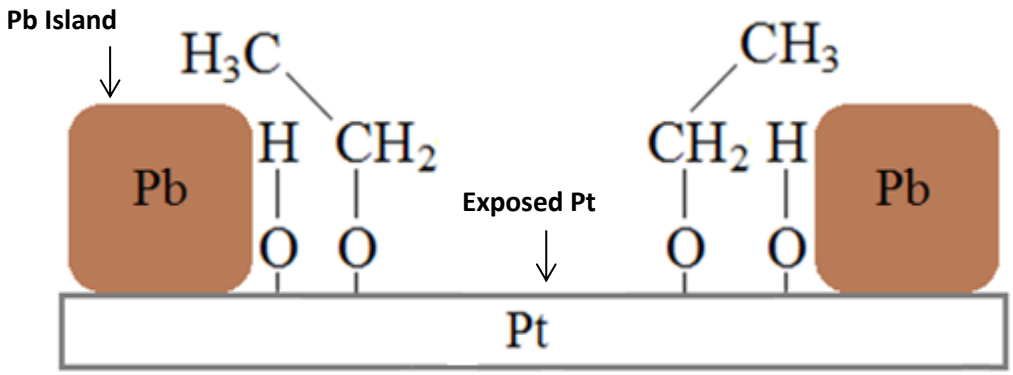

Scheme 4.4. The proposed mechanism for the formation of OH_{ads} on the Pt adjacent to adsorbed Pb islands, thus facilitating complete oxidation of EtOH which is adsorbed next to such sites.

In order to investigate whether the mechanism discussed above depends upon the presence of ethanol in solution (as in the absence of Pb(IV), see figs. 3.16, 3.17(a) and 3.17(b)), an experiment was carried out in which Pb(IV) was pre-deposited at the Pt surface as in the experiment depicted in fig.4.3(a), and then 1 M ethanol +

0.25 M KOH was admitted into the IR cell containing 0.25 M KOH at 0.1 V and the potential held for 30 minutes. The electrolyte was then replaced by 0.25 M KOH (still holding the potential at 0.1 V), reducing the ethanol concentration in solution to $< 10^{-7}$ M. The electrode was then pushed against the prismatic cell window and the FTIR instrument flushed with nitrogen for 60 minutes; a reference spectrum was collected after which the potential of the Pt electrode was stepped up, further spectra taken and normalised to the reference spectrum according to the manipulation in equation (2.11).

Figure 4.12. Comparison of the spectra collected at 0.75 V during the experiments depicted in figs. 4.3 and 4.9, over the spectral range from 1740-1280 cm^{-1}.

Figure 4.13 shows the spectra collected from 0.1 to 0.55 V. From the figure, it may be seen that a gain feature at ca. 1365 cm^{-1} was observed with an onset of 0.15 V. This feature was tracked by loss features at ca. 2960, 2913 and 2840 cm^{-1}, which, following my studies on ethanol oxidation at unmodified Pt (see section 3.2) and the work by Iwasita and Pastor [31][32], may be assigned to the loss of adsorbed ethoxy ($Pt\text{-}OC_2H_5$).

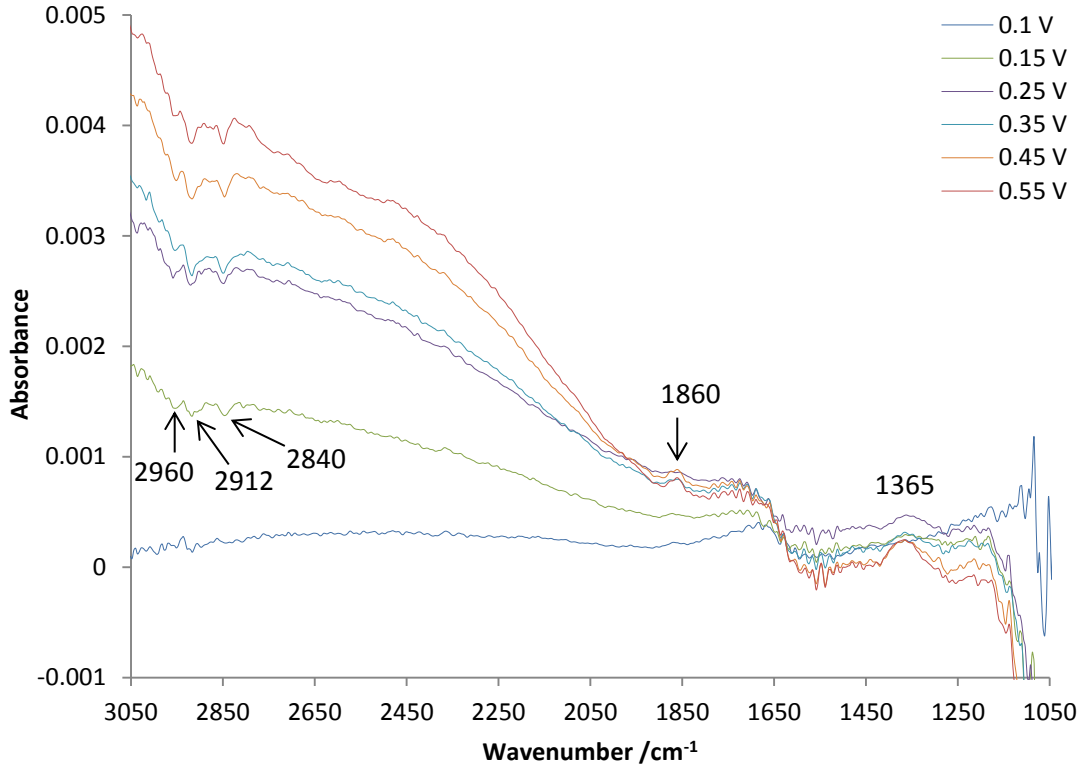

Figure 4.13. Spectra collected from 0.1 to 0.55 V vs. MMO during an experiment in which Pb(IV) was pre-deposited at the Pt electrode from 1 mM Pb(IV) acetate + 0.25 M KOH at 0.1 V vs. RHE, after which ethanol (1 M ethanol in 0.25 M KOH) was chemisorbed at 0.1 V and the solution replaced with 0.25 M KOH. The potential was stepped up to 1.35 V and spectra collected at each step.

During an analogous experiment carried out in the absence of Pb(IV), the loss of adsorbed ethoxy was tracked by a gain of solution carbonate, as indicated by a strong gain feature at ca. 1395 cm^{-1} (see fig. 3.17(b)). In addition, as presented in this chapter, formation of solution carbonate was observed at potentials as low as 0.1 V during the experiment carried out in the presence of pre-adsorbed Pb(IV) and competing EtOH in solution (see fig. 4.3(a)). However, no solution CO_3^{2-} was observed at potentials below 0.65 V in the presence of pre-adsorbed Pb and in the absence of competing EtOH in solution, as may be seen more clearly from fig. 4.14, which shows the spectra collected at 0.1 V and 0.55 V during the experiment depicted in fig. 4.13 enlarged over the spectral range from 2000-1150 cm^{-1}.

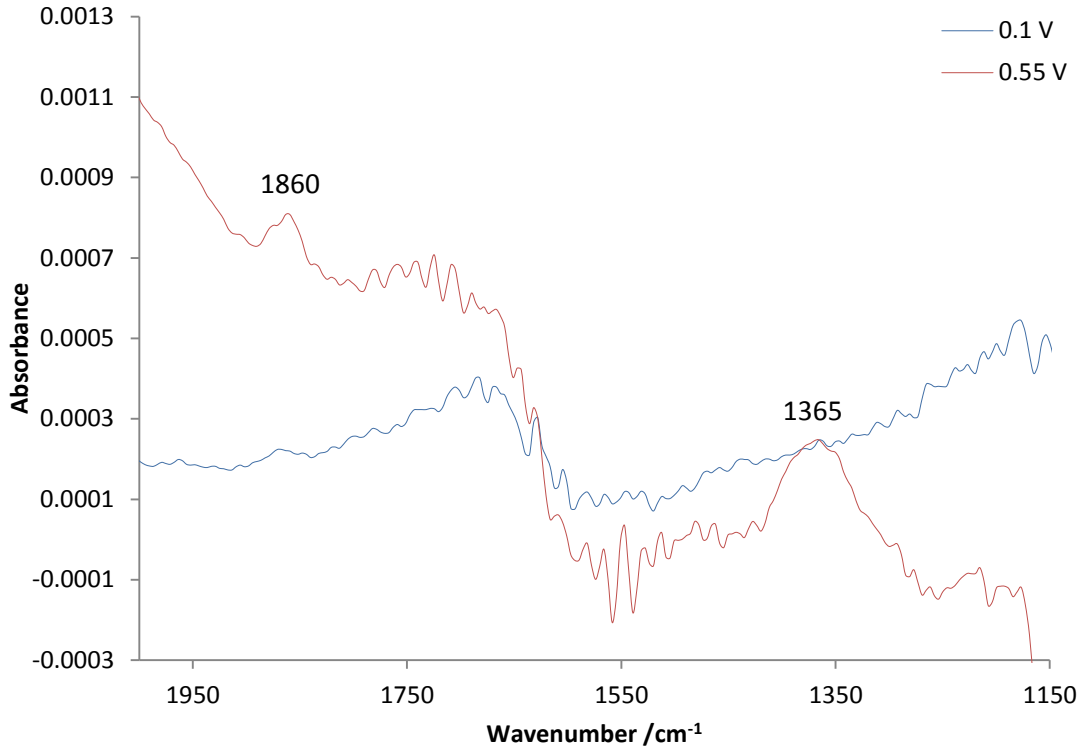

Figure. 4.14. Spectra collected at 0.1 V and 0.55 V during the experiment depicted in fig. 4.14 over the spectral range from 2000 – 1150 cm^{-1}.

The features at ca. 1860 and 1365 cm^{-1} may also be seen more clearly in fig. 4.14. With respect to the 1365 cm^{-1} feature, it is generally accepted [33-37] that a feature in the region of 1370-1300 cm^{-1} is characteristic of the asymmetric C-O stretch of adsorbed unidentate carbonate. Further, a feature between 1860-1850 cm^{-1} has been assigned by several authors [38-44] to bridge-bonded CO_{ads} at Pt. Hence, the bands at 1860 and 1365 cm^{-1} are tentatively assigned, respectively, to the formation of bridge-bonded CO and adsorbed unidentate carbonate. Therefore, it would appear that under conditions of ethanol starvation, C-C bond cleavage at Pb modified Pt is still facile but is not enhanced with respect to the reaction at PtPb when solution ethanol is present. Concerning the latter, it has been postulated previously that the reaction takes place at Pt domains in between Pb islands, where adsorbed ethanol can be oxidised easily, and the site is continually recharged, permitting a catalytic cycle to develop. Based on this, it is not surprising that under conditions of ethanol starvation, significantly less carbonate is produced. In fact, at lower potentials, only adsorbed carbonate is observed, and it is possible that in the absence of competing

ethanol in solution, carbonate is not displaced from the Pt surface once it is formed (and the site is not recharged), as indicated by the feature at 1365 cm^{-1} in fig. 4.13.

Figure 4.15 shows the intensities of the features in fig. 4.13 plotted as a function of potential, from which it may be seen clearly that the loss of ethoxy species is tracked by the gain feature at 1365 cm^{-1} due to adsorbed carbonate. However, the feature at 1860 cm^{-1}, due to CO_{ads}, is present at the reference potential and does not track the ethoxy features as strongly as the feature at 1365 cm^{-1}. It is therefore unclear whether the role of CO_{ads} during the experiment depicted in fig. 4.13 is, in agreement with Lai and Koper's [29] study of EtOH oxidation at Pt single crystals in 0.1 M NaOH, as an intermediate in the oxidation of ethanol to CO_3^{2-}, or conversely, as suggested by Lopez-Atalaya [45] (see section 3.2) during their study of ethanol oxidation at Pt(111) in aqueous NaOH, as a poisoning species at the Pt surface.

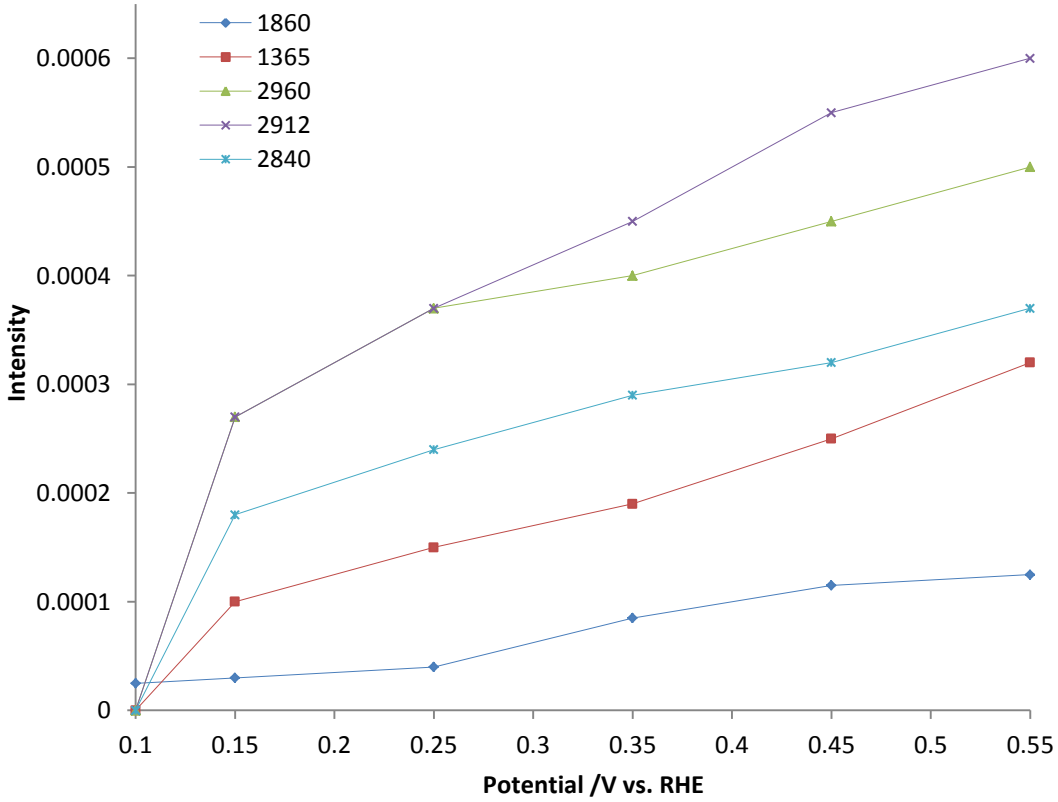

Figure 4.15. Plots of the ethoxy (2960, 2912 and 2840 cm^{-1}), bridge-bonded CO (1860 cm^{-1}) and unidentate carbonate (1365 cm^{-1}) band intensities as a function of potential vs. MMO during the experiment depicted in fig. 4.14.

Figure 4.16 shows the spectra collected from 0.65 to 1.35 V during the experiment in fig. 4.13. As may be seen from the figure, at potentials > 0.55 V, a peak at ca.1395 cm^{-1}, which may be unambiguously attributed to solution CO_3^2, grows under the feature at 1365 cm^{-1}. As discussed previously, at higher potentials, the Pb islands start to become oxidised, and also shrink as the Pb is lost to solution as $HPbO_2^-$. As the islands shrink, the Pt surface exposed becomes more and more similar to normal Pt, giving rise to a transition from carbonate to acetate formation under conditions of ethanol excess. The observations from figs. 4.16(a) and (b) suggest that similar behaviour is observed under conditions of ethanol starvation, giving rise to a transition from adsorbed carbonate to solution CO_3^{2-}, the latter being observed in an analogous experiment at normal Pt (see fig. 3.17(b)). Thus, in contrast to EtOH oxidation at Pt in alkaline solution, there appears to be no benefit from removing solution ethanol during oxidation at PtPb. In fact, significantly more carbonate is observed under conditions of ethanol excess, where a catalytic cycle develops at Pt domains and ethanol is continuously oxidised at 'recharged' sites.

4.3. Conclusions

This chapter presents a study of the oxidation of ethanol at a Pb-modified, polycrystalline Pt anode in 0.25M KOH. Very surprisingly, significant carbonate formation was observed at very low potentials (ie. 0.10V vs RHE); in order to explain these data, a model has been postulated, the essence of which is that carbonate formation takes place at atypical Pt domains between Pb islands. As the Pb is stripped from the surface, the Pt domains become increasingly similar to 'normal' Pt, resulting in increasing acetate formation. If this model is correct, the extent of catalysis is restricted, since only at the particular edges of Pb islands will appropriate conditions exist for oxidation. If this catalysis is to be developed, it will be essential to fabricate a surface in which the formation of Pb islands is carefully controlled so as to leave exposed Pt in regions large enough to act as efficient catalytic centres, but sufficiently small that the highly unusual properties seen in the results presented above can be retained.

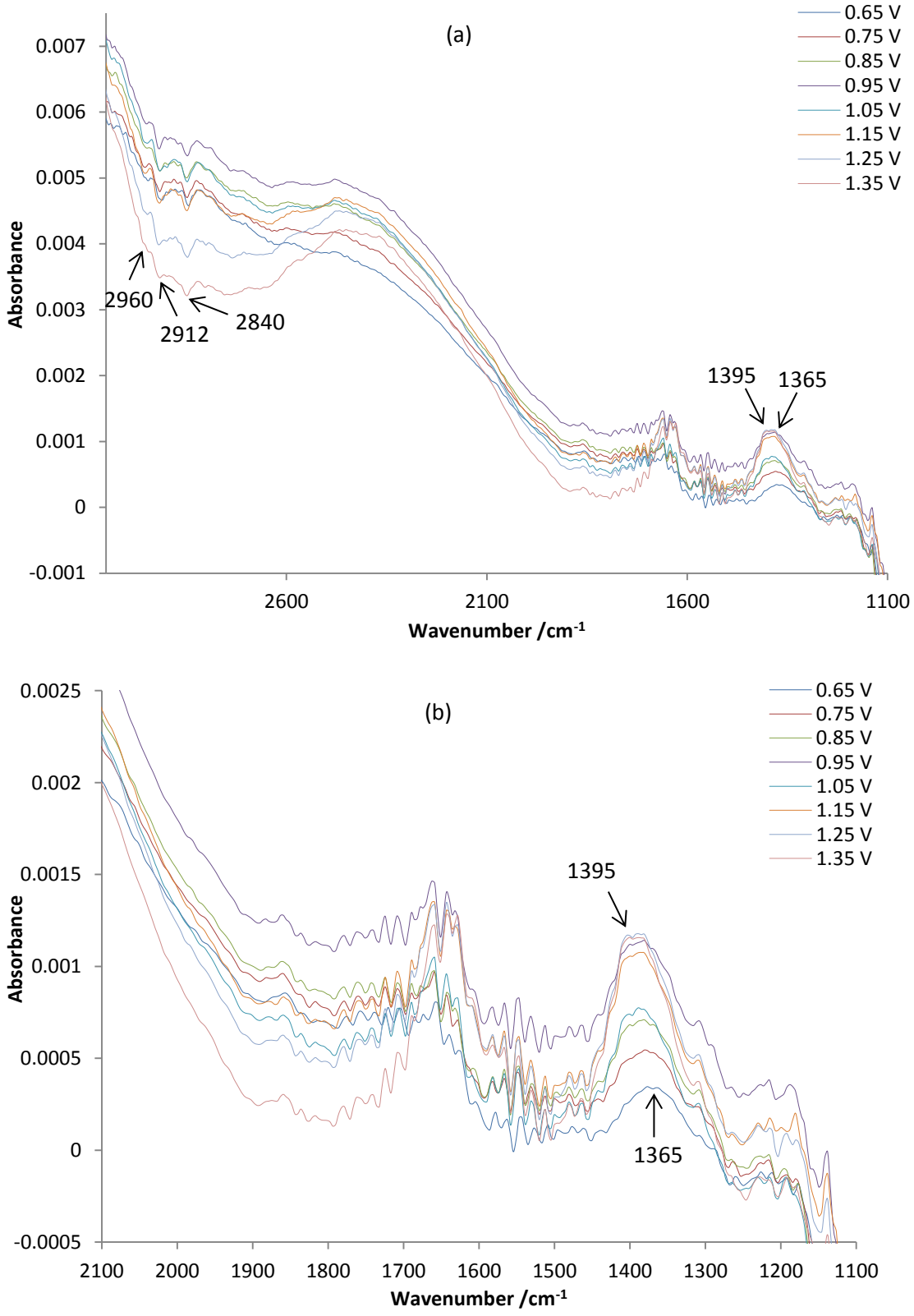

Figure 4.16. Spectra collected from 0.65 to 1.35 V during the experiment depicted in fig. 4.13 (a) over the full spectral range and (b) from 2100-1100 cm^{-1}.

4.4. References

1. Cremers, C.; Bayer, D.; Kintzel, B.; Joos, M.; Krausa, M.; Martin, D., *ECS Trans*., 2009, 17, 517-524.
2. Bayer, D.; Berenger, S.; Joos, M.; Cremers, C. and Tűbke, J., *International Journal of Hydrogen Energy*, 2010, 35, 12660-12667.
3. Shen, S. Y.; Zhao, T. S.; Xu, J. B. and Li, Y. S., *Journal of Power Sources*, 2010, 195, 1001-1006.
4. Li, M.; Zhou, W. –P.; Marinkovic, N. S.; Sasaki, K. and Adzic, R. R., *Electrochimica Acta*, 2013, 104, 456 – 461.
5. Shen, S. Y.; Zhao, T. S. and Xu, J. B., *Electrochim*ica *Acta*, 2010, 55, 9179 - 9184.
6. Tripković, A. V.; Popović, K. Dj. and Lović, J. D., *Electrochimica Acta*, 2001, 46, 3163 - 3173.
7. Cui, G.; Song, S.; Shen, P. K.; Kowal, A. and Bianchini, C., *Journal of Physical Chemistry C*, 2009, 113, 15639 – 15642.
8. He, Q.; Shyam, B.; Macounova, K.; Krtil, P.; Ramaker, D. and Mukerjee, S., *Journal of the American Chemical Society*, 2012, 134, 8655 – 8661.
9. Morin, M. –C.; Lamy, C.; Leger J.-M.; Vasquez, J.-L. Aldaz, A. *Journal of Electroanalytical Chemistry*, 1990, *283*(1-2), 287 – 302
10. Lucas, C. A.; Marković, N. M.; Grgur, B. N. and Ross, P. N., *Surface Science*, 2000, 448, 65 – 76.
11. Lucas, C. A.; Marković, N. M. and Ross, P. N., *Surface Science*, 2000, 448, 77 – 86
12. Clavilier, J.; Orts, J. M.; Feliu, J. M. and Aldaz, A., *Journal of Electroanalytical Chemistry*, 1993, 293, 197 – 208
13. Carr, J. P. and Hampson, N. A., *Chemistry Reviews*, 1972, 72, 679 – 703.
14. Feliu, J. M.; Fernandex-Vega, A.; Orts, J. M. and Aldaz, A., *J. Chim Phys.*, 1991, 88, 1493 – 1518
15. Berke, A.; Dvořák, V.; Němec, I. and Zýka, J., *Journal of Electroanalytical Chemistry*, 1962, 4, 150 – 155.
16. Grgur, B. N.; Marković, N. M. and Ross, P. N. Jr., *Langmuir* 1997, 13, 6370 – 6374.

17. Christensen, P. A. and Linares-Moya, D., *Journal of Physical Chemistry C*, 2009, 114, 1094−1101.
18. Christensen, P. A.; Hamnett, A. and Linares-Moya, D., *Physical Chemistry Chemical Physics*, 2011, 13, 11739−11747.
19. Christensen, P. A.; Jones, S. W. M. and Hamnett, A., *Journal of Physical Chemistry C*, 2012, 116, 24681−24689.
20. Zhou, Z-Y.; Wang, Q.; Lin, J-L.; Tian, N. and Sun, S-G., *Electrochimica Acta*, 2010, 55, 7995 – 7999.
21. Morallón, E.; Vázquez, J. L.; Pérez, J. M. and Aldaz, A., *Journal of Electroanalytical Chemistry*, 1995, 380, 47 – 53.
22. Iwasita, T.; Rodes, A. and Pastor, E., *Journal of Electroanalytical Chemistry*, 1995, 383, 181 – 189.
23. Iwasita, T.; Nart, F. C.; Rodes, A.; Pastor, E. and Weber, M., *Electrochimica Acta*, 1995, 40, 53-59.
24. Lai, S. C. S.; Kleijn, S. E. F.; Fatma, T. Z.; Öztürk, F. T. Z.; van Rees Vellinga, V. C.; Koning, J.; Rodriguez, P.; Koper, M. T. M., *Catalysis Today*., 2010, 154, 92-104.
25. Casado-Rivera, E.; Volpe, D. J.; Alden, L.; Lind, C.; Downie, C.; Vázquez-Alvarez,T.; Angelo, A. C. D.; DiSalvo, F. J. and Abruña, H., *Journal of the American Chemical Society*, 2004, 126, 4043 – 4049.
26. Dreesen, L.; Humbert, C.; Hollander, P.; Mani, A. A.; Ataka, K.; Thiry, P. A. and Peremans, A., *Chemical Physics Letters*, 2001, 333, 327 - 331.
27. Lutz, H. *Bonding and structure of water molecules in solid hydrates. Correlation of spectroscopic and structural data. In Solid Materials*; Springer Berlin / Heidelberg, 1988; Vol. 69; pp 97.
28. Stanek, T. and Pytasz, G., *Acta Physica Polonica* 1977, *A52*, 119.
29. Lai, S. C. S and Koper, M. T. M., *Physical Chemistry Chemical Physics*, 2009, 11, 10446 – 10456
30. Schmidt, T. J.; Ross, P. N. and Marković, N. M., *Journal of Physical Chemistry B*, 2001, 105, 12082 – 12086.
31. Iwasita, T. and Pastor, E., *Electrochimica Acta*. 1994, *39* (4), 531-537.
32. Iwasita, T.; Dalbeck, R.; Pastor, E.; Xia, X. *Electrochimica Acta*, 1994, *39* (11-12), 1817-1823.

33. Fottinger, K.; Schlogl, R.; Rupprechter, G., *Chemistry Communications*, 2008, 320-322
34. Chernyshova, I. V.; Ponnurangam, S.; Somasundaran, P., *Physical Chemistry Chemical Physics*, 2013, 15, 6953-6964
35. Amonette, A. E.; Rai, D., *Clays and Clay Minerals*, 1990, 38(2), 129-136
36. Bollinger, M. A.; Vannice, M. A.; *Applied Catalysis B: Environmental 8.*, 1996, 417-443
37. Davydof, A. A. and Rochester, C. H. (editors), *Infrared Spectroscopy on the Surface of Transition Metal Oxides*, Wiley, Chichester, 1984.
38. Yoshida, H.; Narisawa, S.; Fujita, S.; Ruixia, L.; Arai, M., *Physical Chemistry Chemical Physics*., 2012, 14, 4724–4733.
39. Ruiz-Martinez, J.; Rodriguez-Reinoso, F.; Sepulvida-Escribano, A.; Anderson, J. A., *Physical Chemistry Chemical Physics*, 2009, 11, 917-920.
40. Rodriguez, J. A.; Truong, C. M.; Goodman, D. W., *Journal of Chemical Physics*, 1992, 96(10), 7814-7825
41. Smith, G. W. and Carter, E. A., *Journal of Physical Chemistry*, 1991, 95, 2327-2339
42. Steininger, H.; Lehwald, S.; Ibach, H., *Surface Science*., 1982, 123, 264.
43. Meiher, W. D.; Whitman, L. J.; Ho, W. J.; *Journal of Chemical Physics*, 1989, 91, 3228
44. Kasza, R. V.; Shapter, J. G., Griffiths, K.; Norton, P. R.; Sloan, J. J., *Surface Science*, 1994, 321, L239-L243
45. Lopez-Atalaya, M.; Morallon, E.; Cases, F.; Vazquez, J. L.; Perez, J. M., *Journal of Power Sources.*, 1994, 52(1), 109-117.

5. An *in-situ* FTIR Study on the Effect of Temperature on the Oxidation of Ethanol at Polycrystalline Pt in Alkaline Solution

5.1. Introduction

5.1.1. Overview

The electrochemical oxidation of ethanol at a polycrystalline Pt electrode was studied using in-situ Fourier Transform InfraRed (FTIR) spectroscopy in 0.1M KOH at 25 °C and 50 °C. It was found that the equilibrium between Pt and reversibly-adsorbed OH shifts to favour the latter at 50 °C compared to 25 °C, and this was reflected in the higher oxidation currents observed in the voltammetry, as well as increased production of acetate in the FTIR spectra. Acetate is the only product observed at lower potentials. Above the transition potential, where at least some of the areas of the thin layer in the spectro-electrochemical cell become acidic, acetaldehyde, acetic acid and a small amount of CO_2 are produced. This transition potential depends strongly on temperature: -0.1V at 25 °C and -0.4V at 50 °C. The temperature dependence of the production of acetaldehyde and acetic acid strongly suggests that the rate determining step is the removal of the first proton from the initially-adsorbed ethoxide species, and it is tentatively suggested that this is also the rate determining step under alkaline conditions.

Chapter 3 reported *in-situ* FTIR studies on the electro-oxidation of ethanol at polycrystalline Pt in 0.1M KOH and concluded that the mechanism of ethanol oxidation was as depicted in Scheme 5.1. Thus, initial adsorption of ethanol gives the adsorbed ethoxy intermediate (I). Oxidation of this by adsorbed OH [1] generates (II) and further oxidation by OH_{ads} yields monodentate acetate (III). The presence of ethanol in solution and hence ethanol adsorption replaces (II) at the surface, releasing acetaldehyde; similarly, displacement of (III) releases acetate, which is the predominant product.

Under conditions of ethanol starvation, the bidentate adsorbate (IV) is formed which can undergo further oxidation to give carbonate. The bands attributed to (I) to (IV) are summarized in table 5.1. The work reported in this chapter is an extension of the ethanol studies reported in chapter 3 by considering the effect of temperature, and provides supporting evidence for the model outlined in scheme 1.

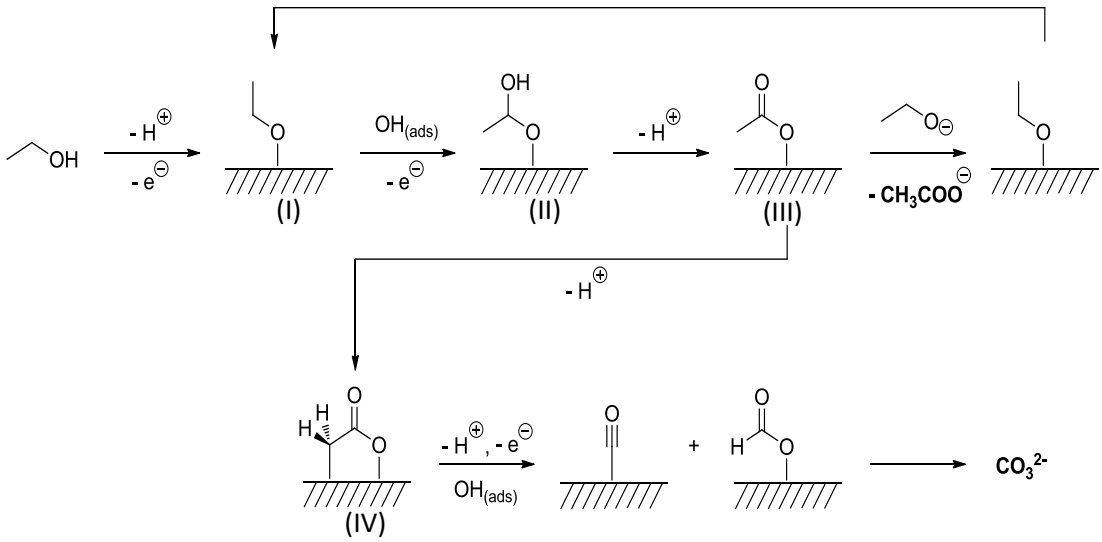

Scheme 5.1. The mechanism of ethanol oxidation at polycrystalline Pt in alkaline solution proposed in chapter 3.

Band /cm^{-1}	**Assignment**
2985, 2913, 2846	C-H stretches of adsorbed ethoxy (I)
1573	ν_s adsorbed unidentate acetate, Pt_s-O-C(=O)CH_3 (III)
1475	C-H deformation of adsorbed unidentate acetate, Pt_s-O-C(=O)CH_3 (III)
1554	ν_{as} solution acetate
1415/1418	ν_s solution acetate
1540	Uncoordinated C=O stretch of bidentate adsorbed carbonate or C=O stretch of Pt_s-CH_2COOPt (IV)
1274	Pt_s-CH(OH)CH_3 (II)

Table 5.1. The assignment of the various features attributed to adsorbed C and O containing species, and bands due to solution acetate. See chapter 3 and references therein.

5.1.2. Ethanol oxidation as a function of temperature in acid solution

Only a few studies were found in the literature concerning the electro-oxidation of ethanol at Pt in alkaline media as a function of temperature [2-6] and, to my knowledge, no studies have been published which report the application *in-situ* FTIR spectroscopy. In light of this, and the drop in pH observed at higher potentials during the experiments reported in chapter 3, it seems reasonable to discuss some of work published on ethanol oxidation as a function of temperature in acid solution. Thus, Behm *et al* [7] investigated the kinetics of the ethanol oxidation reaction over the temperature range from 30 to 60 ^{o}C on a carbon-supported Pt nanoparticle catalyst using cyclic voltammetry and potential-step measurements in conjunction with mass spectroscopy via Differential Electrochemical Mass Spectroscopy (DEMS) (see [7] and references therein). Figure 5.1(a) shows the CVs collected by during oxidation of 0.01 M EtOH in 0.5 M H_2SO_4 at atmospheric pressure. From the figure, it may be seen that the Faradic current for EtOH oxidation increased 4-fold upon increasing the temperature from 30 ^{o}C (dotted line) to 60 ^{o}C (solid line). In order to quantify the distribution of ethanol oxidation products at different temperatures, the authors integrated the Faradaic current (see fig. 5.1(a)) and ion currents for CO_2, acetaldehyde and acetic acid (see figs. 5.1(b)-(d)) over a complete cycle (0.06 to 1.16 V vs. RHE). Thus, upon increasing the temperature from 30 to 60 ^{o}C, the authors calculated a decrease in current efficiency from 8% to 5% for CO_2 and from 66% to 60% for acetic acid production. However, the current efficiency for acetaldehyde formation was calculated to have increased from 26% to 35% upon heating. Consequently, Behm *et al* postulated that for temperatures < 60 ^{o}C, the current efficiency for complete oxidation of ethanol to CO_2 decreases slightly due to a greater increase in acetaldehyde formation with increasing temperature.

In work presented in an open access journal, Wang *et al* [6] studied the electro-oxidation of 0.25 M ethanol in a weak acidic medium at Pt decorated with a Nd-Fe-Mo hybrid-metallic cyano-bridged coordination polymer. From their results, the authors proposed a reaction mechanism in which acetaldehyde was generated via the diffusion-controlled dehydrogenation of ethanol at Pt-$(CO_B)_{ads}$ induced reaction points. The cyclic voltammetry data presented by the authors showed that the peak current of the wave attributed to diffusion-controlled acetaldehyde formation increased upon raising the temperature from 25-75 ^{o}C. In addition, the wave was

observed to move to more positive potentials at higher temperature. However, it should be noted that although an increase in acetaldehyde production from ethanol oxidation at elevated temperatures agrees with the findings by Behm *et al* in acid solution, the diffusion-controlled mechanism proposed by Wang *et al* should be treated with caution as no molecular analysis was presented in their study to confirm the electrode morphologies/compositions they claim to have employed.

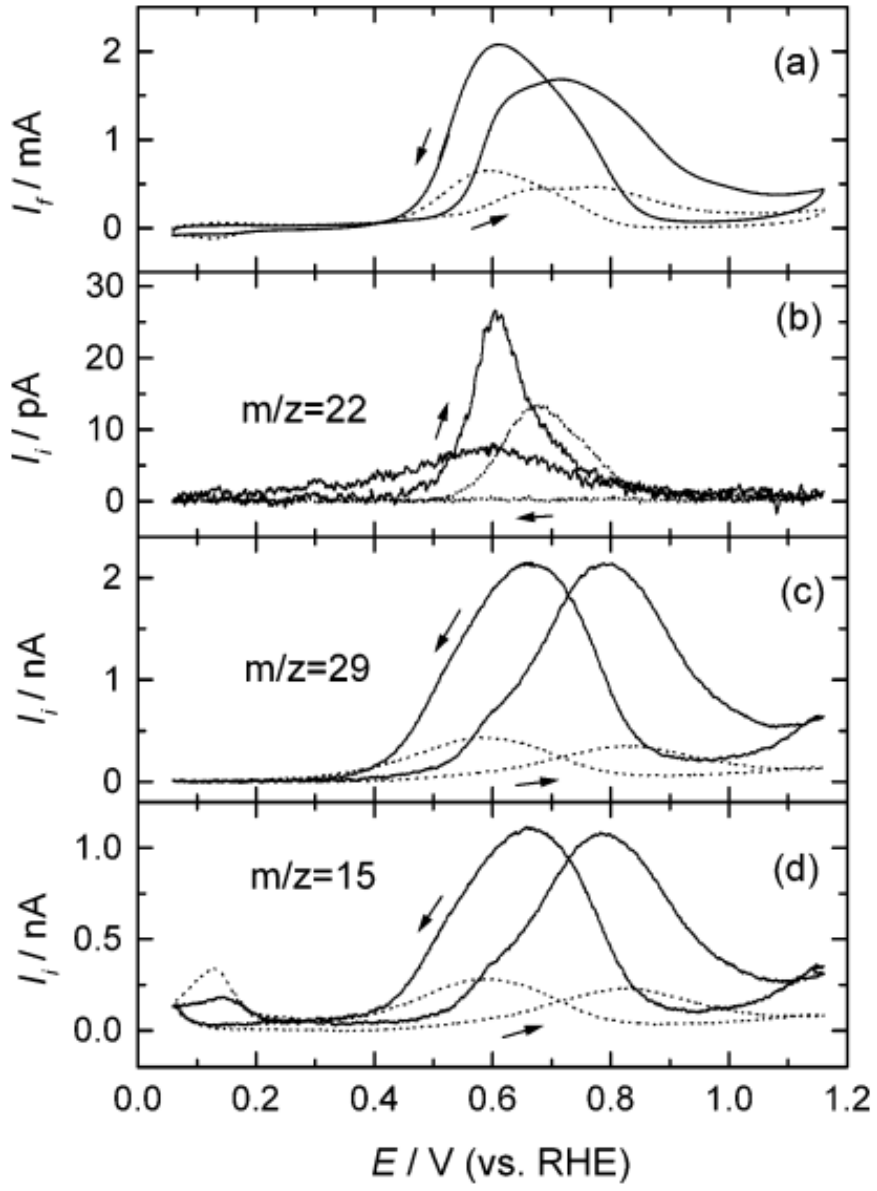

Figure 5.1. Simultaneously recorded (a) CVs and Mass Spectrometric Cyclic Voltammograms (MSCVs) for (b) m/z = 22, (c) m/z = 29 and (d) m/z = 15, collected by Behm et al [7] during oxidation of 0.01M EtOH at Pt/C in 0.5M H_2SO_4.

5.1.2 Ethanol oxidation as a function of temperature in alkaline solution

Figure 5.2 shows the linear sweep voltammograms (LSVs) collected by Dutta and Datta [2] during their study of 1 M ethanol electro-oxidation at Pt/C and PtPd/C in 0.5 M NaOH from 20-80 ^{o}C. From the figure, and in contrast to our work on ethanol oxidation at polycrystalline Pt at room temperature (see section 3.2), Dutta and Datta [2] suggest that at Pt/C at low temperature, significant carbonate formation occurs via dissociative adsorption of ethanol. In addition, the authors observed considerably larger currents when using the PtPd catalyst as opposed to Pt. However, fig. 5.2 clearly shows that ethanol oxidation at Pt/C exhibits a greater proportional increase in current from 20 to 80 ^{o}C than at PtPd/C, although at significantly lower current values. Hence, paying attention specifically to the results presented in this chapter, which focus on ethanol oxidation at unloaded, polycrystalline Pt, it appears that the kinetics of the Ethanol Oxidation Reaction (EOR) are significantly enhanced at such a surface with increasing temperature.

Dutta and Datta [2] obtained Arrhenius plots of the ethanol oxidation current densities from the data in fig. 5.2 and observed a linear relationship, stating that this indicates the EOR mechanism does not change at higher temperature. Further, the oxidation products were qualitatively analyzed by ion-exchange chromatography (IEC) during oxidation of ethanol at PtPd/C at -0.3 V from 20 to 80 ^{o}C. Thus, at temperatures > 60 ^{o}C, the authors observed a significantly greater increase in the product efficiency for acetate production at PtPd/C (15 x greater than that at unloaded Pt) than for carbonate production (2.5 x greater). In the case of unloaded Pt, it was stated that the reaction, although exhibiting sluggish kinetics when compared to PtPd, proceeded via a single pathway that favors carbonate formation over acetate at all the temperatures studied, 20-80 ^{o}C, and increasing with increasing temperature. However, as discussed previously (see section 3.1.4), the ordinate axes on the relevant plots were unlabelled in terms of units, and no attempt appeared to have been made to render the IEC data quantitative.

Figure 5.3 shows the CVs collected by Datta et al [3] during an earlier study which investigated ethanol electro-oxidation under identical conditions to those discussed above. From the figure, it may be seen that in contrast to the LSVs collected in the author's more recent study (see fig. 5.2), the ethanol oxidation current during the

anodic scan was only slightly enhanced (x 1.3) upon increasing the temperature from 20 to 80 ^{o}C. Moreover, the peak currents observed at 40 and 60 ^{o}C were of very similar values (ca. 40 mA cm^{-2}) and decreased by ca. 10 mA cm^{-1} upon heating to 80 ^{o}C.

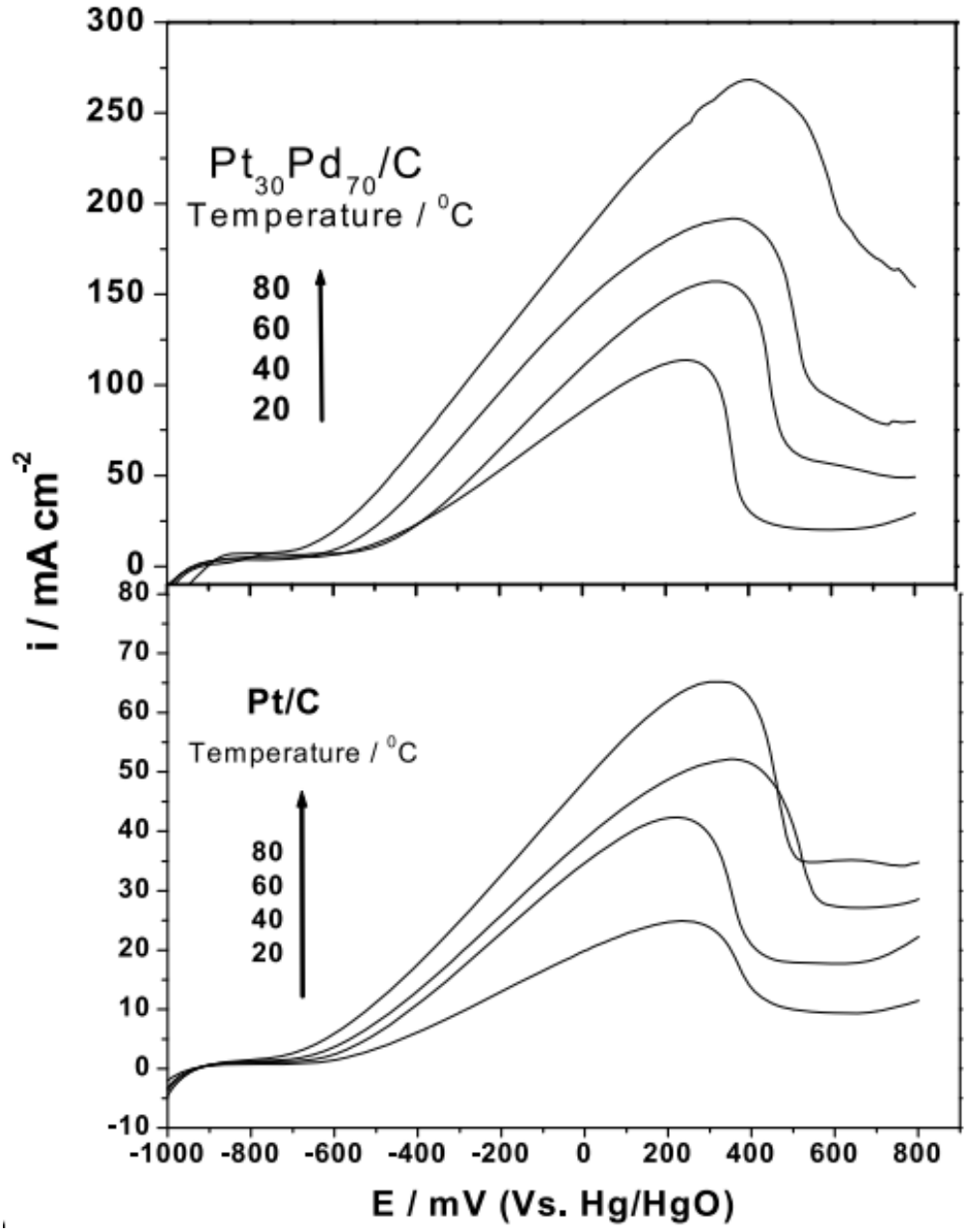

Figure 5.2. Linear sweep voltammetry data collected by Datta and Dutta [2] during their study of the electro-oxidation of 1 M EtOH at Pt/C and PtPd/C in 0.5 M NaOH from 20 to 80 ^{o}C.

As discussed previously (see section 3.1.4), the ratio of the ethanol oxidation peak currents in the forward and back (reverse) sweeps, I_F/I_B, was employed by the authors as a measure of the efficacy of the stripping of the Pt oxide at removing adsorbed, carbonaceous fragments. Figure 5.3 clearly shows that I_F/I_B decreases with increasing temperature, from which the authors postulated that surface activation of Pt/C by OH_{ads} was more facile at higher temperature. However, as discussed in section 3.1.4, it is generally accepted that the oxidation of adsorbed ethanol takes place via reversibly-adsorbed OH_{ads}, and the oxidation of the Pt to Pt-OH or Pt-O inhibits ethanol oxidation at higher potentials [4][8]. Hence, following the work by Lai et al [9] and Dimos and Blanchard [10] (see section 3.1.4), the decrease in I_F/I_B observed by Datta et al [3] most likely indicates a decrease in the influence of strongly adsorbed carbonaceous fragments (such as CO_{ads}) at higher temperatures.

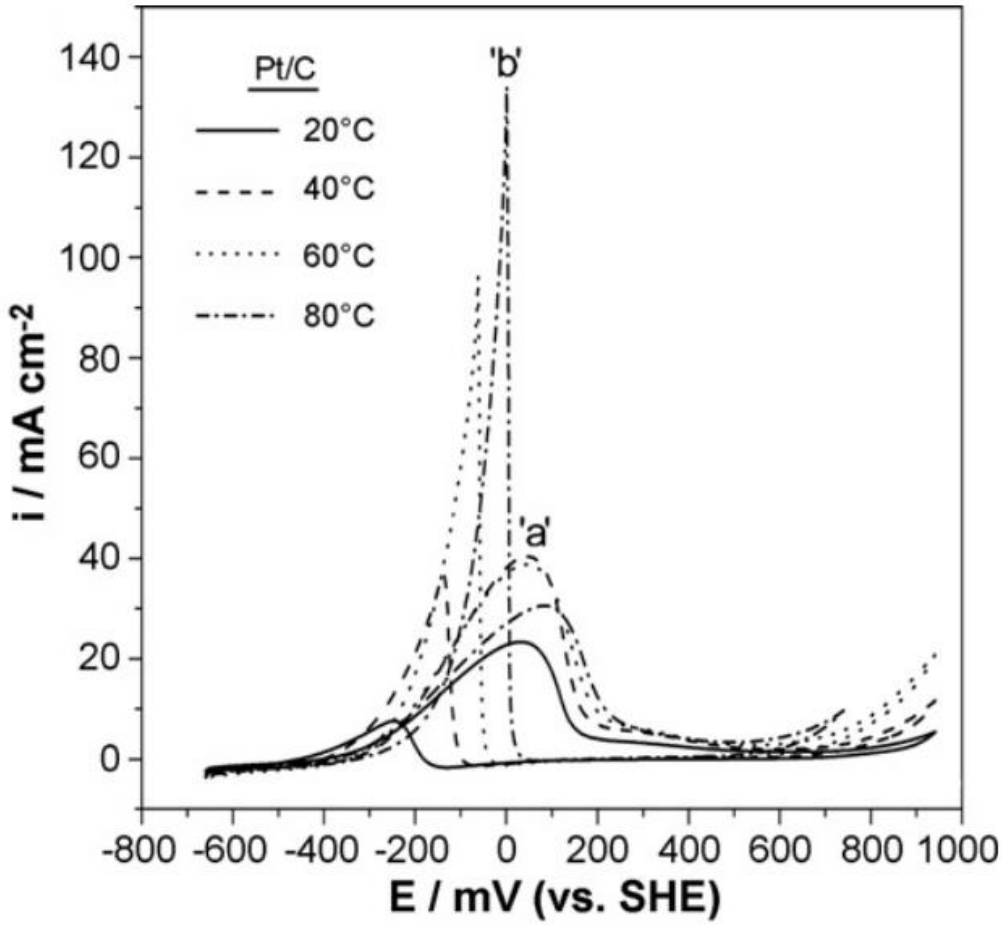

Figure 5.3. Cyclic voltammogramms collected by Datta et al [3] during the oxidation of 1 M EtOH at Pt/C in Ar saturated 0.5 M NaOH as a function of temperature.

With respect to the importance of OH_{ads} in the context of the electro-oxidation of organic molecules in alkaline solution, Ureta-Zanartu *et al* [11], from their CV study of 27.3 mM benzyl alcohol oxidation at Au in pH 11 buffer electrolyte, suggested that Au-OH coverage was very low at room temperature; and that OH_{ads} formation was significantly enhanced upon elevating the temperature to 40 ^{o}C, thus facilitating enhanced benzyl alcohol oxidation.

Returning to the study by Datta *et al* [3], the authors further investigated the oxidation of 1 M ethanol in 0.5 M KOH at Pt/C via chronoamperometry at -0.16 V vs. SHE and the amounts of carbonate and acetate produced were estimated by IEC. Similar to the authors' recent study [2], it was found that significantly more carbonate was formed than acetate at unloaded Pt across all temperatures investigated. In addition, Datta *et al* [3] found that the ratio of carbonate to acetate formation increased significantly upon raising the temperature. It is important to note that in both studies presented by Datta and co-workers, it was stated that significant carbonate formation occurs at temperatures as low as 20 ^{o}C. This is in contrast to the general view in the literature (see the discussion in section 3.1.1), which is that at room temperature, acetate is the predominant oxidation product under conditions of ethanol excess in solution, with carbonate formation having only a minor contribution to the overall oxidation process.

More recently, Ma *et al* [4] investigated the EOR kinetics as a function of temperature at thin film Pt/C and Pd/C electrodes (20 wt% metal on carbon). Figure 5.4 shows the CVs collected by the authors during the oxidation of 1 M EtOH at Pt/C in 0.1 M NaOH. From figure 5.4 it may be seen that upon increasing the temperature to ca. 60 ^{o}C (333 K), the authors observed a significant decrease in the current density at potentials > 0.58 vs. RHE during the positive-going scan. Furthermore, a well-defined shoulder near 0.6 V vs. RHE was observed at 60 ^{o}C in addition to the conventional single ethanol oxidation peak, similar to that observed by Behm *et al* [7] in acid solution (see fig. 5.1(a)).

Ma and co-workers [4] stated that C-C bond cleavage is more facile at Pt/C at elevated temperature, leading to a significant increase in the peak current density during the negative-going scan upon increasing the temperature from 298 to 333 K. On the other hand, the authors also postulated that the formation of strongly

adsorbed, poisoning C_1 species (eg. CO_{ads} and $CH_{x,\ ads}$) is enhanced at elevated temperature, leading to a decrease in the number of active sites available for the formation of active intermediates and OH_{ads}.

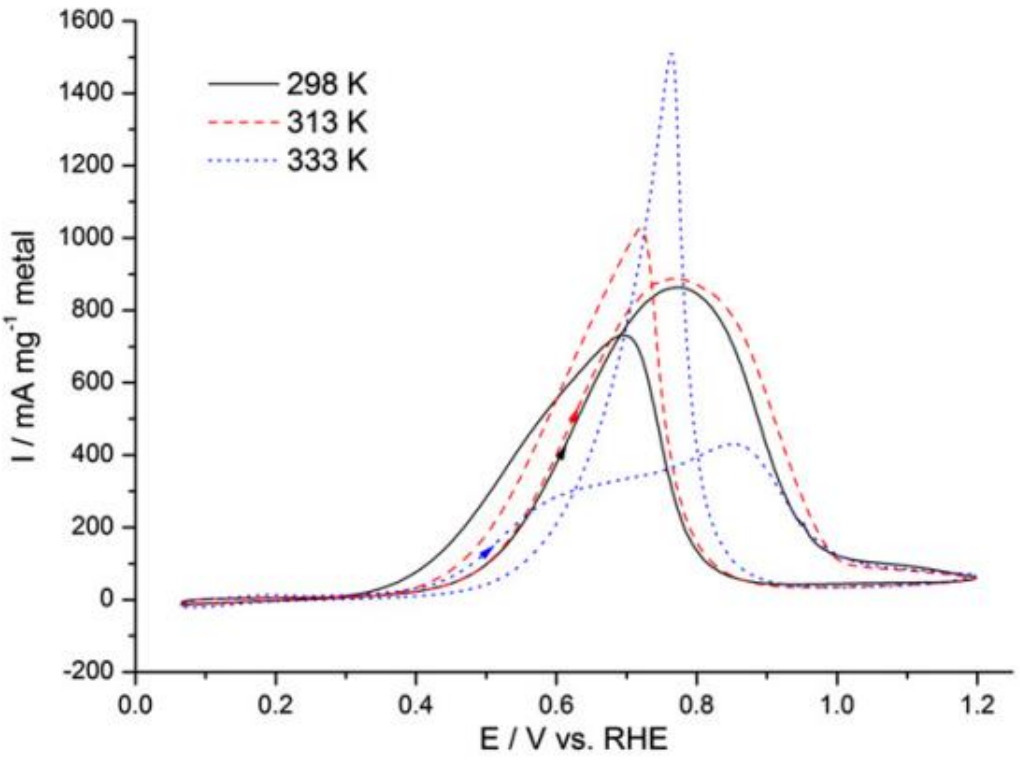

Figure 5.4. Cyclic voltammogramms observed by Ma et al [4] during their study of 1 M EtOH oxidation at Pt/C in Ar saturated 0.1 M NaOH as a function of temperature.

Ma *et al* concluded that since the total current density for ethanol oxidation in alkaline media reflects both carbonate and acetate formation, a decrease in the total current density at potentials > 0.58 V was understandable. This is in contrast to the CVs collected by Behm *et al* [7] in acid solution (see fig. 5.1), where a significant increase in current density was observed during the forward-going scan upon increasing the temperature from 30 to 60 ^{o}C. Furthermore, these findings are in disagreement with the LSVs and CVs presented by Datta and co-workers [2][3] in alkaline media (see figs. 5.2 and 5.3), which for temperatures < 60 ^{o}C, showed an increase in current density upon heating.

Pierozynski *et al* [5] observed a significant increase in the recorded voltammetric oxidation current densities upon increasing the temperature from 23-60 ^{o}C during their study of the electro-oxidation of 0.25 M EtOH at polycrystalline Pt in 0.1 M NaOH. The authors stated that the kinetics of ethanol electro-oxidation reaction at Pt increase significantly at elevated temperature. However, no mechanistic explanation was provided to support their work.

5.1.3. Summary

From the literature presented in this section, it is clear that the kinetics of the EOR in alkaline medium are enhanced at higher temperature. However, there is much confusion surrounding the products that are generated and the mechanism by which this occurs. More specifically, the literature suggests that there are two possible scenarios: (i) C-C bond cleavage is enhanced upon increasing temperature, thus leading to an increase in complete oxidation of ethanol to form carbonate; (ii) no change in the EOR mechanism occurs at higher temperature, but the kinetics of the EOR via retention of the C-C bond are enhanced, subsequently producing more acetate. The characteristic IR features for the oxidation products suggested in (i) and (ii) have been well established both from the literature [12-15] and the results presented in chapter 3 (see table 5.1). Hence, this chapter will focus on the application of *in-situ* FTIR spectroscopy to the analysis of the EOR mechanism at 25 and 50 ^{o}C.

5.2. Results and Discussion

5.2.1. Cyclic Voltammetry

Figure 5.5 shows cyclic voltammograms of a Pt (foil, 1cm x 1cm) electrode immersed in 0.1 M KOH in the absence of ethanol at 25 and 50 ^{o}C. From the figure, it may be seen that features corresponding to the formation of reversibly-adsorbed OH (OH_{ads}, peak near -0.19V) [4][8] and the formation and stripping of chemisorbed hydride and oxide layers on the Pt surface [16] were observed. The charge under the OH_{ads} peak in the anodic scan is higher at 50 ^{o}C than at 25 ^{o}C suggesting that the equilibrium:

$$Pt + OH^{-} \leftrightarrow PtOH + e^{-} \quad (2)$$

shifts to the right at the higher temperature, in agreement with the postulate by Datta and co-workers [2][3] that OH_{ads} formation is more facile at higher temperature in alkaline solution, and hence ethanol oxidation faster. Figure 5.5 also shows that the maximum of the peak due to reduction of the phase oxide, formed at Pt during the anodic sweep of the CV, shifts from ca. -0.16 to -0.10 V upon increasing the temperature from 25 to 50°C.

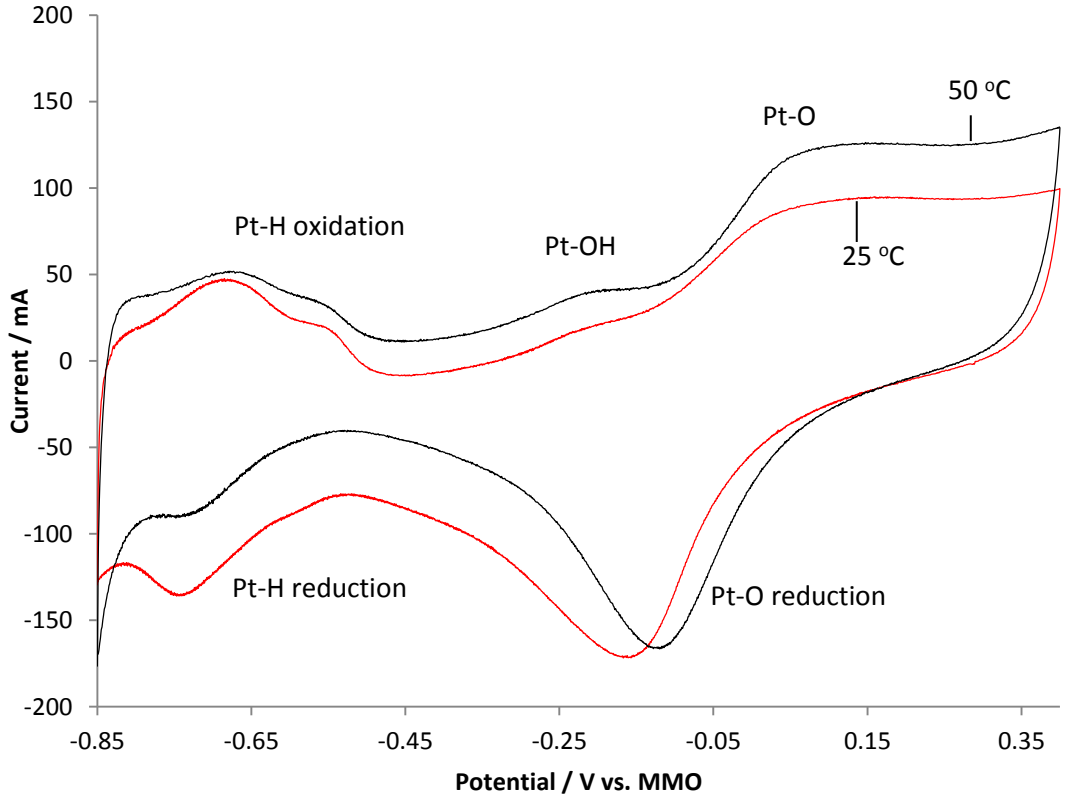

Figure 5.5. CVs of the Pt foil working electrode collected in 0.1M KOH, in the absence of ethanol, at 25 and 50 °C (-0.85 to 0.4 V vs. MMO; scan rate of 100 mVs^{-1}).

Figure 5.6 shows the corresponding cyclic voltammogramms collected in the presence of 1M ethanol. As can be seen from the figure, the hydrogen adsorption region is blocked by chemisorbed fragments of ethanol [4][8][9], and the oxidation of ethanol commences with OH_{ads} formation [4] at both 25 and 50 °C. Both anodic peaks in the forward and reverse sweeps of the CV in fig. 5.6 increase in current with temperature, in contrast to Ma *et al* [4] who have reported a decrease in current density during the forward scan upon increasing the temperature from 40 to 60°C

(see fig. 5.4). As discussed previously (see section 5.1.2), the authors attributed this to an increase in carbonate formation, indicated by an additional peak at ca. 0.5 V vs. RHE in the CV. Datta and co-workers [2][3] have also suggested that the ratio of carbonate to acetate formation increases with increasing temperature. It is difficult to discern from fig. 5.6 whether the anodic peak in the forward scan of the voltammogram is comprised of two waves, as per the work of Jiang et al [8] and Ma and colleagues [4]. In the absence of molecular information, the possible production of carbonate cannot be resolved, hence the in-situ FTIR studies reported below.

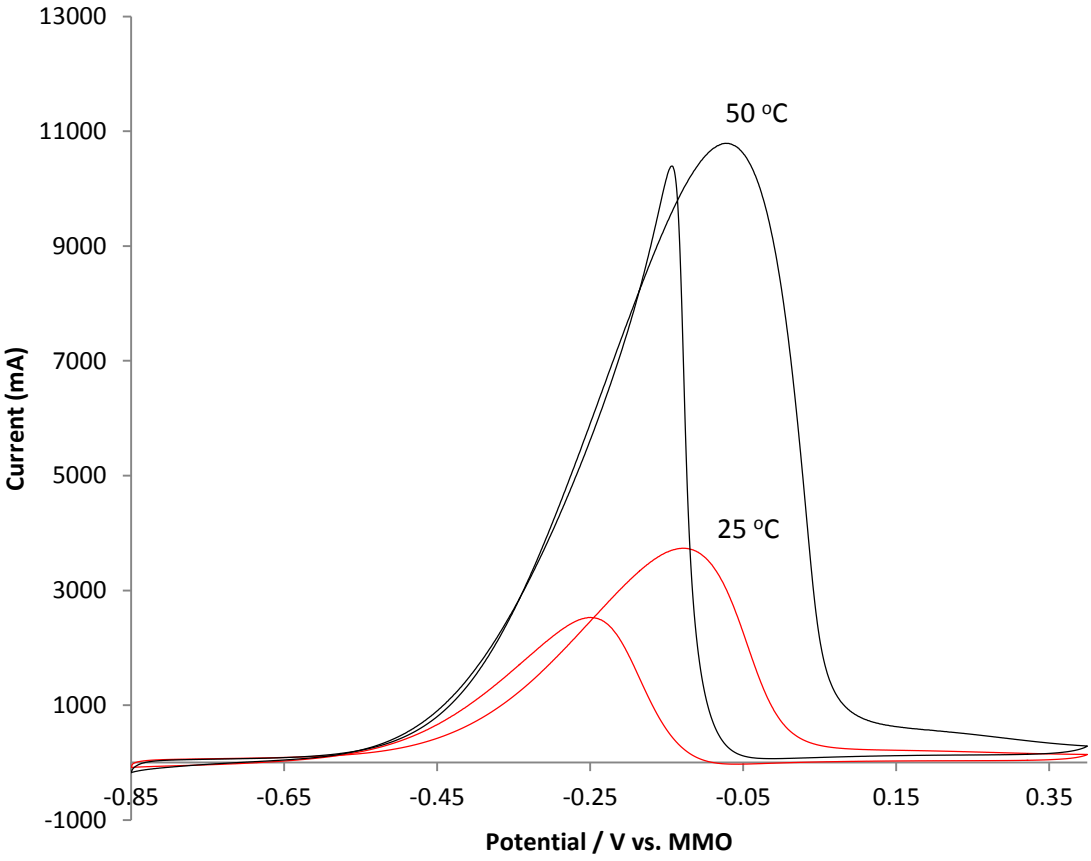

Figure 5.6. CVs of the Pt foil working electrode collected in 0.1M KOH + 1 M EtOH at 25 and 50 °C (-0.85 to 0.4 V vs. MMO; scan rate of 100 mVs^{-1}).

Returning to fig. 5.6, there appears to be no difference in onset potential for ethanol oxidation in the forward sweep, in agreement with Jiang et al [8] and Ma and co-workers [4]; the latter reported that the onset potential depended on the ethanol concentration. However, it is clear that the peak in the forward sweep moves to

higher potentials with increasing temperature; from -0.13V at 25ºC to -0.08V at 50ºC.

As may be seen from fig. 5.6, at all temperatures, the oxidation of ethanol during the forward sweep was suppressed due to the oxidation of the Pt to Pt-OH or Pt-O [8][9]. The potential at which the current falls to ca. 5% of its value at the anodic peak in the forward scan was +0.14V and +0.17V as the temperature was increased from 25 to 50ºC. From fig. 5.5, it can be seen that the onset of formation of the Pt-OH does not seem to vary with temperature, although the coverage of the oxide/hydroxide layer (ie. at potentials > -0.1V) is significantly higher at 50ºC than at the lower temperatures, suggesting that the higher temperature facilitates oxidation of ethanol at the oxidized Pt, as is observed in acid solution [13].

In the reverse sweep in fig. 5.6, the increasing anodic potential of the onset of ethanol oxidation peak appears to follow the temperature dependence of the oxide stripping peak, see fig. 5.5. The data in fig. 5.6 at 50ºC resemble the CV's reported by Lai et al [9] for polycrystalline Pt in 0.1M NaOH+0.5M ethanol at room temperature, in that there is very little hysteresis between the forward and reverse scans at potentials below the anodic peak in the reverse scan, ie. -0.18V vs MMO, suggesting that the steady state coverage of the Pt by carbonaceous fragments is achieved more rapidly at 50 °C compared to 25 °C .

5.2.2. In-situ FTIR Spectroscopy

5.2.2.1. Overview

As described in chapter 3 and in previous papers by other workers in Newcastle [12][17][18], at higher potentials during the *in-situ* FTIR experiments in alkaline solution there is a substantial change in pH in the electrolyte immediately above the electrode and trapped in the thin layer. The swing in pH was ascribed to a combination of: (a) relatively slow diffusion of OH^- ions across the electrode surface [19][20] over a timescale of tens of minutes for an electrode of the radius that we use; and (b) the exhaustion of reactant in the thin electrolyte layer, which leads to further changes in the ambient conditions at the electrode surface [19-20]. Thus, the data presented in this section will be discussed in two sections, i.e. the spectra collected (i) below and (ii) above the transition point.

5.2.2.2. Potentials below the transition point

Figure 5.7 shows the spectra collected during an experiment carried out at 50 °C in 0.1 M KOH + 1 M ethanol. The potential was stepped from -0.85 V to +0.4 V vs MMO, but the figure shows only the spectra collected up to the transition potential of -0.4 V. At 25 °C, this transition occurred at -0.1 V (see section 3.2). The spectra in fig. 5.7 are representative of the data observed at both temperatures, in that the only features observed were due to solution acetate and hydroxide ions, and water. As may be seen from the figure, the spectra are dominated by bands due to the loss of solution hydroxide ions at 1870 and 2750 cm^{-1}, and gain of solution acetate at 1554, 1415 and 1348 cm^{-1} [12][17][18][21][22]. In agreement with López-Atalaya et al [23] and in contrast to the postulated carbonate formation in the various papers reporting IVt data on ethanol oxidation at Pt/C in alkaline solution [2-4][8], there is no evidence for CO_3^{2-} in fig. 5.7.

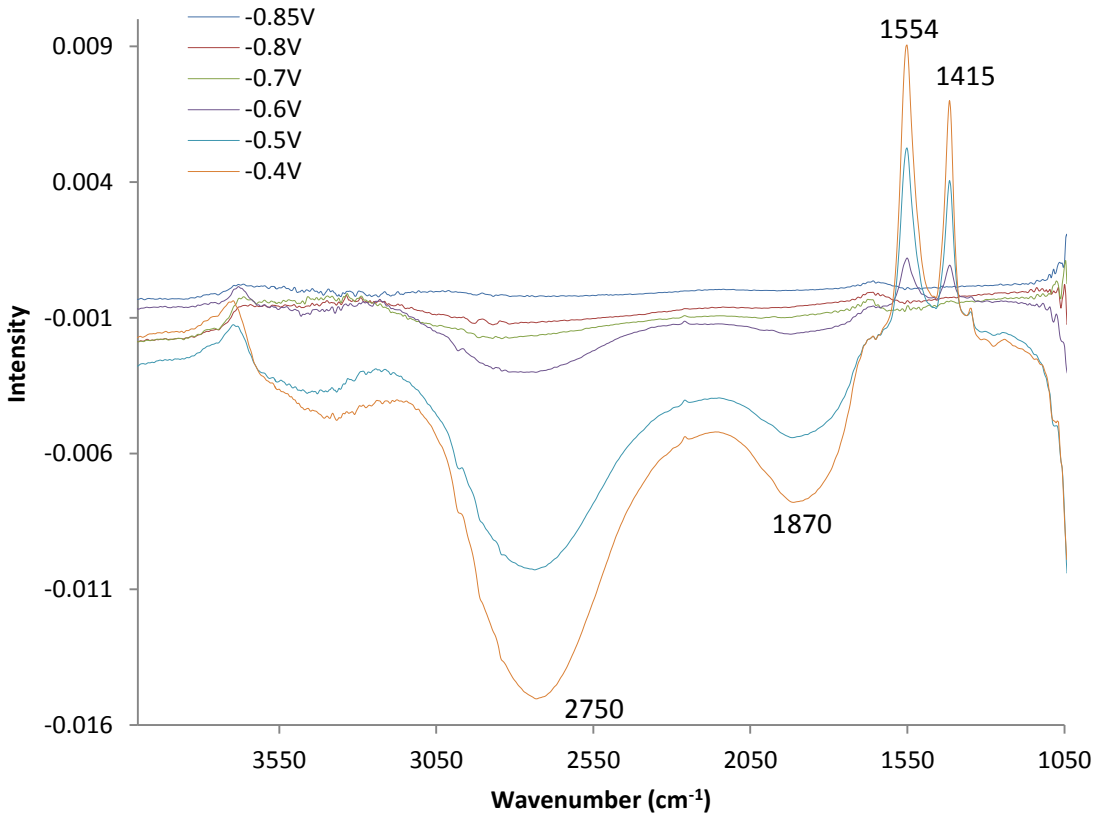

Figure 5.7. Spectra (8 cm^{-1} resolution, 100 scans, 47 s per scan set) collected during the electro-oxidation of 1M ethanol in 0.1M KOH at 50 ^{o}C, before the transition point, from -0.85 to -0.4 V.

Figure 5.8 shows the spectra collected at the transition potentials of -0.1V (25 °C) and -0.4V (50 °C) normalized to the respective reference spectra collected at -0.85V. As can be seen from the figure, the intensities of the acetate features are comparable, despite the 50 °C spectrum having been taken at a potential 300 mV lower than that collected at 25 °C. There is also a difference in terms of the behaviour of the water features (see below). These may be clearly seen in figs. 5.10 (a) and (b) which show plots of the intensities of the various key features in the spectra collected during the experiments depicted in fig. 5.7 as a function of potential (the spectra employed to determine these intensities were all normalized to -0.85V); the arrows in fig. 5.10 (b) mark the transition potentials above which CO_2 and acetic acid were observed. Figure 5.10 (b) shows the plots in fig. 5.10 (a) normalised to their maximum values to highlight concomitant behaviour.

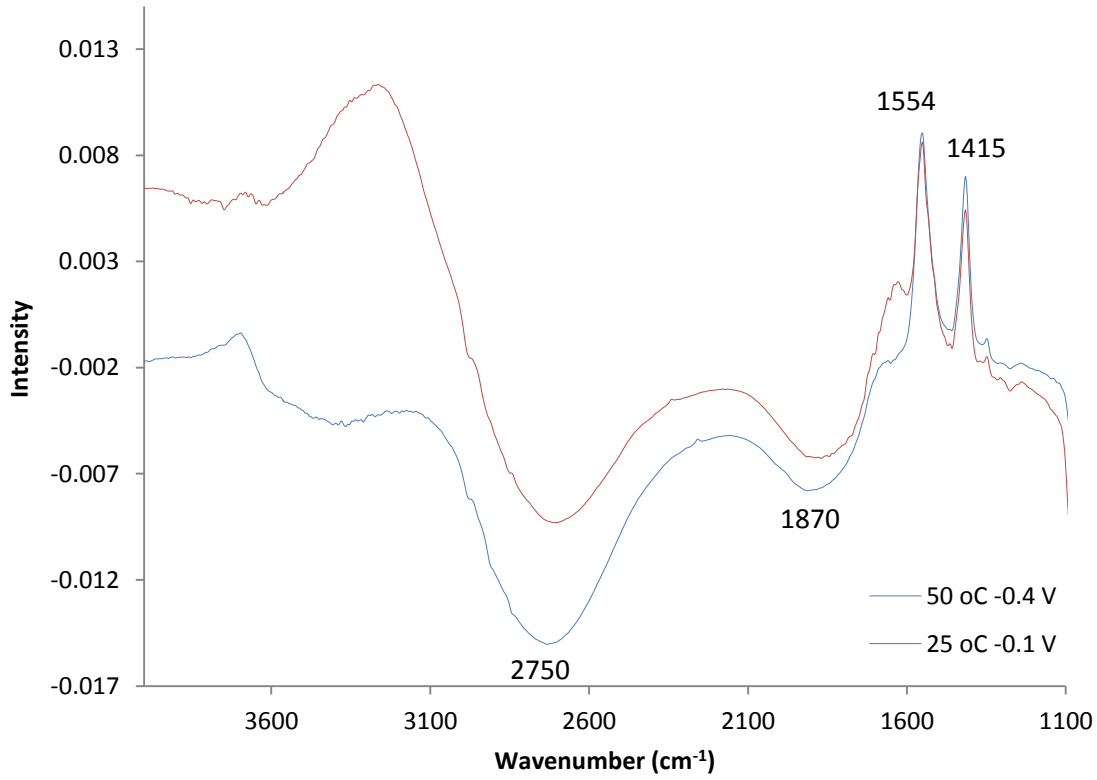

Figure 5.8. Spectra collected during the experiment depicted in fig. 5.7 at the transition potential of -0.4 V, and during the experiment detailed in chapter 3, at the transition potential of -0.1 V at 25 ^{o}C.

Figure 5.9 shows the spectra collected at -0.6 V vs. MMO in the experiments at 25 and 50 ^{o}C. As may be seen from the figure, the intensity of the sharp gain feature at

ca. 3670 cm^{-1}, which may be attributed to isolated OH (ie Pt-O-H free from hydrogen bonding [24][25]), is significantly greater at 50 ^{o}C than at 25 ^{o}C; if this is OH_{ads}, then the data in fig. 5.9 are in agreement with the voltammetry data in figs. 5.5 and 5.6 showing enhanced current for OH_{ads} formation at 50 °C .

Figure 5.9. In-Situ FTIR spectra collected at -0.6 V vs. MMO during the ethanol oxidation experiments carried out in fig. 2.

Similar to the experiment carried out at 25 ^{o}C (see figs. 3.9(a) and 3.9(b)), the spectra in fig. 5.7 are dominated by the solution OH^- loss feature [12][17][18] with peaks near 2750 cm^{-1} and 1870 cm^{-1} due to its reaction with adsorbed ethanol species to form acetate. The intensities of these features increase more rapidly with potential in the spectra collected at 50 ^{o}C than at 25 ^{o}C, see figs 5.10(a) and (b). As can be seen from fig. 5.10(b), at both temperatures, the 1870 cm^{-1} OH^- loss and 1415 cm^{-1} acetate gain features track each other, reflecting the role of the former as a reactant in the oxidation of ethanol:

$$C_2H_5OH + 5\ OH^- \rightarrow CH_3COO^- + 4H_2O + 4e^- \quad (3)$$

It is also clear from figs. 5.10(a) and (b) that the intensities of the water O-H stretch features do not track the acetate bands, lagging some 300 mV behind at each temperature (and the water features at 50 °C appear as losses); this suggests that the processes responsible for the change in water absorptions are associated with events taking place at higher potentials. It appears that the slopes of the two plots in fig. 5.10 both increase at potentials above transition. From fig. 5.10(b) it can be seen that at 50 ^{o}C, the onset potential for acetate production ($\geq$ -0.6V) corresponds to that for the formation of adsorbed OH [1][12][17][18], which then oxidizes the adsorbed ethoxy species to acetate, as was the case at 25 ^{o}C (see section 3.2). Above the transition potentials, the acetate bands cease growing and are replaced by the gain features due to acetic acid [12]. From fig. 5.10(a) it is clear that there is a significant increase in acetate formation at all potentials below transition at 50 °C compared to 25 °C. This marked difference in behavior between the IR response at 50 °C on the one hand, and 25 °C on the other, is reflected in the behavior of the O-H stretches near 3300 cm^{-1}, see fig. 5.11. At 25°C, there is a steady, gain of an O-H stretch feature due to water at 3250 cm^{-1} and an attendant, weaker band near 1635 cm^{-1} due to the H-O-H deformation. In contrast, at 50°C, both the O-H stretch and H-O-H deformation appear as loss features, growing steadily in intensity as the potential is increased. There is no explanation for this behaviour at this time.

From fig. 5.7 it may be seen that the valley between the 1554 and 1415 cm^{-1} acetate absorptions is structured (arrowed) and, in addition, was shown in our previous work [25] to be deeper than that in the spectrum of aqueous sodium acetate. This was attributed to the loss of absorptions in this spectral region, even at potentials as low as -0.7V (at 25 °C), and these losses are described in the next section.

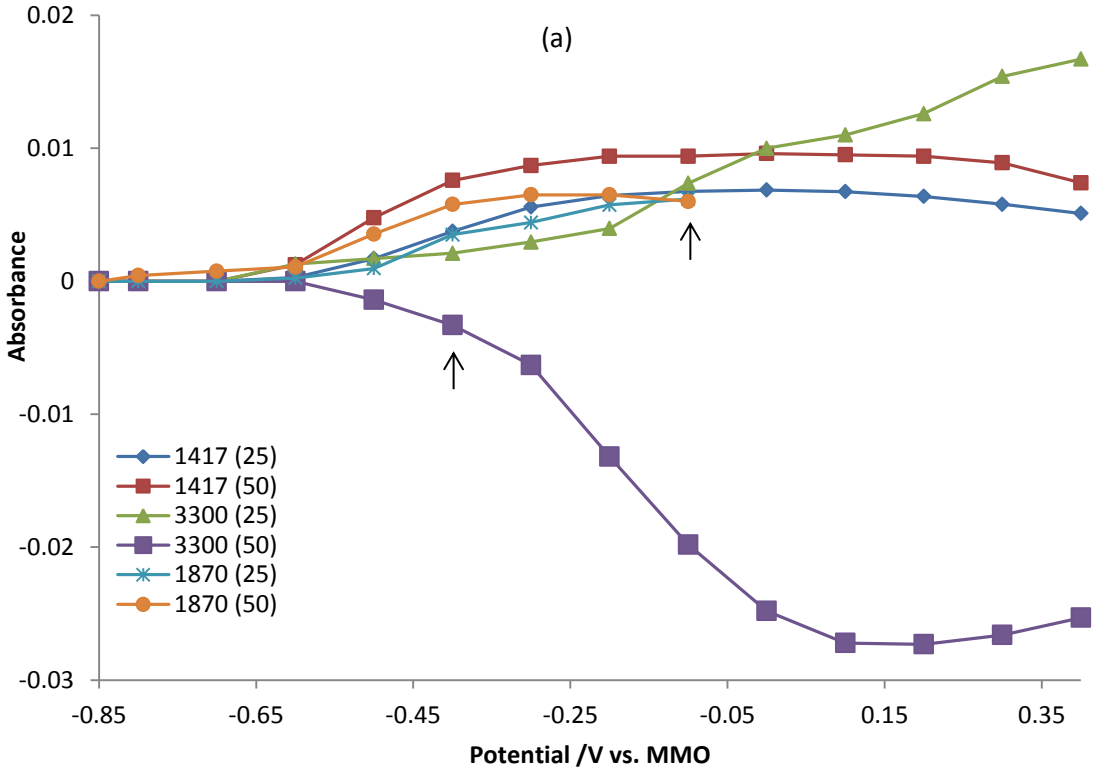

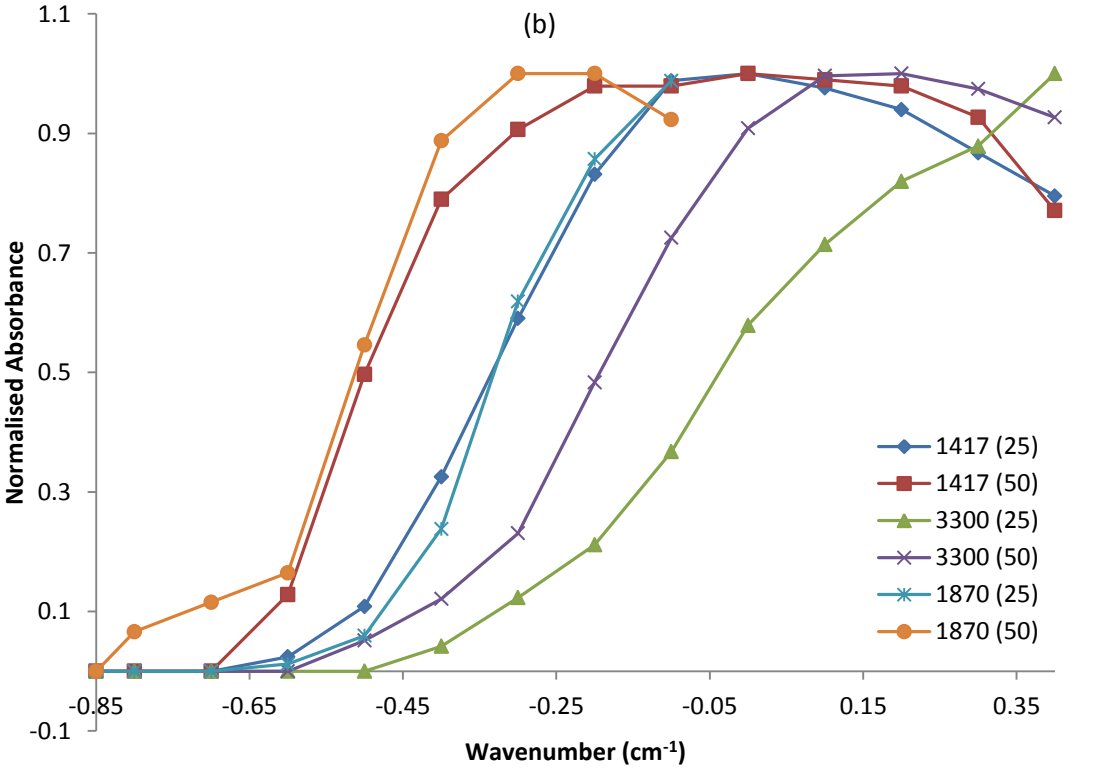

Figure 5.10. (a) Plotted intensities of the features in figs. 5.7 and 2 (b) the intensities of the bands in (a) normalised to their maximum values.

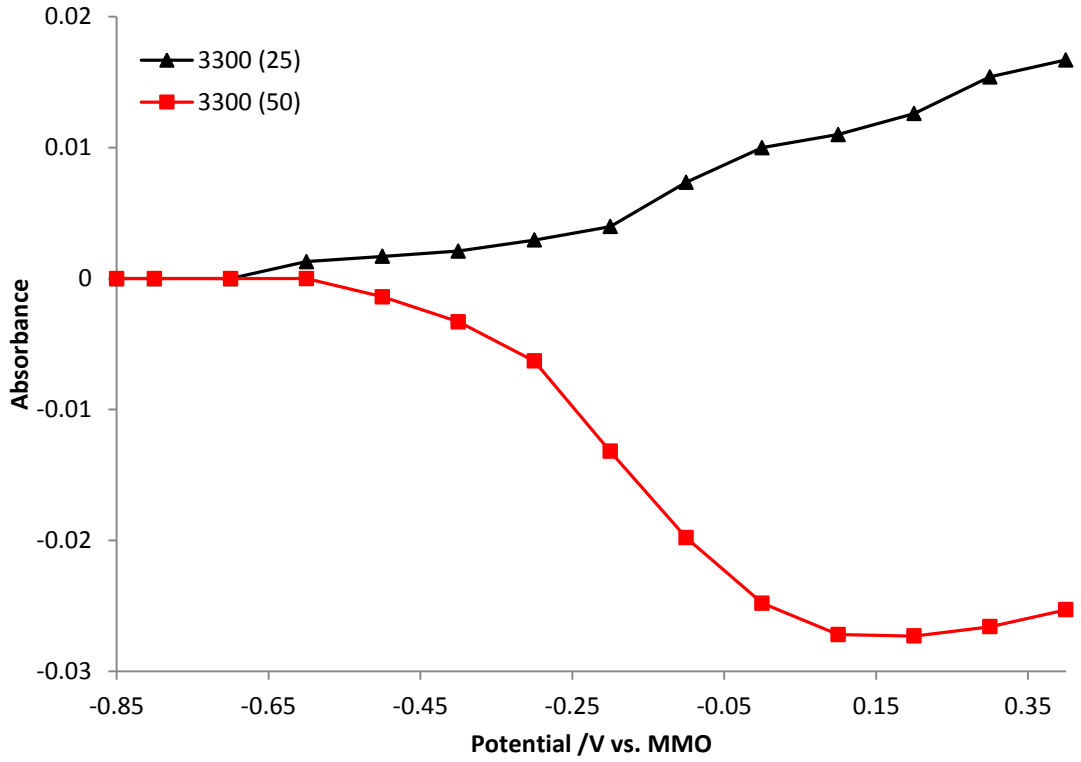

Figure 5.11. Plots of the intensities of the 3300 cm^{-1} water features in fig. 5.7 at 25 and 50 ^{o}C as a function of potential.

5.2.3. In-Situ FTIR spectroscopy: Potentials Above Transition

Figures 5.12(a) and (b) show spectra collected at potentials > -0.3V in the experiment at 50 ºC normalised to that taken at -0.3V. These data were chosen as representative of both temperatures because the various features were observed in both experiments. In addition, the extended potential range possible at the higher temperature (lower transition potential) gave more data points for analysis, and the very weak intensity (or absence of) the 1554 cm^{-1} acetate band facilitated a more accurate determination of the intensities of the 1573 cm^{-1} and 1540 cm^{-1} bands [12].

As can be seen from fig. 5.12(a), there are sharp loss features at 2956, 2913 and 2850 cm^{-1}, the latter two of which appear to be bipolar. These bands were previously attributed to adsorbed ethoxy species (see section 3.2 and references therein). As discussed in section 3.2.3, loss features observed after the transition potential are representative of species that were present before the drop in pH, and hence under alkaline conditions.

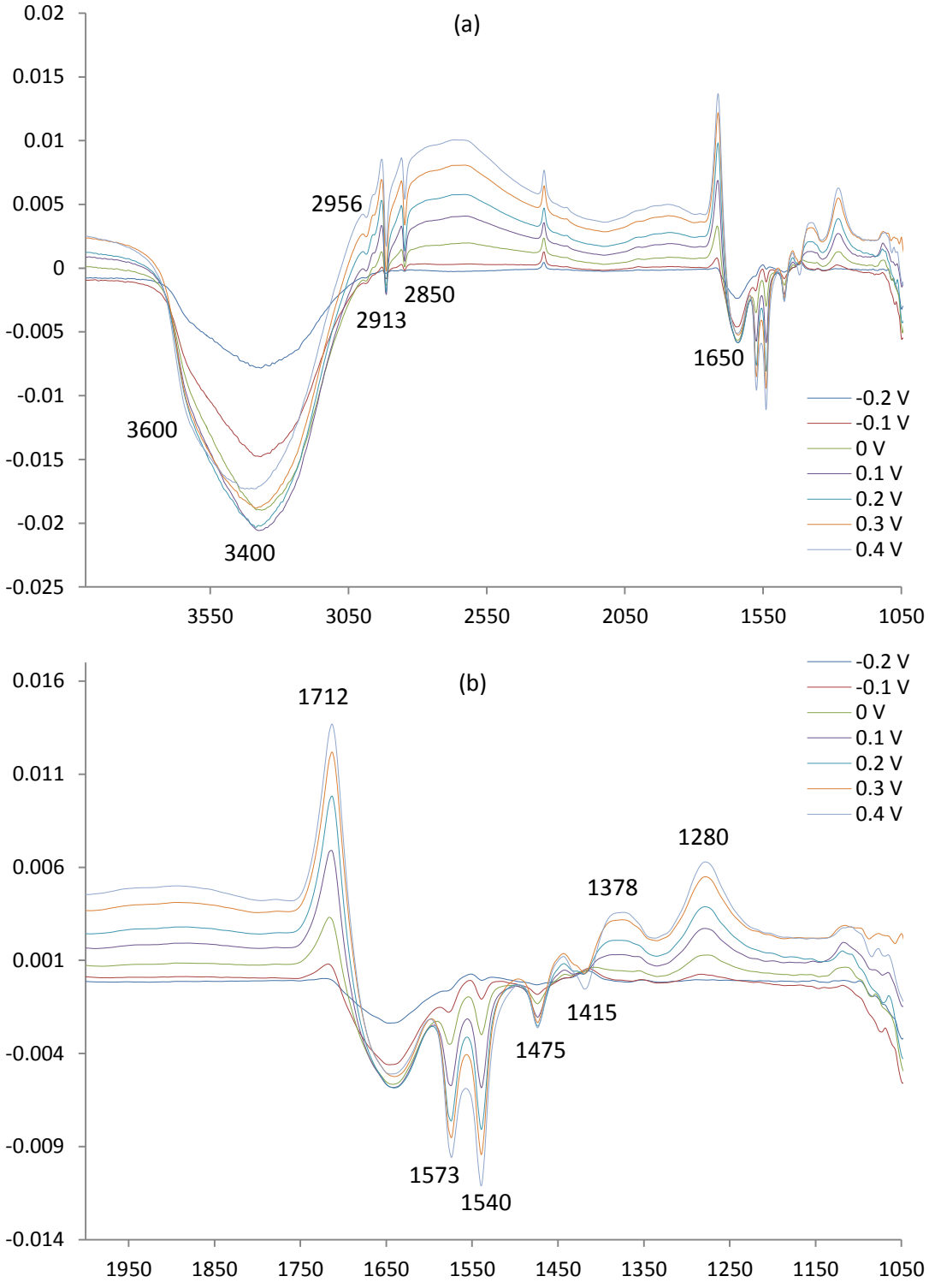

Figure 5.12. Spectra collected above -0.3 V, normalised to that collected at -0.3 V, during the experiment depicted in fig. 1 over the range from (a) 4000-1050 cm^{-1} and (b) below 2000 cm^{-1}.

The gain of CO_2 (band at 2340 cm^{-1}) clearly shows that the pH, at least in some regions of the thin layer, has fallen below the pK_a of carbonic acid, 6.4 [12][17][18]. The gain features at 1715 cm^{-1}, 1378 cm^{-1} and 1280 cm^{-1} may be attributed to acetic acid, but with a contribution to the 1715 cm^{-1} band from acetaldehyde [12], see below. The formation of acetic acid clearly shows that the pH in the thin layer at these potentials is $\leq$ 4.7, the pK_a of acetic acid [14]; this value varies very little between 14 ºC and 45 ºC [15]. The substantial drop in pH in thin-layer FTIR spectroscopic experiments has been modelled by Christensen *et al* [17][18] in terms of the slow diffusion of OH^- ions across the electrode surface coupled with the exhaustion of reactant.

Figure 5.13 shows the spectra collected at 0.4V vs. MMO normalised to the transition potentials of -0.1 and -0.4 V during the ethanol oxidation experiments carried out at 25 and 50 ^oC respectively.

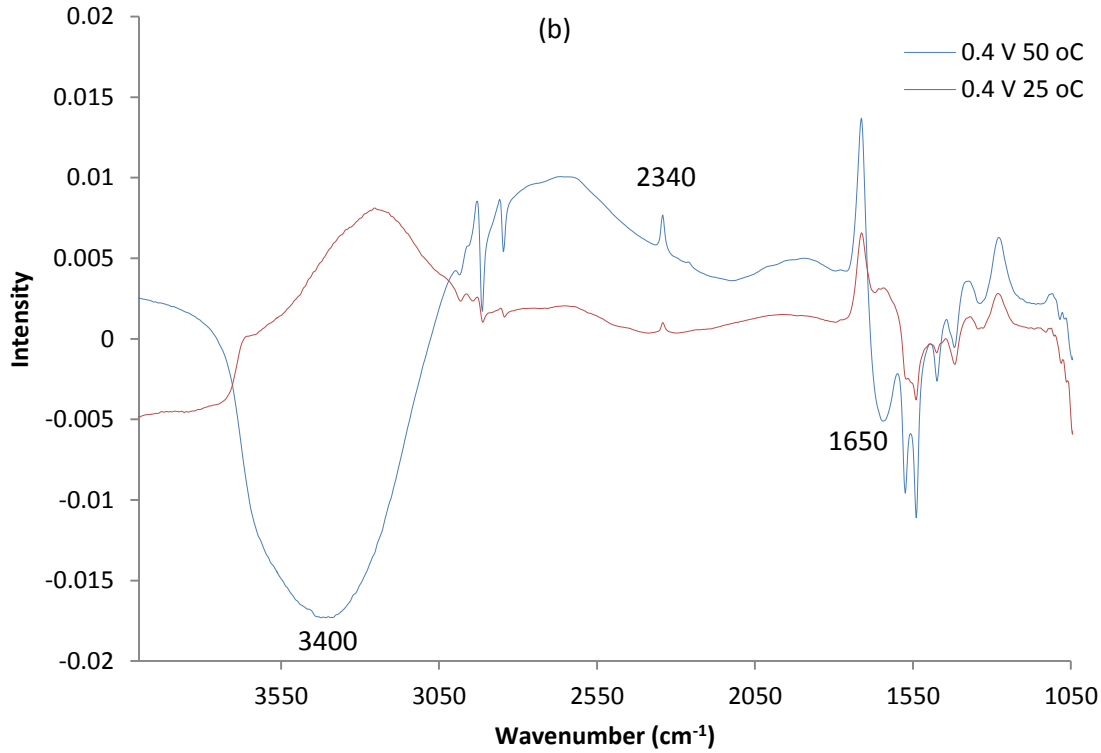

Figure 5.13. In-Situ FTIR spectra collected at 0.4 V during the experiments carried out at 25 and 50 ^oC, normalised to the spectra collected at -0.1 V (25 ^oC) and -0.3 V (50 ^oC).

As may be seen from figs 5.12(a) and 5.13, intense loss features near 3600, 3400 and 1650 cm^{-1} appear and grow after the transition point during the experiment carried out at 50 ^{o}C. In order to determine whether the water loss features observed at 50 °C were associated with the oxidation of ethanol at this temperature, spectra were collected during experiments analogous to those depicted in fig. 5.7 but in the absence of 1 M ethanol, and the results are shown in fig. 5.14.

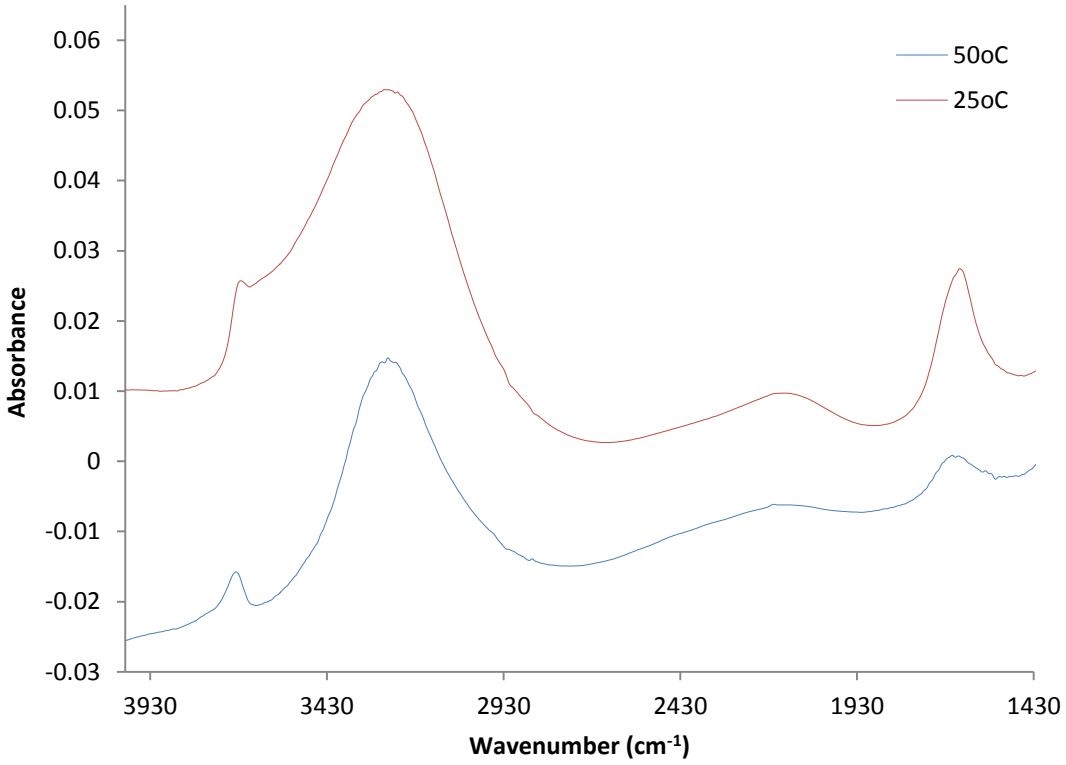

Figure 5.14. In-Situ FTIR spectra collected during experiments analogous to those depicted in fig. 5.7 at 0.4 V, in the absence of 1 M EtOH.

Comparing figs. 5.13 and 5.14 shows that the water gain features above 2750 cm^{-1} and at ca. 1640 cm^{-1} observed during the oxidation of ethanol at 25 ºC and potentials above -0.1 V are also observed in the absence of ethanol. In contrast, there is a clear and marked change in behaviour of the water features at 50 ºC in the absence of ethanol compared to in the presence, with the gain of various water-related bands in the absence of ethanol being replaced by a significant loss, potentially showing a change in mechanism, in contrast to the work of Dutta and co-workers [2][3] and Ma et al [4]. However, similar water loss features were observed in a previous study by

Christensen et al [17] on methanol oxidation in 0.1 M KOH (see fig. 5.15) and attributed to the loss of highly hydrogen-bonded bulk water [28] from the thin layer due to CO_2 gas bubble formation, and this does not seem an unreasonable explanation, particularly given the fact that the other loss features (see table 5.1) and gain features are observed at both temperatures, suggesting a single mechanism.

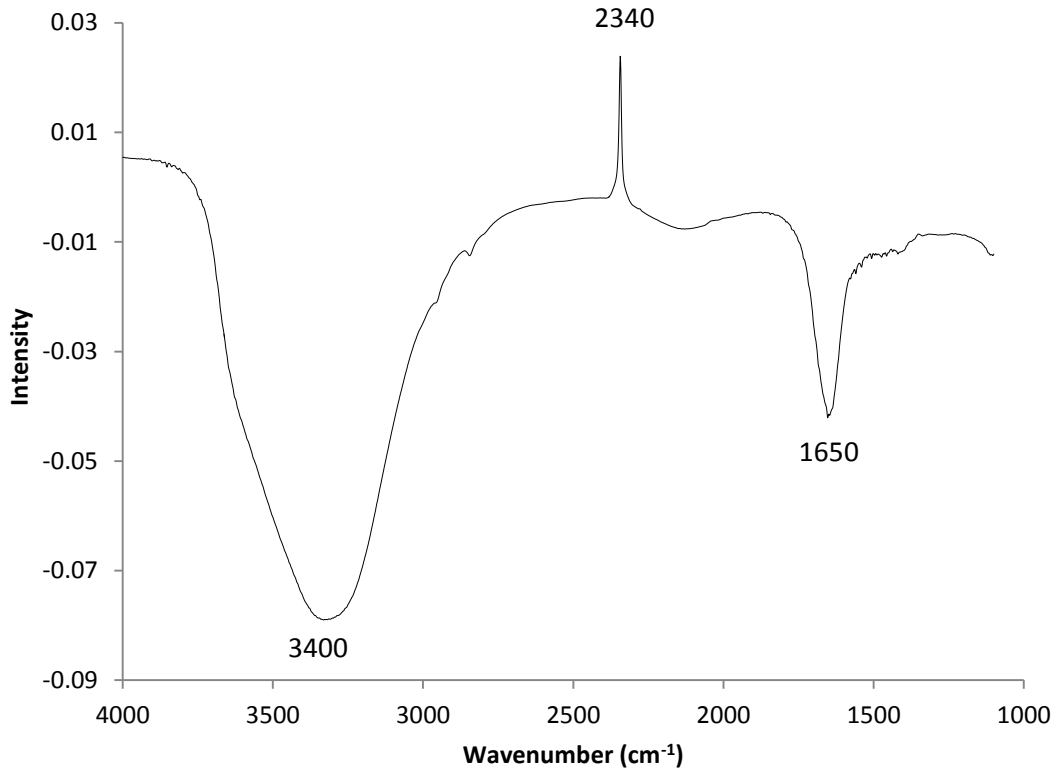

Figure 5.15. In-Situ FTIR spectra collected at -0.6 V vs. MMO by Christensen et al [31] during their study of 1 M MeOH oxidation in 0.1 M KOH.

Taking the gain features in figs. 5.12 and 5.13 first, fig. 5.16 shows the spectra depicted in fig. 5.13 over the range 2050 – 1050 cm^{-1}. As was stated in section 3.2.3, the gain features at 1715 cm^{-1}, 1378 cm^{-1} and 1280 cm^{-1} may be attributed to acetic acid [12][21][29-31]. However, the ratio of the band intensity at 1715 cm^{-1} to that at 1280 cm^{-1} is significantly greater in the spectrum collected at 50 ^{o}C, indicating a contribution to the 1715 cm^{-1} band from (an)other species. It is generally accepted that the carbonyl stretch of acetaldehyde occurs in the same spectral region as the 1715 cm^{-1} carbonyl stretch of acetic acid [30][32], rendering any quantitative assessment of these compounds using these absorptions highly challenging.

However, the 1280 cm^{-1} band of acetic acid is not obscured by any absorptions due to the aldehyde and is the same intensity as the carbonyl feature at 1715 cm^{-1} (see section 3.2 and [12]); hence the difference between the intensities of the 1715 cm^{-1} and 1280 cm^{-1} bands in fig. 5.16 may be taken as a (crude) estimation of the acetaldehyde carbonyl absorption. Close inspection of all the experiments carried out reveals a trend in that the greater the difference between the 1712 cm^{-1} and 1280 cm^{-1} bands, ie. the more acetaldehyde produced, the more pronounced is the bipolar nature of the C-H bands, suggesting that acetaldehyde formation is actually responsible for the bipolar nature of these bands.

Figure 5.16. In-Situ FTIR spectra collected during the experiments depicted in fig. 2.1 over the spectral range from 2050 – 1050 cm^{-1}.

Figure 5.17 shows plots of the intensities of the various features in figs. 5.12(a) and (b) as a function of potential. As can be seen, the amount of acetic acid in the thin layer increases steadily with increasing potential, whilst the acetaldehyde reaches a maximum value at ca. 0.3V. The CO_2 increases relatively slowly as the potential is increased. The intensities of the acetaldehyde C=O band (calculated from the difference in intensities of the 1280 and 1715 cm^{-1} absorptions) and the 1280 cm^{-1}

feature of acetic acid at 0.4 V are presented in table 5.2; as can be seen the ratio of the former to the latter at both temperatures is ca. 1.4:1, with ca. twice as much acetaldehyde and acetic acid produced at 50 °C as at 25 °C.

Temperature /°C	$C=O_{Acid}$ $/10^{-3}$	$C=O_{Ald}$ $/10^{-3}$
25	2.0	2.7
50	4.0	5.8

Table 5.2. The intensities of the acetic acid ($C=O_{Acid}$) and acetaldehyde ($C=O_{Ald}$) absorptions in fig. 7(a) (see text for details).

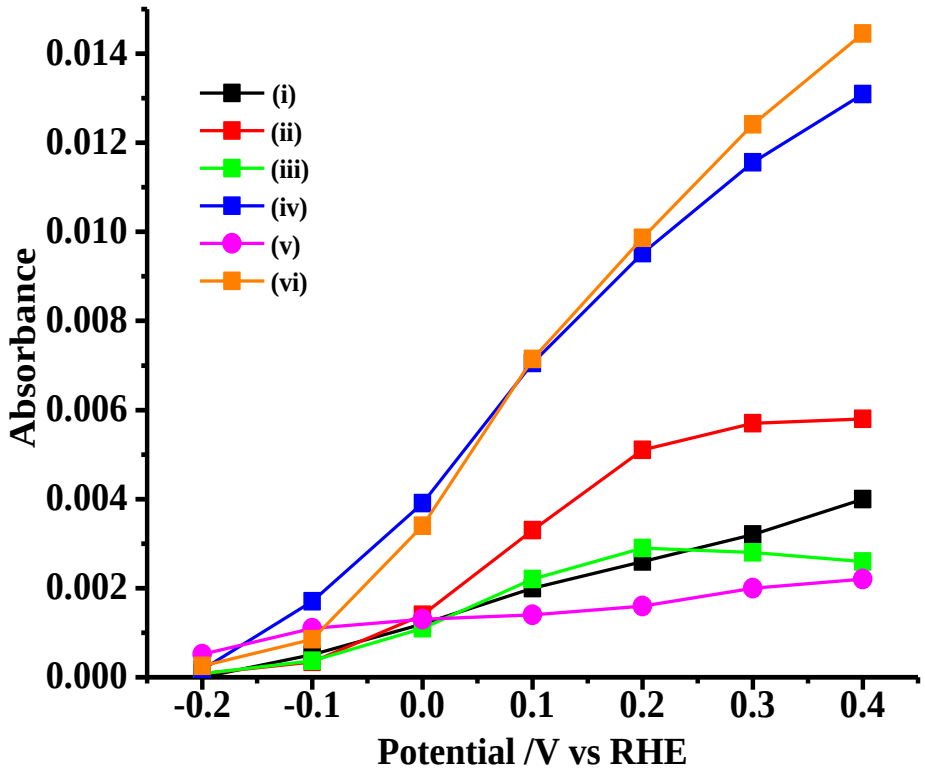

Figure 5.17. The plotted intensities for the various features in figs. 5.12(a) and (b) as a function of potential.

Hence both acetaldehyde and acetic acid are produced faster at the higher temperature, but this increase is the same, maintaining the ratio of the products. *This is a crucial result as it strongly suggests that the rate-determining step in the*

oxidation of ethanol under the acidic conditions in fig. 5.17 is the removal of the first proton from the adsorbed ethoxy species (I), and that the desorption of acetaldehyde and the further oxidation of species (II) to acetate must take place at comparable rates and with similarly low activation energies. It does not seem unreasonable to postulate that this first removal of hydrogen is also the rate determining step in alkaline electrolyte.

Returning to the loss features in figs. 5.12, 5.13 and 5.16, it may be seen that the loss feature at ca. 1540 cm^{-1}, which is attributed to the C=O stretch of bidentate carbonate (see table 5.1), was significantly more intense in the spectra collected at 50 ºC than at 25 ºC. Thus, this suggests that C-C bond scission is enhanced at higher temperature under alkaline conditions. However, the intensity of this feature is very low when compared to the acetate features observed before the transition point and there is no obvious solution carbonate band in the spectra in fig. 5.7, suggesting that even at 50 ^{o}C, complete oxidation of EtOH to carbonate has only a minor contribution to the overall oxidation process.

The 1573 cm^{-1} band was previously assigned (see section 3.2.3 and [12]) to the C=O stretch of acetate adsorbed through one O atom (Pt_s-O-C(=O)CH_3)), and the 1475 cm^{-1} feature to the C-H deformation of the same species [12]; both bands were more intense in the spectra collected at 50 ^{o}C compared to those at 25 ºC. In addition, fig. 5.18 shows the spectra depicted in fig. 5.13 enlarged over the range from 3050 – 2700 cm^{-1}. As may be seen from the figure, the loss features at ca. 2956, 2915 and 2850 cm^{-1}, previously assigned to adsorbed ethoxy (see section 3.2 and [12]), are of much greater intensity in the spectra collected at 50 ^{o}C than those collected at 25 ^{o}C.

Hence, it is clear from fig. 5.18 that increasing the temperature to 50 ^{o}C significantly enhances ethanol adsorption (as Pt-O-C_2H_5) at Pt at low potentials, and its subsequent oxidation to produce acetaldehyde and acetate.

5.3. Conclusions

The surface of the polycrystalline Pt electrode is extensively covered with adsorbed ethoxy at both 25 and 50 ^{o}C even at low potentials in aqueous KOH, with the (non-dissociatve) chemisorption of ethanol enhanced upon increasing the temperature.

Oxidation of the ethoxy species results in acetate, which is the predominant product under conditions of ethanol excess in solution at both temperatures investigated. The oxidation of adsorbed ethanol to form acetate at lower potentials (≤ -0.1V at 25 ºC and ≤ -0.4V at 50 ºC) is enhanced significantly upon heating from 25 ºC to 50 ºC, which is associated with the increased coverage of OH_{ads}.

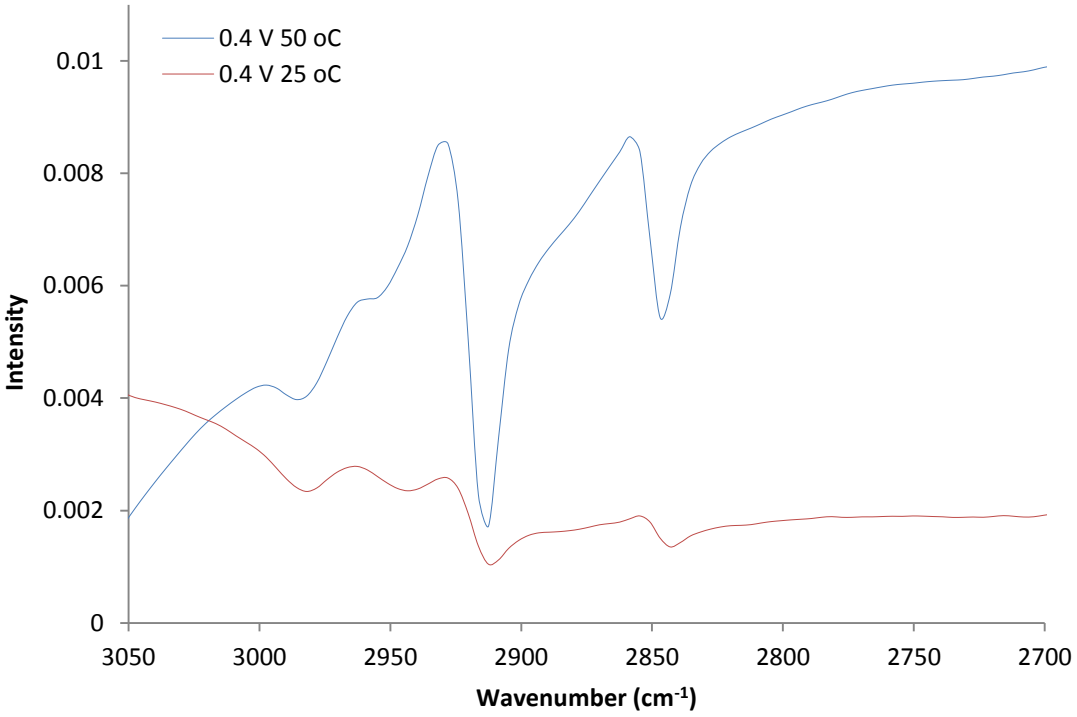

Figure 5.18. In-Situ FTIR spectra collected during the experiments depicted in fig. 2.1 over the spectral range from 3050 – 2700cm^{-1}.

In contrast to some reports in the literature, there is no evidence of carbonate production in the spectra collected below the transition potentials at 25 or 50 ºC. However, the loss feature at ca. 1540 cm^{-1} observed at both 25 and 50 ºC after the transition point may indicate small amounts of carbonate formation under alkaline conditions, with the C_1 route having only a minor contribution to the overall oxidation process even at 50 ºC. Small quantities of carbon dioxide are produced at potentials above transition, where the electrolyte in the thin layer is acidic, and acetic acid and acetaldehyde are also produced; the temperature dependence of this process strongly suggesting that the rate determining step in the oxidation is the removal of the first hydrogen atom from adsorbed ethoxide.

5.4. References

1. Chen, Q. S.; Sun, S. G.; Zhou, Z. Y.; Chen, Y. X.; Deng, S. B., *Physical Chemistry Chemical Physics.,* 2008, 10, 3645-3654.
2. Mahapatra, S. S.; Dutta, A. and Datta, J., *Electrochimica Acta*, 2010, 55, 9097-9104.
3. Dutta, A. and Datta, J., *International Journal of Hydrogen Energy*, 2013, 38, 7789-7800.
4. Ma, L.; Chu, D. and Chen, R., *International Journal of Hydrogen Energy*, 2012, 37, 11185-11194.
5. Pierozynski, B., *International Journal of Electrochemical Science*, 2012, 7, 4261-4271
6. Ma, Y.; Du, Y.; Ye, W.; Su, B.; Yang, M.; Wang, C., *International Journal of Electrochemical Science*, 2012, 7, 2654-2679
7. Heinen, M.; Jusys, Z.; Behm, R. J., *Journal of Physical Chemistry C*. 2010, 114 (21), 9850-9864
8. Jiang, L.; Hsu, A.; Chu, D.; Chen, R., *International Journal of Hydrogen Energy*, 2010, 35, 365-372.
9. Lai, S. C. S. and Koper, M. T. M., *Physical Chemistry Chemical Physics*, 2009, 11, 10446-10456.
10. Dimos, M. M.; Blanchard, G. J., *Journal of Physical Chemistry C.* 2010, *114*, 6019-6026.
11. Ureta-Zanartu, M. S.; González, T.; Fernandez, F.; Báez, D.; Berrios, C.; Gutierrez, C., *International Journal Electrochemical Science*, 2012, 7, 8794-8812
12. Christensen, P. A.; Jones, S. W. M. and Hamnett, A., *Journal of Physical Chemistry C*., 2012, 116, 24681−24689.
13. Lai, S. C. S.; Kleijn, S. E. F.; Öztürk, F. T.; van Rees Vellinga, V. C.; Koning, J.; Rodriguez, P. and Koper, M. T. M., *Catalysis Today*, 2010, 154, 82-104.
14. Iwasita, T. and Pastor, E., *Electrochimica Acta*. 1994, *39* (4), 531-537.
15. Iwasita, T.; Dalbeck, R.; Pastor, E.; Xia, X. *Electrochimica Acta*, 1994, *39* (11-12), 1817-1823.

16. Christensen, P. A. and Hamnett, A., *"Techniques and Mechanisms in Electrochemistry",* Chapman and Hall, London, 1994, 228 – 262
17. Christensen, P. A.; Linares-Moya, D., *Journal of Physical Chemistry C*. 2009, 114 (2), 1094-1101.
18. Christensen, P. A.; Hamnett, A.; Linares-Moya, D., *Physical Chemistry Chemical Physics,* 2011, 13(24), 11739-11747.
19. Rao, V.; Hariyanto. C. C. and Stimming, U., *Fuel Cells*, 2007, 7, 417 – 423.
20. Shao, M. H. and Adzic, R. R., *Electrochimica Acta.,* 2005, 50 (12), 2415-2422.
21. Zhou, Z.-Y.; Wang, Q.; Lin, J.-L.; Tian, N.; Sun, S.G., *Electrochimica Acta*., 2010, 55(27), 7995-7999.
22. Fang, X.; Wang, L.; Shen, P. K.; Cui, G.; Bianchini, C., *Journal of Power Sources*, 2010, *195* (5), 1375-1378.
23. López-Atalaya, M.; Moralloń , E.; Cases, F.; Vaźquez, J. L.; Peŕez, J. M., *Journal of Power Sources.,* 1994, 52 (1), 109-117.
24. Dreesen, L.; Humbert, C.; Hollander, P.; Mani, A. A.; Ataka, K.; Thiry, P. A.;Peremans, A., *Chemical Physics Letters*. 2001, 333, 327.
25. Berná, A.; Delgado, J. M.; Orts, J. M.; Rodes, A.; Feliu, J. M., *Electrochimica Acta*, 2008, 53, 2309.
26. CRC Handbook of Chemistry and Physics, Ed. D. R. Lide, 74th Edition, 1993-1994, Boca Raton, p8-47.
27. Brescia, F., LaMer, V. K. and Nachod, F. C., *Journal of the American Chemical Society*, 1940, 62, 614–617.
28. Wandlowski, T.; Ataka, K.; Pronkin, S.; Diesing, D., *Electrochimica Acta*., 2004, 49, 1233.
29. Camara, G. A.; Iwasita, T., *Journal of Electroanalytical Chemistry*, 2005, *578* (2), 315-321.
30. Xia, X. H.; Liess, H. D.; Iwasita, T., *Journal of Electroanalytical Chemistry,* 1997, *437* (1-2), 233-240.
31. Wang, Q.; Sun, G. Q.; Jiang, L. H.; Xin, Q.; Sun, S. G.; Jiang, Y. X.; Chen, S. P.; Jusys, Z.; Behm, R. J., *Physical Chemistry Chemical Physics,* 2007, *9* (21), 2686-2696.
32. Colmatti, F.; Tremiliosi-Filho, G.; Gonzalez, E. R.; Berna, A.; Herrero, E.; Feliu, J. M., *Faraday Discussions*, 2008, 140, 379−397.

33. Caram, J. A. and Gutiérrez, C., *Journal of Electroanalytical Chemistry*, 1992, 323, 213-230.

34. Freitas, R. G.; Pereira E. C.; Christensen, P. A., *Electrochemistry Communications*., 2011, 13, 1147-1150.

35. Freitas, R. G.; Antunes, E. P.; Christensen, P. A.; Pereira, E. C., *Journal of Power Sources*, 2012, 214, 351-357.

6. An in-situ FTIR study of undoped PolyBenzoImidazole as a function of relative humidity

6.1. Introduction

6.1.1. Overview

Undoped, cast films of PolyBenzoImidazole (PBI) were investigated as a function of humidity using both H_2O and D_2O, and as a function of temperature up to 100 °C in order to better understand the infrared response of this polymer, as well as to provide benchmark data for subsequent studies on acid doped PBI. Marked changes across the mid-IR range were observed during the uptake of water and D_2O. The use of D_2O proved extremely useful in terms of deconvoluting the complex IR response observed and allowed the IR data to be rationalised in terms of the disruption of the N-H…N inter-chain hydrogen bonded network and changes in the morphology of the polymer.

As discussed in section 1.6, PBI is considered as a promising membrane material for High Temperature Polymer-Electrolyte Membrane Fuel Cells (HT-PEMFCs) due to its excellent thermal and chemical stability [1-5], mechanical robustness and high tolerance to CO [6]. PBI has a glass transition temperature of 420 °C and is generally believed to be completely amorphous [7]. The conductivity of the polymer is strongly dependent upon doping with strong acid and can reach 0.25 S cm^{-1} at 180 °C[5].

It is generally believed that there is significant hydrogen bonding between the chains of undoped PBI [8][9][10], see scheme 6.1. Thus, Ramondo et al [11] studied the effect of intermolecular hydrogen bonding on the structure of imidazole. They found that the N…..H separation is unusually short (ca. 2.86 Å compared with ca. 3.21-3.29 Å in *p*-diaminobenzene for example), and hence particularly strong for such a hydrogen bond. This is supported by the high boiling point of imidazole (256 ^oC) and high degree of its association in non-polar solvents [12]. Scheme 6.2 shows the two canonical forms of imidazole described by Ramondo and co-workers as the principal contributors to the electronic structure of the molecule. They postulated that hydrogen bonding is associated with an increased contribution of state (II) with respect to state (I) and that the former is a better proton donor and acceptor than the

latter. Furthermore, the authors stated that an increased contribution from (II) leads to a stronger N-H….N interaction, thus explaining the unusually short hydrogen bonds in crystalline imidazole polymers.

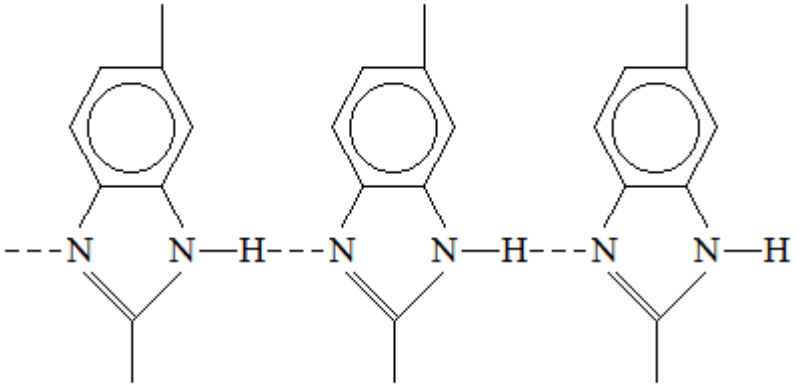

Scheme 6.1. Self-associated PBI, redrawn from [8]

(I) *(II)*

Scheme 6.2. Two canonical forms of imidazole, redrawn from [11].

From their ab initio molecular orbital modelling, Ramondo and co-workers calculated a lengthening of the N_1-H bond upon hydrogen bonding. They also predicted changes in the bonds within the heterocyclic ring, stating that an increase in hydrogen bond strength leads to the shortening of the N_1-C_2 bond by ca. 0.03 Å, and a complimentary increase in the length of C_2-N_3 bond. Hence, when exposed to water vapour, if the uptake of water by PBI does result in the disruption of the inter-chain hydrogen bonds and the formation of hydrogen bonds to water, as shown in scheme 3, this would be expected to have a significant effect upon the IR response of the polymer.

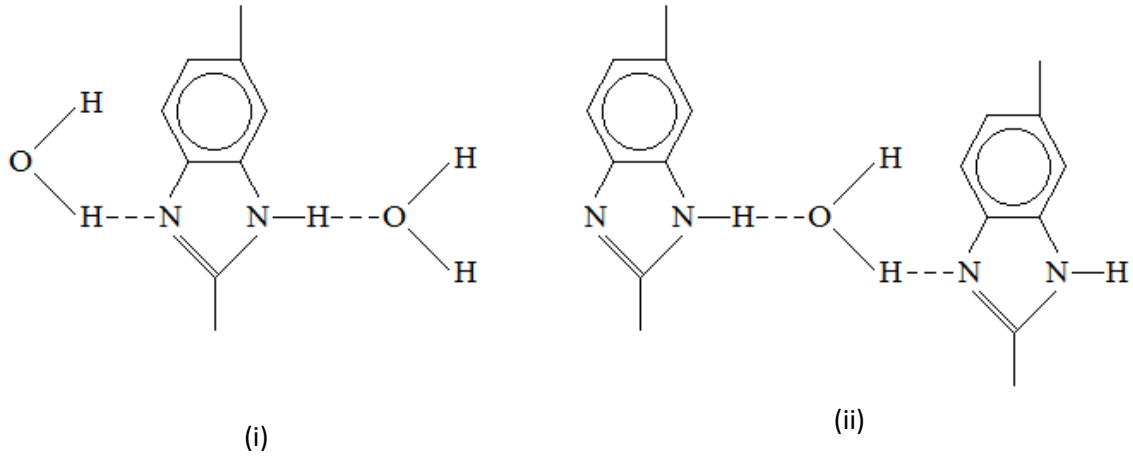

Scheme 6.3. Uptake of water by PBI: (i) 4 and (ii) 2 water molecules per repeat unit, redrawn from [10].

Zielinski and co-workers [13] observed pressure-induced phase transitions in their study of the hydrogen bonding in compressed benzimidazole polymorphs, with the NH….N bonded chains extending along the [011] and [0$\bar{1}$1] lattice planes in phase (α) and along [100] in phases (β) and (γ) (see scheme 6.4). Furthermore, they state that in phase (α), the planes of neighbouring molecules are rotated about the direction of the chain as opposed to phases (β) and (γ), within which molecules are rotated perpendicular to the chain. The consequence of this with respect to the work discussed below is that these phase transitions affect the dimensions and energy of the NH….N bond, with Zielinski and co-workers stating that the shortest and hence strongest of these bonds have angles closest to 180^{o}. Thus, the strength of the NH….N interactions are strongly dependent on the orientation of the H-accepting molecule in the hydrogen bond, the orientation of adjacent PBI chains and thus the structure and morphology of the PBI.

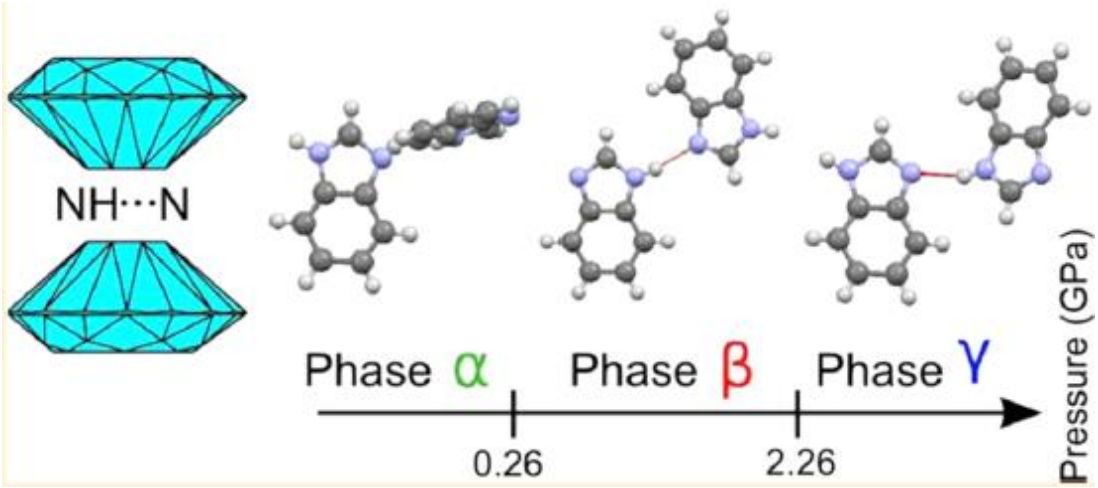

Scheme 6.4. The pressure induced phase-transitions of compressed benzimidazole polymorphs observed by Zielinski et al, parsed from [13].

6.1.2. FTIR Studies on Polybenzimidazole

There are a number of IR studies of PBI as a function of doping [7][14-16], blend composition [5][8-9][17-19] and temperature [5][8][14], and investigating hydrogen bonding in the polymer [8][9][10]. However, with one exception [9], spectral subtraction was not employed and hence small changes in spectral response due to, for example, increasing temperature could not be elucidated. In the work by Musto and colleagues [9] spectral subtraction was employed, but only over the spectral range covering the N-H absorptions of PBI. In fact, discussion of the IR spectra of PBI has largely been confined to the latter region due to the simplicity of the absorptions [14][19] which have, as a consequence, been fully assigned. Figure 6.1 shows the spectrum of PBI collected by Musto *et al* [9] during their study of the hydrogen bonding in thin film (ca. 2-5 μm) PBI/poly(ether imide) blends. As may be seen from the figure, the authors separated the complex N-H absorption of PBI into three distinguishable features at ca. 3415, 3145 and 3063 cm^{-1}. The relatively sharp 3415 cm^{-1} feature was attributed to isolated, non-hydrogen bonded N-H, the broad feature at 3145 cm^{-1} to the asymmetric stretch of self-associated, hydrogen bonded N-H (see scheme 6.1), and 3063 cm^{-1} feature to the stretching modes of aromatic C-H.

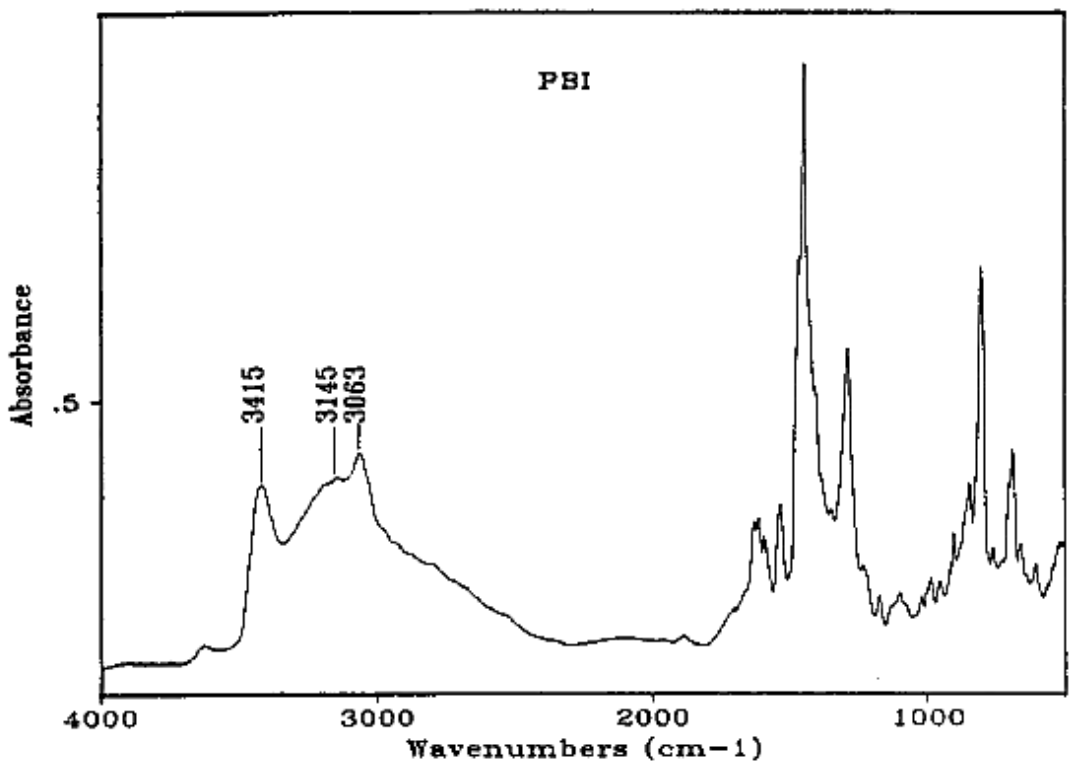

Figure 6.1. FTIR spectrum (200 co-added and averaged scans at 2 cm^{-1} resolution) of the PBI film (ca. 2-5 µm), collected in the study by Musto et al [9].

In a separate study, Musto *et al* [8] used FTIR spectroscopy to investigate the hydrogen bonding in the thin-film PBI samples as a function of temperature. Thus, fig. 6.2 shows the spectra of PBI collected by the authors at 30, 150, 200 and 250 ^{o}C. From the figure, it may be seen that Musto *et al* observed an increase in the intensity of the 3415 cm^{-1} feature and a decrease in the intensity of the 3145 cm^{-1} feature, both of which the authors stated to be reversible. However, no spectral evidence was presented to support the latter statement. It was postulated that the observations in fig. 6.2 indicated the existence of an equilibrium between free and self-associated N-H in PBI; and that upon heating, a significant number of hydrogen bonds in PBI are broken, leading to an increase in the intensity of the free N-H feature at 3415 cm^{-1} and a decrease in the self-associated N-H feature at 3145 cm^{-1}. Based on their model for hydrogen bonding in PBI chains (see scheme 6.1), Musto *et al* [8] suggested that both completely unnassociated N-H groups and terminal N-H groups of the hydrogen bonded chains contribute to the 3415 cm^{-1} feature. Furthermore, the

authors stated that the beadth of the 3145 cm^{-1} feature was related to, among other effects, the presence of hydrogen bonding between chains of different lengths within PBI, each absorbing at a slightly different frequencies. The authors again attributed the feature at ca. 3063 cm^{-1} to the aromatic C-H stretching modes of PBI and stated that this feature was only slightly effected by temperature. However, in contrast to the previous study, no spectral subtraction method was employed with the data shown in fig. 6.2 and hence small changes in the absorbance at 3063 cm^{-1}, and indeed the entire region for N-H absorption, could not be identified. The 3620 cm^{-1} feature was not discussed by the authors in context of the data presented in fig. 6.2, but was attributed later in the paper [8] to the O-H stretch of free water.

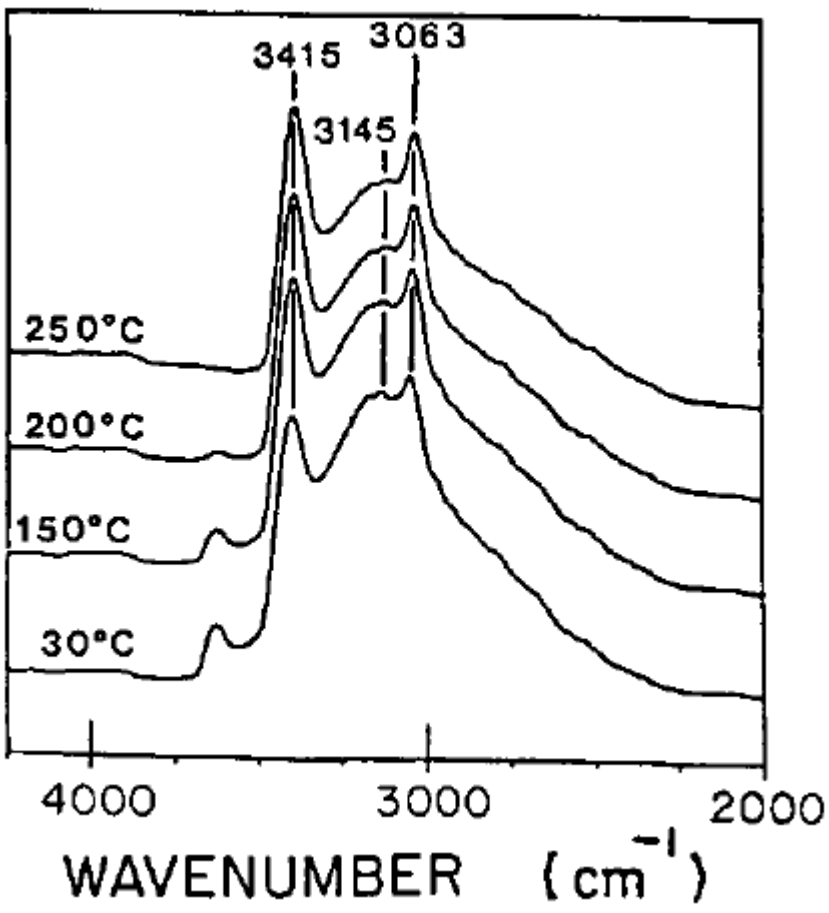

Figure 6.2. Spectra (200 co-added and averaged scans at 2 cm^{-1} resolution) of thin-film PBI collected by Musto et al [8] at 30, 150, 200 and 250 ^{o}C, over the spectral range from 4000-2100 cm^{-1}.

Figure 6.3 shows the FTIR spectra of wet and dry PBI collected by Brooks and co-workers [10] during their study of water uptake in thin PBI films (ca. 10 µm, cast from DMAc). The dry films were prepared by drying in a vacuum for 24 hours at 180 ^{o}C and the wet films by immersing in a beaker of water overnight. As may be seen from the figure, the feature at ca. 3620 cm^{-1} (3 on figure 6.3), attributed by the authors to the O-H stretch of free water, was present in the spectra of both the dry and wet samples. Brooks *et al* stated that the former was due to the uptake of water in the dry PBI film during its transfer from the oven to the spectrometer. A similar feature was observed in the spectra presented by Musto et al [8] (see fig. 6.2), suggesting that water uptake in dry PBI occurs in air at ambient temperature and humidity. This seems reasonable given that PBI is able to absorb up to ca. 15 wt.% H_2O at 100% RH [10][15].

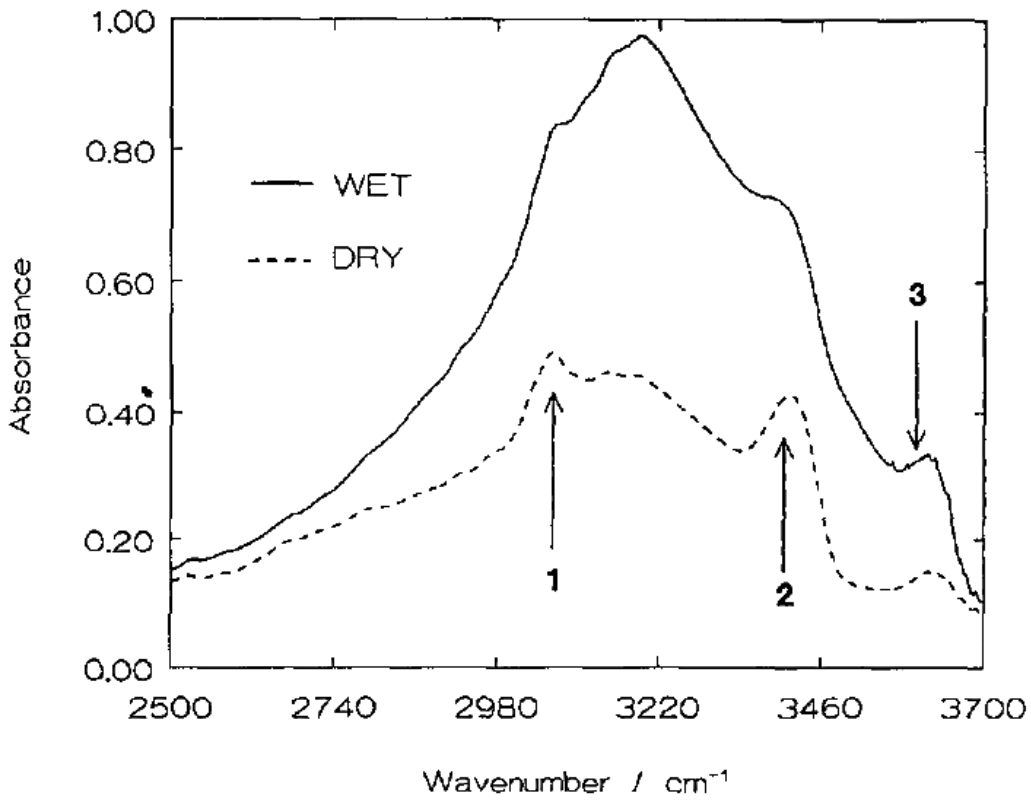

Figure 6.3. FTIR spectra of wet and dry PBI films (ca. 10 µm, cast from DMAc solution) collected by Brooks et al [10]. The authors assigned the spectral features as follows: (1) aromatic C-H stretch, (2) free N-H stretch of imidazole and (3) the O-H stretch of water.

Returning to fig. 6.3, it may be seen that the intensities of all of the features in the spectrum of the wet film were significantly greater than those in the spectrum of the dry film. Furthermore, the intensity of 3415 cm^{-1} feature relative to the feature at 3145 cm^{-1} was significantly greater in the wet sample, although this was not discussed by the authors. In fact, the authors stated that no specific information about the PBI hydrogen-bonding network in both the dry and wet samples could be elucidated from the spectra presented in fig. 6.3. This does not seem unreasonable when considering the fact that, as stated by Musto *et al* [8-9], the breadth of the complex N-H absorption region is due to hydrogen-bonded PBI chains of different lengths, thus producing a broad band with contributions from several absorptions. As discussed previously, employing a difference protocol would have again proved highly useful in elucidating small changes in the N-H absorptions and hence would have revealed more information about the differences in the hydrogen-bonding network between the wet and dry PBI films.

Figure 6.4 shows the spectra of a hydrated PBI film (ca. 20 µm, 1 g PBI cast from 10 ml DMSO) collected by Glipa *et al* [14] during their study of the conduction properties in H_3PO_4 and H_2SO_4 doped PBI membranes. The authors assigned the peaks in the N-H absorption region in fig. 6.4 according to the work by Musto *et al* [8-9] (see figs. 6.1 and 6.2). From the figure, it may be seen that the spectra are of very poor quality, making it difficult to discern many of the features in the spectral region below 2000 cm^{-1}. Nonetheless, the authors stated that the features in the region from 1600-1500 cm^{-1} were characteristic of benzimidazoles. More specifically, a feature at ca. 1612 cm^{-1} was attributed to the C=C/C=N stretch and two intense features at ca. 1543 and 1443 cm^{-1} to the in-plane deformation of the benzimidazole group in PBI. Further, a broad absorption at ca. 1240 cm^{-1} was attributed by the authors to the breathing mode of the imidazole ring and two features at ca. 1230 and 1090 cm^{-1} were assigned to C-H deformation vibrations, which the authors stated to be characteristic of substituted benzimidazoles such as PBI. From the data presented in fig. 6.4, Glipa and co-workers [14] suggested that upon heating the PBI film, the only significant spectral changes observed were in the region above 2000 cm^{-1}. However, due to the poor quality of the spectra and the fact that, again, no spectral subtraction

was employed, it is not clear that the authors could be certain that the region below 2000 cm^{-1} is not significantly affected upon heating to 230 ^{o}C.

Another example of not utilising a subtraction method when collecting spectra as a function of temperature comes from a more recent study by Li *et al* [6]. Hence, the authors could not discern any significant changes in the ATR-FTIR spectra of PBI films (20-80 µm, cast from DMAc solution (5 wt.% PBI)) upon heating to 400 ^{o}C in an Ar atmosphere. The authors only presented absolute spectra and omitted the 4000-2400 cm^{-1} region for clarity. This seems confusing given that, as established throughout the literature [8-9][10][14], this region contains key information about the hydrogen bonding within, and hence stability of, the PBI chains. In a more recent study [15], Li and co-workers presented FTIR spectra of PBI films (4-6 µm) over the spectral range from 3800 – 2000 cm^{-1} but summarised the features of the PBI spectrum across the full spectral range (see table 6.1).

Returning to the study by Glipa et al [14], and with respect to the features above 2000 cm^{-1}, the authors observed a decrease in the broad feature near ca. 3145 cm^{-1}, attributed by the authors to hydrogen-bonded N-H, upon heating the PBI film from 30 to 230 ^{o}C. This is similar to the behaviour observed in the spectra of PBI presented by Musto *et al* [8] (see fig. 6.2) during heating from 30 to 250 ^{o}C.

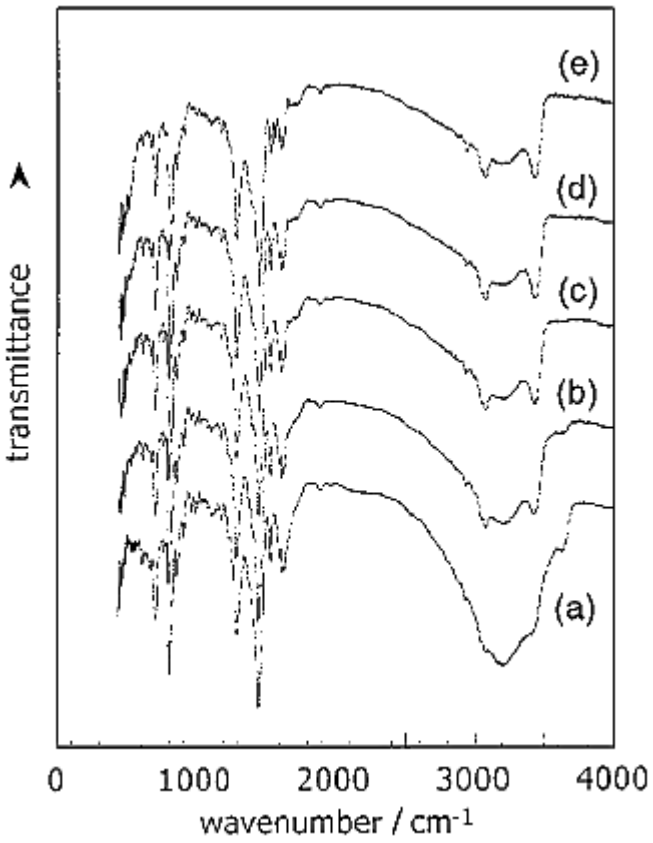

Figure 6.4. FTIR spectra of a hydrated PBI film (ca. 20 µm, 1 g PBI cast from 10 ml DMSO) collected by Glipa et al [14] at (a) 25, (b) 50, (c) 80, (d) 120 and (e) 230 ^{o}C.

6.1.3. Summary

In light of the literature discussed above, and despite the significant number of studies on the IR response of PBI under various conditions, there are none to my knowledge seeking to study in detail the absorptions in the fingerprint region of the polymer. Hence, the aim of this chapter is to study the effect of humidity on the mid-IR spectrum of undoped PBI using in-situ difference spectroscopy to provide benchmark spectral data for a planned FTIR study on acid doped PBI. This study was carried out using 4 PBI films: PBI1 had a thickness of ca. 4.4 µm and PBI2, PBI3 and PBI4 had thicknesses of ca. 7.9 µm.

6.2. Results and Discussion

6.2.1. Absolute spectra

Figure 6.5(a) shows absolute reflectance spectra (ie using an uncoated Ti disc as the reference) of 4.4 and 7.9 μm thick PBI films (PBI1 & PBI2, respectively) over the range from 4000 to 500 cm^{-1}, and fig. 6.5(b) the same spectra over a restricted range. The absolute spectra were collected as difference spectra according to the data manipulation in eq. 2.10 (see section 2.3.2). The frequencies of the various features are presented in table 6.1, along with those reported by Li *et al* [15] and Musto *et al* [19].

The 3620 cm^{-1} band has been attributed to the O-H stretch of free water within the film, which as discussed previously (see section 6.1.2), can be absorbed during the exposure to air of dry films [10][14], and hence the shoulders near 3620 cm^{-1} on both spectra in fig. 6.5(a) suggest that "free" water is present. It is important to be careful with respect to what is meant by "free" water here, as it is unclear from the literature what form of water is being referred to. Such a high stretching frequency, and narrow bandwidth, is generally associated with O-H stretches free from hydrogen bonding[21][22], rather than liquid/bulk water.

The 3145 cm^{-1} (ca. 3200 cm^{-1} in the spectrum of the thicker film) and 3413 cm^{-1} bands have been studied in detail, and as discussed previously (see section 6.1.2), there is general agreement with respect to their assignment[8-10][15][17– 19] to the stretching of self-associated and free N-H bonds (unassociated and terminal), respectively. The former are due to hydrogen bonding between PBI chains, as shown in scheme 6.1.

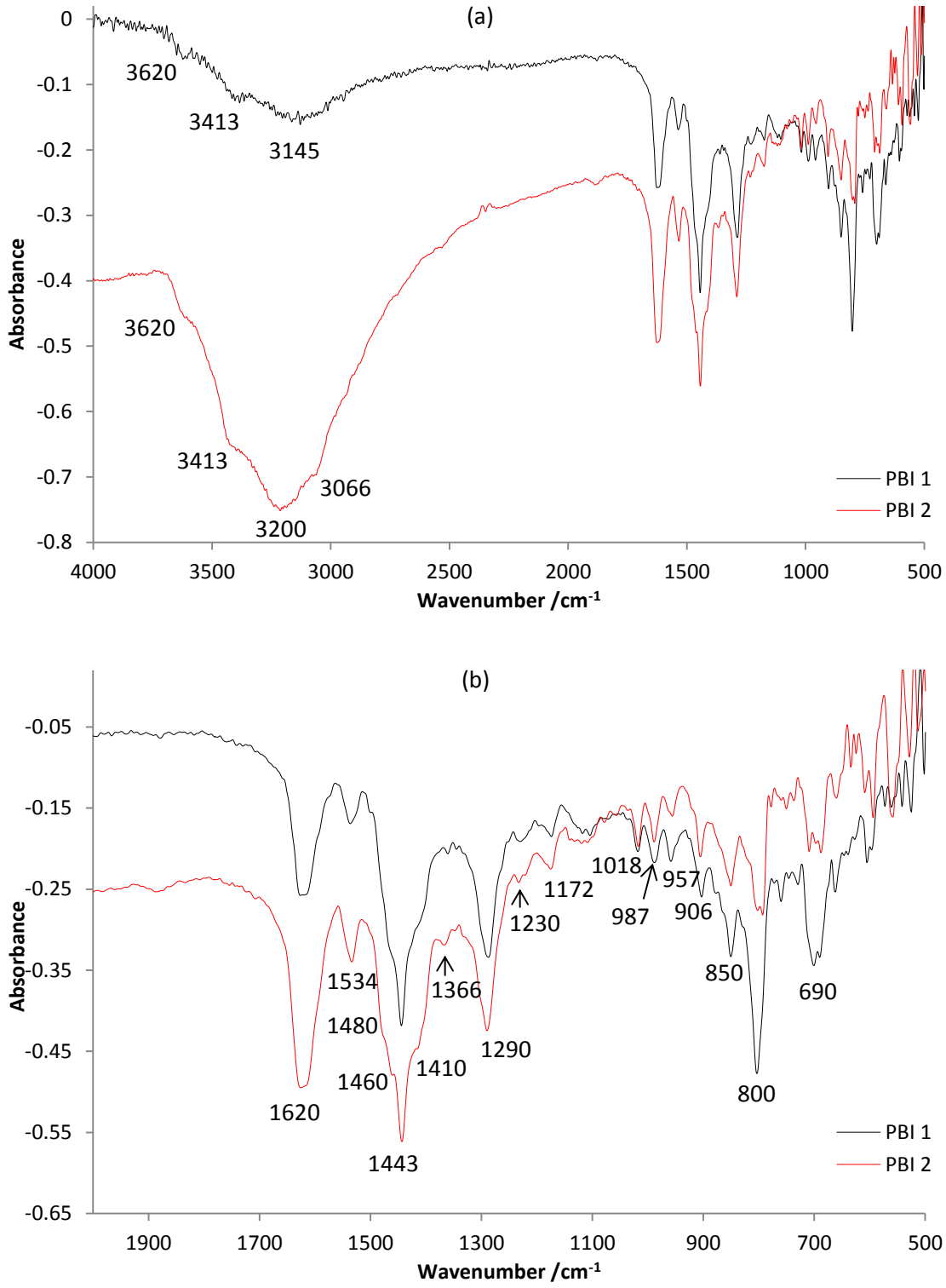

Figure 6.5. Spectra (250 co-added and averaged scans at 4 cm^{-1} resolution, ca. 5 minutes per scanset) of films (i) PBI1 (4.4 µm) and (ii) PBI2 (7.9 µm); (a) full spectral range, (b) 500 – 2000 cm^{-1}. The films were cast on a polished, 0.95 cm^2 Ti disc. The spectra were ratioed to the reference spectrum of the uncoated disc as according to equation (1).

This work	Li et al[15]	Musto et al[19]	Assignment[19]
690	701 vs	705 m	Heterocyclic ring vibration
760	760 w		
800	797 vs	801 s	Heterocyclic ring vibration or C-H out-of-plane bend of 3 adjacent H in substituted benzene ring.
850	840 w	846 m	C-H out-of-plane bend of 2 adjacent H in substituted benzene ring.
906	897 m	902 w	C-H out-of-plane bend of single H in substituted benzene ring.
957	943 m		
987		980 w	Benzene ring vibration
1018	1012 w	1011 w	Benzene ring vibration
1172	1170 m		
1230	1230 w	1226 w	In-plane C-H deformation of 2,6-disubstituted benzimidazole
1290	1285 vs	1286 m	Imidazole ring breathing
1366			
1410 sh		1410 m,sh	C-C stretching
1443	1440 vs	1443 vs	In-plane ring vibration characteristic of 2,6-disubstituted benzimidazole
1460 sh			
1480 sh			
1534	1530 s	1534 m	In-plane ring vibration characteristic of 2-substituted benzimidazole
1590	1599 w	1590 m	Ring vibration characteristics of conjugation between benzene and imidazole rings
1620	1621 vs	1612 m	C=C/C=N stretching
3065	3065 m	3063 w	Aromatic C-H stretching
3145	3145 br	3145 br	Self-associated N-H stretching
3413	3410 s	3415 s	Free, non-hydrogen bonded N-H stretching
3620	3620 m		O-H stretch of free water

Table 6.1. The features observed in the spectra in figs. 6.5(a) and (b) and those observed by Li et al[6] and Musto et al[19].

The breadth of the 3145 cm^{-1} feature is due to the variation in hydrogen-bonded 'chain length' [8][17] and the form of the absorptions in the N-H region is highly dependent upon the structure and composition, and in all likelihood, the morphology, of the polymer, as was discussed above. Evidence for the potential variability of the structure/morphology of the PBI between films nominally produced by the same method may be found by comparing figs. 6.5(a) and (b) to comparable spectra in the literature; this reveals marked variation in the ratio of the intensity of

the C=C/C=N band at 1620 cm^{-1} to the 1443 cm^{-1} in-plane benzimidazole ring vibration, suggesting a concomitant wide variation in polymer morphology. Thus, from the figures, it can be seen that the intensity of the 1620 cm^{-1} feature in the spectrum of PBI1 is ca. 56% of the intensity of the 1443 cm^{-1} feature; in the spectrum of PBI2, this same ratio is ca. 79%. In contrast, in all but one of the papers reporting mid-IR data on PBI [5][7-9][15][17-18], the 1620 cm^{-1} band is considerably (5 – 8x) weaker than the 1443 cm^{-1} feature. The exception is the paper by Pu and co-workers[16], where the C=C/C=N band is of comparable intensity to the 1443 cm^{-1} feature. There is also some variability in the frequency of the former. The only clear difference between the study of Pu et al and the other studies is the source of the PBI: Pu *et al* obtained their PBI sample from Aldrich, whereas all the other groups sourced their material from Celanese. The PBI employed in the work reported in this study was sourced from Between Lizenz, Stuttgart, Germany. Further, as can be seen from fig. 2(b), whilst the features of both films in the range 1000 – 1800 cm^{-1} are of similar intensity, the 800 cm^{-1} band in the spectrum of PBI1 is 2.4x the intensity of that of PBI2, yet the N-H absorptions of PBI2 are ca. 3.2x more intense than those of PBI1. It is not unreasonable to postulate that the structure and morphology of the PBI polymer chains are encoded in the IR spectra, rather as the amide I C=O absorptions contain information about the secondary structure of proteins [23].

As may be seen from fig. 6.5(b), the 1443 band is accompanied by shoulders near ca. 1410, 1460 and 1480 cm^{-1}; this complex group also appears in the spectra reported by other workers, with the relative intensities of the component peaks varying from group to group, (although the frequencies of the shoulders are generally not specified) see for example [7]. Thus, the variation in the relative intensities and, in some cases, frequencies of the IR bands of undoped PBI across the literature suggests that the IR response of such films is dependent upon their structure and morphology and, most likely, their synthesis method and thus the supplier/source of the polymer. Further, the fact that the relative intensities of the various features change suggests that the IR spectrum of a particular sample is a composite of the IR responses of the component chains of varying length/packing/etc.

6.2.2. The effect of humidity

Figure 6.6(a) shows spectra collected from PBI1 as a function of relative humidity up to ca. 90% ratioed to the reference spectrum collected in pure, dry N_2, according to the data manipulation in eq. 2.10 (see section 2.3.2). The spectra show a broad gain in intensity across the spectral range from 2600 to 3700 cm^{-1}, ie the range covering absorption by self-associated N-H, with increasing humidity, along with broad gains with maxima between 2000 and 2500 cm^{-1}, and near 716 cm^{-1}, the intensities of which appear to track that of the higher frequency feature.

Figure 6.6(b) shows the spectrum taken at 90% RH subtracted from that collected at 32% in order to ameliorate the effect of the features due to water vapour, over a restricted spectral range. On replacing the 90% RH atmosphere in the cell by pure, dry N_2, the spectra in figs 6.6(a) and (b) returned to baseline after 30 minutes, showing that the processes responsible for the changes in the spectra were reversible.

It is clear from figs. 6.6(a) and (b) that increasing humidity has a marked effect on the IR absorptions of the PBI, presumably due to the incorporation of water in the polymer structure: the key question is then where is the water incorporated? Musto et al[8] state that the spectrum of (undoped) PBI below 2000 cm^{-1} is characterized by narrow peaks attributable to ring vibrations, and the work of Ramondo et al [11] on imidazole and Zelinski and co-workers [13] on benzoimidazole suggest that the disruption of the N-H…..N hydrogen bonding (N-H self-association) by the incorporation of hydrogen-bonded water between the PBI chains (see scheme 6.2) would be expected to have a significant effect upon these ring vibration absorptions due to the impact on C-N and C-C bond lengths. Scheme 6.2 is redrawn from the paper by Brooks et al [10] who studied the uptake of water into dry, undoped PBI using, among other techniques, FTIR and NMR.

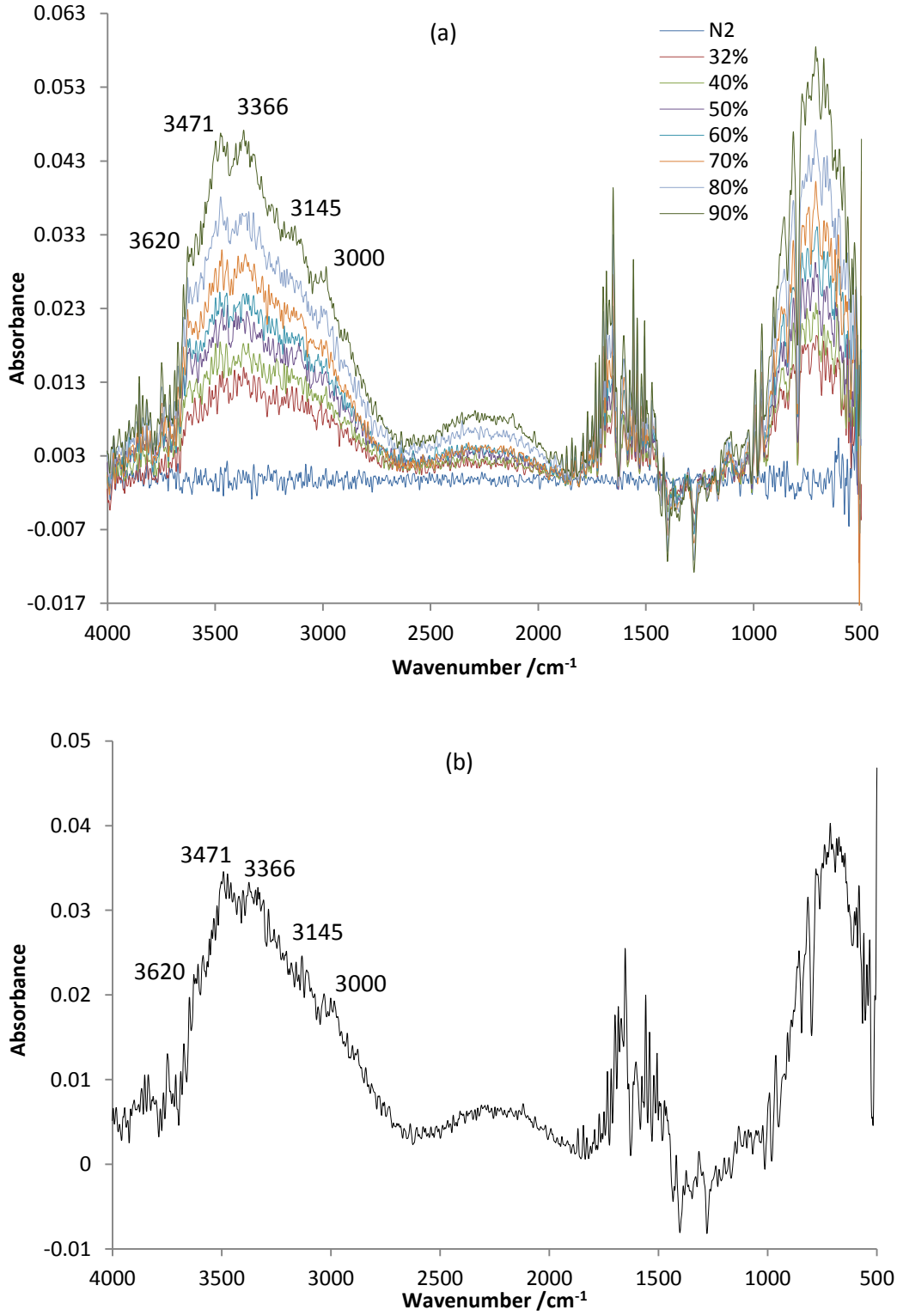

Figure 6.6. (a) Spectra of film PBI1 collected during an experiment in which the relative humidity (RH) was varied from 32% to 90%. A spectrum in N_2 was taken to check the stability of the system after the reference spectrum was collected. (b) The spectrum collected at 32% RH in fig. 6.2(a) subtracted from that taken at 90% RH in the same figure.

With respect to the FTIR data presented by Brooks et al [10], unfortunately, the authors only considered the IR spectral range between 2500 cm^{-1} and 3700 cm^{-1}; apart from commenting on seeing an increase in the free water band at 3620 cm^{-1}, they concluded that the data was inconclusive with respect to the formation of H-bonded water. In contrast, the NMR data, rate of water uptake and equilibrium water content vs RH were all interpreted in terms of the incorporation of the water into the polymer matrix without interaction, ie. without H-bonding between water and the PBI chains. However, this conclusion is in direct conflict with the generally-held view that incorporation of water is via hydrogen bonding; see for example [15].

The broad, relatively featureless gain between 2600 and 3700 cm^{-1} in fig. 6.6(a) suggests the gain of hydrogen bonded N-H….H-O-H with varying degrees of association (hence the breadth). The broad gain feature between ca. 1850 and 2750 cm^{-1} may be attributed to the combination band of bulk water [24]. The broad band centred near 720 cm^{-1} is featureless, but has sharp loss and gain bands superimposed upon it, and may be due to the gain of librational absorptions [25] associated with the incorporated water; however, the intensity of the latter feature seems disproportionately large, and further work is required to clarify its assignment.

Figure 6.6(b) clearly shows the presence of weak gain and loss features across the spectral range from ca. 1700 to 500 cm^{-1}; however, they are too weak to discern clearly. Thus, fig. 6.7 shows the spectrum in fig. 6.6(a) collected at 90% RH and also spectra collected at ca. 90% RH at the end of two repeats of the experiment in figs. 6.6(a) and (b) using films PBI3 & PBI4 which were both ca. 7.9 μm thick (0.9 mg cff 0.5 mg loading of PBI1). The broad gain feature having a maximum between 2000 and 2500 cm^{-1} in fig. 6.7 may again be attributed to the combination band of bulk or liquid water; this, along with the clear gain feature near 1670 cm^{-1} (the exact frequency of which is obscured by the loss feature near 1620 cm^{-1}) lending support to the postulated existence of this form of water in the film.

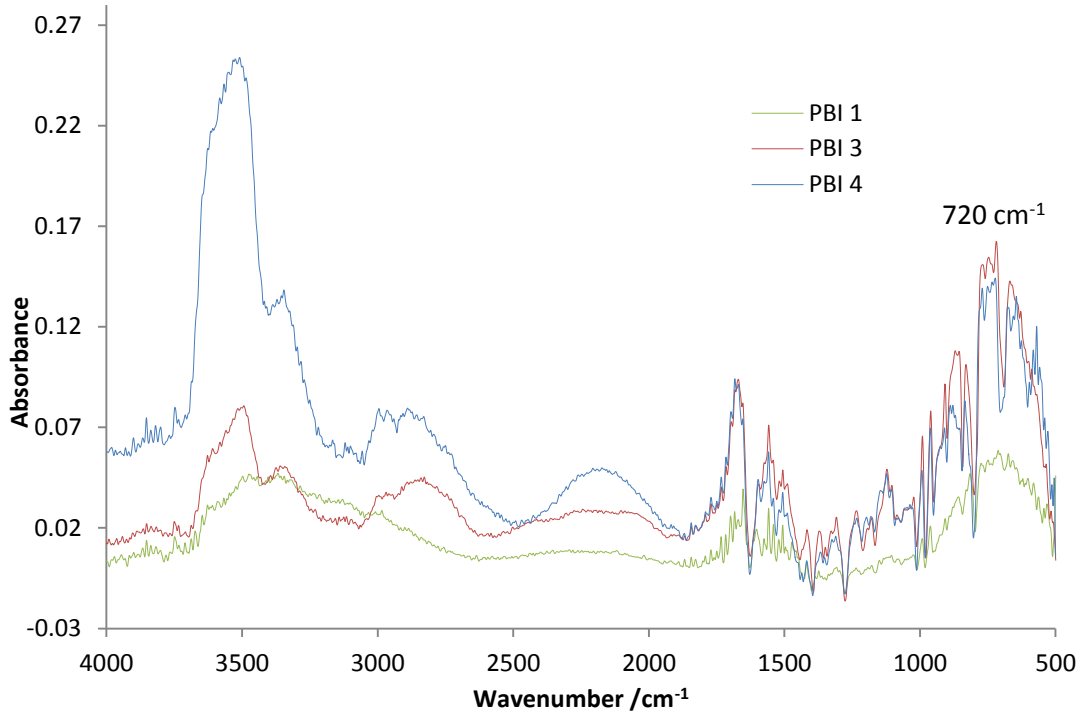

Figure 6.7. Spectra collected at 90% RH during repeats of the experiment depicted in fig. 6.6(a): (i) film PBI3 (7.9 µm) and (ii) PBI4 (7.9 µm) and (iii) the spectrum of PBI1 collected at 90% RH in fig. 2(a).

As may be seen from the figure, the loss and gain features below 2000 cm^{-1} are clear; in fact, the increase in the intensities of these bands is disproportionately large compared to the ca. 80% increase in PBI loading. These features may be seen more clearly in fig. 6.8 which shows the spectral range from 2000 to 500 cm^{-1} and omits the spectrum from PBI1. As can be seen, there are a plethora of sharp features, both gain and loss, which bear little resemblance to the spectrum in fig. 6.5(b). Again, the disparity between the intensities of the N-H absorptions relative to the sharp features below 2000 cm^{-1} suggests differences in morphology, although detailed analysis is hindered by the highly structured nature of the absorptions above 2500 cm^{-1}, possibly suggesting that this region is dominated by loss features due to the N-H absorptions superimposed upon which are gain features due to water as the N-H hydrogen-bonded networks are disrupted by the incoming water. In order to test the validity of this theory, the experiment represented by figs. 6.6, 6.7 and 6.8 was repeated using saturated NaCl in D_2O to produce the humid atmosphere, and the results are discussed in the next section.

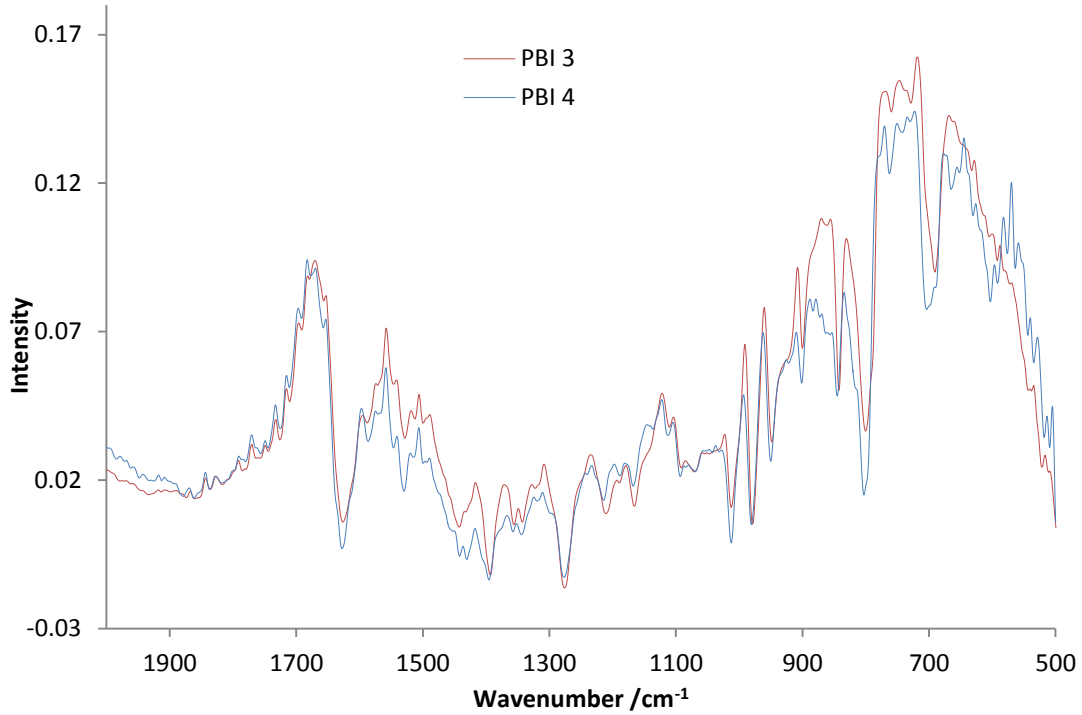

Figure 6.8. The spectra of (i) PBI3 and (ii) PBI4 in fig. 3(a) over the range 500 – 2000 cm^{-1}.

6.2.3. The effect of D_2O

The effect of D_2O vapour on PBI2 is shown in figs. 6.9 - 6.11. Figure 6.9 shows the spectra collected as a function of D_2O RH from 30 to 90% and figures 6.10 and 6.11 show the spectrum collected at 90% D_2O RH and the spectrum collected at 90% H_2O RH using PBI4 in figs. 6.7(a) and (b). Both films were nominally 7.9 μm thick, and the spectra ratioed to reference spectra collected in dry N_2.

Figure 6.10(b) clearly shows the gain of a broad feature giving a maximum near 2386 cm^{-1} attributable to the O-D stretch[26], and the loss of a well-defined, broad feature having a maximum near 3200 cm^{-1}. A comparison of figs. 6.5(a) and 6.10(a) clearly shows that the latter is due to H-bonded N-H moieties and a shoulder near 3413 cm^{-1} due to the "free" N-H stretch. Thus, the absorption due to the gain of the O-H stretch of bulk water is overlain by the N-H loss features in fig. 6.7(a); by using D_2O instead of water, the gain absorption due to the O-D stretch now appears very clearly, and the loss features due to the N-H bands are now also very clear: hence the use of D_2O rather than H_2O has clearly separated the water features from the changes

in the N-H region. This can also be seen from the absence of the gain feature near 1672 cm^{-1} (the precise frequency of which is obscured by the C=C/C=N loss feature) in the spectrum of PBI2 that is present in the spectra of PBI1, 3 and 4, and may be attributed to the H-O-H deformation associated with the O-H stretch of free water. The broad gain feature with a maximum near 720 cm^{-1} in the spectra obtained using H_2O is also absent when D_2O was employed. It is clear from the data in fig. 6.10(a) that, as well as water being hydrogen bonded between the polymer chains, it is also incorporated as bulk water, presumably in pores in the polymer. It is also clear that the incorporation of hydrogen bonding-free water is relatively minor.

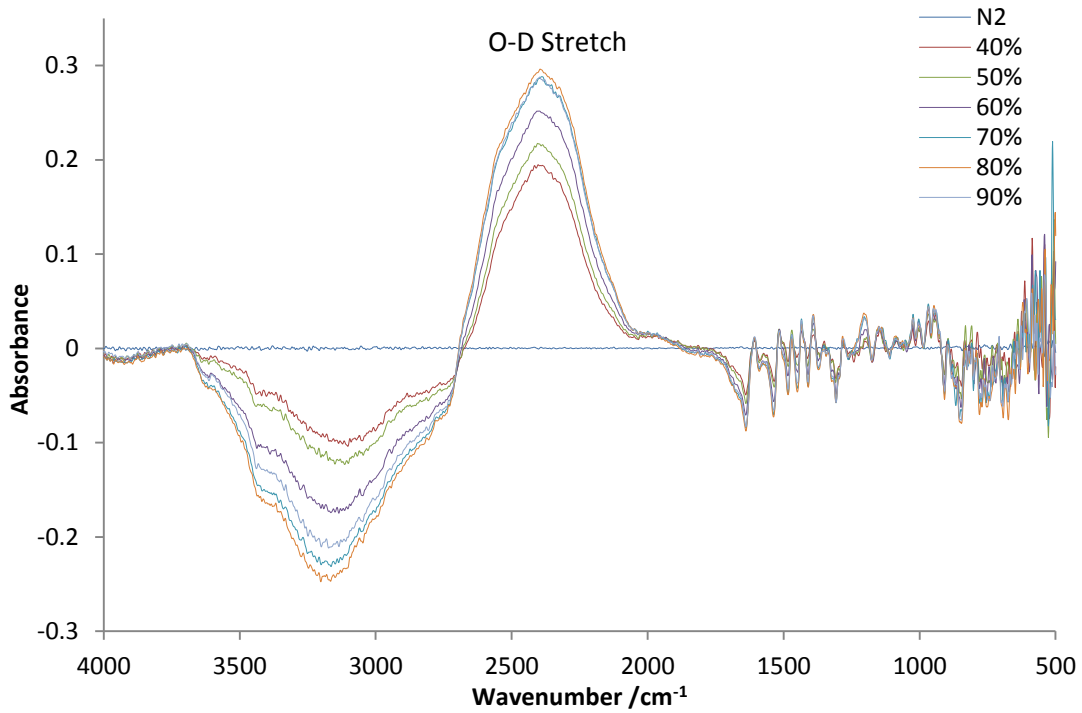

Figure 6.9. Spectra of film PBI2 collected during an experiment in which the D_2O RH was varied from 32 to 90%.

It may be seen from figs. 6.10(b) and 6.11 that there are more loss features in the D_2O spectrum than in the H_2O spectrum (although these bands may be attributed to the PBI, see table 6.1), with most being bipolar, with the bands shifting to lower frequency, suggesting that the uptake of D_2O has perturbed the PBI significantly more than the uptake of H_2O.

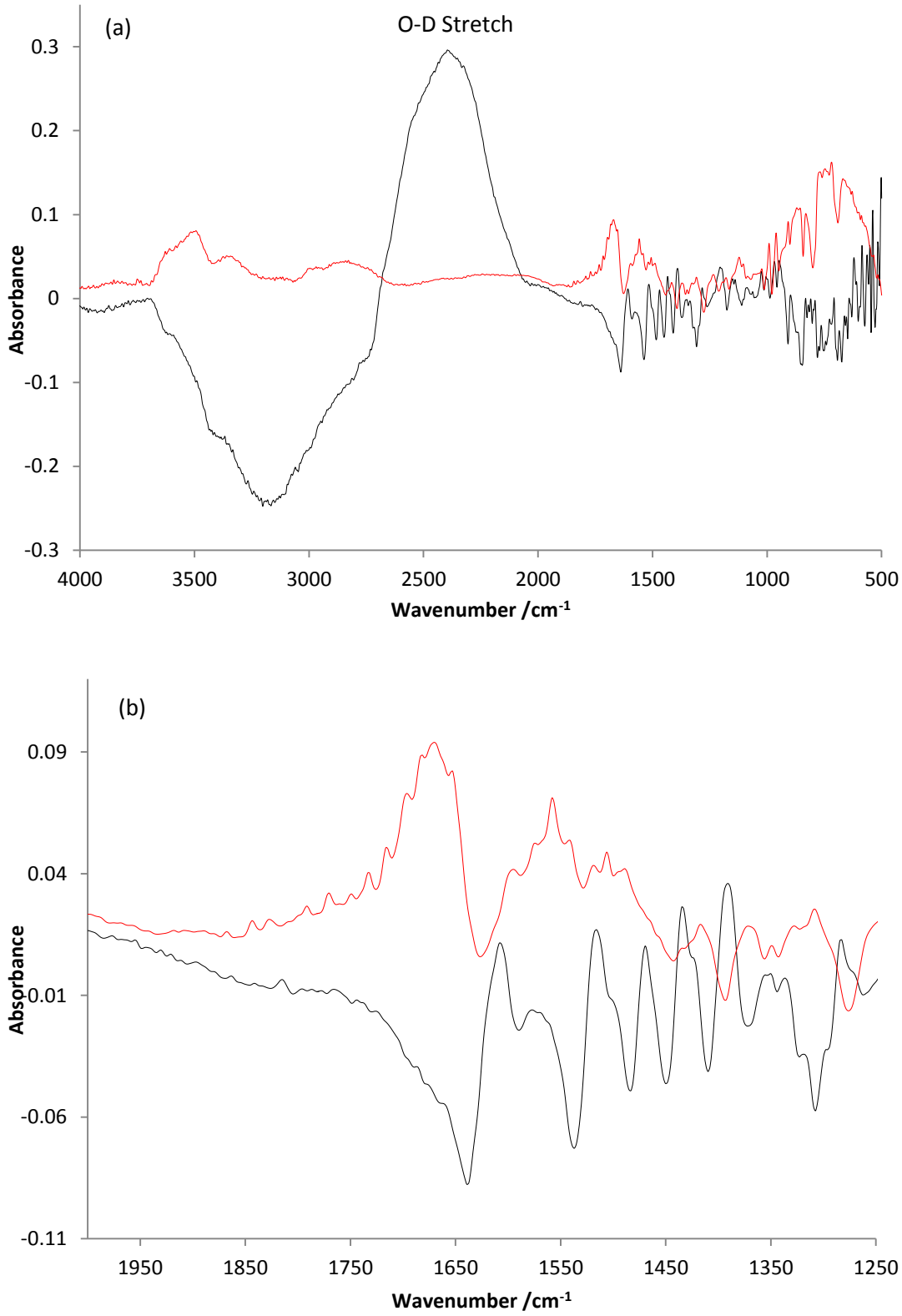

Figure 6.10. Spectra collected at 90%RH in (i) D_2O (PBI2) and (ii) H_2O (PBI4, spectrum from fig. 3(a)): (a) full spectral range, (b) 1250 – 2000 cm^{-1}.

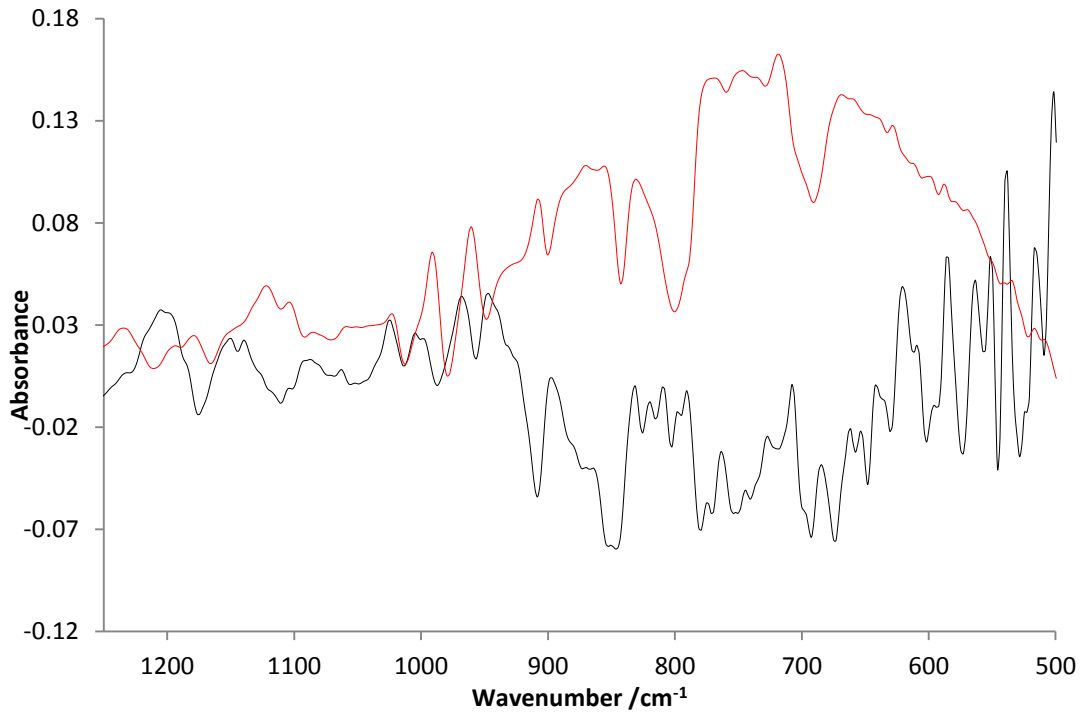

Figure 6.11. Spectra depicted in fig. 6.10(a) enlarged over the spectral range from 1250-500 cm^{-1}.

Given the postulated marked dependence of the ring vibrations on the degree of hydrogen bonding between the PBI chains discussed above, then it does not seem unreasonable to postulate that the uptake of D_2O results in the exchange of the N-H for N-D, with concomitant changes in the IR ring absorptions over and above those observed with water uptake. Thus, in contrast to the conclusions of Brooks and co-workers [10], the uptake of water by PBI, as well as resulting in regions of 'free' water, also disrupts the N-H…..N hydrogen bonded network due to the formation of hydrogen-bonded water as in scheme 6.2.

6.2.4. The effect of temperature

Figure 6.12 shows the effect of heating PBI4 to 100 °C in dry N_2. This experiment was carried out prior to that depicted in figs. 6.6(a) and (b). The film had been exposed to air during the drying process following casting. It is clear that significant water uptake took place during this time; this is not surprising given that the relative humidity in the UK does not fall below 70% and that, as discussed previously, PBI is able to absorb up to ca. 15 wt.% H_2O at 100% RH [10][15]. Figure 6.13 shows the

90% RH PBI4 spectrum in fig. 6.6(a) and that taken at 100 °C in fig. 6.12; from the figures, it is clear that the two spectra are essentially mirror images, as would be expected if water uptake was reversible.

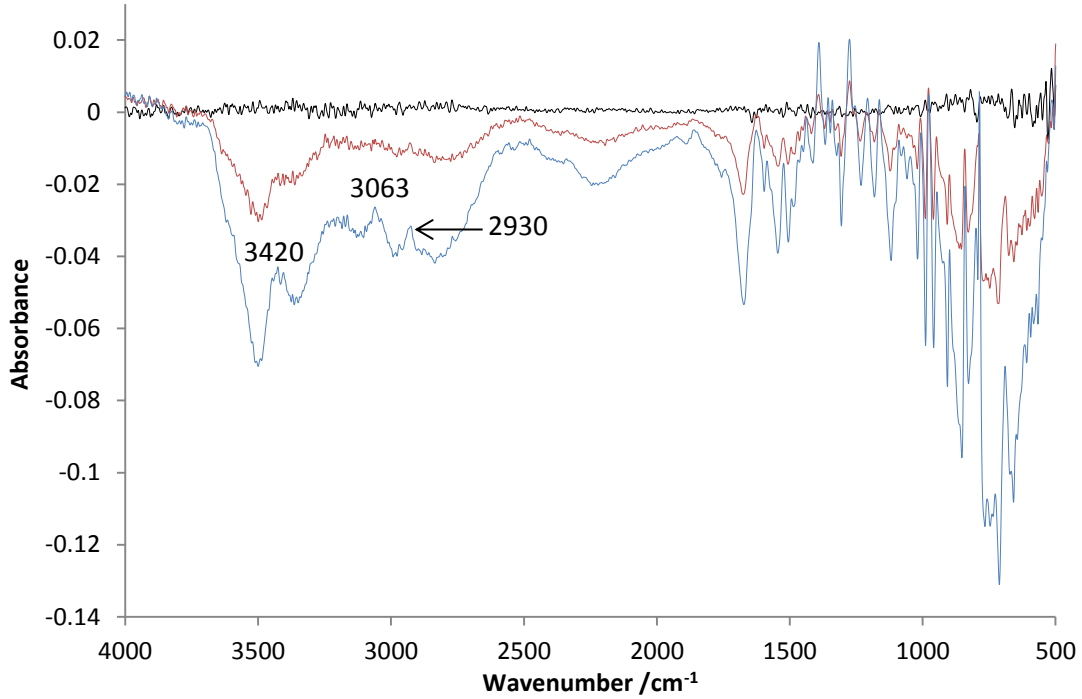

Figure 6.12. Spectra collected at (i) 25 °C (second spectrum), (ii) 50 °C and (iii) 100 °C from PBI4. The spectra were ratioed to the reference spectrum taken at 25 °C (first spectrum). The experiment was conducted prior to the humidity experiment depicted in figs. 6.6(a) and (b).

6.3. Conclusions

The absorption of water from the atmosphere by freshly-cast films of PBI is appreciable and relatively rapid. The two primary models of water uptake are either: (1) incorporation without disruption of the interchain hydrogen bonding, as bulk water in pores or as hydrogen bonding-free water or (2) incorporation of water between the polymer chains with the formation of hydrogen bonds and consequent disruption of the interchain hydrogen bonds. The data clearly show that all of these processes take place: some small incorporation of "free" water, as well as more significant incorporation of bulk or liquid water, and also clear and marked disruption of the interchain, N-H….H hydrogen bonds due to the insertion of water

between the chains with the formation of hydrogen bonds between these water molecules and the PBI chains.

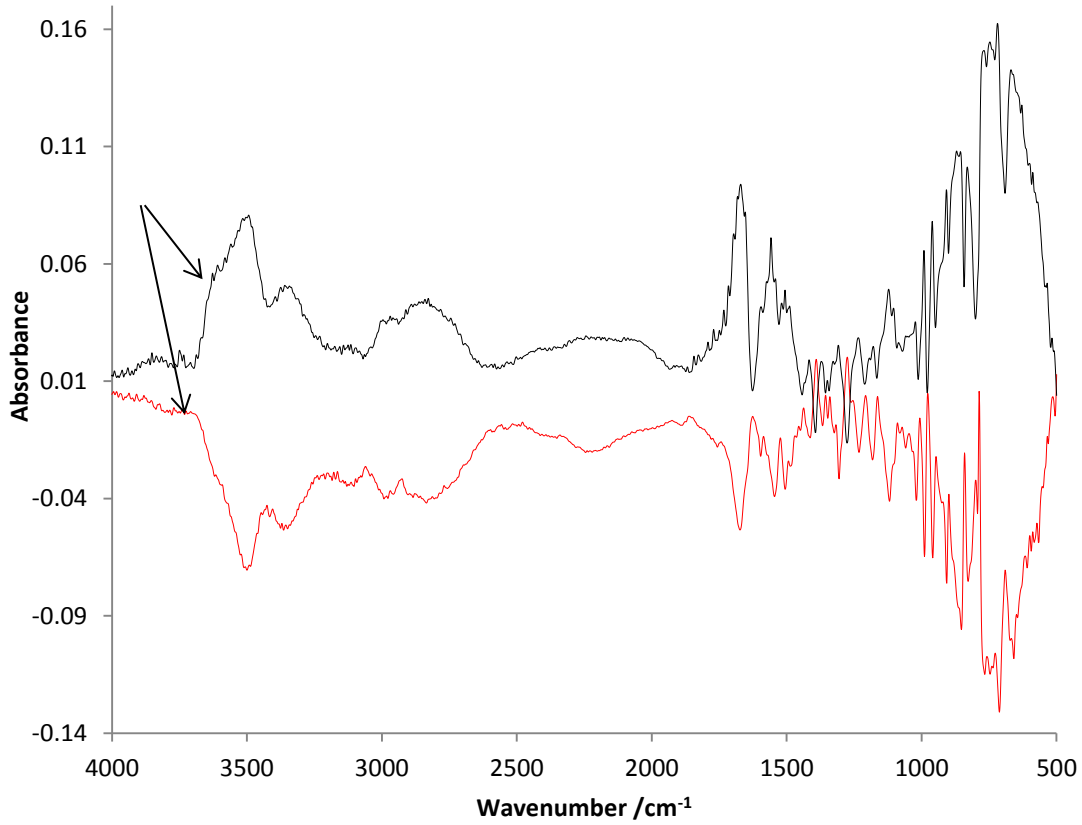

Figure 6.13. (i) The spectrum of PBI4 collected at 90% RH during the experiment depicted in fig. 6.6(a) and (ii) that taken at 100 °C in fig. 6.10(a).

Finally, the structure and morphology of the PBI films appear to vary between samples, even between samples prepared by nominally identical procedures, as evinced by changes in the relative intensities of various features in the IR spectra. The possible consequence of this is that significant information on the structure of PBI films is encoded in their IR spectra, but further work is required to elucidate this.

6.4. References

1. Samms, S. R.; Wasmus, S.; Savinell, R.F., Journal of the Electrochemical Society, 1996, 143, 1225

2. Kerres, J.; Ullrich, A.; Meier, F.; Haring, T., *Solid State Ionics*, 1999, 125, 243
3. Cassidy, P. E., *Polybenzimidazoles. In: Thermally stable polymers: synthesis and properties.* Marcel Dekker, Inc., New York, 1980, Sect. 6.10, 6.18-2
4. Hogarth, W. H J.; Diniz da Costa, J. C.; Lu, G.Q., *Journal of Power Sources*, 2005, 142, 223
5. Aili, D.; Cleemann, L. N.; Li, Q.; Christensen, E.; Bjerrum, N. J., Journal of Materials Chemistry, 2012, 22, 5444
6. Li, Q.; He, R.; Gao, J.; Jensen, J. O.; Bjerrum, N.J., Journal of the Electrochemical Society, 2003, 150, A1599
7. Bouchet, R; Siebert, E., *Solid State Ionics*, 1999, 118, 287
8. Musto, P.; Karasz, F.E.; MacKnight, W.J., *Polymer*, 1989, 30, 1012
9. Musto, P.; Wu, L.; Karasz, F. E.; MacKnight, W.J., *Macromol*, 1991, 24, 4762
10. Brooks, N.W.; Duckett, R.A.; Rose, J.; Ward, I.M.; Clements, J., *Polymer* 1993, 34, 4038.
11. Ramondo F, Bencivenni L, Gustavo P, Domenicano A, *Structural Chemistry*, 5, 1994, pp1-7.
12. Hofmann K., *Imidazole and Its Derivatives, Part I: Interscience*: New York, 1953; pp5-25.
13. Zieliński, W.; Katrusiak, *Crystal Growth & Design*, 2012, 13, 696-700.
14. Glipa, X.; Bonnet, B.; Mula, B.; Jones, D.J.; Rozière, Journal of Materials Chemistry, 1999, 9, 3045
15. Li, Q.; He, R.; Berg, R.W.; Hjuler, H.A.; Bjerrum, N.J., 2004, *Solid State Ionics*, 168, 177
16. Pu, H; Liu, Q; Yang, Z., *Polymer Engineering and Science*, 2005, 1395
17. Guerra, G.; Choe, S; Williams, D.J.; Karasz, F.E.; MacKnight, W.J.; 1988, *Macromol*, 21:231
18. Musto, P.; Wu, L.; Karasz, F.E.; MacKnight, W.J., 1991, *Polymer*, 32, 3
19. Musto, P.; Karasz, F.E.; MacKnight, W.J., 1993, *Polymer*, 34, 2934.
20. Boedeker, 2013, *Celazole Polybenzimidazole Specifications*, [Accessed 8th October 2013], Avaialble from: http://www.boedeker.com/celazole.htm

21. Dreesen, L.; Humbert, C.; Hollander, P.; Mani, A. A.; Ataka, K.; Thiry, P. A.; Peremans, A. *Chemical Physics Letters*, 2001, *333*, 327.
22. Berná, A.; Delgado, J. M.; Orts, J. M.; Rodes, A.; Feliu, J. M., *Electrochimica Acta*, 2008, *53*, 2309.
23. Barth, A.; Zscherp, C., *Quarterly Review of Biophysics*, 2002, 35, 369-430.
24. Giguere, P. A.; Harvey, K. B., *Canadian Journal of Chemistry*, 1956, 34, 708-808
25. Keutsch, F. N.; Fellers, R.S.; Brown, M.G.; Viant, M.R.; Petersen, P.B.; Saykally, R.J., 2001, *Journal of the American Chemical Society*, 123, 5938.
26. Lappi, S. E.; Smith, B.; Franzen, S., *Spectrochimica Acta*, 2004, Part A 60, 2611–2619

7. Conclusions and Future Work

The *in-situ* FTIR studies on the electro-oxidation of ethanol at Pt in 0.1 M KOH have shown that the reaction involves primarily adsorption through O and successive two-electron oxidations to CH_3CHO and CH_3COO^-. It has been established that under conditions of ethanol starvation, the adsorbed acetate species can form a further intermediate that we have tentatively identified at Pt_s-CH_2-C(=O)-O-Pt_s on the basis of IR and chemical likelihood, and this is the dominant route under ethanol starvation conditions. Hence, Pt is intrinsically capable of fully oxidising ethanol to carbonate in alkaline solution, but under normal fuel-cell operating conditions this is unlikely to be the dominant route. The investigation of ethanol electro-oxidation at 50 ^oC revealed that the production of acetaldehyde and acetic acid is temperature dependent, strongly suggesting that the rate determining step in this process is the removal of the first proton from the initially-adsorbed ethoxide species, and it was tentatively suggested that this is also the rate determining step under alkaline conditions.

The FTIR studies at a Pb-modified, polycrystalline Pt anode in 0.25 M KOH have shown, surprisingly, that significant carbonate may be formed at very low potentials, and it was postulated that this takes place at Pt domains between Pb islands. The extent of catalysis is restricted since only at the particular edges of Pb islands will appropriate conditions exist for oxidation. Hence, if this catalysis is to be developed further, a surface must be fabricated in which the formation of Pb islands is carefully controlled, thus leaving exposed Pt in regions large enough to act as efficient catalytic centres, but sufficiently small that the highly unusual properties seen in the results presented in Chapter 4 can be retained. Future work may also include the application of FTIR to the analysis of EtOH electro-oxidation at PtPb with Pb in solution. However, optical problems due to Pb deposition taking place during spectral data collection must be overcome in order to obtain reliable data.

Bi is generally accepted as a facile source of OH, and hence would be interesting to investigate as adatoms on polycrystalline Pt to supplement the studies on Pb. Preliminary experiments should focus on the voltammetry of Bi-modified Pt in the absence and presence of ethanol, both pre-adsorbed and in solution, supported by appropriate in-situ FTIR experiments.

The preliminary FTIR studies on PBI as a function of humidity and temperature have shown that water uptake by PBI is appreciable and relatively rapid. The two primary models of water uptake are either: (1) incorporation without disruption of the interchain hydrogen bonding, as bulk water in pores or as hydrogen bonding-free water or (2) incorporation of water between the polymer chains with the formation of hydrogen bonds and consequent disruption of the interchain hydrogen bonds. The data presented in Chapter 6 clearly show that all of these processes take place. Further, the structure and morphology of the PBI films appear to vary between samples, causing changes in the relative intensities of various features in the IR spectra. It is therefore likely that significant information on the structure of PBI films is encoded in their IR spectra, but further work is required to elucidate this. Unfortunately, time did not allow for FTIR studies of acid-doped PBI films (eg. H_3PO_4), and it does not seem unreasonable to suggest this as the next stage of research. As a first step, absolute spectra of the doped films should be collected in order to elucidate changes in the hydrogen bonding network caused by the uptake of acid by the polymer, before progressing to studies as a function of humidity and temperature.

A potential application of the *in-situ* FTIR experimental system employed in the PBI studies, which has not yet been realized, is to the analysis of HT-PEMFC anodes as a function of temperature and gas composition (eg. CO, H_2). This was originally included as part of the Supergen project but, due to the intriguing nature of the work on ethanol oxidation and PBI, it was not possible to commence these studies. Another potential application is to the analysis of porous Pt catalyst/electrode films interfaced with yttria-stabilised-zirconia (YSZ) solid electrolyte membranes, which have found application in solid oxide fuel cells. Initial research should be focussed on the fundamental IR studies of Pt-YSZ under open circuit potential as a function of temperature and gas composition within the environmental chamber.